Thermal Field Theory in the Presence of a Background Magnetic Field and its Application to QCD

Munshi G. Mustafa[a,*], Aritra Bandyopadhyay[b], Chowdhury Aminul Islam[c]

[a] *Department of Physics, Indian Institute of Technology Bombay, Pawai, Mumbai 400076, India*
[b] *Department of Physics, West University of Timişoara, Bd. Vasile Pârvan 4, Timişoara 300223, Romania*
[c] *Institut für Theoretische Physik, Johann Wolfgang Goethe-Universität, Max-von-Laue-Str. 1, D-60438 Frankfurt am Main, Germany*

Abstract

This review has explored the fundamental principles of thermal field theory in the context of a background magnetic field, highlighting its theoretical framework and some of its applications to the thermo-magnetic QCD plasma generated in heavy-ion collisions. Our discussion has been limited to equilibrium systems for clarity and conciseness. We analyzed bulk thermodynamic characteristics including the phase diagram as well as real-time observables, shedding light on the behaviour and dynamics of the thermo-magnetic QCD medium relevant to heavy-ion physics.

Keywords: Non-Central Relativistic Heavy-Ion collisions, Quark-Gluon Plasma (QGP), Finite Temperature Field Theory, Background Magnetic Field, Quantum Chromodynamics (QCD), Dilepton Rate, Heavy Quark, Phase Diagram

Contents

*Corresponding author: Ex-senior Professor, Theory Division, Saha Institute of Nuclear Physics, HBNI, 1/AF Bidhan Nagar, Kolkata 700064, India
   Email address: munshigolam.mustafa@saha.ac.in (Munshi G. Mustafa)

1. Introduction

The Quark-Gluon Plasma (QGP) is a state of hot, dense matter in which quarks and gluons, the fundamental components of Quantum Chromodynamics (QCD), are no longer confined within protons and neutrons. This state is believed to have existed briefly, only a few microseconds after the Big Bang. Understanding and characterizing the QGP remains a major focus of modern nuclear physics, involving extensive international collaboration. Currently, the QGP is studied in high-energy collisions of heavy nuclei at particle accelerators, such as the Relativistic Heavy Ion Collider (RHIC) at Brookhaven National Laboratory (BNL) and the Large Hadron Collider (LHC) at CERN. These experiments, conducted

at relativistic speeds, continue to yield valuable data on the properties of this fleeting state of matter. In addition, the upcoming Facility for Antiproton and Ion Research (FAIR) at GSI will explore collisions at energies between 10 and 40 GeV per nucleon with high luminosity. This research aims to investigate the deconfinement phase transition at high baryon densities, complementing the studies at RHIC and LHC. A deeper theoretical understanding of the QGP, including both its static and dynamic properties, is essential for interpreting these experimental results and advancing knowledge of hot and dense deconfined matter.

Recent studies [1–14] have highlighted intriguing properties of non-central heavy ion collisions (HIC). A schematic of non-central HIC is shown in the left panel of Fig. 1.1, while the right panel illustrates a cross-sectional view along the beam axis (y-axis) of two colliding heavy ions, each with radius R and electric charge Ze, where e represents the electron charge. The distance between the centers of the colliding nuclei, known as the impact parameter b, determines the degree of non-centrality-the larger the impact parameter, the more non-central the collision becomes. The $z = 0$ plane defines the reaction plane. The magnetic field generation in such collisions can be understood as follows: the overlapping region of the colliding nuclei contains participant particles, forming a fireball. The remaining particles, called spectators, do not undergo scattering and continue to move with nearly the same rapidity as the beam. Due to the relative motion between the participants and spectators, a significant anisotropic magnetic field can be generated according to the Biot-Savart law in the center-of-mass frame [15–17] as

$$B_z \sim \gamma Ze\frac{b}{R^3}\,, \tag{1.1}$$

in the direction perpendicular to the reaction plane (i.e., z-axis). The Lorentz factor is given by $\sqrt{s_{NN}}/2m_N$. Now one can estimate the magnetic field produced at different centre-of-mass energy. At RHIC $\sqrt{s_{NN}} = 200$ GeV per nucleon that leads to $\gamma = 100$ with he number proton for gold nucleus $Z = 79$ and $b \sim R_A \sim 7$ fm, one can estimate $eB_z \approx m_\pi^2 \sim 10^{18}$ G. For LHC one can estimate $eB_z \approx 15m_\pi^2$. We note that the magnetic field generated on earth in a form of electromagnetic shock wave is of the order of 10^7 G [18], in neutron star is in the range of $(10^{10} - 10^{13})$ G and in magnetar up to 10^{15} G [19–22]. Therefore, the scales generated in HICS due to the magnetic field are relevant to QCD and that is why non-central HIC is gaining more and more attention from the heavy ion community.

1.1. Generation of Magnetic Field

In the this subsection 1.1, we will discuss the generation of magnetic field in different physical situations [15–17, 24, 25].

1.1.1. Single charge moving with constant velocity in vacuum

For a single moving charge with constant velocity $\vec{v}$ in vacuum, the electromagnetic field can be obtained from Liéneard-Wiechert potentials [26] as

$$e\vec{E}(\vec{r}, t) = \alpha \left[\frac{\left(\hat{\boldsymbol{R}} - \vec{v}/c \right)}{\gamma^2 R^2 \left(1 - (\hat{\boldsymbol{R}} \cdot \vec{v})/c \right)^3} \right]_{\text{ret}}, \tag{1.2a}$$

$$e\vec{B}(\vec{r}, t) = -\alpha \left[\frac{\hat{\boldsymbol{R}} \times \vec{v}}{\gamma^2 R^2 \left(1 - (\hat{\boldsymbol{R}} \cdot \vec{v})/c \right)^3} \right]_{\text{ret}}. \tag{1.2b}$$

Let's recall what everything in these expressions mean. The particle traces out a trajectory $\vec{x}(t)$, while one sits at some position $\vec{r}$ which is where the electromagnetic fields are evaluated. The vector $\vec{\boldsymbol{R}}(t)$ is the difference: $\vec{\boldsymbol{R}} = \vec{r} - \vec{x}$, the Lorentz factor is given as $\gamma = 1/\sqrt{1 - v^2/c^2}$ and α is the electromagnetic coupling constant. The 'ret' subscript means
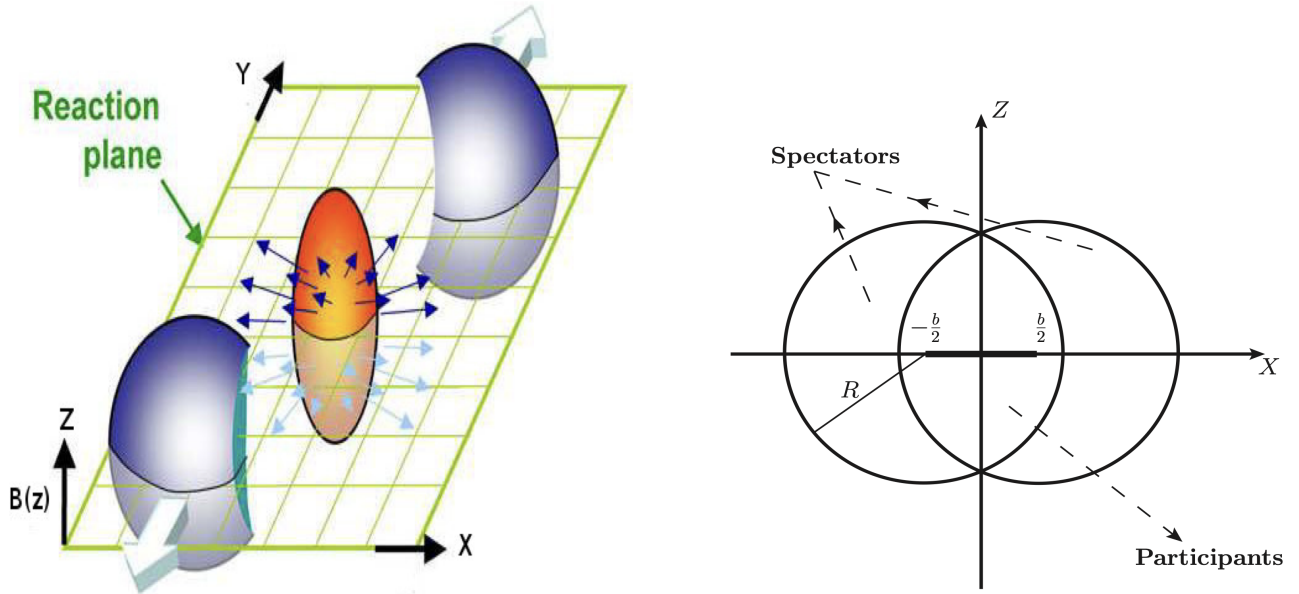
Figure 1.1: **Left panel**: the schematic illustration of a non-central heavy-ion collision **Right panel**: the cross-sectional view of the non-central HIC along the beam axis (y-axis) depicts the overlapping region of the two colliding nuclei. These figures are adopted from Ref. [23].

one evaluate everything inside the square brackets at retarded time $t' = t - R(t')/c$.

We note that (1.2a) drops like of as $1/R^2$ which becomes usual Coulomb field. It can be thought of as the part of the electric field that remains bound to the particle. The fact that it is proportional to $\hat{\mathbf{R}}$, with a slight off-set from the velocity, means that it is roughly isotropic. We see that the (1.2b) has a similar form to the electric field in (1.2a). This also falls off as $1/R^2$ and is also bound to the particle. It vanishes when $\vec{v} = 0$ which tells us that a charged particle only gives rise to a magnetic field when it moves.

1.1.2. Heavy-ion collisions without medium

The magnetic field in high energy pp collisions was first estimated in Ref. [27] and for HIC in Ref. [24] by considering a realistic proton distribution in a nucleus. The electromagnetic fields at point $\vec{r}$ produced by two heavy-ions traveling in positive and negative y-direction are evaluated from Liéneard-Wiechert potentials [15, 16] as[1]

$$e\vec{E}(\vec{r}, t) = \alpha \sum_a \frac{\left(1 - \vec{v}_a^2\right) \vec{R}_a}{R_a^3 \left[1 - (\vec{R}_a \times \vec{v}_a)^2/R_a^2\right]^{3/2}}, \tag{1.3a}$$

$$e\vec{B}(\vec{r}, t) = -\alpha \sum_a \frac{\left(1 - \vec{v}_a^2\right)(\vec{R}_a \times \vec{v}_a)}{R_a^3 \left[1 - (\vec{R}_a \times \vec{v}_a)^2/R_a^2\right]^{3/2}}, \tag{1.3b}$$

where $\vec{R}_a = \vec{r} - \vec{r}_a(t)$ and the sum runs over all Z protons in each nucleus along with their positions and velocities are, respectively, $\vec{r}_a$ and $\vec{v}_a$. The $v_a = \sqrt{1 - (2m_p/\sqrt{s_{NN}})^2}$, where m_p is the mass of the proton. Using the standard models[2] of the nuclear charge density the positions of protons are in heavy-ions are determined. The magnetic field is numerically obtained from (1.3b) by taking into consideration the small baryon stopping effect. This is displayed in Fig. 1.2 as a

---

[1]These formulas have been obtained in the eikonal approximation, considering that protons move on straight lines before and after the scattering. This is a good approximation because baryon stopping has a small effect at high energies.

[2]The hard sphere model was employed in Ref. [24], whereas a bit more realistic Woods-Saxon distribution was used in Ref. [28].
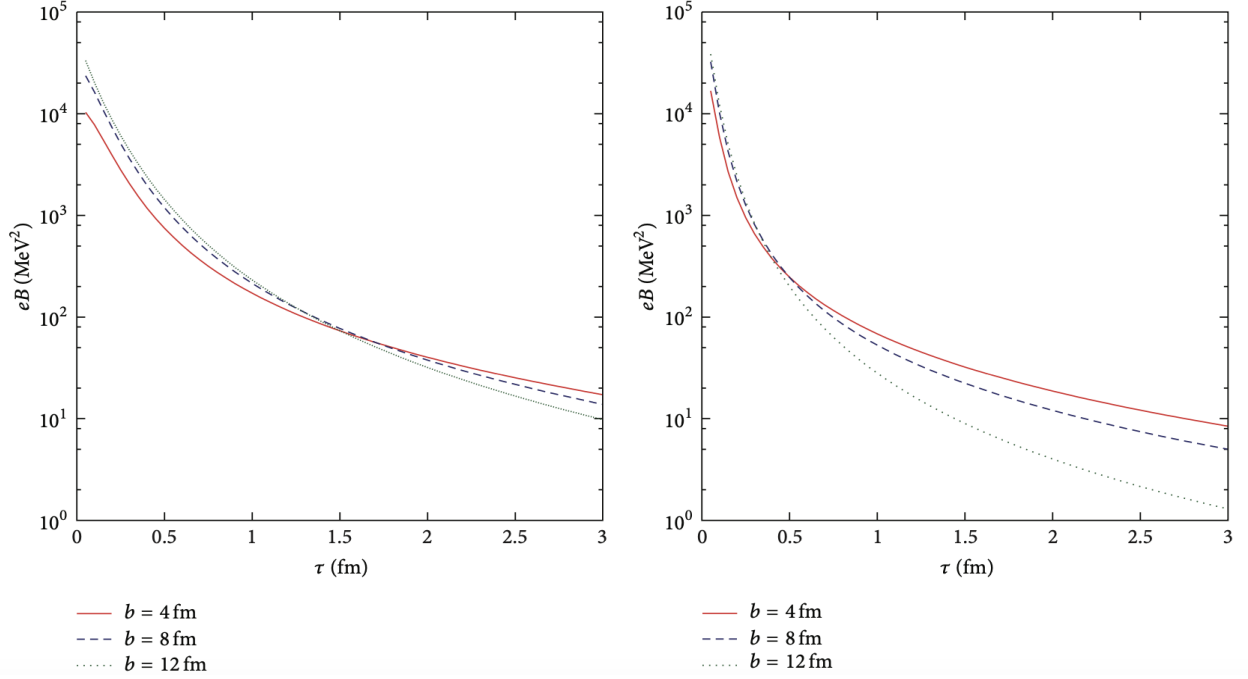
Figure 1.2: The variation of the magnitude of the magnetic field ($\vec{B} = eB\hat{z}$) with proper time τ at the origin $\vec{r} = 0$ in collisions of two gold ions at beam energies: Left panel: at $\sqrt{S_{NN}} = 62$ GeV and Reft panel: at $\sqrt{S_{NN}} = 200$ GeV. These figures are taken from Refs. [15, 24].

function of proper time $\tau = \sqrt{t^2 - y^2}$. It is found that the initial magnitude of the magnetic field can be very high at the time of the collision and then it decreases very fast, being inversely proportional to the square of time [24, 25].

We note that the event-by-event fluctuations of electromagnetic field have also been computed in Ref [28] due to event-by-event fluctuations of proton positions in nuclear charge distribution instead of event averaged distribution protons [15]. There are also other elaborate calculations [29–31] exit in the literature which also give qualitative similar results and relaxation time.

1.1.3. Heavy-ion collisions with static medium (QGP)

In this subsection we consider the generation of magnetic field in heavy-ion collisions with medium formation (QGP), which has been treated as a static one for simplicity. This requires to take into consideration the electrical conductivity, σ, through the ohm's law $\vec{J} = \sigma \vec{E}$ which describes current induced in the medium. In medium, where a charge e moving in y-direction with velocity $\vec{v}$, the Maxwell's equation can be written as

$$\vec{\nabla} \cdot \vec{E} = e\delta(y - vt)\delta(\vec{b}) \,, \tag{1.4a}$$

$$\vec{\nabla} \cdot \vec{B} = 0 \,, \tag{1.4b}$$

$$\vec{\nabla} \times \vec{E} = -\frac{\partial \vec{B}}{dt} \,, \tag{1.4c}$$

$$\vec{\nabla} \times \vec{B} = \frac{\partial \vec{E}}{dt} + \sigma \vec{E} + ev\hat{y}\delta(y - vt)\delta(\vec{b}) \,, \tag{1.4d}$$

where the observation point is defined as $\vec{r} = y\hat{y} + \vec{b}$ with the longitudinal coordinate y and transverse one $\vec{b}$. As can be seen from (1.4d) that a calculation of magnetic field involves response of medium determined by its electrical conductivity.

The lattice calculations [32, 33] have computed that the gluon[3] contribution to electrical conductivity of static quark-gluon plasma is

$$\sigma = (5.8 \pm 2.9) \frac{T}{T_c} \ \text{MeV} \,, \tag{1.5}$$

where T is the QGP temperature and T_c is the critical temperature. We note that (1.5) is odds with previous calculation [34]. We will use (1.5) as a reasonable one to compute the magnetic field.

Solving the (1.4d), one obtains [15, 16] the magnetic field in presence of σ as

$$e\vec{B}(\vec{r}, t) = \hat{z} \frac{\alpha b \sigma}{2(t - y)^2} e^{-b^2 \sigma / 4(t - y)} \,. \tag{1.6}$$

One can also obtain [15, 16] the magnetic field in absence of σ as

$$e\vec{B}(\vec{r}, t) = \hat{z} \frac{\alpha b \gamma}{\left(b^2 + \gamma^2 (t - y)^2\right)^{3/2}} \,, \tag{1.7}$$

which agrees with (1.3b) for a single proton when one sets $\vec{R}_a = \vec{b} + (y - vt)\hat{y}$. At the origin $y = 0$, the field is constant at times $t < b/\gamma$ while it varies as $B_\infty \propto 1/t^3$ at times $t \gg b/\gamma$. At time $t \approx b$, the ratio of the two becomes $B_0/B_\infty = 1/\gamma^3 \ll 1$.

The magnetic field with σ in (1.6) vanishes both at $t = 0$ and ∞ and attains a maximum at $t = b^2\sigma/8$ which is much larger than b/γ. One obtains magnetic field at that time

$$eB_{\max} = \frac{32 e^{-2} \alpha}{b^3 \sigma} \,, \tag{1.8}$$

where e in the right hand side is the base of the logarithm and not to confuse with electric charge. This is smaller than the maximum field in vacuum

$$\frac{B_{\max}}{B_0} = \frac{32 e^{-2}}{\sigma b \gamma} \,, \tag{1.9}$$

even though it is huge. Now in Fig. 1.3 we plot the relaxation of magnetic field at $y = 0$ without conducting medium as given in (1.7) and with conducting medium medium as obtained in (1.6). The main features of these two equations are discussed above. As found the magnetic field with conducting medium survives for a quite long time.

1.1.4. Heavy-ion collisions with expanding medium (QGP)

In this subsection we will discuss the generation of magnetic field from expanding QGP medium created in heavy-ion collisions. For simplicity, we assume one dimensional expansion, which is isentropic expansion known as Bjorken expansion [35]. So there is no distinction between time t and proper time τ in midrapidity region, i.e., at the collision centre $y = 0$. It follows from Bjorken expansion that $T \propto t^{-1/3}$ and from (1.5) one can write $\sigma \propto t^{-1/3}$. This has been parametrised in Ref. [15] as

$$\sigma(t) = \sigma_0 \left(\frac{t_0}{t_0 + t} \right)^{1/3} \,, \tag{1.10}$$

where one can choose, for estimation purpose, the initial time $t_0 \approx 0.5$ fm and $\sigma_0 \approx 16$ MeV.

Now, following Ref. [15] one can solve (1.4d) for magnetic field for expanding medium with time dependent σ and $y = 0$ as

$$\vec{B}(0, \vec{b}, \rho) = \frac{ev}{\beta} \int \frac{d^2 k_\perp}{(2\pi)^2} e^{i\vec{k}_\perp \cdot \vec{b}} \frac{i}{2\pi} \left(\vec{k}_\perp \times \hat{y} \right) \int_0^\rho d\rho' e^{-(k_\perp^2/\beta)(\rho - \rho')} \frac{\sqrt{\pi\beta}}{\sqrt{\rho - \rho'}} e^{-v^2 t_0^2 \beta [(\rho' + 1)^{3/4} - 1]^2 / 4(\rho - \rho')} \,, \tag{1.11}$$

---

[3]Quark contribution is neglected.
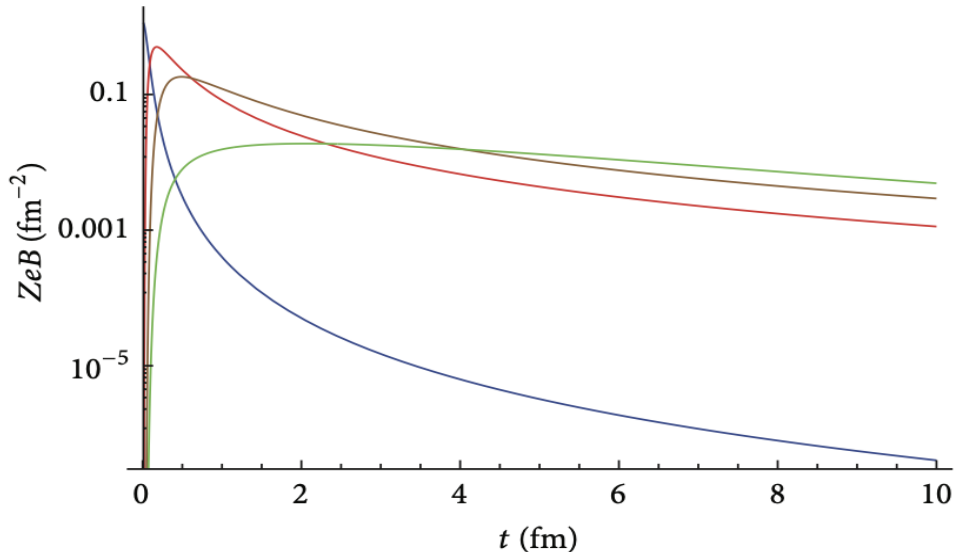
Figure 1.3: The variation of magnetic field at $y = 0$ in vacuum (blue) as given in (1.7), in static conducting medium as given in (1.6) at $\sigma = 5.8$ MeV (red) and at $\sigma = 16$ MeV (brown),and in the expanding medium (green) as given in (1.13). This figures is taken from Ref. [15].

where $\vec{k} = k_y \hat{y} + \vec{k}_\perp$ and the parameter $\beta = (4\sigma_0)/(3t_0) = 43$ MeV/fm. The new time variable ρ is defined as

$$\rho = \left(\frac{1+t}{t_0}\right)^{4/3} - 1 \,, \tag{1.12}$$

and $(\rho - \rho') = \zeta$ comes from translational invariance of the Green's function. Integrating over azimuthal angle ϕ and then over $k_\perp$, one can write the z-component of the magnetic field [15] as

$$eB_z(0, \vec{b}, \rho) \equiv eB = \frac{\alpha v b \beta^{3/2}}{2\sqrt{\pi}} \int\limits_0^\rho d\zeta \; \zeta^{-5/2} e^{-b^2\beta/4\xi} e^{-v^2 t_0^2 \beta[(\rho-\zeta+1)^{3/4}-1]^2/4\zeta} \,. \tag{1.13}$$

This (1.13) is solved numerically and displayed in Fig. 1.3 with green line and the effect is almost similar to the static medium with time independent electrical conductivity as given in as given in (1.6). We conclude that the magnetic field essentially freezes in the plasma for as long as plasma exists due to finite electrical conductivity in QGP. This quite similar to the phenomenon, known as skin effect [26], found in good conductors placed in time-varying magnetic field. In Ref. [15] the diffusion of magnetic field has been discussed which has been found similar to that in (1.6).

An intense research effort is currently focused on understanding the behavior of strongly interacting matter in the presence of an external magnetic field, leading to the discovery of several intriguing phenomena. Key examples include the chiral magnetic effect [4, 5, 24, 25, 36], magnetic catalysis at finite temperature [2, 37–41], inverse magnetic catalysis [8, 42–49], and vacuum superconductivity [6]. Further exploration has revealed insights into the breaking and restoration of chiral and color symmetries [7, 50–52], thermodynamic properties [11, 53–58], and meson behavior, including refractive indices and decay constants in hot magnetized media [59, 60]. Notable findings also include soft photon production from conformal anomaly in heavy-ion collisions (HICs)[61–63], modifications of dispersion relations in magnetized QED and QCD media[64–67], and synchrotron radiation [16]. Research also encompasses photon production and damping rates [68], fermion damping rates [69], dilepton production in hot magnetized QCD plasmas [15–17, 70–75]. Additionally, studies have examined strongly coupled plasmas in the presence of strong magnetic fields [76], transport coefficients [77–81], and energy loss mechanisms [82]. Heavy quark dynamics have also been explored in this context [83–85], alongside studies on neutrino properties [86, 87] and the field theory of Faraday effects [88, 89]. Investigations into pion self-energy and

9

dispersion properties have been conducted at zero temperature using weak field approximations [90], as well as at finite temperatures with full propagators [91]. Moreover, detailed studies of the spectral properties of ρ mesons in magnetic fields have been carried out, both at zero temperature [92, 93] and at non-zero temperatures [94], revealing important insights into their behavior in magnetized environments. Recently, the rotational stability of magnetic field in rotating QGP has been studied [95]. We draw attention to the readers on several review articles [11–14] that detailed the various concepts and physical phenomena occurring in presence of an external magnetic field.

Experimental evidence of photon anisotropy, reported by the PHENIX Collaboration [96], has presented significant challenges to existing theoretical models. In response, some theoretical explanations have been proposed, attributing this anisotropy to the presence of a strong anisotropic magnetic field in heavy-ion collisions [61]. This highlights the growing need to study the effects of intense background magnetic fields on various observables and aspects of non-central heavy-ion collisions. The presence of such external anisotropic fields necessitates modifications to current theoretical frameworks, enabling more accurate investigations into the properties of the quark-gluon plasma (QGP) under these conditions. Adapting these tools will be essential for advancing our understanding of QGP behavior in magnetized environments.

Below we also outline the notation we shall be following throughout:

$$a^\mu = (a^0, a^1, a^2, a^3) = (a_0, \vec{a}); \quad a \cdot b \equiv a_0 b_0 - \vec{a} \cdot \vec{b}; \quad g^{\mu\nu} = \text{diag}\,(1, -1, -1, -1),$$

$$a^\mu = a^\mu_{\shortparallel} + a^\mu_\perp; \quad a^\mu_{\shortparallel} = (a^0, 0, 0, a^3); \quad a^\mu_\perp = (0, a^1, a^2, 0)$$

$$g^{\mu\nu} = g^{\mu\nu}_{\shortparallel} + g^{\mu\nu}_\perp; \quad g^{\mu\nu}_{\shortparallel} = \text{diag}(1, 0, 0, -1); \quad g^{\mu\nu}_\perp = \text{diag}(0, -1, -1, 0),$$

$$(a \cdot b) = (a \cdot b)_{\shortparallel} - (a \cdot b)_\perp; \quad (a \cdot b)_{\shortparallel} = a^0 b^0 - a^3 b^3; \quad (a \cdot b)_\perp = a^1 b^1 + a^2 b^2,$$

$$\slashed{a} = \gamma^\mu a_\mu = \slashed{a}_{\shortparallel} + \slashed{a}_\perp; \quad \slashed{a}_{\shortparallel} = \gamma^0 a_0 - \gamma^3 a^3; \quad \slashed{a}_\perp = \gamma^1 a^1 + \gamma^2 a^2 \tag{1.14}$$

where $\shortparallel$ and $\perp$ are, respectively, the parallel and perpendicular components, which would be separated out due to the presence of background magnetic field.

This review is organised as follows: after a brief introduction on QCD plasma and generation magnetic field in such medium, we explored in Section 2 the impact of a magnetic field on the Dirac equation and the resulting changes to the energy spectrum of fermions. In Section 3, we investigated the adjustments to the free propagators of charged scalars and fermions within a magnetic background. Furthermore, we derived the expressions for the free fermion propagator under both strong and weak magnetic field limits. In Section 4, we presented a brief summary of field theory in a thermal environment, discussing the imaginary-time and real-time formalisms. We examined the unique challenges of finite-temperature systems, such as the emergence of scale hierarchies, and emphasized the shortcomings of bare perturbation theory in this context. In Section 5, we extended the framework of thermal field theory to include the effects of a background magnetic field. We derived the general structures of two-point functions, focusing on the self-energy and propagator for both fermions and gauge bosons in a thermo-magnetic medium. The necessity of employing strong and weak magnetic field approximations for calculating various physical quantities was emphasized, with particular attention given to the scale hierarchies inherent to the weak field regime. Additionally, we studied the dispersion relations and collective dynamics of quarks and gluons by analyzing their two-point functions within a thermo-magnetic QCD medium. We calculated the Debye screening mass for an arbitrary magnetic field and demonstrated its behaviour in the strong and weak field limits. Furthermore, we provided a brief discussion on the effects of strong coupling and the choice of renormalization scales. Lastly, we derived the quark-gluon three-point function as well as the two quark – two gluon four-point function. In Section 6, we established a systematic approach leveraging the general structure of two-point functions for fermions and gauge bosons to calculate the QCD free energy and pressure. This framework was tailored to

address complex environments, explicitly incorporating the simultaneous effects of a thermal background and an external magnetic field. In Section 7, we evaluated the soft contribution to the damping rate of a hard photon in a weakly magnetized QED medium, focusing on the scenario where the momentum of one fermion in the loop is soft. Additionally, we calculated the fermion damping rate for the case of an arbitrary external magnetic field. In Section 8, we investigated the electromagnetic spectral function by computing the one-loop photon polarization tensor with quarks in the loop, emphasizing the strong-field regime where the magnetic field surpasses the thermal scale. We also derived the dilepton production rates in this regime. Furthermore, we calculated the hard dilepton production rate from a weakly magnetized deconfined QCD medium using the one-loop photon self-energy within the HTL approximation, incorporating one hard quark and one thermomagnetically resummed quark propagator in the loop. Lastly, we analyzed the various processes of lepton pair production from a hot and dense QCD medium under the influence of an arbitrary external magnetic field. Section 9 explores the transport characteristics of heavy quarks (HQs) in a magnetized medium, with a particular focus on their momentum diffusion coefficients. We have carefully laid out the steps required to compute the HQ scattering rate and, consequently, the momentum diffusion coefficients in the most general case, considering a finite-momentum HQ and an external magnetic field of arbitrary strength. Furthermore, we have presented and examined the results for HQ momentum diffusion coefficients in a medium with an arbitrary magnetic field, considering both the static limit and the scenario where the HQ has finite momentum. Discussion of a magnetised QCD matter is incomplete without bringing up the QCD phase diagram. This is done in Section 10, in which we try to cover the novel features of a magnetised QCD matter in the $T - eB$-plane, such as decreasing crossover temperature, inverse magnetic catalysis effect etc. To put the novel features into perspective we draw a comparison with the previous understanding of the subject matter. We trace back the reasons behind our revised understanding. The discussion on the past and revised understandings revolve around lattice QCD, a first principle numerical method for solving QCD. However, we finally switch to the effective descriptions of QCD and point out how studying magnetised QCD matter helps reveal the working principles of effective models. Finally, in Section 11 we have presented summary and outlook of this review.

2. Dirac Equation in Magnetic Field

We consider magnetic field is along z direction. So we choose magnetic vector potential as $\vec{A} = (-By, 0, 0)$ in Landau gauge [4]. The modified Dirac equation in presence of magnetic field can be written as,

$$i\frac{\partial \Psi}{\partial t} = H_B \Psi \,, \tag{2.1}$$

where modified Hamiltonian is given by

$$H_B = \vec{\alpha} \cdot \vec{\Pi} + \beta m \,, \tag{2.2}$$

where $\vec{\alpha} = \gamma_0 \vec{\gamma}$, $\beta = \gamma_0$ and

$$\alpha_i = \gamma_0 \gamma_i = \begin{pmatrix} 0 & \sigma_i \\ \sigma_i & 0 \end{pmatrix} \,, \tag{2.3a}$$

$$\beta = \gamma_0 = \begin{pmatrix} 1 & 0 \\ 0 & -1 \end{pmatrix} \,, \tag{2.3b}$$

---

[4]One can write this in other gauge also.

along with the modified momentum in presence of magnetic field is

$$\vec{\Pi} \ \ = -i\vec{\nabla} - q\vec{A}, \tag{2.4}$$

where q is the electric charge of a fermion.

The solution of Dirac equation is 4 component vector and one can write plane wave solution of (2.1) as

$$\Psi = e^{-iEt} \begin{pmatrix} \phi \\ \chi \end{pmatrix}. \tag{2.5}$$

Now (2.1) implies,

$$E \begin{pmatrix} \phi \\ \chi \end{pmatrix} e^{-iEt} = \begin{pmatrix} m & \vec{\sigma}\cdot\vec{\Pi} \\ \vec{\sigma}\cdot\vec{\Pi} & -m \end{pmatrix} \begin{pmatrix} \phi \\ \chi \end{pmatrix} e^{-iEt}$$

$$\begin{pmatrix} E\phi \\ E\chi \end{pmatrix} = \begin{pmatrix} m\,\phi + \vec{\sigma}\cdot\vec{\Pi}\,\chi \\ \vec{\sigma}\cdot\vec{\Pi}\,\phi - m\,\chi \end{pmatrix}. \tag{2.6}$$

So we get two coupled equations as

$$(E - m)\phi = (\vec{\sigma}\cdot\vec{\Pi})\,\chi\,, \tag{2.7a}$$

$$(E + m)\chi = (\vec{\sigma}\cdot\vec{\Pi})\,\phi\,. \tag{2.7b}$$

One can decouple (2.7a) and (2.7b) as

$$(E - m)\vec{\sigma}\cdot\vec{\Pi}\,\phi = (\vec{\sigma}\cdot\vec{\Pi})^2\chi \ \Rightarrow \ (E + m)(E - m)\chi = (\vec{\sigma}\cdot\vec{\Pi})^2\chi\,, \tag{2.8a}$$

$$(E + m)\vec{\sigma}\cdot\vec{\Pi}\,\chi = (\vec{\sigma}\cdot\vec{\Pi})^2\phi \ \Rightarrow \ (E + m)(E - m)\phi = (\vec{\sigma}\cdot\vec{\Pi})^2\phi\,. \tag{2.8b}$$

In Landau gauge, one can write the various components of the modified momentum from (2.4) as

$$\Pi^1 = -i\frac{\partial}{\partial x} + qBy\,, \ \Pi^2 = -i\frac{\partial}{\partial y}\,, \ \Pi^3 = -i\frac{\partial}{\partial z}\,. \tag{2.9}$$

We use the well known identity

$$(\vec{\sigma}\cdot\vec{a})(\vec{\sigma}\cdot\vec{b}) = \vec{a}\cdot\vec{b} + i(\vec{a}\times\vec{b})\cdot\vec{\sigma} \left(\vec{\sigma}\cdot\vec{\Pi}\right)^2 \ \ = \ \ \left(\vec{\sigma}\cdot\vec{\Pi}\right)\left(\vec{\sigma}\cdot\vec{\Pi}\right) = (\Pi)^2 + i\left(\vec{\Pi}\times\vec{\Pi}\right)\cdot\vec{\sigma}$$

$$= \ \ (\Pi)^2 + i\epsilon_{ijk}\Pi_j\Pi_k\sigma_i\,, \tag{2.10}$$

where we note that, $\vec{\Pi}\times\vec{\Pi} \neq 0$. Now, we can write

$$i\epsilon_{ijk}\Pi_j\Pi_k\sigma_i \ \ = \ \ i\epsilon_{312}\Pi_1\Pi_2\sigma_3 + i\epsilon_{321}\Pi_2\Pi_1\sigma_3\,, \ \ (\text{0ther terms vanish})$$

$$= \ \ i\Pi_1\Pi_2\sigma_3 - i\Pi_2\Pi_1\sigma_3 = i\left[\Pi_1, \Pi_2\right]\sigma_3\,, \tag{2.11}$$

and

$$\Pi^1\Pi^2\psi = (-i\frac{\partial}{\partial x} + qBy)(-i\frac{\partial}{\partial y})\psi = (-i\frac{\partial}{\partial x} + qBy)(-i\frac{\partial\psi}{\partial x^2}\psi) = -\frac{\partial^2\psi}{\partial x\,\partial y} - iqBy\frac{\partial\psi}{\partial y}\,, \tag{2.12a}$$

$$\Pi^2\Pi^1\psi = (-i\frac{\partial}{\partial y})(-i\frac{\partial}{\partial x} + qBy)\psi = (-i\frac{\partial}{\partial y})(-i\frac{\partial\psi}{\partial x} + qBy\psi) = -\frac{\partial^2\psi}{\partial y\,\partial x} - iqBxy\frac{\partial\psi}{\partial y} - iqB\psi\,. \tag{2.12b}$$

Using (2.12a) and (2.12b), we get[5]

$$\left[\Pi_1, \Pi_2\right] = iqB\,. \tag{2.13}$$

Combining (2.11), (2.13) and (2.10), one can get

$$\left(\vec{\sigma}\cdot\vec{\Pi}\right)^2 \ \ = \ \ (\Pi)^2 - qB\sigma_3\,, \tag{2.14}$$

and using this (2.8b) becomes

$$((\Pi)^2 - qB\sigma_3)\phi \ \ = \ \ (E^2 - m^2)\phi\,. \tag{2.15}$$

---

[5] ψ and it's derivatives need to be well behaved to satisfy $\frac{\partial^2\psi}{\partial x\,\partial y} = \frac{\partial^2\psi}{\partial y\,\partial x}$.

We can now expand the LHS of (2.15) as

$$\left[-\frac{\partial^2}{\partial x^2} + (i\frac{\partial}{\partial y} + qBx)^2 - \frac{\partial^2}{\partial z^2} - qB\sigma_3\right]\phi \;=\; \left[-\nabla^2 + 2iqBx\frac{\partial}{\partial y} + q^2B^2x^2 - qB\sigma_3\right]\phi, \tag{2.16}$$

where only y is explicitly present in the expression. y and z are cyclic co-ordinates[6]. So we now write trial solution of (2.15) as

$$\phi = e^{i(p_x x + p_z z)}f(y). \tag{2.17}$$

We note that σ_3 is 2×2 matrix, so $f(y)$ must be 2 component vector and we can write $f(x)$ in eigen basis of σ_3 as

$$f(y) = F_+(y)\begin{pmatrix} 1 \\ 0 \end{pmatrix} + F_-(y)\begin{pmatrix} 0 \\ 1 \end{pmatrix} = \begin{pmatrix} F_+(y) \\ F_-(y) \end{pmatrix}. \tag{2.18}$$

Now (2.16) becomes

$$\left[-\nabla^2 - 2iqBy\frac{\partial}{\partial x} + q^2B^2y^2 - qB\sigma_3\right]e^{i(p_x y + p_z z)}\begin{pmatrix} F_+(y) \\ F_-(y) \end{pmatrix}$$

$$= \left[\left(-\frac{d^2}{dy^2} + p_x^2 + p_z^2 + 2qByp_x + q^2B^2y^2\right)\mathbb{1} - qB\sigma_3\right]e^{i(p_x x + p_z z)}\begin{pmatrix} F_+(y) \\ F_-(y) \end{pmatrix}$$

$$= \left[\hat{A}\mathbb{1} - qB\sigma_3\right]\left[F_+(y)\begin{pmatrix} 1 \\ 0 \end{pmatrix} + F_-(y)\begin{pmatrix} 0 \\ 1 \end{pmatrix}\right]e^{i(p_y y + p_z z)}$$

$$= \left\{\hat{A}F_+\begin{pmatrix} 1 \\ 0 \end{pmatrix} - qB(+1)F_+\begin{pmatrix} 1 \\ 0 \end{pmatrix} + \hat{A}F_-\begin{pmatrix} 0 \\ 1 \end{pmatrix} - qB(-1)F_-\begin{pmatrix} 0 \\ 1 \end{pmatrix}\right\}e^{i(p_x x + p_z z)}. \tag{2.19}$$

Using (2.19) in (2.15), one gets

$$\begin{pmatrix} \hat{A}F_+ - qBF_+ \\ \hat{A}F_- + qBF_- \end{pmatrix} = (E^2 - m^2)\begin{pmatrix} F_+ \\ F_- \end{pmatrix}. \tag{2.20}$$

One can write (2.20) in compact notation as

$$\hat{A}F_s - sqBF_s = (E^2 - m^2)F_s \;,\; s = \pm 1$$

$$-\frac{d^2F_s}{dy^2} - (p_x - qBy)^2 F_s + (E^2 - m^2 - p_z^2 + sqB)F_s = 0. \tag{2.21}$$

Now we change the variable.

$$\xi = \sqrt{|qB|}\left(\frac{p_x}{qB} - y\right) \tag{2.22}$$

where $\xi^2 = \frac{|qB|}{(qB)^2}(p_x - qyB)^2$. Also

$$\frac{d}{dy} = \frac{d}{d\xi}\frac{d\xi}{dy} = -\sqrt{|qB|}\frac{d}{d\xi}, \tag{2.23a}$$

$$\frac{d^2}{dy^2} = \frac{d}{dy}\left(-\sqrt{|qB|}\frac{d}{d\xi}\right) = |qB|\frac{d^2}{d\xi^2}. \tag{2.23b}$$

Using these equations in (2.21) we get

$$\left[|qB|\frac{d^2}{d\xi^2} - |qB|\xi^2 + (E^2 - m^2 - p_z^2 + sqB)\right]F_s = 0$$

$$\left[\frac{d^2}{d\xi^2} - \xi^2 + a_s\right]F_s = 0. \tag{2.24}$$

where $a_s = \frac{1}{|qB|}(E^2 - m^2 - p_z^2 + sqB)$.

Again we apply a variable transformation as

$$F_s = e^{-\frac{\xi^2}{2}}H(\xi), \tag{2.25a}$$

---

[6]We have chosen $A^\mu = (-By, 0, 0)$, so y and z become cyclic. For symmetric gauge, z is cyclic and corresponding momentum is conserved.

$$\frac{dF_s}{d\xi} = -e^{-\frac{\xi^2}{2}}\xi H(\xi) + e^{-\frac{\xi^2}{2}}H'(\xi)\,, \tag{2.25b}$$

$$\frac{d^2 F_s}{d\xi^2} = e^{-\frac{\xi^2}{2}}(\xi^2 - 1)H(\xi) - 2e^{-\frac{\xi^2}{2}}\xi H'(\xi) + e^{-\frac{\xi^2}{2}}H''(\xi)\,. \tag{2.25c}$$

Using these equations, (2.24) becomes

$$[H'' - 2\xi H' + (a_s - 1)H] = 0\,. \tag{2.26}$$

The solution of (2.26)) is Hermite polynomial when $a_s - 1 = 2k$. with $k \geq 0$ and the energy can be obtained as

$$E^2 = m^2 + p_z^2 - sqB + (2k+1)|qB|\,. \tag{2.27}$$

There number of points which have been discussed below:

1. When $s = +1$ and $q = +(ve)$

$$E^2 = m^2 + p_z^2 + 2k|qB|\,. \tag{2.28}$$

2. When $s = +1$ and $q = -(ve)$

$$E^2 = m^2 + p_z^2 + 2(k+1)|qB| = m^2 + p_z^2 + 2k'|qB|\,, \tag{2.29}$$

   where $k' = k + 1$.

3. When $s = -1$ and $q = +(ve)$

$$E^2 = m^2 + p_z^2 + 2k'|qB|\,. \tag{2.30}$$

4. When $s = -1$ and $q = -(ve)$

$$E^2 = m^2 + p_z^2 + 2k|qB|\,. \tag{2.31}$$

We note that the energy of fermion becomes quantised in presence of magnetic field as

$$E_n(p_z) = \pm\sqrt{m^2 + p_z^2 + 2n|qB|}\,, \tag{2.32}$$

where various values of n in (2.32) gives various Landau levels. As shown in (2.32), the transverse momenta p_x and p_y become quantized in the presence of an anisotropic magnetic field oriented along the z-axis. This scenario is illustrated in Fig. 2.1, where a fermion in the lowest Landau level (LLL) is depicted as being confined to the smallest circle among the concentric circles representing higher Landau levels. The quantization of these Landau levels significantly influences the quantum fluctuations of charged fermions in the Dirac sea at $T = 0$ and the thermal fluctuations at $T \neq 0$. These effects play a crucial role in understanding the behavior of fermions in magnetized environments.

In case of lowest Landau level ($n = 0$) $k = -1$ for case 2 and 3 which are not allowed for Hermite polynomial. This means for negative charge particle $q = -e$ with $s = +1$ state (spin up) and for positive charge particle $q = +e$ with $s = -1$ state (spin down) are, respectively, not possible for LLL[7].

3. Free Propagator in Background Magnetic Field

Julian Schwinger's groundbreaking 1951 paper [97], provides a formulation for propagators in the presence of an external electromagnetic field. In this approach, the propagator is expressed using an integral over the proper-time parameter. Nevertheless, the integral can be restructured to express the fermion propagator as an infinite sum over Landau levels,

---

[7]So fermion in LLL can not have spin along magnetic field direction. In case of QED interaction in presence of external magnetic field, for an anti-fermion spin is along the magnetic field direction and for a fermion spin is along the opposite direction (spin down). So, photon spin along the magnetic field direction is zero.
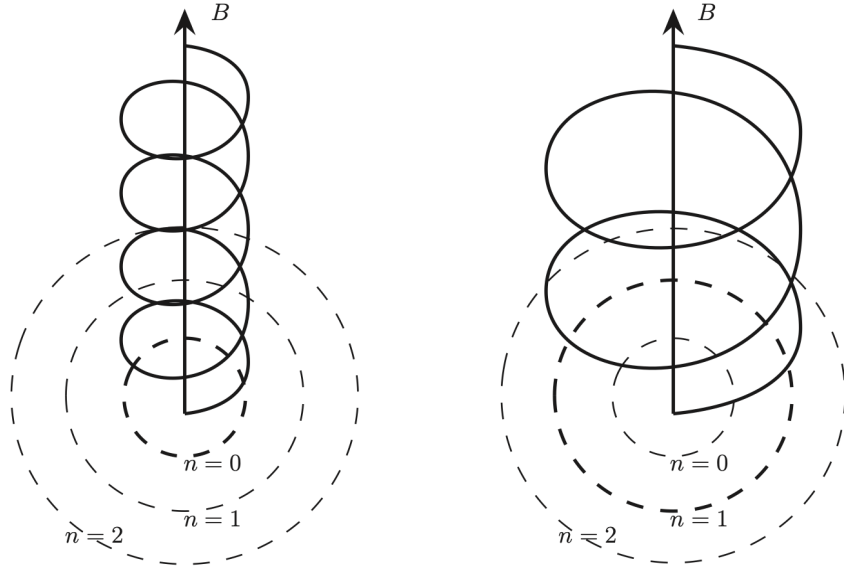
Figure 2.1: The orientation of Landau levels in presence of a magnetic field. This figure is adopted from Ref. [23].

a form that closely resembles the conventional treatment of an electron gas in an external magnetic field within non-relativistic quantum mechanics. In this section we will derive the free charged scalar and fermion propagator in presence of background magnetic field.

3.1. Free Charged Scalar Propagator

The behaviour of a charged particle gets altered in the presence of magnetic field. Suppose, there is a uniform space-time independent background magnetic field B is acting on a system in the z direction. Here, in the context of this background field, some important points should be kept in mind. The background field is classical, i.e., we are not going to quantize it and treat it as an operator. The field has no dynamics, i.e., in the Lagrangian of our system there is no such term like $F_{\mu\nu}F^{\mu\nu}$. The vector potential of the system can be chosen in Landau gauge as :

$$\vec{A} = (-By, 0, 0)$$

In field theoretic language an important ingredient of any perturbative calculation is the knowledge of the propagator. So, in this section, our aim is to find the propagator of the charged scalar field in presence of an external magnetic field, as described above.

Let us consider the Green's function $G(x, x')$ of a generic operator $H(x, p)$ which we call the *Hamiltonian* of the system. The Green's function in turn satisfies

$$H(x, p)G(x, x') = \delta^{(4)}(x - x'). \tag{3.1}$$

In ordinary quantum mechanics, the state vectors are elements of a infinite dimensional vector space called the *Hilbert space*. A set of complete set of state vectors that spans the space is called *basis*. Examples of such basis are position basis $\{|\vec{x}\rangle\}$, momentum basis $\{|\vec{p}\rangle\}$ etc. They satisfy completeness relations of the form

$$\int d^3x \, |\vec{x}\rangle \langle \vec{x}| = 1$$

$$\int \frac{d^3p}{(2\pi)^3} \, |\vec{p}\rangle \langle \vec{p}| = 1$$

Time t acts as a parameter in QM. Here we extend this idea a little further and define the space-time basis vectors as $|x\rangle = |t, \vec{x}\rangle = |x^0, x^1, x^2, x^3\rangle$ and momentum basis vector as $|p\rangle = |E, \vec{p}\rangle = |p^0, p^1, p^2, p^3\rangle$. They satisfy similar completeness relations like

$$\int d^4x \, |x\rangle \langle x| = 1 \tag{3.2}$$

$$\int \frac{d^4p}{(2\pi)^4} \, |p\rangle \langle p| = 1 \tag{3.3}$$

Like QM we also introduce "position" and "momentum" four-operator $\hat{X}_\mu$ and $\hat{P}_\mu$. They, like QM, obey the commutation relations

$$[\hat{X}_\mu, \hat{X}_\nu] = 0, \tag{3.4}$$

$$[\hat{X}_\mu, \hat{P}_\nu] = -i g_{\mu\nu} \hat{\mathbf{1}} \tag{3.5}$$

From now on we'll drop the hat sign over operator and denote it by just capital letter ($\hat{X}$ will be denoted by just X). The orthonormality conditions

$$\langle x|x'\rangle = \delta^{(4)}(x - x') \tag{3.6}$$

$$\langle p|p'\rangle = \delta^{(4)}(p - p') \tag{3.7}$$

will hold.

We know in QM

$$\langle \vec{x}|\vec{p}\rangle = \exp(i\vec{p} \cdot \vec{x})$$

We define

$$\langle x|p\rangle = \exp(-ip \cdot x) \tag{3.8}$$

Note that the occurrence of minus sign. It is important to keep the plus sign before the $\vec{p} \cdot \vec{x}$. Now a quantity of special interest is the matrix element of P_μ in spacetime basis, i.e.

$$\begin{aligned}
\langle x|P_\mu|x'\rangle &= \int \frac{d^4p}{(2\pi)^4} \langle x|P_\mu|p\rangle \langle p|x'\rangle \\
&= \int \frac{d^4p}{(2\pi)^4} p_\mu \langle x|p\rangle \langle p|x'\rangle \\
&= i\partial_\mu \left(\int \frac{d^4p}{(2\pi)^4} e^{-ip\cdot(x-x')} \right) \\
&= i\partial_\mu \delta^{(4)}(x - x') \\
&= -i\partial'_\mu \delta^{(4)}(x - x'),
\end{aligned}$$

where ∂'_μ represents the spatial derivatives with respect to x'_μ. Let us introduce the "proper time" evolution operator $U(x, x'; s)$. The word proper time is kept in quotation since the "proper time" s does not have the dimension of time. It is just a parameter whose mathematical role is very similar to that of time in QM. It satisfies the following differential equation

$$i\frac{\partial}{\partial s} U(x, x'; s) = H U(x, x'; s) \tag{3.9}$$

with the boundary conditions

$$U(x, x'; s \to 0) = \delta^{(4)}(x - x'), \tag{3.10}$$

$$U(x, x'; s \to -\infty) = 0. \tag{3.11}$$

The solution therefore comes out to be

$$U(x, x'; s) = \langle x | e^{-isH} | x' \rangle$$
$$= \langle x | U(s) | x' \rangle . \tag{3.12}$$

Note that this subsequently implies that the Greens function is given by

$$G(x, x') = -i \int_{-\infty}^{0} ds \ U(x, x'; s) \tag{3.13}$$

which we prove below.

$$\text{Proof:} \quad H(x, p) G(x, x') = -i H(x, p) \int_{-\infty}^{0} ds \ U(x, x'; s)$$
$$= -i \int_{-\infty}^{0} ds \ H(x, p) U(x, x'; s)$$
$$= \int_{-\infty}^{0} ds \ \frac{\partial}{\partial s} U(x, x'; s)$$
$$= U(x, x'; 0) - U(x, x'; -\infty)$$
$$= \delta^{(4)}(x - x').$$

From (3.13), one can notice that to evaluate $G(x, x')$ we first have to compute the proper time evolution operator $U(x, x'; s)$. To do the same, note that

$$i \partial_s \langle x | U(s) | x' \rangle = i \langle x | \partial_s U(s) | x' \rangle$$
$$= \langle x | H(X, P) U(s) | x' \rangle$$
$$= \langle x | U(s) U^\dagger(s) H(X, P) U(s) | x' \rangle$$
$$= \langle x(s) | H(X(s), P(s)) | x'(0) \rangle , \tag{3.14}$$

where in the last step we used $U^\dagger(s) H(X, P) U(s) = H(X(s), P(s))$ (it's like going from Schrodinger to Heisenberg picture in QM) and $\langle x(s) | \equiv \langle x | U(s)$. The goal is now to express the operator $H(X(s), P(s))$ as a function of operators $X(s)$, $X(0)$ in adequate order such that $X(s)$ is on the *left* and $X(0)$ is on the *right* in each term. Then we will have

$$\langle x(s) | H(X(s), P(s)) | x'(0) \rangle = f(x, x', s) \langle x(s) | x'(0) \rangle . \tag{3.15}$$

Since $\langle x(s) | x'(0) \rangle = \langle x | U(s) | x' \rangle = U(x, x'; s)$, subsequently from (3.14) we will obtain

$$i \partial_s U(x, x'; s) = f(x, x'; s) U(x, x'; s), \tag{3.16}$$

which gives us the solution as

$$U(x, x'; s) = C(x, x') \exp \left[-i \int^{s} ds' \ f(x, x'; s') \right] . \tag{3.17}$$

Finally, we will put this solution in (3.13) to obtain the expression for Green's function, i.e. the propagator for a charged scalar field in the presence of an external magnetic field. Having made the layout clear, in the following let us proceed with the steps.

The Hamiltonian operator for the charged scalar field is given by

$$H(X, P) = (P_\mu - e A_\mu(X))(P^\mu - e A^\mu(X)) - m^2 \tag{3.18}$$

With $\Pi_\mu \equiv P_\mu - e A_\mu(X)$, it is

$$H(X, P) = \Pi_\mu \Pi^\mu - m^2 = \Pi^2 - m^2 \tag{3.19}$$

The operators X_μ, Π_μ satisfies Heisenberg equation of motion in proper time variable s,

$$\frac{dX_\mu(s)}{ds} = -i[X_\mu(s), H] \tag{3.20}$$

17

$$\frac{d\Pi_\mu(s)}{ds} = -i[\Pi_\mu(s), H] \tag{3.21}$$

Let us compute the commutators.

The 1st one is relatively easy,

$$[X_\mu, H] = [X_\mu, \Pi_\nu \Pi^\nu]$$

$$= -2i\Pi_\mu, \tag{3.22}$$

where we have used $[X_\mu, \Pi_\nu(X)] = [X_\mu, P_\nu] = -ig_{\mu\nu}$ as $[X_\mu, A_\nu(X)] = 0$ since A is function of X and $[X_\mu, X_\nu] = 0 \; \forall \mu, \nu$.

Next the 2nd one,

$$[\Pi_\mu, H] = [\Pi_\mu, \Pi_\nu \Pi^\nu]$$

$$= 2\Pi^\nu [\Pi_\mu, \Pi_\nu] \tag{3.23}$$

Now

$$[\Pi_\mu, \Pi_\nu] = [P_\mu - eA_\mu(X), P_\nu - eA_\nu(X)]$$

$$= [P_\mu, P_\nu] - e\left([P_\mu, A_\nu(X)] + [A_\mu(X), P_\nu]\right) + [A_\mu, A_\nu]$$

$$= -e\left([P_\mu, A_\nu(X)] + [A_\mu(X), P_\nu]\right) \tag{3.24}$$

Consider, the first term of the last line,

$$[P_\mu, A_\nu(X)] = \int d^4x d^4x' \, |x\rangle \langle x|[P_\mu, A_\nu(X)]|x'\rangle \langle x'|$$

Now,

$$\langle x|[P_\mu, A_\nu(X)]|x'\rangle = \int d^4x'' \left(\langle x|P_\mu|x''\rangle \langle x''|A_\nu(X)|x'\rangle - \langle x|A_\nu(X)|x''\rangle \langle x''|P_\mu|x'\rangle\right)$$

$$= i\int d^4x'' \left(A_\nu(x')\delta^{(4)}(x'' - x')\partial_\mu \delta^{(4)}(x - x'') - A_\nu(x'')\delta^{(4)}(x - x'')\partial_\mu'' \delta^{(4)}(x'' - x')\right)$$

$$= i\int d^4x'' \left(A_\nu(x')\delta^{(4)}(x'' - x')\partial_\mu \delta^{(4)}(x - x'') + A_\nu(x'')\delta^{(4)}(x - x'')\partial_\mu' \delta^{(4)}(x'' - x')\right)$$

$$= i\left[A_\nu(x')\partial_\mu \delta^{(4)}(x - x') + \partial_\mu'\left(A_\nu(x')\delta^{(4)}(x - x')\right)\right]$$

$$= i\left[A_\nu(x')\left(\partial_\mu \delta^{(4)}(x - x') + \partial_\mu' \delta^{(4)}(x - x')\right) + \delta^{(4)}(x - x')\partial_\mu' A_\nu(x')\right]$$

$$= i\delta^{(4)}(x - x')\partial_\mu' A_\nu(x') \tag{3.25}$$

Similarly

$$\langle x|[P_\nu, A_\mu(X)]|x'\rangle = i\delta^{(4)}(x - x')\partial_\nu' A_\mu(x') \tag{3.26}$$

So,

$$[\Pi_\mu, \Pi_\nu] = -e\left([P_\mu, A_\nu(X)] - [P_\nu, A_\mu(X)]\right)$$

$$= -e\int d^4x d^4x' \, |x\rangle \left(\langle x|[P_\mu, A_\nu(X)]|x'\rangle - \langle x|[P_\nu, A_\mu(X)]|x'\rangle\right) \langle x'|$$

$$= -ie\int d^4x d^4x' \delta^{(4)}(x - x')\left(\partial_\mu' A_\nu(x') - \partial_\nu' A_\mu(x')\right) |x\rangle \langle x'|$$

$$= -ie\int d^4x d^4x' F_{\mu\nu}(x') |x\rangle \langle x'|$$

$$= -ie\int d^4x \, |x\rangle \langle x| \, F_{\mu\nu}(x) \tag{3.27}$$

Now the components of $F_{\mu\nu}(x)$ are just electric field or magnetic fields which is, in the present case, does not depend on

space-time coordinate. So the $F_{\mu\nu}(x)$ is just a constant number or $F_{\mu\nu}(x) = F_{\mu\nu}$. Here $F_{\mu\nu}$ is just a constant. So in the last equation we can take $F_{\mu\nu}$ outside the x integral and obtain

$$[\Pi_\mu, \Pi_\nu] = -ieF_{\mu\nu},$$

and hence,

$$[\Pi_\mu, H] = -2ieF_{\mu\nu}\Pi^\nu. \tag{3.28}$$

So the equation of motion of $X_\mu(s)$ and $\Pi_\mu(s)$ becomes

$$\frac{dX_\mu(s)}{ds} = -2\Pi_\mu(s) \tag{3.29}$$

$$\frac{d\Pi_\mu(s)}{ds} = -2eF_{\mu\nu}\Pi^\nu(s) \tag{3.30}$$

Now for our present case, the form of $F_{\mu\nu}$ is

$$F_{\mu\nu} = F^{\mu\nu} = \begin{pmatrix} 0 & 0 & 0 & 0 \\ 0 & 0 & -B & 0 \\ 0 & B & 0 & 0 \\ 0 & 0 & 0 & 0 \end{pmatrix} \tag{3.31}$$

So the equation of motion takes the following form

$$\frac{dX^i(s)}{ds} = -2\Pi^i(s) \tag{3.32}$$

$$\frac{d\Pi^i(s)}{ds} = -2eF_{ij}\Pi^j(s) \tag{3.33}$$

for $i, j = 1, 2$ and

$$\frac{dX^i(s)}{ds} = -2\Pi^i(s) \tag{3.34}$$

$$\frac{d\Pi^i(s)}{ds} = 0 \tag{3.35}$$

for $i = 0, 3$. Here F_{ij} is the ij^{th} element of the following 2×2 matrix

$$F = \begin{pmatrix} 0 & 1 \\ -1 & 0 \end{pmatrix}$$

We will now write the $i = 1, 2$ and $i = 0, 3$ sets compactly by defining $\Pi_\perp(s)$ and $\Pi_\parallel$ as

$$\Pi_\perp(s) = \begin{pmatrix} \Pi^1(s) \\ \Pi^2(s) \end{pmatrix} ; \quad \Pi_\parallel(s) = \{\Pi^0(s), \Pi^3(s)\},$$

and $X_\perp$ and $X_\parallel$ as

$$X_\perp(s) = \begin{pmatrix} X^1(s) \\ X^2(s) \end{pmatrix} ; \quad X_\parallel(s) = \{X^0(s), X^3(s)\}.$$

So the equation (3.32) and (3.33) takes the following matrix form

$$\frac{dX_\perp(s)}{ds} = -2\Pi_\perp(s) \tag{3.36}$$

$$\frac{d\Pi_\perp(s)}{ds} = -2eBF\Pi_\perp(s) \tag{3.37}$$

The solution of the above equation are given by

$$\Pi_\perp(s) = \exp\left[-2eBFs\right]\Pi_\perp(0) \tag{3.38}$$

$$X_\perp(s) - X_\perp(0) = -(eB)^{-1}F\left[\exp\left(-2eBFs\right) - \mathbb{1}_{2\times2}\right]\Pi_\perp(0) \tag{3.39}$$

We can simplify equation (3.39) by noting that

$$F = \begin{pmatrix} 0 & -i^2 \\ i^2 & 0 \end{pmatrix} = i\sigma_y$$

19

Where σ_y is the $y-$component of Pauli Spin matrix. Also $F^T = -F$ and $F^2 = -\mathbb{1}_{2\times 2}$. Now using the formula,

$$\exp\left[i(\hat{n} \cdot \vec{\sigma})\phi\right] = \mathbb{1}_{2\times 2}\cos(\phi) + i(\hat{n} \cdot \vec{\sigma})\sin(\phi), \tag{3.40}$$

we get,

$$F\left[\exp(-2eBFs) - \mathbb{1}_{2\times 2}\right] = 2\sin(eBs)\exp(-eBFs).$$

This implies

$$X_\perp(s) - X_\perp(0) = -2(eB)^{-1}\sin(eBs)\exp(-eBFs)\,\Pi_\perp(0). \tag{3.41}$$

Inverting equation (3.41) we get

$$\Pi_\perp(0) = -\frac{eB}{2\sin(eBs)}\exp(eBFs)\left[X_\perp(s) - X_\perp(0)\right] \tag{3.42}$$

Substituting equation (3.42) in equation (3.38) we get,

$$\Pi_\perp(s) = -\frac{eB}{2\sin(eBs)}\exp(-eBFs)\left[X_\perp(s) - X_\perp(0)\right] \tag{3.43}$$

Now focusing on the other set, equations (3.34) and (3.35) take the following matrix form

$$\frac{dX_{\shortparallel}(s)}{ds} = -2\Pi_{\shortparallel}(s) \tag{3.44}$$

$$\frac{d\Pi_{\shortparallel}(s)}{ds} = 0 \tag{3.45}$$

which gives us the following solution,

$$\Pi_{\shortparallel}(s) = \Pi_{\shortparallel}(0) \tag{3.46}$$

$$X_{\shortparallel}(s) - X_{\shortparallel}(0) = -2s\Pi_{\shortparallel}(0). \tag{3.47}$$

Hence we finally obtain,

$$\Pi_{\shortparallel}(s) = -\frac{1}{2s}\left[X_{\shortparallel}(s) - X_{\shortparallel}(0)\right]. \tag{3.48}$$

So,

$$\begin{aligned}
\Pi_\perp^T(s)\,\Pi_\perp(s) &= \frac{(eB)^2}{4\sin^2(eBs)}\left(X_\perp(s) - X_\perp(0)\right)^T \exp\left[-eB\left(F^T + F\right)s\right]\left(X_\perp(s) - X_\perp(0)\right) \\
&= \frac{(eB)^2}{4\sin^2(eBs)}\left(X_\perp(s) - X_\perp(0)\right)^T\left(X_\perp(s) - X_\perp(0)\right) \\
&= \frac{(eB)^2}{4\sin^2(eBs)}\left(X^i(s)X^i(s) - 2X^i(s)X^i(0) + X^i(0)X^i(0) - \left[X^i(0),\,X^i(s)\right]\right),
\end{aligned}$$

for $i = 1, 2$. The commutator can be simplified as

$$\begin{aligned}
\left[X^i(0),\,X^i(s)\right] &= -\frac{2\sin(eBs)}{eB}\left\{\exp(-eBFs)\right\}^{ij}\left[X^i(0),\,\Pi^j(0)\right] \\
&= -\frac{2\sin(eBs)}{eB}\left\{\exp(-eBFs)\right\}^{ij}\delta^{ij} \\
&= -\frac{2i\sin(eBs)}{eB}Tr\left[\exp(-eBFs)\right] \\
&= -\frac{2i\sin(eBs)}{eB}\cos(eBs)\,Tr[1]_{2\times 2} \\
&= -i\frac{4\sin(eBs)}{eB}\cos(eBs),
\end{aligned}$$

which yields, $\quad \Pi_\perp^T(s)\,\Pi_\perp(s) = \frac{(eB)^2}{4\sin^2(eBs)}\left(X^i(s)X^i(s) - 2X^i(s)X^i(0) + X^i(0)X^i(0)\right) + \frac{ieB}{\tan(eBs)}.$

So,

$$\langle x(s)|\,\Pi_\perp^T(s)\,\Pi_\perp(s)\,|x'(0)\rangle = \frac{(eB)^2}{4\sin^2(eBs)}\left(x - x'\right)_\perp^2\langle x(s)|x'(0)\rangle + \frac{ieB}{\tan(eBs)}\langle x(s)|x'(0)\rangle. \tag{3.49}$$

Now for the other set, i.e. $i = 0, 3$,

$$\Pi(s) \cdot \Pi(s)_\parallel = \frac{1}{4s^2} \left(X(s) - X(0) \right) \cdot \left(X(s) - X(0) \right)_\parallel$$

$$= \frac{1}{4s^2} \left(X(s) \cdot X(s)_\parallel - 2 \, X(s) \cdot X(0)_\parallel + X(0) \cdot X(0)_\parallel - \left[X^0(0) , \, X^0(s) \right] + \left[X^3(0) , \, X^3(s) \right] \right)$$

$$= \frac{1}{4s^2} \left(X(s) \cdot X(s)_\parallel - 2 \, X(s) \cdot X(0)_\parallel + X(0) \cdot X(0)_\parallel + 2s \, \left[X^0(0) , \, \Pi^0(0) \right] - 2s \, \left[X^3(0) , \, \Pi^3(0) \right] \right)$$

$$= \frac{1}{4s^2} \left(X(s) \cdot X(s)_\parallel - 2 \, X(s) \cdot X(0)_\parallel + X(0) \cdot X(0)_\parallel \right) - \frac{i}{s}.$$

So,

$$\langle x(s)| \, \Pi(s) \cdot \Pi(s)_\parallel \, |x'(0)\rangle = \frac{1}{4s^2} (x - x')^2_\parallel \, \langle x(s)|x'(0)\rangle - \frac{i}{s} \, \langle x(s)|x'(0)\rangle . \tag{3.50}$$

Thus combining (3.49) and (3.50), we obtain

$$\langle x(s)| \, \Pi^2(s) \, |x(0)\rangle = \left[\frac{1}{4s^2} (x - x')^2_\parallel - \frac{(e \, B)^2}{4 \, \sin^2(e \, B \, s)} \, (x - x')^2_\perp - \frac{i}{s} - \frac{i \, e \, B}{\tan(e \, B \, s)} \right] \langle x(s)|x'(0)\rangle . \tag{3.51}$$

So finally,

$$\langle x(s)| \, H \, |x'(0)\rangle = \langle x(s)| \, \Pi^2(s) - m^2 \, |x'(0)\rangle$$

$$= \left[\frac{1}{4s^2} (x - x')^2_\parallel - \frac{(e \, B)^2}{4 \, \sin^2(e \, B \, s)} \, (x - x')^2_\perp - \frac{i}{s} - \frac{i \, e \, B}{\tan(e \, B \, s)} - m^2 \right] \langle x(s)|x'(0)\rangle . \tag{3.52}$$

Comparing (3.15) and (3.73), we can identify $f(x, x'; s)$ as

$$f(x, x'; s) = \frac{1}{4s^2} (x - x')^2_\parallel - \frac{(e \, B)^2}{4 \, \sin^2(e \, B \, s)} \, (x - x')^2_\perp - \frac{i}{s} - \frac{i \, e \, B}{\tan(e \, B \, s)} - m^2 . \tag{3.53}$$

Now, we will use (3.17) to obtain the proper time evolution operator $U(x, x'; s)$. By integrating w.r.t s' and evaluating the exponential we get

$$U(x, x'; s) = C(x, x') \frac{e^{ism^2}}{s \sin(eBs)} \exp \left[\frac{i}{4s} \left((x - x')^2_\parallel - \frac{eBs}{\tan(eBs)} (x - x')^2_\perp \right) \right] . \tag{3.54}$$

One can write down the Green's function from (3.54) in a straightforward way as

$$G(x, x') = -i \int_{-\infty}^{0} ds \ \ U(x, x'; s)$$

$$= -i \int_{0}^{\infty} ds \ \ U(x, x'; -s)$$

$$\therefore G(x, x') = -iC(x, x') \int_{0}^{\infty} ds \ \ \frac{e^{-ism^2}}{s \sin(eBs)} \exp \left[-\frac{i}{4s} \left((x - x')^2_\parallel - \frac{eBs}{\tan(eBs)} (x - x')^2_\perp \right) \right] . \tag{3.55}$$

3.2. Free Fermion Propagator

In this subsection we are going to derive fermion propagator in presence of a constant background classical electromagnetic field following the Schwinger proper-time representation [97]. There exists several methods for deriving the fermion propagator in the presence of an external magnetic field. One widely used approach is the Ritus eigenfunction method [40, 98–102], which provides an alternative to other formulations. In contrast to these methods, there is also a method [2], where the sum over Landau levels naturally emerges from the completeness relation of wavefunctions – solutions to the Dirac equation in a constant magnetic field. Notably, with straightforward manipulations, the Schwinger proper-time representation can be recovered not only from the Ritus method [101] but also from the approach in Ref. [2]

To find the propagator of the system we need to find the Green's function of the system. The Green's function $G(x, x')$ of the fermion field in presence of external electromagnetic field satisfies the following differential equation

$$(i\gamma^\mu \partial_\mu + e\gamma^\mu A_\mu(x) - m)G(x, x') = \delta^{(4)}(x - x') \tag{3.56}$$

We follow the convention where $G(x, x')$ is considered as a matrix element of an operator G viz. $G(x, x') = \langle x | G | x' \rangle$. Similar to the previous section, defining the conjugate momentum operator in presence of external field Π_μ as $\Pi_\mu = P_\mu + eA_\mu(X)$, where P_μ is four-momentum and X_μ is four-position operator respectively, the equation (3.56) becomes

$$(\gamma^\mu \Pi_\mu - m)G = 1 \tag{3.57}$$

This implies

$$G = (\gamma^\mu \Pi_\mu - m)^{-1}$$
$$= ((\gamma \cdot \Pi)^2 - m^2)^{-1} (\gamma^\mu \Pi_\mu + m)$$

Applying the matrix identity,

$$(A + i\epsilon)^{-1} = -i \int_0^\infty ds \, \exp[is(A + i\epsilon)],$$

where $\epsilon > 0$ is introduced for convergence of the integral at infinity, we have

$$G = -i \int_0^\infty ds (\gamma^\mu \Pi_\mu + m) \exp[-is(m^2 - (\gamma \cdot \Pi)^2)] \tag{3.58}$$

This implies

$$G(x, x') = -i \int_0^\infty ds \, \langle x | \exp[-is(m^2 - (\gamma \cdot \Pi)^2)](\gamma^\mu \Pi_\mu + m) | x' \rangle$$
$$= -i \int_0^\infty ds \, \langle x | U(s)(\gamma^\mu \Pi_\mu + m) | x' \rangle e^{-ism^2}$$
$$= -i \int_0^\infty ds \, \langle x(s) | (\gamma^\mu \Pi_\mu + m) | x'(0) \rangle e^{-ism^2}$$
$$= -i \int_0^\infty ds \, [\gamma^\mu \langle x(s) | \Pi_\mu(0) | x'(0) \rangle + m \langle x(s) | x'(0) \rangle] e^{-ism^2}, \tag{3.59}$$

where $H = -(\gamma \cdot \Pi)^2$ and $U(s) = e^{-isH}$ and we have defined $\langle x(s) | \equiv \langle x | U(s)$, $|x'(0)\rangle = |x'\rangle$ and $\Pi_\mu(0) \equiv \Pi_\mu$. The quantity s is "proper time" defined earlier.

Now the Hamiltonian H can be simplified further as

$$H = -(\gamma \cdot \Pi)^2 = -\gamma^\mu \Pi_\mu \gamma^\nu \Pi_\nu$$
$$= -\frac{1}{2} \Pi_\mu \Pi_\nu \left(\{\gamma^\mu, \gamma^\nu\} + [\gamma^\mu, \gamma^\nu] \right)$$
$$= -\Pi_\mu \Pi_\nu (g^{\mu\nu} - i\sigma^{\mu\nu})$$
$$= -\Pi^2 - \frac{1}{2} e\sigma^{\mu\nu} F_{\mu\nu}$$

In the above derivation, we have used the defination $\sigma^{\mu\nu} \equiv \frac{i}{2}[\gamma^\mu, \gamma^\nu]$, the anticommutation relation $\{\gamma^\mu, \gamma^\nu\} = 2g^{\mu\nu}$, antisymmetry property of $\sigma^{\mu\nu}$ i.e. $\sigma^{\mu\nu} = -\sigma^{\nu\mu}$ and the commutation relation of the conjugate momentum operator $[\Pi_\mu, \Pi_\nu] = ieF_{\mu\nu}$. The Heisenberg equation of motion of the operators $x_\mu(s)$ and $\Pi_\mu(s)$ is

$$\frac{dX_\mu}{ds}(s) = -i[X_\mu, H] = 2\Pi_\mu(s) \tag{3.60}$$

$$\frac{d\Pi_\mu}{ds}(s) = -i[\Pi_\mu, H] = -2eF_{\mu\nu}\Pi^\nu(s) = -2ieF_{\mu\nu}g^{\nu\lambda}\Pi_\lambda(s) \tag{3.61}$$

These equations can be caste in the following form for convenience of our calculation

$$\frac{dX^\mu}{ds}(s) = 2\Pi^\mu(s) \tag{3.62}$$

$$\frac{d\Pi^\mu}{ds}(s) = -2eF^\mu{}_\nu \Pi^\nu(s) \tag{3.63}$$

Similar to the charged scalar case, the equations of motions can be separated as

$$\frac{dX_\parallel}{ds}(s) = 2\Pi_\parallel \tag{3.64}$$

$$\frac{d\Pi_\parallel}{ds}(s) = 0 \tag{3.65}$$

$$\frac{dX_\perp}{ds}(s) = 2\,\Pi_\perp \tag{3.66}$$

$$\frac{d\Pi_\perp}{ds}(s) = -2\,e\,B\,F^{ij}\,\Pi^j \qquad i,j = 1,2. \tag{3.67}$$

Here F^{ij} is ij^{th} element of the following matrix

$$F = \begin{pmatrix} 0 & 1 \\ -1 & 0 \end{pmatrix} = i\begin{pmatrix} 0 & -i \\ i & 0 \end{pmatrix} = i\,\sigma_y,$$

and

$$\Pi_\parallel(s) = \begin{pmatrix} \Pi^0(s) \\ \Pi^3(s) \end{pmatrix} ; \qquad\qquad \Pi_\perp(s) = \begin{pmatrix} \Pi^1(s) \\ \Pi^2(s) \end{pmatrix}$$

and similarly for $X_\parallel(s)$ and $X_\perp(s)$.

The solutions of equation (3.65) and equation (3.64) are given by

$$\Pi_\parallel(s) = \Pi_\parallel(0) \tag{3.68}$$

$$X_\parallel(s) - X_\parallel(0) = 2\,s\,\Pi_\parallel(0) \tag{3.69}$$

respectively. Also for equation (3.67) and equation (3.66)

$$\Pi_\perp(s) = \exp\left(-2\,e\,B\,F\,s\right)\Pi_\perp(0) \tag{3.70}$$

$$X_\perp(s) - X_\perp(0) = (e\,B\,F)^{-1}\left[1 - \exp\left(-2\,e\,B\,F\,s\right)\right]\Pi_\perp(0) \tag{3.71}$$

Agian, like the charged scalar case, here also our goal is to express every operators in terms of $X(s)$ and $X(0)$. And hence proceeding in an exactly similar way we obtain

$$\Pi_\perp^T(s)\,\Pi_\perp(s) = \frac{(e\,B)^2}{4\,\sin^2(e\,B\,s)}\left(X^i(s)X^i(s) - 2\,X^i(s)X^i(0) + X^i(0)X^i(0)\right) - \frac{i\,e\,B}{\tan(e\,B\,s)}$$

yielding

$$\langle x(s)|\,\Pi_\perp^T(s)\,\Pi_\perp(s)\,|x'(0)\rangle = \frac{(e\,B)^2}{4\,\sin^2(e\,B\,s)}\,(x - x')_\perp^2\,\langle x(s)|x'(0)\rangle - \frac{i\,e\,B}{\tan(e\,B\,s)}\,\langle x(s)|x'(0)\rangle,$$

and

$$\Pi(s)\cdot\Pi(s)_\parallel = \frac{1}{4s^2}\left(X(s)\cdot X(s)_\parallel - 2\,X(s)\cdot X(0)_\parallel + X(0)\cdot X(0)_\parallel\right) + \frac{i}{s}$$

yielding,

$$\langle x(s)|\,\Pi(s)\cdot\Pi(s)_\parallel\,|x'(0)\rangle = \frac{1}{4s^2}(x - x')_\parallel^2\,\langle x(s)|x'(0)\rangle + \frac{i}{s}\,\langle x(s)|x'(0)\rangle.$$

Thus

$$\langle x(s)|\,\Pi^2(s)\,|x(0)\rangle = \left[\frac{1}{4s^2}(x - x')_\parallel^2 - \frac{(e\,B)^2}{4\,\sin^2(e\,B\,s)}(x - x')_\perp^2 + \frac{i}{s} + \frac{i\,e\,B}{\tan(e\,B\,s)}\right]\langle x(s)|x'(0)\rangle. \tag{3.72}$$

Now

$$\frac{1}{2}e F_{\mu\nu}\sigma^{\mu\nu} = e F_{12}\sigma^{12} = \frac{ie}{2}F_{12}\left(2\gamma^1\,\gamma^2 - \{\gamma^1,\,\gamma^2\}\right) = i\,e\,B\,\gamma^1\,\gamma^2$$

So finally

$$\langle x(s)|\,H\,|x'(0)\rangle = -\,\langle x(s)|\,\Pi^2(s)\,|x'(0)\rangle - \frac{1}{2}e\,F_{\mu\nu}\,\sigma^{\mu\nu}\,\langle x(s)|x'(0)\rangle$$

$$\langle x(s)|\,H\,|x'(0)\rangle = \left[-\frac{1}{4s^2}(x - x')_\parallel^2 + \frac{(e\,B)^2}{4\,\sin^2(e\,B\,s)}(x - x')_\perp^2 - \frac{i}{s} - \frac{i\,e\,B}{\tan(e\,B\,s)} - i\,e\,B\,\gamma^1\,\gamma^2\right]\langle x(s)|x'(0)\rangle \tag{3.73}$$

Following the same procedure as in the charged scalar field we define $f(x,x';s)$ as $\langle x(s)|\,H\,|x'(0)\rangle \equiv f(x,x';s)\,\langle x(s)|\,|x'(0)\rangle$.

Also

$$\langle x(s)|x'(0)\rangle = C(x,x')\exp\left(-i\int^s ds'\,f(x,x';s')\right)$$

23

In this context, we can identify $f(x, x'; s)$ from (3.73) as

$$f(x, x'; s) = -\frac{1}{4s^2}(x - x')_\parallel^2 + \frac{(eB)^2}{4\sin^2(eBs)}(x - x')_\perp^2 - \frac{i}{s} - \frac{ieB}{\tan(eBs)} - ieB\gamma^1\gamma^2 \tag{3.74}$$

Thus after integrating and exponentiating we obtain finally

$$\langle x(s)|x'(0)\rangle = C(x, x')\frac{1}{s\sin(eBs)}\exp\left[-\frac{i}{4s}\left((x - x')_\parallel^2 - \frac{eBs}{\tan(eBs)}(x - x')_\perp^2\right)\right]\exp\left(-eBs\gamma^1\gamma^2\right) \tag{3.75}$$

Now we need to determine $\gamma^\mu\langle x(s)|\Pi_\mu(0)|x'(0)\rangle$ for Greens function.

So

$$\gamma^\mu\langle x(s)|\Pi_\mu(0)|x'(0)\rangle = \gamma^0\langle x(s)|\Pi^0(0)|x'(0)\rangle - \gamma^3\langle x(s)|\Pi^3(0)|x'(0)\rangle - \left(\gamma^1\langle x(s)|\Pi^1(0)|x'(0)\rangle + \gamma^2\langle x(s)|\Pi^2(0)|x'(0)\rangle\right)$$

From equation (3.69) and (3.68), the first two terms of the above gives $= \frac{1}{2s}\gamma\cdot(x - x')_\parallel$.

The last two terms

$$\sum_{i=1}^{2}\gamma^i\langle x(s)|\Pi^i(0)|x'(0)\rangle = \sum_{i=1}^{2}\sum_{j=1}^{2}\frac{eB}{2\sin(eBs)}\gamma^i\left(e^{-eBsF}\right)^{ij}\langle x(s)|\left(x^j(s) - x^j(0)\right)|x'(0)\rangle$$

$$= \frac{eB}{2\sin(eBs)}\sum_{i=1}^{2}\sum_{j=1}^{2}\gamma^i(\delta^{ij}\cos(eBs) - F^{ij}\sin(eBs))(x^j - x'^j)$$

$$= \frac{eB}{2}\left[\cot(eBs)\sum_{i=1}^{2}\gamma^i(x^i - x'^i) - \sum_{i=1}^{2}\sum_{j=1}^{2}\gamma^iF^{ij}(x^j - x'^j)\right]$$

$$= \frac{eB}{2}\left[\cot(eBs)\sum_{i=1}^{2}\gamma^i(x^i - x'^i) - \sum_{i=1}^{2}\sum_{j=1}^{2}\epsilon^{3ij}\gamma^i(x^j - x'^j)\right]$$

$$= \frac{eB}{2}\left[\cot(eBs)\,\gamma\cdot(x - x')_\perp - \left(\gamma^1(x^2 - x'^2) - \gamma^2(x^1 - x'^1)\right)\right]$$

Now,

$$\gamma^1(x^2 - x'^2) - \gamma^2(x^1 - x'^1) = -\gamma^1\gamma^2\,\gamma\cdot(x - x')_\perp$$

So,

$$\sum_{i=1}^{2}\gamma^i\langle x(s)|\Pi^i(0)|x'(0)\rangle = \frac{eB}{2}\left(\cot(eBs) + \gamma^1\gamma^2\right)\gamma\cdot(x - x')_\perp$$

Thus,

$$\gamma^\mu\langle x(s)|\Pi^\mu(0)|x'(0)\rangle = \frac{1}{2s}\gamma\cdot(x - x')_\parallel - \frac{eB}{2\sin(eBs)}\left(\cos(eBs) + \gamma^1\gamma^2\sin(eBs)\right)\gamma\cdot(x - x')_\perp$$

Finally,

$$\gamma^\mu\langle x(s)|\Pi^\mu(0)|x'(0)\rangle = \frac{1}{2s}\gamma\cdot(x - x')_\parallel - \frac{eB}{2\sin(eBs)}\exp\left(-ieBs\Sigma_3\right)\gamma\cdot(x - x')_\perp \tag{3.76}$$

Where $\Sigma_3 \equiv \begin{pmatrix} \sigma_3 & 0 \\ 0 & \sigma_3 \end{pmatrix} = i\gamma^1\gamma^2$.

This leads to

$$G(x, x') = -iC(x, x')\int_0^\infty ds\,\frac{1}{s\sin(eBs)}\exp\left(-im^2s + ieBs\Sigma_3\right)\exp\left[-\frac{i}{4s}\left((x - x')_\parallel^2 - \frac{eBs}{\tan(eBs)}(x - x')_\perp^2\right)\right]$$

$$\times\left[m + \frac{1}{2s}\left(\gamma\cdot(x - x')_\parallel - \frac{eBs}{\sin(eBs)}\exp\left(-ieBs\Sigma_3\right)\gamma\cdot(x - x')_\perp\right)\right] \tag{3.77}$$

The term $C(x, x')$ do not have any s dependence. It satisfies the following differential equations

$$\left[i\partial_\mu + eA_\mu(x) - \frac{1}{2}eF_{\mu\nu}(x' - x)^\nu\right]C(x, x') = 0 \tag{3.78}$$

24

$$\left[-i\,\partial'_\mu + e\,A_\mu\,(x') + \frac{1}{2}\,e\,F_{\mu\nu}\,(x'-x)^\nu \right] C\,(x,x') = 0 \tag{3.79}$$

Integrating equation (3.78) and (3.79), we get

$$C(x,x') = C'(x',x') \exp\left[i\,e\int_{x'}^{x} d\xi^\mu \left(A_\mu(\xi) + \frac{1}{2}F_{\mu\nu}(\xi - x')^\nu \right) \right] \tag{3.80}$$

$$C(x,x') = C'(x,x) \exp\left[i\,e\int_{x'}^{x} d\xi^\mu \left(A_\mu(\xi) + \frac{1}{2}F_{\mu\nu}(\xi - x)^\nu \right) \right] \tag{3.81}$$

Equating (3.80) and (3.81), we have

$$C'(x',x') \exp\left[i\,e\int_{x'}^{x} d\xi^\mu \left(A_\mu(\xi) + \frac{1}{2}F_{\mu\nu}(\xi - x')^\nu \right) \right] = C'(x,x) \exp\left[i\,e\int_{x'}^{x} d\xi^\mu \left(A_\mu(\xi) + \frac{1}{2}F_{\mu\nu}(\xi - x)^\nu \right) \right]$$

$$or,\ C'(x',x') \exp\left[i\,e\int_{x'}^{x} d\xi^\mu \left(\frac{1}{2}F_{\mu\nu}(x - x')^\nu \right) \right] = C'(x,x)$$

$$or,\ C'(x',x') \exp\left[i\,\frac{e}{2}\,(x - x')^\mu F_{\mu\nu}(x - x')^\nu \right] = C'(x,x)$$

$$\therefore\ C'(x',x') = C'(x,x)$$

The last step follows from the fact that, since $F_{\mu\nu}$ is antisymmetric, $(x - x')^\mu F_{\mu\nu}(x - x')^\nu = 0$. Thus we conclude from the last line that $C'(x,x)$ is just a constant.

Note that the the integral in (3.81) is independent of the integration path connecting the points x and x', since the curl of the term $A_\mu(\xi) + \frac{1}{2}F_{\mu\nu}(\xi - x)^\nu$ is vanishes. Now the curl of a four-vector is not a four-vector like ordinary three-vector. It is a 2nd rank tensor. For any four-vector $V_\mu(x)$, it is proportional to the term $\frac{\partial}{\partial x^\mu}V_\nu(x) - \frac{\partial}{\partial x^\nu}V_\mu(x)$. In our case $V_\mu(\xi) = A_\mu(\xi) + \frac{1}{2}F_{\mu\nu}(\xi - x)^\nu$ and we can show that $\frac{\partial}{\partial \xi^\mu}V_\nu(\xi) - \frac{\partial}{\partial \xi^\nu}V_\mu(\xi) = 0$.

Proof:

$$\frac{\partial}{\partial \xi^\mu}V_\nu(\xi) - \frac{\partial}{\partial \xi^\nu}V_\mu(\xi)$$

$$= \frac{\partial}{\partial \xi^\mu}A_\nu(\xi) - \frac{\partial}{\partial \xi^\nu}A_\mu(\xi) + \frac{1}{2}\left[F_{\nu\alpha}\frac{\partial}{\partial \xi^\mu}(\xi^\alpha - x'^\alpha) - F_{\mu\alpha}\frac{\partial}{\partial \xi^\nu}(\xi^\alpha - x'^\alpha) \right]$$

$$= F_{\mu\nu} + \frac{1}{2}\left[F_{\nu\alpha}\delta_\mu{}^\alpha - F_{\mu\alpha}\delta_\nu{}^\alpha \right]$$

$$= F_{\mu\nu} + \frac{1}{2}\left[F_{\nu\mu} - F_{\mu\nu} \right]$$

$$= F_{\mu\nu} + F_{\nu\mu}$$

$$= 0 \qquad\qquad (QED)$$

This gives us freedom to choose the path connecting x' and x as a straight line. The straight line is parameterized through a parameter t as follows

$$\xi^\mu(t) = x'^\mu + t\,(x^\mu - x'^\mu) \qquad\qquad t \in [0,1] \tag{3.82}$$

This choice is consistent as can be seen by noting that $\xi^\mu(1) = x'^\mu$ and $\xi^\mu(0) = x^\mu$. Here $d\xi^\mu(t) = (x^\mu - x'^\mu)\,dt$. In symmetric gauge $A^\mu(x) = \frac{B}{2}(0, -y, x, 0)$ which leads to

$$\int_{x'}^{x} d\xi^\mu A_\mu(\xi) = \frac{B}{2}\left[\int_0^1 dt\,(x^1 - x'^1)\left(-x'^2 - t\,(x^2 - x'^2) \right) + \int_0^1 dt\,(x^2 - x'^2)\left(x'^1 + t\,(x^1 - x'^1) \right) \right]$$

$$= \frac{B}{2}\left[\left\{ -x'^2(x^1 - x'^1) + x'^1(x^2 - x'^2) \right\}\int_0^1 dt + (x^1 - x'^1)(x^2 - x'^2)\left(-\int_0^1 dt\,t + \int_0^1 dt\,t \right) \right]$$

$$= \frac{B}{2}\left(x'^1 x^2 - x'^2 x^1 \right)$$

The term

$$\int_{x'}^{x} d\xi^\mu\,\frac{1}{2}F_{\mu\nu}\,(\xi - x)^\nu = \int_0^1 dt\,(x^\mu - x'^\mu)\frac{1}{2}F_{\mu\nu}(x^\nu - x'^\nu)(t - 1)$$

25

$$= (x^\mu - x'^\mu)\frac{1}{2}F_{\mu\nu}(x^\nu - x'^\nu) \int_0^1 dt\,(t-1)$$

$$= 0.$$

So in the symmetric gauge $\Phi(x,x') \equiv \exp\left[i\,e \int_{x'}^x d\xi^\mu \left(A_\mu(\xi) + \frac{1}{2}F_{\mu\nu}(\xi-x)^\nu\right)\right] = \exp\left[\frac{i\,e\,B}{2}\left(x'^1 x^2 - x'^2 x^1\right)\right]$. The four-vector potential enjoys gauge symmetry. So for the same field configuration, we can choose another four-vector potential defined by

$$A'_\mu(\xi) \equiv A_\mu(\xi) + \frac{\partial}{\partial \xi^\mu}\Lambda(\xi)$$

where $\Lambda(\xi)$ is a function of ξ which we choose as

$$\Lambda(\xi) = \frac{B}{2}\left(y\,\xi^1 - x\,\xi^2\right)$$

So, in the A' gauge

$$\Phi(x,x') = \exp\left[i\,e \int_{x'}^x d\xi^\mu \left(A'_\mu(\xi) + \frac{1}{2}F_{\mu\nu}(\xi-x)^\nu\right)\right]$$

$$= \exp\left[i\,e \int_{x'}^x d\xi^\mu \left(A_\mu(\xi) + \frac{1}{2}F_{\mu\nu}(\xi-x)^\nu\right) + i\,e \int_x^{x'} d\xi^\mu\,\Lambda(\xi)\right]$$

$$= \exp\left[i\,e \int_{x'}^x d\xi^\mu \left(A_\mu(\xi) + \frac{1}{2}F_{\mu\nu}(\xi-x)^\nu\right)\right] \exp\left[i\,e \int_x^{x'} d\xi^\mu\,\frac{\partial}{\partial \xi^\mu}\Lambda(\xi)\right]$$

$$= \exp\left[\frac{i\,e\,B}{2}\left(x'^1 x^2 - x'^2 x^1\right)\right] \exp\left[i\,e\,(\Lambda(x') - \Lambda(x))\right]$$

$$= \exp\left[\frac{i\,e\,B}{2}\left(x'^1 x^2 - x'^2 x^1\right)\right] \exp\left[-\frac{i\,e\,B}{2}\left(x'^1 x^2 - x'^2 x^1\right)\right]$$

$$= 1$$

So essentially, in a special gauge, $C(x,x')$ is just a constant and we can choose it to be $C = -i(4\pi)^{-2}$.

Thus, from (3.77), $G(x,x')$ becomes

$$G(x,x') = -(4\pi)^{-2} \int_0^\infty ds\, \frac{1}{s \sin(e\,B\,s)} \exp\left(-im^2 s + i\,e\,B\,s\,\Sigma_3\right) \exp\left[-\frac{i}{4\,s}\left((x-x')_\parallel^2 - \frac{e\,B\,s}{\tan(e\,B\,s)}(x-x')_\perp^2\right)\right]$$

$$\times \left[m + \frac{1}{2\,s}\left(\gamma \cdot (x-x')_\parallel - \frac{e\,B\,s}{\sin(e\,B\,s)} \exp\left(-i\,e\,B\,s\,\Sigma_3\right) \gamma \cdot (x-x')_\perp\right)\right] \quad (3.83)$$

It is evident that, in general, the greens function can be written as

$$G(x,x') = \Phi(x,x')\mathcal{G}(x-x'),$$

where $\mathcal{G}(x-x')$ is given by

$$\mathcal{G}(x-x') = -(4\pi)^{-2} \int_0^\infty ds\, \frac{1}{s \sin(e\,B\,s)} \exp\left(-im^2 s + i\,e\,B\,s\,\Sigma_3\right) \exp\left[-\frac{i}{4\,s}\left((x-x')_\parallel^2 - \frac{e\,B\,s}{\tan(e\,B\,s)}(x-x')_\perp^2\right)\right]$$

$$\times \left[m + \frac{1}{2\,s}\left(\gamma \cdot (x-x')_\parallel - \frac{e\,B\,s}{\sin(e\,B\,s)} \exp\left(-i\,e\,B\,s\,\Sigma_3\right) \gamma \cdot (x-x')_\perp\right)\right]$$

$$(3.84)$$

From the last equation, it is clear that $\mathcal{G}(x-x')$ is tranlationally invariant. But $\Phi(x,x')$ is not, in general, translationally invariant as is evident in the case of symmetric gauge. Also different choice of gauge leads to different $\Phi(x,x')$. So, $\Phi(x,x')$ is not also gauge invariant. So, we loosely say the $\Phi(x,x')$ *breaks* both translational and gauge inavarience of the Green's function fermion in presence of background magnetic field.

Let us take the fourier transformation of $\mathcal{G}(x-x')$.

$$\tilde{\mathcal{G}}(p) = \int d^4 x\, e^{i\,p\cdot(x-x')}\mathcal{G}(x-x').$$

Changing variable from $x - x'$ to x and putting equation (3.84) in the last equation we get,

$$\tilde{\mathcal{G}}(p) = -(4\pi)^{-2} \int_0^\infty ds\, \frac{1}{s\sin(eBs)} e^{-im^2 s + ieBs\,\Sigma_3} \int d^4x\, \exp\left[-\frac{i}{4s}\left(x_\parallel^2 - \frac{eBs}{\tan(eBs)}x_\perp^2\right)\right] e^{ip\cdot x}$$

$$\times \left[m + \frac{1}{2s}\left(\gamma\cdot x_\parallel - \frac{eBs}{\sin(eBs)}e^{-ieBs\,\Sigma_3}\gamma\cdot x_\perp\right)\right]$$

$$= -(4\pi)^{-2}\int_0^\infty ds\,\frac{1}{s\sin(eBs)}e^{-im^2 s + ieBs\,\Sigma_3}\left[m\,J_1 + \frac{1}{2s}\left(J_2 - \frac{eBs}{\sin(eBs)}e^{-ieBs\,\Sigma_3}J_3\right)\right],$$

where

$$J_1 \equiv \int d^4x\, \exp\left[-\frac{i}{4s}\left(x_\parallel^2 - \frac{eBs}{\tan(eBs)}x_\perp^2\right)\right] e^{ip\cdot x} \tag{3.85}$$

$$J_2 \equiv \int d^4x\, \exp\left[-\frac{i}{4s}\left(x_\parallel^2 - \frac{eBs}{\tan(eBs)}x_\perp^2\right)\right] e^{ip\cdot x}\,\gamma\cdot x_\parallel \tag{3.86}$$

$$J_3 \equiv \int d^4x\, \exp\left[-\frac{i}{4s}\left(x_\parallel^2 - \frac{eBs}{\tan(eBs)}x_\perp^2\right)\right] e^{ip\cdot x}\,\gamma\cdot x_\perp \tag{3.87}$$

To compute the above integrals we note that $\int d^4x = \int d^2x_\parallel \int d^2x_\perp$ and $p\cdot x = p\cdot x_\parallel - p\cdot x_\perp$. Now,

$$J_1 = \int d^2x_\parallel \exp\left[-i\left(\frac{1}{4\,s}x_\parallel^2 - p\cdot x_\parallel\right)\right]\int d^2x_\perp \exp\left[-i\left(-\frac{eB}{4\tan(eBs)}x_\perp^2 + p\cdot x_\perp\right)\right]$$

$$= \int dx^0 \exp\left[-i\left(\frac{1}{4\,s}(x^0)^2 - p^0 x^0\right)\right]\int dx^0 \exp\left[-i\left(-\frac{1}{4\,s}(x^3)^2 + p^3 x^3\right)\right]\int dx^1 \exp\left[-i\left(-\frac{eB}{4\tan(eBs)}(x^1)^2 + p^1 x^1\right)\right]$$

$$\times \int dx^2 \exp\left[-i\left(-\frac{eB}{4\tan(eBs)}(x^2)^2 + p^2 x^2\right)\right]$$

Using the identity

$$\int_{-\infty}^{-\infty} dv\, \exp\left[-i\left(av^2 + bv\right)\right] = \sqrt{\frac{\pi}{i\,a}}\exp\left(i\frac{b^2}{4\,a}\right)$$

we get

$$J_1 = \sqrt{\frac{\pi}{i(4\,s)^{-1}}}\cdot\sqrt{\frac{\pi}{-i(4\,s)^{-1}}}\cdot\sqrt{\frac{4\pi\sin(eBs)}{-ie\,B}}\cdot\sqrt{\frac{4\pi\sin(eBs)}{-ie\,B}}\exp\left[i\,s\left(p_\parallel^2 - \frac{\tan(e\,B\,s)}{e\,B\,s}p_\perp^2\right)\right]$$

$$\therefore J_1 = i(4\pi)^2\frac{s}{e\,B}\tan(e\,B\,s).\exp\left[i\,s\left(p_\parallel^2 - \frac{\tan(e\,B\,s)}{e\,B\,s}p_\perp^2\right)\right]$$

Using

$$\int_{-\infty}^\infty dv\, v\exp\left[-i\left(av^2 + bv\right)\right] = -\frac{b}{2\,a}\sqrt{\frac{\pi}{i\,a}}\exp\left(i\frac{b^2}{4\,a}\right)$$

we get,

$$J_2 = i(4\pi)^2\frac{2\,s^2}{e\,B}\tan(e\,B\,s).\exp\left[i\,s\left(p_\parallel^2 - \frac{\tan(e\,B\,s)}{e\,B\,s}p_\perp^2\right)\right]\gamma.p_\parallel$$

and

$$J_3 = i(4\pi)^2\frac{2s}{(e\,B)^2}\tan^2(e\,B\,s).\exp\left[i\,s\left(p_\parallel^2 - \frac{\tan(e\,B\,s)}{e\,B\,s}p_\perp^2\right)\right]\gamma.p_\perp$$

Putting the expressions of J_1, J_2 & J_3 in the last expression of $\tilde{\mathcal{G}}(p)$, we have,

$$\tilde{\mathcal{G}}(p) = -i\int_0^\infty \frac{ds}{e\,B\cos(e\,B\,s)}\exp\left[i\,s\left(p_\parallel^2 - \frac{\tan(e\,B\,s)}{e\,B\,s}p_\perp^2 - m^2\right)\right]\left[\exp(i\,e\,B\,s\,\Sigma_3)\left(m + \gamma.p_\parallel\right) - \frac{\gamma.p_\perp}{\cos(e\,B\,s)}\right]$$

Now there is a serious problem. The propagator, in fact, blows up in the limit $B \longrightarrow 0$ due to the factor of $e\,B$ in the denominator of above expression. If we had chosen $C = -e\,B\,(4\pi)^{-2}$ instead of just $-(4\pi)^{-2}$ the propagator would converge and give the same form as that of our known. So we choose $C = -eB(4\pi)^{-2}$. Thus our momentum space propagator finally becomes

$$i\tilde{\mathcal{G}}(p) = \int_0^\infty ds\,\frac{1}{\cos(e\,B\,s)}\exp\left[i\,s\left(p_\parallel^2 - \frac{\tan(e\,B\,s)}{e\,B\,s}p_\perp^2 - m^2\right)\right]\left[\exp(i\,e\,B\,s\,\Sigma_3)\left(m + \gamma.p_\parallel\right) - \frac{\gamma.p_\perp}{\cos(e\,B\,s)}\right] \tag{3.88}$$

27

So our momentum-space propagator becomes

$$\tilde{\mathcal{G}}(p) = -i \int_0^\infty ds \, \frac{1}{\cos(e\,B\,s)} \exp\left[i\,s\,\left(p_\parallel^2 - \frac{\tan(e\,B\,s)}{e\,B\,s}p_\perp^2 - m^2\right)\right] \left[(\cos(e\,B\,s) + \gamma_1\gamma_2\sin(e\,B\,s))\left(m + \gamma\cdot p_\parallel\right) - \frac{\gamma\cdot p_\perp}{\cos(e\,B\,s)}\right].$$

(3.89)

To get to a different form of the free fermion propagator which will be really useful in practical purposes, we make the following change of variable $v = e\,B\,s$. so $ds = (e\,B)^{-1}dv$. So

$$\tilde{\mathcal{G}}(p) = -i \int_0^\infty dv \, \frac{1}{e\,B\,\cos v} \exp\left[i\,\frac{v}{e\,B}\left(p_\parallel^2 - \frac{\tan v}{v}p_\perp^2 - m^2\right)\right] \left[(\cos v + \gamma_1\gamma_2\sin v)\left(m + \gamma\cdot p_\parallel\right) - \frac{\gamma\cdot p_\perp}{\cos v}\right]$$

With the defination, $\rho = (e\,B)^{-1}(m^2 - p_\parallel^2)$ and $\alpha = (e\,B)^{-1}p_\perp^2$, the last equation takes the form

$$\tilde{\mathcal{G}}(p) = -i \int_0^\infty dv \, \frac{1}{e\,B\,\cos v} \exp\left(-i\,\alpha\,\tan v\right)\exp\left(-i\,\rho\,v\right)\left[(\cos v + \gamma_1\gamma_2\sin v)\left(m + \gamma\cdot p_\parallel\right) - \frac{\gamma\cdot p_\perp}{\cos v}\right]$$

$$= -i \int_0^\infty dv \, \exp\left(-i\,\rho\,v\right)\frac{1}{e\,B}\left[(I_1 + (\gamma_1\gamma_2)\,I_2)\left(m + \gamma\cdot p_\parallel\right) - (\gamma\cdot p_\perp)\,I_3\right],$$

where we define

$$I_1(v) \equiv \exp(-i\,\alpha\,\tan v) \tag{3.90}$$

$$I_2(v) \equiv \exp(-i\,\alpha\,\tan v)\,\tan v \tag{3.91}$$

$$I_3(v) \equiv \frac{1}{\cos^2 v}\exp(-i\,\alpha\,\tan v). \tag{3.92}$$

Note that, $I_j(v) = I_j(v + 2\pi)$ for $j = 1, 2, 3$.

Now consider the integral

$$J_j = \int_0^\infty dv \, \exp\left(-i\rho\,v\right)I_j(v)$$

$$= \left(\int_0^\pi + \int_\pi^{2\pi} + \int_{2\pi}^{3\pi} + \cdots\right) dv \, \exp\left(-i\rho\,v\right)I_j(v)$$

$$= \sum_{n=0}^\infty \int_{n\pi}^{(n+1)\pi} dv \, \exp\left(-i\rho\,v\right)I_j(v)$$

We make the following change of variable $v \to v - n\pi$ and get

$$J_j = \sum_{n=0}^\infty \exp\left(-i\,n\,\pi\,\rho\right)\int_0^\pi dv \exp\left(-i\rho v\right)I_j(v)$$

$$= \frac{1}{1 - e^{-i\pi\rho}}A_j,$$

where we have defined $A_j \equiv \int_0^\pi dv \exp\left(-i\rho v\right)I_j$. Note that

$$A_2 = i\frac{\partial}{\partial\alpha}A_1 \tag{3.93}$$

$$A_3 = -\frac{i}{\alpha}\left(1 - e^{-i\pi\rho}\right) - \frac{\rho}{\alpha}A_1 \tag{3.94}$$

proof:

$$i\frac{\partial}{\partial\alpha}A_1 = i\frac{\partial}{\partial\alpha}\int_0^\pi dv \exp\left(-i\rho v\right)\exp(-i\,\alpha\,\tan v) = i\int_0^\pi dv \exp\left(-i\rho v\right)\frac{\partial}{\partial\alpha}\exp(-i\,\alpha\,\tan v)$$

$$= \int_0^\pi dv \exp\left(-i\rho v\right)\exp(-i\,\alpha\,\tan v)\,\tan v = \int_0^\pi dv \exp\left(-i\rho v\right)I_2 = A_2$$

This proves equation (3.93). And we note that $\frac{i}{\alpha}\frac{\partial}{\partial v}I_1(v) = I_3(v)$.

$$A_3 = \frac{i}{\alpha}\int_0^\pi dv \, \exp(-i\rho v)\frac{\partial}{\partial v}I_1(v)$$

$$= \frac{i}{\alpha}\left\{[\exp(-i\pi\rho)I_1(\pi) - I_1(0)] - \int_0^\pi dv \, I_1\frac{\partial}{\partial v}\exp(-i\rho v)\right\}$$

28

$$= \frac{i}{\alpha} \left\{ [\exp(-i\pi\rho) - 1] + i\rho \int_0^\pi dv \, \exp(-i\rho v) I_1(v) \right\}$$

$$= \frac{-i}{\alpha} (1 - \exp(-i\pi\rho)) - -\frac{\rho}{\alpha} A_1$$

This proves equation (3.94). We need to evaluate A_1 and using equations (3.93) and (3.94), from that we get A_2 and A_3 respectively. The term $\exp[-i\alpha \tan(\nu)]$ can be written as

$$\exp[-i\alpha \tan(v)] = \exp\left[\alpha \frac{-e^{-2iv} + 1}{-e^{-2iv} - 1}\right]$$

The RHS of the above equation can be further simplified using the identity

$$\exp\left[-\frac{xZ}{1-Z}\right] \exp\left[-\frac{x}{2}\right] = \exp\left[\frac{x}{2}\frac{Z+1}{Z-1}\right]$$

to

$$\exp[-i\alpha \tan(v)] = e^{-\alpha} \exp\left[2\alpha \frac{e^{-2iv}}{1+e^{-2iv}}\right], \tag{3.95}$$

with the identification $x \equiv 2\alpha$ and $Z \equiv -e^{-2iv}$. The generating function of Laggure polynomial is defined by the following relation

$$\frac{\exp[-xZ/1-Z]}{1-Z} = \sum_{n=0}^\infty L_n(x) Z^n$$

for $|Z| << 1$.

Now,

$$\exp[-xZ/1-Z] = (1-Z) \sum_{n=0}^\infty L_n(x) Z^n$$

$$= \sum_{n=0}^\infty (L_n(x) - L_{n-1}(x)) Z^n.$$

Here we have used the fact that $L_{-1}(x) = 0$. So,

$$\exp[-i\alpha \tan(v)] = e^{-\alpha} \sum_{n=0}^\infty (-1)^n (L_n(2\alpha) - L_{n-1}(2\alpha)) e^{-2inv} \tag{3.96}$$

Using the last identity, we evalute A_1 as

$$A_1 = \int_0^\pi dv \, \exp(-i\rho v) I_1$$

$$= e^{-\alpha} \sum_{n=0}^\infty (-1)^n (L_n(2\alpha) - L_{n-1}(2\alpha)) \int_0^\pi dv \, \exp(-i(\rho + 2n)v)$$

$$= i e^{-\alpha} (e^{-i\pi\rho} - 1) \sum_{n=0}^\infty (-1)^n (L_n(2\alpha) - L_{n-1}(2\alpha)) \frac{1}{\rho + 2n}$$

$$= -i e^{-\alpha} (1 - e^{-i\pi\rho}) \sum_{n=0}^\infty (-1)^n \frac{C_n(2\alpha)}{\rho + 2n}$$

$$= -i (1 - e^{-i\pi\rho}) \sum_{n=0}^\infty \frac{d_n(\alpha)}{\rho + 2n}$$

where $C_n(2\alpha) \equiv L_n(2\alpha) - L_{n-1}(2\alpha)$ and $d_n(\alpha) \equiv e^{-\alpha}(-1)^n C_n(2\alpha)$. So

$$J_1 = -i \sum_{n=0}^\infty \frac{d_n(\alpha)}{\rho + 2n}$$

$$J_2 = \sum_{n=0}^\infty \frac{d'_n(\alpha)}{\rho + 2n}$$

$$J_3 = -\frac{i}{\alpha} + i\frac{\rho}{\alpha} \sum_{n=0}^\infty \frac{d_n(\alpha)}{\rho + 2n}$$

. Now

$$\tilde{\mathcal{G}}(p) = -\frac{i}{eB} \left[(m + \gamma.p_{\parallel})(J_1 + (\gamma_1 \gamma_2) J_2) - (\gamma.p_\perp) J_3\right]$$

So $\tilde{\mathcal{G}}(p)$ becomes

$$\tilde{\mathcal{G}}(p) = -\frac{i}{eB}\left[\left(m+\gamma.p_\parallel\right)\left(-i\sum_{n=0}^\infty \frac{d_n(\alpha)}{\rho+2n} + \sum_{n=0}^\infty \frac{\gamma_1\gamma_2 d_n'(\alpha)}{\rho+2n}\right) + i\frac{\gamma.p_\perp}{\alpha} - i\sum_{n=0}^\infty \left(\gamma.p_\perp\right)\frac{\rho}{\alpha}\frac{d_n(\alpha)}{\rho+2n}\right]$$

$$= -\sum_{n=0}^\infty \{\left(m+\gamma.p_\parallel\right) + \frac{\rho}{\alpha}\left(\gamma.p_\perp\right)\}\frac{d_n(\alpha)}{eB\rho + 2neB} - i\sum_{n=0}^\infty \{\left(m+\gamma.p_\parallel\right)\gamma_1\gamma_2\}\frac{d_n'(\alpha)}{eB\rho + 2neB} + \frac{\gamma.p_\perp}{eB\alpha}$$

$$= \sum_{n=0}^\infty \{\left(m+\gamma.p_\parallel\right) + \frac{\rho}{\alpha}\left(\gamma.p_\perp\right)\}\frac{d_n(\alpha)}{p_\parallel^2 - m^2 - 2neB} + i\sum_{n=0}^\infty \{\left(m+\gamma.p_\parallel\right)\gamma_1\gamma_2\}\frac{d_n'(\alpha)}{p_\parallel^2 - m^2 - 2neB} + \frac{\gamma.p_\perp}{p_\perp^2}$$

$$= \sum_{n=0}^\infty \frac{D\, d_n(\alpha) + i\bar{D}\, d_n'(\alpha)}{p_\parallel^2 - m^2 - 2neB} + \frac{\gamma.p_\perp}{p_\perp^2}$$

where $D \equiv \left(m+\gamma.p_\perp\right) + \frac{\rho}{\alpha}\left(\gamma.p_\perp\right) = \left(m+\gamma.p_\parallel\right) - \frac{p_\parallel^2 - m^2}{p_\perp^2}\left(\gamma.p_\perp\right)$ and $\bar{D} = \left(m+\gamma.p_\perp\right)\gamma_1\gamma_2$.

So,

$$i\tilde{\mathcal{G}}(p) = \sum_{n=0}^\infty \frac{id_n(\alpha)\, D - d_n'(\alpha)\, \bar{D}}{p_\parallel^2 - m^2 - 2neB} + i\frac{\gamma.p_\perp}{p_\perp^2} \tag{3.97}$$

This propagator can be caste in the following form

$$i\tilde{\mathcal{G}}(p) = i\, e^{-\alpha}\sum_{n=0}^\infty (-1)^n \frac{\left(\gamma.p_\parallel + m\right)\left[\left(1 - i\,\gamma_1\gamma_2\right)L_n(2\alpha) - \left(1 + i\,\gamma_1\gamma_2\right)L_{n-1}(2\alpha)\right] + 4\,\gamma.p_\perp L_{n-1}^1(2\alpha)}{p_\parallel^2 - m^2 - 2neB}, \tag{3.98}$$

where the second term in the R.H.S of (3.97) gets canceled with the zeroth component of $\frac{id_0(\alpha)D}{p_\parallel^2 - m^2}$.

So, one can use (3.89) or (3.98) as the final expression for the free-fermion propagator within the most general scenario of any arbitrary external magnetic field. Next we will briefly discuss the limiting scenarios, i.e. a strongly or weakly magnetized medium.

3.2.1. Strong field approximation

In the limit of very strong external magnetic field, one can effectively assume that the fermions within such strong magnetic field will be trapped only in the lowest Landau levels, as all the other Landau levels get pushed to infinity. This fact can be established also by plotting the dispersion relation for fermions in a magnetized medium as a function of the external magnetic field, as shown in Fig. 3.1. This is why, strong field approximation is synonymous to lowest Landau level or LLL approximation. To obtain the free fermion propagator within the LLL approximation we put $n = 0$ in (3.98) which gives us :

$$i\tilde{\mathcal{G}}_{LLL}(p) = i\, e^{-\alpha}\frac{\left(\gamma.p_\parallel + m\right)\left(1 - i\,\gamma_1\gamma_2\right)}{p_\parallel^2 - m^2}, \tag{3.99}$$

where we have used the properties of the Laguerre polynomials, i.e. $L_0(x) = 1$ and $L_{-1}(x) = 0$. Eq. (3.99) clearly demonstrates that a dimensional reduction from $3+1 \rightarrow 1+1$ takes place in presence of a strong magnetic field which in turn reflects the fact that the motion of these charged particles is restricted in perpendicular directions of the magnetic field. In the following sections of this review, we will see that in multiple scenarios this simplified expression within the LLL approximation will become useful.

3.2.2. Weak field approximation

On the other end of the spectrum, for a weak enough external magnetic field one can think of the magnetic field as a perturbation. In such scenario, we start with eq. (3.89) and expand it in the powers of the magnetic field eB. First of all, let us rearrange the eq. (3.89) as :
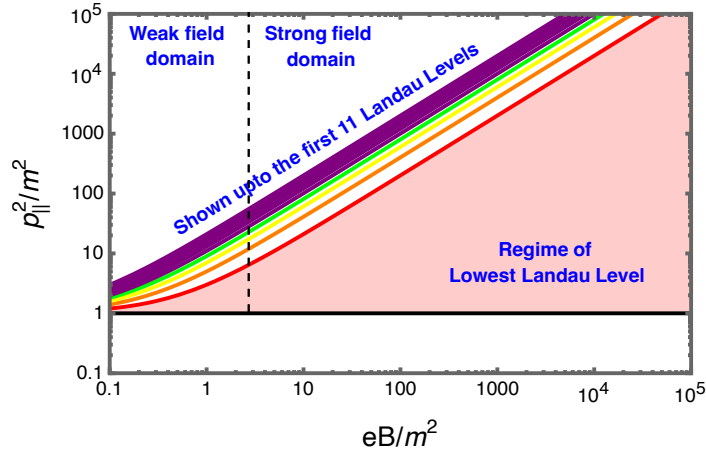
Figure 3.1: Thresholds corresponding to a few Landau Levels are displayed as a function of the external magnetic field. The regime of the lowest Landau level at strong magnetic field approximation is shown by the shaded area.

$$\tilde{\mathcal{G}}(p) = -i \int_0^\infty ds \, \exp\left[i \, s \, \left(p_\parallel^2 - \frac{\tan(e \, B \, s)}{e \, B \, s}p_\perp^2 - m^2\right)\right]\left[(1 + \gamma_1\gamma_2\tan(e \, B \, s))\left(\slashed{p}_\parallel + m\right) - \slashed{p}_\perp\left(1 + \tan^2(e \, B \, s)\right)\right].$$

(3.100)

Now expanding the exponential and tangent functions, we immediately get $\tilde{\mathcal{G}}(p)$ as a series in powers of eB. To order $(eB)^2$ it is given by :

$$\tilde{\mathcal{G}}_w(p) = \frac{\slashed{p} + m}{p^2 - m^2} + eB \, \frac{i(\slashed{p}_\parallel + m)\gamma_1\gamma_2}{(p^2 - m^2)^2} - 2(eB)^2 \, \left[\frac{\slashed{p}_\perp}{(p^2 - m^2)^3} - \frac{p_\perp^2(\slashed{p} + m)}{(p^2 - m^2)^4}\right].$$

(3.101)

4. Field Theory with Thermal Background

Thermal Field Theory (TFT) merges Quantum Field Theory and Statistical Mechanics to tackle complex many-body problems involving interactions at finite temperature and chemical potential. It provides a comprehensive framework for describing large ensembles of interacting particles, including those governed by gauge interactions, in thermal environments. TFT also accounts for phenomena and processes that do not occur in vacuum field theory. There are two primary formalisms in Thermal Field Theory: i) Imaginary Time (Matsubara) Formalism [103]: This approach is well-suited for systems in thermal equilibrium, using periodic (bosonic) or anti-periodic (fermionic) boundary conditions in imaginary time. ii) Real Time (Schwinger-Keldysh) Formalism [104–106]: This method handles non-equilibrium scenarios and provides a framework for real-time dynamics in thermal systems. Several textbooks [107–111] and review articles [112] offer detailed discussions on finite temperature field theory. Additionally, advanced techniques such as hard thermal loop perturbation theory are covered in recent reviews [113], providing insights into improved perturbative methods. A brief outline of these concepts follows.

4.1. Imaginary Time Formalism

4.1.1. Connection to imaginary time and Matsubara formalism

For a given Schrödinger operator, $\mathcal{A}$, the Heisenberg operator, $\mathcal{A}_H(t)$ can be written as

$$\mathcal{A}_H(t) = e^{i\mathcal{H}t} \, \mathcal{A} \, e^{-i\mathcal{H}t} \, .$$

(4.1)

The thermal correlation function of two operators can also be written [109, 112, 113] as

$$\langle \mathcal{A}_H(t)\mathcal{B}_H(t')\rangle_\beta \;=\; \mathcal{Z}^{-1}(\beta)\mathrm{Tr}\left[e^{-\beta\mathcal{H}}\mathcal{A}_H(t)\mathcal{B}_H(t')\right] = \langle \mathcal{B}_H(t')\mathcal{A}_H(t+i\beta)\rangle_\beta \;. \tag{4.2}$$

To derive Eq.(4.2), we utilized Eq.(4.1), inserted the unit operator $1 = e^{-\beta\mathcal{H}}e^{\beta\mathcal{H}}$, and applied the cyclic property of the trace. The resulting Eq. (4.2) is recognized as the Kubo-Martin-Schwinger (KMS) relation. Notably, this relation holds universally, regardless of the Grassmann parity of the operators, meaning it applies to both bosonic and fermionic operators. For bosons, the KMS relation enforces periodic boundary conditions, while for fermions, it leads to anti-periodicity due to their respective commutation and anti-commutation relations. Importantly, the thermal evolution operator $e^{-\beta\mathcal{H}}$ resembles a time evolution operator $(e^{-i\mathcal{H}t})$ when the inverse temperature β is analytically continued to imaginary time $((\beta = it)$. While this resemblance may appear coincidental, it suggests the possibility of a deeper, yet unexplored, connection between thermal and quantum time evolution.

This implies a relationship between temperature and imaginary time, given by $\beta = it$, as illustrated in Fig. 4.1. This transformation is known as a Wick rotation. Since $\beta = 1/T, \beta$ becomes finite at finite temperatures. By utilizing the time evolution operator, one can derive the S-matrix, Feynman rules, and corresponding Feynman diagrams. The Matsubara (imaginary time) formalism offers a framework for evaluating the partition function and other thermodynamic quantities using a diagrammatic approach, similar to the methods employed in zero-temperature field theory. This formalism allows for the systematic application of perturbative techniques to finite-temperature systems.
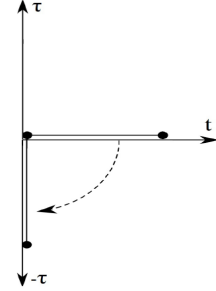
Figure 4.1: The Wick rotation in the imaginary time axis is represented by $t = -i\tau$.

4.1.2. Periodicity (Anti-periodicity) of the Green's function

The thermal Green's function [109, 112, 113] for $\tau > \tau'$:

$$G_\beta(\vec{x}, \vec{x}';\tau,\tau') \;=\; \mathcal{Z}^{-1}(\beta)\,\mathrm{Tr}\left(e^{-\beta\mathcal{H}}\mathcal{T}\left[\Phi_H(\vec{x},\tau)\Phi_H(\vec{x}',\tau')\right]\right) = \pm\, G_\beta(\vec{x},\vec{x}';\tau,\tau'+\beta), \tag{4.3}$$

where we have used same procedure as (4.2) and the time evolution of the state: $\Phi_H(\vec{x}',\tau'+\beta) = e^{\beta\mathcal{H}}\Phi_H(\vec{x}',\tau')e^{-\beta\mathcal{H}}$ to obtain (4.3). Since the Green's function for a Dirac field changes sign after one period of β, this implies that Dirac fields must be antiperiodic in imaginary time. In contrast, bosonic fields remain positive and periodic since they do not change sign. Mathematically, this is expressed as: $\Phi(\vec{x},\tau) = \pm\Phi(\vec{x},\tau+\beta)$, where the plus sign applies to bosonic fields and the minus sign to fermionic fields. It is important to note that the spatial directions remain unaffected in this formalism, maintaining open boundary conditions: $-\infty \le x \le \infty \Rightarrow$ open. This distinction highlights that only the imaginary time direction undergoes periodic or antiperiodic treatment, while spatial directions retain their standard range and continuity.

In $T = 0$ (Minkowski space-time), both space and time are open, meaning their ranges are: $-\infty \le x \le \infty$ and $-\infty \le \tau \le \infty$. The topology of the space-time is $R^4 = R^3 \times R^1$, where both space and time are treated symmetrically, and both are on equal footing. This maintains the usual Lorentz invariance. On the other hand, in $T \ne 0$ (Euclidean space with imaginary time), the spatial direction remains open, i.e., $-\infty \le x \le \infty \Rightarrow R^3$, but the temporal direction becomes closed, i.e., $0 \le \tau \le \beta \Rightarrow R^1 \to S^1$ (circle) Thus, at $T \ne 0$ the topology of space-time changes to $R^4 = R^3 \times R^1 \Rightarrow R^3 \times S^1$. when transitioning from Minkowski space to Euclidean space. This modification alters the temporal components, while the spatial components remain unchanged, leading to the decoupling of space and time. As a result, the theory loses

Lorentz invariance, as the symmetry between space and time is broken in the Euclidean space formulation.

The introduction of a chemical potential in a field theory is typically achieved by modifying the temporal component of the gauge field. This is done by substituting ∂_0 with $\partial_0 - i\mu$ in the Lagrangian, where μ represents the chemical potential. This modification affects only the temporal component of the gauge field, leaving the spatial components unchanged. As a result, this substitution effectively decouples space and time, breaking the symmetry between them. Consequently, the theory loses its Lorentz invariance since the temporal direction is modified while the spatial directions remain unaffected. In addition to explicitly breaking Lorentz invariance, the introduction of a chemical potential may also have deeper consequences. It can break other internal symmetries, such as particle-hole symmetry or charge conjugation symmetry, depending on the specific nature of the system under consideration. This could lead to changes in the physical properties of the system, such as the behavior of the equation of state, the thermodynamic potentials, or the response to external fields.

At finite T and nonzero μ, the field theory becomes equivalent to quantizing a quantum system within a finite-sized box. Specifically, this corresponds to a one-dimensional box in the Euclidean time (τ) direction, with $0 \leq \tau \leq \beta$. However, the spatial dimensions remain unbounded, leading to a spacetime topology of $R^3 \times S^1$. In this setup, the compactification of the Euclidean time direction explicitly breaks Lorentz invariance, distinguishing the temporal direction from the spatial ones. The compactness of the Euclidean time direction at finite temperature imposes a discrete structure on the allowed energy modes, giving rise to Matsubara frequencies ω_n [109, 112, 113]. These frequencies emerge due to the specific boundary conditions imposed on fields in imaginary time and are expressed as

$$k_0 = ik_4 = i\omega_n = \begin{cases} \frac{2n\pi i}{\beta} & \text{for boson ,} \\ \frac{(2n+1)\pi i}{\beta} & \text{for fermion.} \end{cases}$$

4.1.3. Frequency sum in contour integral method

In thermal field theory, evaluating the partition function and matrix elements associated with a given Feynman diagram requires summing over discrete Matsubara frequencies. These frequency sums naturally arise due to the compactification of the Euclidean time direction, reflecting the quantization of energy modes in the imaginary-time formalism. Properly handling these sums is essential for incorporating thermal effects and ensuring consistency in finite-temperature calculations. There are two types of frequency sums: bosonic and fermionic.

A) Bosonic frequency Sum:

In general, the form of the bosonic frequency sum can be written as

$$\frac{1}{\beta} \sum_{n=-\infty}^{n=+\infty} f(k_0 = i\omega_n = 2\pi i nT) = \frac{1}{\beta} \sum_{n=-\infty}^{n=+\infty} f(k_0 = i\omega_n = 2\pi i nT) \operatorname{Res}\left[\frac{\beta}{2} \coth\left(\frac{\beta k_0}{2}\right)\right], \tag{4.4}$$

where k_0 is the fourth (temporal) component of momentum in Minkowski space-time and the function $f(k_0)$ is a meromorphic function We know the hyperbolic cotangent has poles at $\coth(n\pi i)$ (see Fig. 4.2) at

$$\coth\left(\frac{\beta k_0}{2}\right) = \coth(n\pi i) \Rightarrow k_0 = \frac{2\pi i n}{\beta} = i\omega_n \tag{4.5}$$

with residues $2/\beta$, and $\operatorname{Res}\left[\frac{\beta}{2} \coth\left(\frac{\beta k_0}{2}\right)\right]$ evaluates to unity. This property allows for the insertion of a hyperbolic cotangent function with an appropriately chosen argument to facilitate the summation over discrete Matsubara frequencies. By utilizing this approach, frequency sums can be systematically converted into contour integrals, enabling a more convenient evaluation in thermal field theory calculations. Then, without any loss of generality, one can express the right-hand side
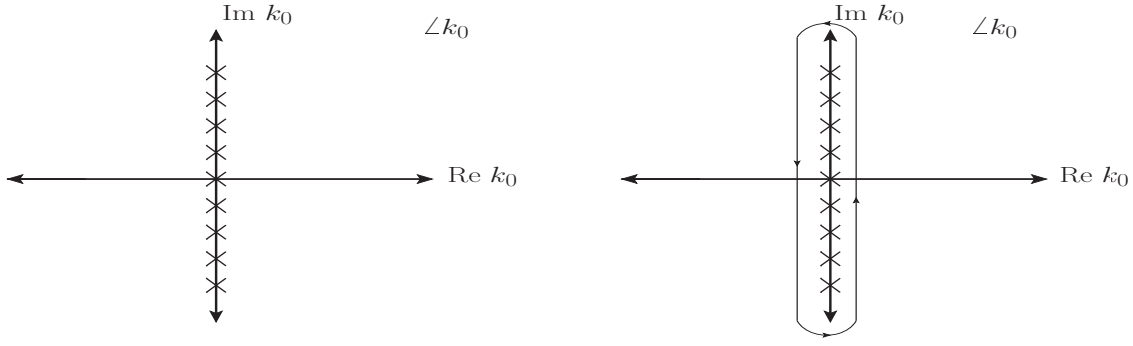
Figure 4.2: Poles of $\coth(\beta k_0/2)$ occur at $k_0 = 2\pi i n T; n = 0, \pm 1, \pm 2 \cdots$, in complex k_0 plane.

(RHS) of Eq. (4.4) as

$$\frac{1}{\beta} \sum_{n=-\infty}^{n=+\infty} f(k_0) \operatorname{Res}\left[\frac{\beta}{2} \coth\left(\frac{\beta k_0}{2}\right)\right] = \frac{1}{\beta} \sum_{n=-\infty}^{n=+\infty} \frac{\beta}{2} \operatorname{Res}\left[f(k_0) \coth\left(\frac{\beta k_0}{2}\right)\right]; \Rightarrow \text{poles}: k_0 = i\omega_n = \frac{2\pi i n}{\beta}. \quad (4.6)$$

Employing the residue theorem in reverse, the sum over residues is possible to expresse as an integral over a contour C in $\angle k_0$ enclosing the poles of the meromorphic function $f(k_0)$ but excluding the poles of the hyperbolic cotangent $(k_0 = i\omega_n = 2\pi i T)$ as [107, 112, 113]

$$\frac{1}{\beta} \sum_{n=-\infty}^{n=+\infty} f(k_0 = i\omega_n) = \frac{1}{\beta} \sum_{n=-\infty}^{n=+\infty} \operatorname{Res}\left[f(k_0) \frac{\beta}{2} \coth\left(\frac{\beta k_0}{2}\right)\right] = \frac{1}{2\pi i} \oint_{C_1 \cup C_2} dk_0 \, f(k_0) \frac{1}{2} \coth\left(\frac{\beta k_0}{2}\right)$$

$$= \frac{1}{2\pi i} \int_{-i\infty}^{+i\infty} dk_0 \, \frac{1}{2}\Big[f(k_0) + f(-k_0)\Big] + \frac{1}{2\pi i} \int_{\epsilon - i\infty}^{\epsilon + i\infty} dk_0 \Big[f(k_0) + f(-k_0)\Big] \frac{1}{\exp(\beta k_0) - 1}. \quad (4.7)$$
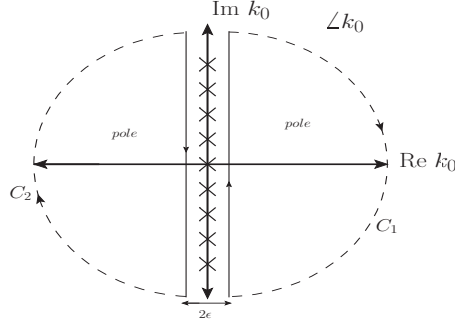
Figure 4.3: Contours C_1 and C_2 are used to encompass the poles of the meromorphic function $f(k_0)$ in complex k_0 plane. These contours are shifted by an amount $\pm\epsilon$ away from the $\text{Im} k_0$ axis to avoid the poles of $\coth(\beta k_0/2)$ at $k_0 = 2\pi i n T$.

Now, some important points to note in Eq. (4.7):

i) The function $[\exp(\beta k_0) - 1]^{-1}$ vis-à-vis $\coth(\beta k_0/2)$ is related to the Bose-Einstein distribution and has poles at the Matsubara frequencies $k_0 = i\omega_n = 2\pi i T$. The function is bounded and analytic everywhere except at these poles.

ii) The function $f(k_0 = i\omega_n)$s described as meromorphic, meaning that it is analytic everywhere except for isolated simple poles. The function does not have any essential singularities or branch cuts, which makes it a well-behaved meromorphic function in the complex k_0-plane.

iii) The function $f(k_0 = i\omega_n)$ must not have poles at the same positions as the poles of the Bose-Einstein distribution function, $[\exp(\beta k_0) - 1]^{-1}$. If the poles of $f(k_0 = i\omega_n)$ coincide with the poles of the thermal distribution function, then there could be complications when summing over these frequencies, leading to divergent behaviour or improper convergence.

iv) The contour C in the complex k_0 plane can be decomposed into two semicircular contours, C_1 and C_2, without enclosing the poles of the Bose-Einstein distribution function, $[\exp(\beta k_0) - 1]^{-1}$, or equivalently, those of $\coth(\beta k_0/2)$ [107]. However, the contours must enclose the poles of the function $f(k_0)$, as illustrated in Fig.4.3. To ensure the validity of this contour integration approach, the meromorphic function $f(k_0)$ should decay sufficiently fast at large $|k_0|$, ensuring convergence of the integral.

v) If all the aforementioned properties hold, then the Matsubara summation $T \sum_{n=-\infty}^{n=+\infty} f(k_0 = i\omega_n)$ can be replaced by contour integration.This procedure effectively corresponds to analytically continuing from Euclidean time, where frequencies are discrete (Matsubara frequencies in Euclidean space), to real time, where frequencies become continuous (Minkowski space-time).

vi) In the second line of Eq. (4.7), the first term represents the vacuum contribution, while the second term corresponds to the matter contribution, arising from thermal effects.

B) Fermionic frequency sum for zero chemical potential ($\mu = 0$):

Using a similar procedure as in the bosonic case, the fermionic frequency sum with discrete frequency $\omega_n = (2n+1)\pi T$ can be expressed [107, 112, 113]

$$
\frac{1}{\beta} \sum_{n=-\infty}^{n=+\infty} f(k_0 = i\omega_n) = \frac{1}{2\pi i} \oint_{C_1 \cup C_2} dk_0 \, f(k_0) \frac{1}{2} \tanh\left(\frac{\beta k_0}{2}\right)
$$
$$
= \frac{1}{2\pi i} \int_{-i\infty}^{+i\infty} d(k_0) \frac{1}{2}\Big[f(k_0) + f(-k_0)\Big] + \frac{1}{2\pi i} \int_{\epsilon-i\infty}^{\epsilon+i\infty} d(k_0)\Big[f(k_0) + f(-k_0)\Big] \frac{1}{\exp(\beta k_0) + 1}. \quad (4.8)
$$

C) Fermionic frequency sum in presence of a chemical potential μ:

In a similar way, the fermionic frequency sum in the presence of a chemical potential μ can be expressed as [107]

$$
T \sum_{n=-\infty}^{n=+\infty} f(k_0 = i\omega_n + \mu) = \frac{1}{2\pi i} \oint_C dk_0 \, f(k_0) \frac{1}{2} \tanh\left(\frac{\beta k_0 - \mu}{2}\right) = \frac{1}{2\pi i} \oint_C d(k_0) \, f(k_0) + \frac{1}{2\pi i} \int_{-i\infty}^{+i\infty} d(k_0) \, f(k_0)
$$
$$
- \frac{1}{2\pi i} \int_{-i\infty+\mu+\epsilon}^{i\infty+\mu+\epsilon} d(k_0) f(k_0) \frac{1}{e^{\beta(k_0-\mu)} + 1} - \frac{1}{2\pi i} \int_{-i\infty+\mu-\epsilon}^{i\infty+\mu-\epsilon} d(k_0) f(k_0) \frac{1}{e^{\beta(\mu-k_0)} + 1}. \quad (4.9)
$$

The first term represents the T-independent contribution, which accounts for the finite-density effects at zero temperature ($T = 0$. This term arises from the presence of a chemical potential and remains even in the vacuum state. The second term corresponds to the vacuum contribution (zero-temperature and zero-density) and remains independent of temperature. The last two terms capture the contributions from fermions and antifermions in the medium. These terms explicitly depend on temperature and vanish in the limit $T \to 0$. reflecting their thermal nature. This classification highlights the distinction between vacuum effects, finite-density effects at zero temperature, and thermal effects at finite temperature.

4.1.4. Frequency sum in Saclay method

We introduce the Saclay method [114], a practical technique for evaluating frequency sums involving multiple propagators in loop diagrams. This method simplifies the computation of Matsubara sums by reorganizing the terms in a way that facilitates analytical continuation and contour integration.

The scalar parts of the bosonic and fermionic propagators in momentum space are given by:

$$
\Delta_{\left(\frac{B}{F}\right)}(K) = \frac{1}{K^2 - m^2} = \frac{1}{k_0^2 - E_k^2} = \frac{1}{2E_k}\left(\frac{1}{k_0 - E_k} - \frac{1}{k_0 + E_k}\right) = \sum_{s=\pm 1} \frac{s}{2E} \frac{1}{k_0 - sE_k} \quad (4.10)
$$

where $E_k = \sqrt{k^2 + m^2}$ is the particle energy. Now, the bosonic propagator can also be written as

$$
\Delta_B(K) = -\int_0^\beta d\tau \, e^{k_0\tau} \Delta_B(\tau, E_k), \quad (4.11)
$$

where

$$\Delta_B(\tau, E_k) = -T \sum_{k_0=2n\pi iT} e^{-k_0\tau}\Delta_B(K) = \frac{1}{2E_k}\Big[\{1+n_B(E_k)\}e^{-E_k\tau} + n_B(E_k)e^{E_k\tau}\Big] = \sum_{s=\pm 1}\frac{s}{2E_k}\Big[1+n_B(sE_k)\Big]e^{-sE_k\tau}. \quad (4.12)$$

The above equation is derived from (4.7) using contour integration. The Bose-Einstein distribution $n_B(E_k)$ is given as

$$n_B(E_k) = \frac{1}{e^{\beta E_k}-1}. \quad (4.13)$$

The fermionic propagator is represented as $S(K) = (\slashed{K}+m)\Delta_F(K)$. The quantity $\Delta_F(K)$ can be written in a mixed representation as

$$\Delta_F(K) = -\int_0^\beta d\tau\, e^{k_0\tau}\Delta_F(\tau, E_k), \quad (4.14)$$

where

$$\Delta_F(\tau, E_k) = -T \sum_{k_o=(2n+1)\pi iT} e^{-k_0\tau}\Delta_F(K) = \frac{1}{2E_k}\Big[\big(1-n_F^+(E_k)\big)e^{-E_k\tau} - n_F^-(E_k)e^{E_k\tau}\Big] = \sum_{s=\pm 1}\frac{s}{2E_k}\Big[1-n_F^+(sE_k)\Big]e^{-sE_k\tau}, \quad (4.15)$$

where the Fermi-Dirac distribution is given as $n_F^\pm(E_k) = 1/\big(e^{\beta(E_k\mp\mu)}+1\big)$, where $(+)ve$ sign in the superscript represents fermion whereas $(-)ve$ sign represents antifermion.

4.1.5. Functional integration and the partition function relation

We consider a system that evolves from an initial state at $t=0$ and evolves to its initial state after a time evolution up to time t, The time evolution can be represented by the transition amplitude: $\langle \phi_b|e^{-i\mathcal{H}t}|\phi_a\rangle$, here, $\mathcal{H}$ denotes the Hamiltonian of the system, assumed to be time-independent. This assumption simplifies the calculation, as the time evolution operator $e^{-i\mathcal{H}t}$ acts consistently across all states, preserving the system's energy eigenstates. The transition amplitude quantifies the probability amplitude for the system to evolve from state $|\phi_a\rangle$ to state $|\phi_b\rangle$ over time t. This formulation is crucial in thermal field theory and statistical mechanics, where such time evolution plays a fundamental role in determining equilibrium properties and correlation functions.

We consider a problem in statistical thermodynamics involving a system that evolves from an initial state at $t=0$ and returns to its initial state after a time evolution up to time t, then transition amplitude can be expressed in Minkowski space-time as

$$\langle \phi_a|e^{-i\mathcal{H}t}|\phi_a\rangle = \int \mathcal{D}\pi \int \mathcal{D}\phi \exp\left[i\int_0^t dt \int d^3x \Big(\pi(X)\,\partial_t\phi(X) - \mathcal{H}_d(\pi(X),\phi(X))\Big)\right], \quad (4.16)$$

where $\mathcal{D}$ is the functional or path integral runs over all possible paths of momentum $\pi(X)$ and field $\phi(x)$. These fields are not restricted by boundary conditions while going from initial time $t=0$ to final time $t_f=t$.

The Hamiltonian of the system is $\mathcal{H} = \int \mathcal{H}_d\, d^3x$ along with the Hamiltonian density[8] is given as

$$\mathcal{H}_d = \pi(X)\partial_t\phi(X) - \mathcal{L}(\phi(X)\dot\phi(X)), \quad (4.17)$$

where $\mathcal{L}$ is Lagrangian density in Minkowski space-time. Using (4.17) in (4.16) one can write the transition amplitude in $\mathcal{L}$ and/or action $\mathcal{S}$ as

$$\langle \phi_a|e^{-i\mathcal{H}t}|\phi_a\rangle = \int \mathcal{D}\phi \, \exp\left[i\int_0^t dt \int d^3x\, \mathcal{L}\right] = \int \mathcal{D}\phi\, e^{i\int d^4x\, \mathcal{L}} = \int \mathcal{D}\phi\, e^{i\mathcal{S}[\phi]}, \quad (4.18)$$

where action in Minkowski space-time is written as

$$\mathcal{S}[\phi] = \int d^4x\, \mathcal{L} = \int_0^t dt \int d^3x\, \mathcal{L}. \quad (4.19)$$

Now, the partition function reads as $\mathcal{Z} = \text{Tr}\rho = \text{Tr}\big(e^{-\beta\mathcal{H}}\big) = \sum_n \langle n|e^{-\beta\mathcal{H}}|n\rangle$. In this context, the summation over n runs over all possible energy eigenstates of the system within the Hilbert space. However, in the continuum limit, the

---

[8]If there is a conserved charge density $\mathcal{N}(\pi,\phi)$ one should also include it as $\mathcal{H}_d - \mu\mathcal{N}(\pi,\phi)$, where μ is the associated chemical potential.

summation transforms into an integral over the complete energy eigenstates $|\phi\rangle$, each characterized by an energy E_ϕ. Thus, the partition function becomes

$$\mathcal{Z} = \int \, d\phi \, \langle\phi\,|e^{-\beta\mathcal{H}}|\,\phi\rangle = \int d\phi e^{-\beta E_\phi} \ . \tag{4.20}$$

A comparison between Eqs. (4.18) and (4.20) reveals a deep connection between the path integral formulation of quantum mechanics and the partition function in statistical mechanics, provided the following correspondence is made:

- In the transition amplitude described by Eq.(4.18), the time interval $[0, t]$ corresponds to the inverse temperature interval $[0, \beta]$ in the partition function. The connection between time t and imaginary time $\tau = it$. This process, referred to as Wick rotation, involves rotating the time variable by $90°$ in the complex plane, effectively transforming real time into imaginary time (see Fig.4.1).

- The field ϕ satisfies either periodic or anti-periodic boundary conditions, $\phi(x, 0) = \pm\phi(x, \beta)$, as previously discussed in subsec 4.1.2. The choice of sign depends on the nature of the field, with bosonic fields obeying periodic conditions and fermionic fields following anti-periodic conditions in the imaginary-time formalism.

With this, the transition amplitude can be viewed as the partition function within the path integral approach as

$$\mathcal{Z} = \text{Tr}\rho \quad = \quad \text{Tr}\left(e^{-\beta\mathcal{H}}\right) = \int \, d\phi \, \langle\phi\,|e^{-\beta\mathcal{H}}|\,\phi\rangle = \int \mathcal{D}\phi \, e^{i\int_0^t dt \int d^3x \, \mathcal{L}}$$

$$\underset{t\to-i\tau}{=} \int\limits_{\phi(x,0)=\pm\phi(x,\beta)} \mathcal{D}\phi \, e^{\int_0^\beta d(it) \int d^3x \, \mathcal{L}(t\to-i\tau)} = \int\limits_{\phi(x,0)=\pm\phi(x,\beta)} \mathcal{D}\phi \, e^{\int_0^\beta d\tau \int d^3x \, \mathcal{L}(t\to-i\tau)} . \tag{4.21}$$

At this point, it is important to note that the partition function can be computed directly in Euclidean time τ and discrete frequency $i\omega_n$ using Eq. (4.21). In this approach, the time evolution is treated in imaginary time, making the evaluation of thermodynamic quantities straightforward in a finite-temperature framework. Alternatively, one can transform the Minkowski action in Eq. (4.21) into momentum space and then replace the four momentum integral by the frequency sum.

4.2. Real Time Formalism

The Imaginary Time Formalism is specifically suited for studying static and equilibrium properties of a system at finite temperature. In this approach, time is treated as a compactified, periodic variable τ, and thermodynamic quantities are computed by summing over discrete Matsubara frequencies. Time dependence in physical observables arises only after performing an analytical continuation back to real time. However, this formalism is limited to equilibrium systems and cannot describe processes involving time evolution or systems driven out of equilibrium.

Conversely, the Real Time Formalism (RTF) provides a more general framework capable of handling out-of-equilibrium systems. It allows for a direct description of the time evolution of quantum fields, making it suitable for studying dynamical processes such as phase transitions, particle production, and the evolution of the early universe. This approach involves contour integration in the complex time plane, where both forward and backward time evolutions are accounted for, enabling a natural treatment of non-equilibrium effects.

The RTF was initially developed by Schwinger and Keldysh [104, 106] to study systems out of equilibrium. This formalism is widely used in thermal field theory for investigating time-dependent processes and non-equilibrium phenomena. Below, we provide a brief overview of the real-time method, as outlined in references [108, 109, 111].

To build intuition, we begin with the concept of the partition function in quantum mechanics. At a finite temperature

$\beta = 1/T$, the partition function is given by

$$\text{Tr}e^{-\beta H} = \int_{-\infty}^{\infty} dq\,\langle q,t|e^{-\beta H}|q,t\rangle. \tag{4.22}$$

This is analogous to the transition amplitude in vacuum quantum mechanics, which describes the evolution of a system from an initial state q at time t to a final state q' at time t' and is given by:

$$\langle q',t'|q,t\rangle = \langle q',t'|e^{-iH(t'-t)}|q,t\rangle, \tag{4.23}$$

where H is the Hamiltonian of the system. In Minkowski space, the operator $e^{-iH(t'-t)}$ describes the evolution from time t to t'. Similarly, in analogy with vacuum, the partition function at finite temperature can be interpreted as the evolution of the system along a complex time path C as $e^{-\beta H} = e^{-iH(\tau-i\beta-\tau)}$. Here τ is the intermediate point in the complex time contour and the system evolves from time τ to $\tau - i\beta$ in the complex time path C.

Thermal scalar field propagator is defined as

$$
\begin{aligned}
D(X, X') &= i\langle T\phi(X)\phi(X')\rangle = \theta(\tau - \tau')i\langle\phi(X)\phi(X')\rangle + \theta(\tau' - \tau)i\langle\phi(X')\phi(X)\rangle, \\
&= \theta(\tau - \tau')D_+(X, X') + \theta(\tau' - \tau)D_-(X, X').
\end{aligned} \tag{4.24}
$$

Here, τ and τ' are the points on the contour with $\theta(\tau - \tau')$ is the contour-odered theta function. $D_+(\vec{x}, \vec{x}'; \tau, \tau')$ is defined in domain $-\beta \leq \text{Im}(\tau - \tau') \leq 0$ whereas, $D_-(\vec{x}, \vec{x}'; \tau, \tau')$ is defined in domain $\beta \geq \text{Im}(\tau - \tau') \geq 0$. The thermal propagator satisfies the corresponding differential equation ensuring correct periodicity and analytic continuation as

$$(\Box^2 + m^2)D(X, X') = \delta^4(X - X'), \tag{4.25}$$

with boundary condition $D_-(\vec{x}, \vec{x}'; \tau, \tau') = D_+(\vec{x}, \vec{x}'; \tau - i\beta, \tau')$, known as KMS relation (shown in Eq. (4.2)). By performing a spatial Fourier transform and solving the differential equation, one readily obtains

$$D(\vec{k}; \tau - \tau') = \frac{i}{2\omega}\left\{\left[\theta(\tau - \tau') + n_B\right]e^{-i\omega(\tau-\tau')} + \left[\theta(\tau' - \tau) + n_B\right]e^{i\omega(\tau-\tau')}\right\}, \tag{4.26}$$

where $n_B(\omega) = 1/(e^{\beta\omega} - 1)$ is the single particle thermal distribution function with $\omega^2 = \vec{k}^2 + m^2$.

IN RTF, the time contour C is carefully chosen to handle thermal systems by evolving along both real and imaginary time axes. The contour typically consists of the following segments (as described in Fig. 4.4). i) First Segment: moves forward along the real time axis from $-\bar{t}$ to $+\bar{t}$ in real axis. ii) Second Segment: drop vertically from $\bar{t}$ to $\bar{t} - i\beta/2$. iii) Third Segment: moves backward along a line parallel to the real axis from $\bar{t} - i\beta/2$ to $-\bar{t} - i\beta/2$. iv) Fourth Segment: again drops vertically from $-\bar{t} - i\beta/2$

Figure 4.4: The contour for the real-time formalism is depicted.

to $-\bar{t} - i\beta$. This choice of contour, known as the Schwinger-Keldysh contour, allows the system to return to its original state after a complete traversal, ensuring that the thermal properties are properly captured.

Note that $D(\vec{k}, \tau_h, \tau_v)$ vanishes along vertical paths, as stated by the Riemann-Lebesgue lemma, where τ_v and τ_h are points on vertical and horizontal lines, respectively. This is because the vertical segments contribute oscillatory terms that decay exponentially for large imaginary times, leading to a zero contribution when integrated over. Since we are only interested in the time evolution along the real axis, the vertical segments can be ignored. Thus, the relevant propagator involves contributions only from the two horizontal paths. So, we are left with two lines parallel to real axes and the propagator can be written in form of 2×2 matrix. The propagator is given in ij-th element as

$$D(\vec{k}; \tau_i - \tau_j') = \frac{i}{2\omega}\left\{\left[\theta(\tau_i - \tau_j') + n_B\right]e^{-i\omega(\tau_i-\tau_j')} + \left[\theta(\tau_j' - \tau_i) + n_B\right]e^{i\omega(\tau_i-\tau_j')}\right\}. \tag{4.27}$$

Now, we can write down the contour ordering in terms of the usual time (t) ordering. When τ and τ' are on line 1 (real axis from $-\bar{t}$ to $\bar{t}$), $\theta(\tau_1 - \tau_1') = \theta(t - t')$. If τ and τ' are on line 2 (real axis from $\bar{t} - i\beta/2$ to $-\bar{t} - i\beta/2$), it is written as $\theta(\tau_2 - \tau_2') = \theta(t' - t)$. When the points are on different lines, we note that $\theta(\tau_1 - \tau_2') = 0$ and $\theta(\tau_2 - \tau_1') = 1$.

Now, the components of propagator in the momentum space are written by taking temporal Fourier transform as

$$D_{ij}(\vec{k}, k_0) = \int_{-\infty}^{\infty} e^{ik_0(t-t')} D(\vec{k}; \tau_i, \tau_j') dt. \tag{4.28}$$

Performing the integration, they can take the forms

$$D_{11} = \Delta_F(k) + 2i\pi n_B(\omega)\delta(k^2 - m^2), \tag{4.29a}$$

$$D_{12} = 2i\pi\sqrt{n_B(\omega)(1 + n_B(\omega))}\delta(k^2 - m^2), \tag{4.29b}$$

whereas the other components are written as $D_{21} = D_{12}$, and $D_{22} = -D_{11}^*$. Finally, we can write the momentum space scalar propagator in terms of matrix as

$$D(k_0, \vec{k}) = \begin{bmatrix} \Delta_F(k) + 2i\pi n_B\delta(k^2 - m^2) & 2i\pi\sqrt{n_B(1 + n_B)}\delta(k^2 - m^2) \\ 2i\pi\sqrt{n_B(1 + n_B)}\delta(k^2 - m^2) & -\Delta_F(k)^* + 2i\pi n_B\delta(k^2 - m^2) \end{bmatrix}, \tag{4.30}$$

where $\Delta_F(k)$ is the free scalar propagator.

4.3. General Structure of Fermionic Two point functions at finite temperature

4.3.1. Fermion self-energy

The chiral invariance, alongside preserving parity invariance, for a theory containing only massless fermions and gauge bosons implies two crucial aspects: i) Chiral symmetry ensures that no mass term or condensate $\bar{\psi}\psi$ appears in any finite order of perturbation theory. This is because the mass term explicitly breaks chiral symmetry. ii) According to Ref. [115], the fermion self-energy can be expressed in a general form that respects chiral symmetry as $\Sigma(P) = -\mathcal{A}\slashed{P}$, where $\slashed{P} = \gamma^\mu P_\mu$ is the fermion momentum $P \equiv (p_0 = \omega, \vec{p})$, with $p = |\vec{p}|$. Here, $\mathcal{A}$ represents a Lorentz invariant structure function dependent on P^2.

The effective propagator reads as (see subsec 4.3.2 below)

$$S(P) = \frac{1}{\slashed{P} - \Sigma(P)} = \frac{\slashed{P}}{(1 + \mathcal{A})P^2}. \tag{4.31}$$

The poles, $P^2 = 0$, lie on the light cone $\omega = p$. The term $(1 + \mathcal{A})$ modifies the residues.

At finite temperature, while point (i) the absence of a $\bar{\psi}\psi$ coupling remains valid due to chiral symmetry whereas point (ii), concerning the form of the fermion self-energy, does not hold in its vacuum-like form. This is because the heat bath, containing the appearance of antiparticles in equal numbers to particles at such high temperatures, introduces a preferred frame of reference, breaking Lorentz invariance and modifying the self-energy. Hence, the heat bath introduces a specific rest frame characterized by a four-velocity $u^\mu = (1, 0, 0, 0)$ with $u^\mu u_\mu = 1$. This implies that the heat bath defines a preferred time direction, distinguishing time from spatial directions, thereby breaking the Lorentz invariance of the theory. Consequently, at finite temperature, the fermion self-energy acquires a more general form, dependent on both the momentum and the heat bath's velocity [115] as

$$\Sigma(P) = -\mathcal{A}\slashed{P} - \mathcal{B}\slashed{u}, \tag{4.32}$$

where $\mathcal{B}$ is another Lorentz invariant structure function in addition to $\mathcal{A}$. Since $P^2 = \omega^2 - p^2$, one can interpret $\omega = p_0 = P^\mu u_\mu$ and $p = (P^\mu u_\mu - P^2)^{1/2}$ as Lorentz invariant energy and momentum, respectively. The Lorentz invariant structure functions are obtained following the calculation in Ref. [112] as

$$\mathcal{A}(\omega, p) = \frac{1}{4}\frac{\text{Tr}[\Sigma\slashed{P}] - (P \cdot u)\,\text{Tr}[\Sigma\slashed{u}]}{(P \cdot u)^2 - P^2}, \quad \text{and} \quad \mathcal{B}(\omega, p) = \frac{1}{4}\frac{P^2\text{Tr}[\Sigma\slashed{u}] - (P \cdot u)\,\text{Tr}[\Sigma\slashed{P}]}{(P \cdot u)^2 - P^2}. \tag{4.33}$$

4.3.2. Fermion propagator

Figure 4.5: Pictorial representation of an effective or resummed fermion propagator, known as Dyson-Schwinger equation.

The effective fermion propagator, denoted by $S(P)$ is derived from the Dyson-Schwinger equation in Fig. 4.5, which relates the bare fermion propagator $S_0(P)$ and the self-energy $\Sigma(P)$. Following Fig. 4.5, the Dyson equation is given [112] by:

$$
\begin{aligned}
S(P) &= S_0(P) + S_0(P)\Sigma(P)S(P) \\
S(P)S^{-1}(P) &= S_0(P)S^{-1}(P) + S_0(P)\Sigma(P)S(P)S^{-1}(P) \\
S^{-1}(P) &= \slashed{P} - \Sigma(P).
\end{aligned}
\tag{4.34}
$$

Now, the effective fermion propagator can be obtained from (4.34) as

$$
S(P) = \frac{1}{\slashed{P} - \Sigma(P)}.
\tag{4.35}
$$

Using (4.32) one can write the effective propagator as

$$
S(P) = \frac{1}{(1+\mathcal{A})\slashed{P} + \mathcal{B}\slashed{u}} = \frac{(1+\mathcal{A})\slashed{P} + \mathcal{B}\slashed{u}}{[(1+\mathcal{A})\slashed{P} + \mathcal{B}\slashed{u}]^2} = \frac{\slashed{P} - \Sigma(P)}{\mathcal{D}} = \frac{S^{-1}(P)}{\mathcal{D}},
\tag{4.36}
$$

where the Lorentz invariant quantity $\mathcal{D}$ is given [112] as

$$
\mathcal{D}(p,u) = [(1+\mathcal{A})\slashed{P} + \mathcal{B}\slashed{u}]^2 = (1+\mathcal{A})^2 \slashed{P}^2 + 2(1+\mathcal{A})\mathcal{B}P \cdot u + \mathcal{B}^2.
\tag{4.37}
$$

In the rest frame of heat bath, Eq. (4.37) reads [112] as

$$
\mathcal{D}(p,\omega) = \mathcal{D}_+ \mathcal{D}_-,
\tag{4.38}
$$

where

$$
\mathcal{D}_\pm(p,\omega) = (1+\mathcal{A})(\omega \mp p) + \mathcal{B}.
\tag{4.39}
$$

In free case, $\mathcal{A} = \mathcal{B} = 0$ and Eq. (4.39) becomes

$$
d_\pm(p,\omega) = \omega \mp p.
\tag{4.40}
$$

Combining (4.38) and (4.36), one can write [112, 113] the effective propagator as

$$
S(P) = \frac{S^{-1}(P)}{\mathcal{D}_+ \mathcal{D}_-}.
\tag{4.41}
$$

We can write [112] the self-energy in (4.32) as

$$
\Sigma(P) = -\frac{1}{2}\left[(\mathcal{A}(\omega + p) + \mathcal{B})(\gamma_0 - \vec{\gamma} \cdot \hat{\boldsymbol{p}}) + (\mathcal{A}(\omega - p) + \mathcal{B})(\gamma_0 + \vec{\gamma} \cdot \hat{\boldsymbol{p}})\right].
\tag{4.42}
$$

Now we can also write [112, 113]

$$
\slashed{P} = \gamma_0 \omega - p\vec{\gamma} \cdot \hat{\boldsymbol{p}} = \frac{1}{2}\left[(\omega - p)(\gamma_0 + \vec{\gamma} \cdot \hat{\boldsymbol{p}}) + (\omega + p)(\gamma_0 - \vec{\gamma} \cdot \hat{\boldsymbol{p}})\right].
\tag{4.43}
$$

In the rest frame of the heat bath, the inverse of the effective propagator in (4.34) can now be written as

$$
S^{-1}(P) = \slashed{P} - \Sigma(P) = \frac{1}{2}(\gamma_0 + \vec{\gamma} \cdot \hat{\boldsymbol{p}})\mathcal{D}_+ + \frac{1}{2}(\gamma_0 - \vec{\gamma} \cdot \hat{\boldsymbol{p}})\mathcal{D}_-
\tag{4.44}
$$

Using (4.44) in (4.41), one finally obtains the effective fermion propagator as

$$
S(P) = \frac{1}{2}\frac{\gamma_0 - \vec{\gamma} \cdot \hat{\boldsymbol{p}}}{\mathcal{D}_+(\omega, p)} + \frac{1}{2}\frac{\gamma_0 + \vec{\gamma} \cdot \hat{\boldsymbol{p}}}{\mathcal{D}_-(\omega, p)},
\tag{4.45}
$$

which is decomposed in helicity eigenstates. We clarify the implications of charge invariance and the parity properties of the functions $\mathcal{D}_\pm(-\omega, p)$, $\mathcal{A}(\omega, p)$ and $\mathcal{B}(-\omega, p)$. The charge invariance demands that $\mathcal{D}_\pm(-\omega, p) = -\mathcal{D}_\mp(\omega, p)$ imposes

constraints on the symmetry of the structure functions: $\mathcal{A}(-\omega, p) = \mathcal{A}(\omega, p)$ (even function in ω) and $\mathcal{B}(-\omega, p) = -\mathcal{B}(\omega, p)$ (odd function in ω). The even and odd nature of $\mathcal{A}(\omega, p)$ and $\mathcal{B}(-\omega, p)$ suggest distinct contributions to the spectral functions and propagators in a medium. For space like momenta $P(p_0^2 < p^2)$, $\mathcal{D}(\omega, p)$ acquires an imaginary part. We now define the parity properties for both real and imaginary parts of $\mathcal{D}(\omega, p)$ as $\mathrm{Re}\mathcal{D}_+(-\omega, p) = -\mathrm{Re}\mathcal{D}_-(\omega, p)$ (real part is antisymmetric between $\pm$) and $\mathrm{Im}\mathcal{D}_+(-\omega, p) = \mathrm{Im}\mathcal{D}_-(\omega, p)$ (imaginary part is symmetric between $\pm$). The distinction between the real and imaginary parts is crucial for analyzing spectral densities and the dispersion relations of excitations in the plasma.

The dispersion relations for a quark in a thermal medium are determined by the zeros of $\mathcal{D}_\pm(\omega, p)$. For $\mathcal{D}_+(\omega, p) = 0$, the solutions are poles at $\omega = \omega_+(p)$ and $\omega = -\omega_-(p)$, while $\mathcal{D}_-(\omega, p) = 0$ has poles at $\omega = \omega_-(p)$ and $\omega = -\omega_+(p)$. The mode with energy ω_+ corresponds to the propagation of a particle-like excitation in the medium, characterized as a Dirac spinor and an eigenstate of $(\gamma_0 - \vec{\gamma} \cdot \hat{\boldsymbol{p}})$ with a chirality-to-helicity ratio of $+1$. In contrast, the plasmino mode, a unique low-momentum excitation, is associated with energy ω_- and is an eigenstate of $(\gamma_0 + \vec{\gamma} \cdot \hat{\boldsymbol{p}})$, having a chirality-to-helicity ratio of -1. Interestingly, the ω_- branch exhibits a minimum [112, 113] at small momenta before converging to the free-particle dispersion relation at higher momenta. Additionally, the structure of $\mathcal{D}_\pm^{\mathrm{e}}(\omega, p)$ includes a discontinuity related to *Landau damping*, arising from the logarithmic term in self-energy. Below we show the chairality-to-helicity ratio of above two modes:

The helicity operator is defined as

$$\hat{h} = \frac{\vec{\boldsymbol{S}} \cdot \vec{\boldsymbol{p}}}{p} = \vec{\boldsymbol{S}} \cdot \hat{\boldsymbol{p}}, \tag{4.46}$$

where for a Dirac particle

$$\vec{\boldsymbol{S}} = \frac{1}{2}\gamma^5\gamma^0\vec{\gamma}. \tag{4.47}$$

We consider

$$\hat{h}(\gamma_0 - \vec{\gamma} \cdot \hat{\boldsymbol{p}}) = \frac{1}{2}\gamma^5\gamma^0(\vec{\gamma} \cdot \hat{\boldsymbol{p}})[\gamma_0 - \vec{\gamma} \cdot \hat{\boldsymbol{p}}] = \frac{1}{2}\gamma^5\gamma^0[(\vec{\gamma} \cdot \hat{\boldsymbol{p}})\gamma_0 + 1] = -\frac{1}{2}\gamma^5(\vec{\gamma} \cdot \hat{\boldsymbol{p}}) + \frac{1}{2}\gamma^5\gamma^0 = \frac{1}{2}\gamma^5[\gamma_0 - \vec{\gamma} \cdot \hat{\boldsymbol{p}}], \tag{4.48}$$

and

$$\hat{h}(\gamma_0 + \vec{\gamma} \cdot \hat{\boldsymbol{p}}) = \frac{1}{2}\gamma^5\gamma^0(\vec{\gamma} \cdot \hat{\boldsymbol{p}})[\gamma_0 + \vec{\gamma} \cdot \hat{\boldsymbol{p}}] = \frac{1}{2}\gamma^5\gamma^0[(\vec{\gamma} \cdot \hat{\boldsymbol{p}})\gamma_0 - 1] = -\frac{1}{2}\gamma^5(\vec{\gamma} \cdot \hat{\boldsymbol{p}}) - \frac{1}{2}\gamma^5\gamma^0 = -\frac{1}{2}\gamma^5[\gamma_0 + \vec{\gamma} \cdot \hat{\boldsymbol{p}}], \tag{4.49}$$

The chairality operator is defined as

$$\hat{\chi} = \frac{1}{2}\gamma^5. \tag{4.50}$$

Therefore,

$$\frac{\hat{\chi}[\gamma_0 - \vec{\gamma} \cdot \hat{\boldsymbol{p}}]}{\hat{h}[\gamma_0 - \vec{\gamma} \cdot \hat{\boldsymbol{p}}]} = \frac{\frac{1}{2}\gamma^5[\gamma_0 - \vec{\gamma} \cdot \hat{\boldsymbol{p}}]}{\frac{1}{2}\gamma^5[\gamma_0 - \vec{\gamma} \cdot \hat{\boldsymbol{p}}]} \quad \Rightarrow \quad \frac{\hat{\chi}}{\hat{h}} = 1, \tag{4.51}$$

and

$$\frac{\hat{\chi}[\gamma_0 + \vec{\gamma} \cdot \hat{\boldsymbol{p}}]}{\hat{h}[\gamma_0 + \vec{\gamma} \cdot \hat{\boldsymbol{p}}]} = \frac{\frac{1}{2}\gamma^5[\gamma_0 + \vec{\gamma} \cdot \hat{\boldsymbol{p}}]}{-\frac{1}{2}\gamma^5[\gamma_0 + \vec{\gamma} \cdot \hat{\boldsymbol{p}}]} \quad \Rightarrow \quad \frac{\hat{\chi}}{\hat{h}} = -1, \tag{4.52}$$

In free fermion case, the propagator becomes

$$S_0(P) = \frac{1}{2}\frac{(\gamma_0 - \vec{\gamma} \cdot \hat{\boldsymbol{p}})}{d_+(\omega, p)} + \frac{1}{2}\frac{(\gamma_0 + \vec{\gamma} \cdot \hat{\boldsymbol{p}})}{d_-(\omega, p)}. \tag{4.53}$$

4.4. General Structure of a Gauge Boson Two-point Function at finite temperature

4.4.1. Tensor decomposition

The gauge boson self-energy in vacuum follows the general structure:

$$\Pi^{\mu\nu}(P^2) = V^{\mu\nu}\Pi(P^2), \tag{4.54}$$

where the Lorentz invariant form factor $\Pi(P^2)$ depends solely on the four-scalar P^2, preserving Lorentz symmetry in the absence of any external background. The vacuum projection operator is

$$V^{\mu\nu} = \eta^{\mu\nu} - \frac{P^\mu P^\nu}{P^2}, \tag{4.55}$$

and it satisfies the gauge invariance through the transversality condition:

$$P_\mu \Pi^{\mu\nu} = 0, \tag{4.56}$$

where $\eta^{\mu\nu} \equiv (1, -1, -1, -1)$ and $P \equiv (\omega, \vec{p})$. Additionally, it is symmetric under the exchange of μ and ν as $\Pi_{\mu\nu}(P^2) = \Pi_{\nu\mu}(P^2)$.

At finite temperature, the Lorentz invariance is broken due to the presence of a heat bath, characterized by the four-velocity $u^\mu = (1, 0, 0, 0)$ in the rest frame. The gauge boson self-energy tensor must be constructed to reflect this symmetry breaking. The possible tensors, which include the vacuum structures P^μ and $\eta^{\mu\nu}$ from vacuum, along with the four-velocity u^μ of the heat bath. From these, four types of basis tensors can be formed: $P^\mu P^\nu, P^\mu u^\nu + u^\mu P^\nu, u^\mu u^\nu$ and $\eta^{\mu\nu}$ [109, 116]. The transversality condition for the self-energy reduces the four possible tensors to two independent projection tensors, ensuring gauge invariance. These projection tensors are orthogonal, ensuring the construction of Lorentz-invariant structure of the gauge boson two-point functions at finite temperature. These two tensors are [109]

$$A^{\mu\nu} = \tilde{\eta}^{\mu\nu} - \frac{\tilde{P}^\mu \tilde{P}^\nu}{\tilde{P}^2}, \qquad \text{and} \qquad B^{\mu\nu} = \frac{P^2}{\tilde{P}^2} \bar{u}^\mu \bar{u}^\nu = \frac{\bar{u}^\mu \bar{u}^\nu}{\bar{u}^2}, \tag{4.57}$$

where

$$A^{\mu\nu} + B^{\mu\nu} = V^{\mu\nu} = \eta^{\mu\nu} - \frac{P^\mu P^\nu}{P^2}. \tag{4.58}$$

To properly describe the interactions of gauge bosons and fermions in such a system, we define the following Lorentz scalars, vectors, and tensors that characterize the heat bath:

$$u^\mu = (1, 0, 0, 0), \qquad \text{and} \qquad P^\mu u_\mu = P \cdot u = \omega. \tag{4.59}$$

In the presence of a heat bath, similar to the vacuum case, we can define a modified transverse metric tensor $\tilde{\eta}^{\mu\nu}$ that is transverse to the four-velocity u^μ of the heat bath. This tensor helps to project out components of vectors and tensors that are parallel to u^μ, thus capturing the transverse components in the frame of the heat bath. The transverse metric is defined as:

$$\tilde{\eta}^{\mu\nu} = \eta^{\mu\nu} - u^\mu u^\nu, \tag{4.60a}$$

$$u_\mu \tilde{\eta}^{\mu\nu} = u_\mu \eta^{\mu\nu} - u_\mu u^\mu u^\nu = u^\nu - u^\nu = 0. \tag{4.60b}$$

So u^μ and $\tilde{\eta}^{\mu\nu}$ are transverse.

Any four-vector can be decomposed into components parallel and orthogonal to the four-velocity of the heat bath. This decomposition is crucial in finite temperature field theory as it helps to separate the directions along and perpendicular to the heat bath's flow. These parallel and orthogonal component with respect to u^μ are

$$P_\parallel^\mu = (P \cdot u) u^\mu = \omega u^\mu, \qquad \text{and} \qquad P_\perp^\mu = \tilde{P}^\mu = P^\mu - P_\parallel^\mu = P^\mu - \omega u^\mu. \tag{4.61a}$$

$$\tilde{P}^2 = (P^\mu - \omega u^\mu)(P_\mu - \omega u_\mu) = P^2 - \omega^2 - \omega^2 + \omega^2 = P^2 - \omega^2 = -p^2. \tag{4.61b}$$

We can also define any four vector parallel and perpendicular to P^μ

$$u_\parallel^\mu = \frac{(P \cdot u) P^\mu}{P^2} = \frac{\omega P^\mu}{P^2}, \quad \text{and} \ \ \bar{u}^\mu \equiv u_\perp^\mu = u^\mu - u_\parallel^\mu = u^\mu - \frac{\omega P^\mu}{P^2}. \tag{4.62}$$

So, $P^\mu \bar{u}_\mu = 0$. Finally, one can obtain [112] from (4.57)

$$A^{\mu\nu} = \frac{1}{P^2 - \omega^2} \left[(P^2 - \omega^2)(\eta^{\mu\nu} - u^\mu u^\nu) - P^\mu P^\nu - \omega^2 u^\mu u^\nu + \omega(P^\mu u^\nu + u^\mu P^\nu) \right], \tag{4.63a}$$

$$B^{\mu\nu} = \frac{1}{P^2 (P^2 - \omega^2)} \left[P^4 u^\mu u^\nu + \omega^2 P^\mu P^\nu - \omega P^2 (P^\mu u^\nu + u^\mu P^\nu) \right]. \tag{4.63b}$$

One can see that the two independent second rank symmetric tensors at finite temperature have been constructed from $\eta^{\mu\nu}, P^\mu P^\nu, u^\mu u^\nu,$ and $P^\mu u^\nu + u^\mu P^\nu$ which are orthogonal to P^μ.

4.4.2. General structure of self-energy of a gauge boson

The self-energy of a vector particle in a medium (finite temperature/density) can be expressed as

$$\Pi_{\mu\nu} = \Pi_T(\omega, p) A_{\mu\nu} + \Pi_L(\omega, p) B_{\mu\nu}, \tag{4.64}$$

which satisfies current conservation $P^\mu \Pi_{\mu\nu} = 0$. Substituting A_{00} and B_{00} from (4.63a) and (4.63b), respectively, in Π_{00} in (4.64), one can obtain [109, 112, 113]

$$\Pi_L(\omega, p) = \left(-\frac{P^2}{p^2}\right) \Pi_{00}(\omega, p). \tag{4.65}$$

Now, operating $\eta^{\mu\nu}$ on self-energy in (4.64), then using (4.63a) and (4.63b) one can obtain [109, 112, 113]

$$\Pi_T(\omega, p) = \frac{1}{D-2}\left[\Pi^\mu_\mu(\omega, p) - \Pi_L(\omega, p)\right] = \frac{1}{2}\left[\Pi^\mu_\mu(\omega, p) - \Pi_L(\omega, p)\right]. \tag{4.66}$$

where $D = 4$, the space-time dimension.

4.4.3. General structure of a massless vector gauge boson propagator in covariant gauge
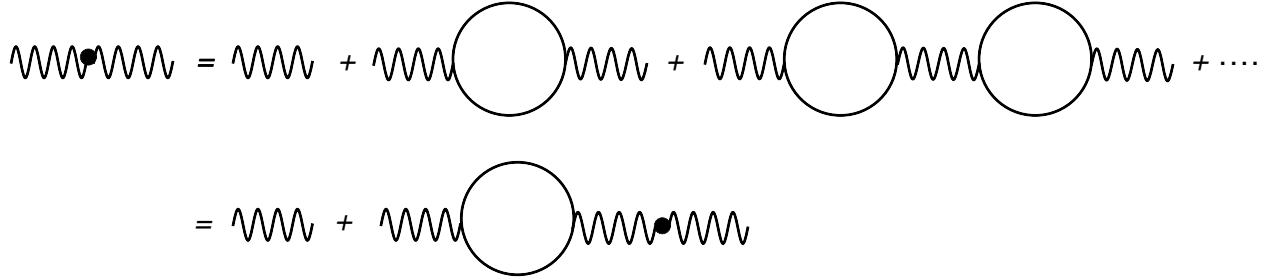
Figure 4.6: Resummed gauge boson propagator, known as Dyson-Schwinger equation.

Dyson-Schwinger equation provides a relation between the full propagator $D_{\mu\nu}$ the bare propagator $D^0_{\mu\nu}$, and the self-energy $\Pi_{\mu\nu}$ in terms of a perturbative expansion. We can write the full gauge boson propagator in Fig. 4.6 as

$$\begin{aligned} D^{\mu\rho} &= D^{0\mu\rho} + D^{0\mu\alpha}\Pi_{\alpha\beta}D^{\beta\rho} \\ D^{\mu\rho}D^{-1}_{\rho\nu} &= D^{0\mu\rho}D^{-1}_{\rho\nu} + D^{0\mu\alpha}\Pi_{\alpha\beta}D^{\beta\rho}D^{-1}_{\rho\nu} \\ D^{-1}_{\nu\gamma} &= (D^0_{\nu\gamma})^{-1} - \Pi_{\nu\gamma}. \end{aligned} \tag{4.67}$$

For massless gauge boson the propagator is given as

$$D^0_{\mu\nu} = -\frac{\eta_{\mu\nu}}{P^2} + (1-\xi)\frac{P_\mu P_\nu}{P^4}, \tag{4.68}$$

where $\xi = 1$ in Feynman gauge and $\xi = 0$ in Landau gauge. Following the details calculation in Refs. [109, 112, 113] where the self-energy corrections are included, the full propagator of the gauge boson in the thermal medium can be written as:

$$D_{\mu\nu} = -\frac{\xi}{P^4}P_\mu P_\nu - \frac{1}{P^2 + \Pi_T}A_{\mu\nu} - \frac{1}{P^2 + \Pi_L}B_{\mu\nu}. \tag{4.69}$$

We note here that the general structure of two-point functions for both fermion and gauge boson are applicable to both QED and QCD. The poles of the propagator give rise to dispersion mode. The condition $P^2 + \Pi_L = 0$ leads to the propagation of longitudinal mode, known as plasmon, which appears due to the thermal bath. The condition $P^2 + \Pi_T = 0$ leads to doubly degenerate transverse mode. The energy of gluon separated into two modes due to Lorentz symmetry breaking in presence of heat bath.

4.5. Scale Separation at Finite Temperature

In finite temperature field theory, a key aspect is the introduction of various energy scales that emerge due to the interactions and the nature of the thermal medium. The periodicity or anti-periodicity over Euclidean time introduces a scale present in the non-interacting theory where momentum, $p \sim 2\pi T$, known as hard scale. The momentum sets a natural cutoff in the non-interacting theory, and it corresponds to the high-energy modes of the system. In this case, the non-interacting theory does not introduce any additional mass or screening effects, so the bosonic zero modes (like the Matsubara frequencies) do not acquire any scale beyond the temperature. However, at high temperature once interactions are considered, they give rise to additional energy scales such as the soft and ultra-soft scales. The soft scale $p \sim gT$, smaller than the hard scale, arises from the collective excitations of the electric component of gauge field in the thermal medium due to interactions. It corresponds to momentum scales where the thermal medium begins to affect the dynamics of the system. The ultra-soft scale is associated with the magnetic component of the gauge fields. When, the momentum is of order $p \sim g^2 T$, which is smaller than the soft scale. This scale corresponds to the momentum where non-perturbative effects [117, 118] become significant. It represents magnetic excitations or fluctuations in the system that are not screened in a simple manner. This hierarchy of energy scales is critical in understanding the behaviour of gauge theories at finite temperature, especially in the context of quantum chromodynamics (QCD) or other gauge field theories where the medium effects can lead to important modifications of particle interactions.

There is an expansion parameter related to bosonic fluctuations with momentum (or mass) scale p of the form

$$\epsilon_{\rm b} \sim \frac{1}{\pi} g^2 (2\pi T) n_B(p) = \frac{g^2(2\pi T)}{\pi(e^{p/T} - 1)} \overset{p < T}{\sim} \frac{g^2(2\pi T)T}{\pi p} . \tag{4.70}$$

Below, we outline some key features of these scales:

4.5.1. Hard scale:

- Scale of thermal fluctuations: momenta $p \sim 2\pi T$; length $\sim 1/T$. The hard scale refers to the momentum scale set due to thermal fluctuations temperature This is typically associated with the dynamics of high-energy excitations that are not affected by the medium's interactions. The hard scale is the dominant scale for the momentum of particles.

- It generates inverse mass of non-static field modes ($p_0 \neq 0$).

- It produces purely perturbative contributions appear from (4.70) in even power of coupling as g^{2n}, where n is the number of loop.

4.5.2. Soft (electric) scale:

- Scale of static chromoelectric fluctuations: momenta $\sim gT$; length $\sim 1/gT$. The soft scale corresponds to the characteristic momentum of collective excitations in the thermal medium, typically momenta of order $\sim gT$; length $\sim 1/gT$. These excitations are predominantly associated with electric components of the gauge field. This scale is small than the hard one.

- Generates inverse Debye screening (electric screening) mass of longitudinal gauge field (A_0) and scalar field. This describes the suppression of long-range interactions between charged particles in the medium.

- Contribution appears from (4.70) in odd powers of g and $\log(g)$ and naive perturbation theory breaks down.

- Requires resummation of an infinite subset of diagrams.

4.5.3. Ultra-soft (magnetic) scale:

- The ultra-soft scale corresponds to the static chromomagnetic fluctuations of the gauge field, momenta of oder $p \sim g^2 T$; length $\sim 1/g^2 T$.

- Generates inverse magnetic mass. Unlike the electric component, the magnetic field is not screened in a simple perturbative way. The magnetic component is screened only at a non-perturbative scale, typically, $p \sim g^2 T$.

- From (4.70) it can seen that there does not exist any perturbative series at all [117, 118] (Linde problem) and has to be determined non-perturbatively.

- Generates a single non-perturbative contribution to pressure starting at 4-loop order (Linde Problem).

In finite-temperature field theory, naive perturbation theory involves expanding around the free (non-interacting) theory using the coupling constant g. In this case, both static and dynamic quantities can be computed using free propagators and vertices. The contributions appear in even powers of the coupling constant, g^{2n}, as discussed above because interactions modify the system perturbatively. While this approach works at the hard scale ($p \sim 2\pi T$), it encounters significant challenges at softer scales due to infrared divergences, collinear singularities, and gauge dependence issues (for details see a review article [113]). Infrared singularities arise from contributions at low momentum. Both electric and magnetic sectors contribute to infrared divergences, leading to sensitivity to soft and ultra-soft regions of phase space. Collinear singularities occur when particles move nearly parallel, leading to divergences in loop integrals. Infrared problems are typically associated with bosonic excitations because their expansion parameter can become small for $p \ll T$. However, for fermions, Pauli blocking keeps the expansion parameter finite for $p < T$, mitigating the problem. At soft scale, the free theory no longer captures the physics accurately, and naive expansions lead to infrared divergences. Therefore, perturbation theory breaks down at the soft scale ($p \sim gT$) because collective effects emerge in the thermal medium. To handle these divergences, perturbation theory needs to be reorganized. The correct treatment of the soft scale involves resumming certain classes of diagrams. This is done through the effective field theory like the hard thermal loop (HTL) resummation [119–124].

4.6. Hard Thermal Loop (HTL) Resummation and HTL Perturbation Theory

As mentioned in previous subsection. 4.5, the naive perturbation theory encounters infrared and collinear singularities, as well as gauge and sign dependence, in thermal field theory. The root cause of these issues lies in the failure to account for certain classes of diagrams that, although higher order in the loop expansion, contribute at the same order in the coupling constant as the leading-order diagrams [119]. This requires careful scale separation and the inclusion of relevant diagrams through resummation techniques. These diagrams can be identified through the scale separation as discussed below.

Considering the loop momenta to be hard ($\sim 2\pi T$), the amplitude for higher-order loop diagrams [119] can be written through power counting as

$$\sim \frac{g^2 T^2}{P^2} \times \text{Tree level amplitude}, \tag{4.71}$$

where P is the external momentum.

When the external momentum is hard, $P \sim T$, then the contributions from loop diagrams are perturbatively suppressed by g^2 of its tree level amplitude. Since the hard momenta dominate, naive perturbation theory works, and the one-loop correction remains subleading compared to the tree-level amplitude.

When the external momentum , $P \sim gT$, the dynamics of the system are significantly altered, leading to contributions from higher-order diagrams that match the order of the tree-level amplitude. This phenomenon arises due to the interplay between hard scale arising from loop momenta and soft scale from external momenta, requiring a resummation of certain class of diagrams. The Hard Thermal Loop (HTL) effective theory provides a framework systematically accounts for these diagrams, ensuring consistent calculations at the soft (electric) scale. This is as illustrated below:

1. These HTL diagrams can be resummed systematically by organizing them into a geometrical series, which leads to the construction of effective propagators and vertices. This resummation ensures gauge invariance and consistency, guided by identities such as the Ward-Takahashi identity in QED and the Slavnov-Taylor identity in QCD.

2. HTL resummation captures essential medium effects, such as electric screening, thermal masses, and Landau damping, by modifying propagators and vertices. The effective N-point functions can be used in perturbation theory resulting a framework, HTL perturbation theory (HTLpt), allows for gauge-independent, consistent, and systematically improvable perturbative calculations in the thermal medium.

3. Infrared divergences are a significant challenge, particularly in gauge theories like QED and QCD, at finite temperature. While electric screening (Debye mass) mitigates some of these issues, magnetic screening presents unique challenges that remain unsolved at leading order in HTL resummation. This is because In gauge theories, static magnetic fields are not screened at leading order since the 1-loop transverse photon/gluon self-energy vanishes in the static, low-momentum limit. HTLpt can consistently handle calculations up to order g^5 by resumming electric contributions but breaks down at g^6 order due to the absence of magnetic screening [117, 118] as perturbative techniques cannot handle this.

Hard Thermal Loop perturbation theory (HTLpt) [125–141] is a powerful framework designed to compute thermodynamic quantities in gauge theories at finite temperature while addressing infrared divergences and incorporating thermal medium effects via HTL resummation. The HTLpt framework allows for a systematic analytic reorganization of perturbative series based on the HTL effective Lagrangian. Furthermore, it is manifestly gauge invariant and also very useful to calculate both static and dynamical quantities. The HTLpt can be viewed as an extension of screened perturbation theory (SPT) [142–146], which was initially developed for scalar field theories. Both approaches aim to address infrared divergences in finite-temperature field theory, but HTLpt extends the concepts of SPT to more complex gauge theories, incorporating the effects of thermal screening in a more systematic and comprehensive way. For details of the HTL approximation and HTLpt readers are referred to recent reviews on HTL [113, 147].

The HTLpt has been extensively used in QCD to study the properties of the Quark-Gluon Plasma (QGP), a state of matter that exists at extremely high temperatures and energy densities. The various quantities are, viz., the thermodynamic properties [125–141, 148–152], dilepton production rate [153–166], photon production rate [160, 161, 167–172], single quark and quark-antiquark potentials [173–180], fermion damping rate [181–187], photon damping rate [188, 189], gluon damping rate [190–192] and parton energy-loss [186, 193–203], plasma instabilities [204–210], applications of HTL transport theory to high density QCD in a phase with color superconductivity [211], thermal axion production [212] and lepton asymmetry during leptogenesis [213, 214]. Very recently, HTL is extended to calculate the free energy of $\mathcal{N} = 4$ supersymmetric Yang-Mills in four spacetime dimensions in Ref. [215–217].

We also note that dimensional reduction [218–222] provides a powerful alternative to HTLpt by integrating out high-energy modes to yield a simpler 3D effective theory. It efficiently handles thermodynamic quantities and exploits the natural separation of three aforementioned energy scales in finite-temperature field theory.

5. Thermal Field Theory with Background Magnetic Field

In previous sections 2 and 3, the modification of Dirac equation and free propagators in vacuum have been discussed in presence of a background magnetic field. Also the field theory with thermal background has been discussed brielfly in section 4. We have noticed that finite temperature breaks the Lorentz (boost) symmetry by introducing a preferred time direction in the system, leading to an anisotropic response of the system to changes in momentum and energy. On the hand background magnetic field breaks the rotational symmetry by introducing a preferred spatial direction, modifying the dynamics of charged particles and collective excitations in the plasma. In a hot magnetized system under the influence of an external magnetic field, it is often useful to define a new four-vector, n^μ that is associated with the electromagnetic field tensor $F^{\mu\nu}$. This new vector can help in understanding the anisotropic behaviour of the system due to the magnetic field and facilitate the analysis of the effects of the magnetic field on the system's dynamics.

We define the electromagnetic field tensor as

$$F^{\mu\nu} = \begin{pmatrix} 0 & 0 & 0 & 0 \\ 0 & 0 & -B & 0 \\ 0 & B & 0 & 0 \\ 0 & 0 & 0 & 0 \end{pmatrix}.$$

(5.1)

In a hot magnetized medium, when a fermion moves in a nontrivial background such as a thermal bath with an external magnetic field, the four-vector n^μ in the rest frame of the heat bath is defined as the projection of the electromagnetic field tensor $F^{\mu\nu}$ along u^μ as

$$n_\mu = \frac{1}{2B}\epsilon_{\mu\nu\rho\lambda}\, u^\nu F^{\rho\lambda} = \frac{1}{B}u^\nu \tilde{F}_{\mu\nu} = (0,0,0,1),$$

(5.2)

which is in the z-direction. This also establishes a connection between heat bath and the magnetic field. The introduction of an external anisotropic field into the thermal medium necessitates adapting existing theoretical frameworks to properly analyse various properties of thermo-magnetic system. In this section we would like to discuss how the presence of a background magnetic field modifies the N-point functions in thermal field theory in several significant ways. These modifications arise from the interaction between the magnetic field and the thermal medium, leading to anisotropies in the system. The key effects include changes in fermion propagators, modifications to gauge boson propagators, fermion-gauge boson vertices, their collective behaviours and the emergence of new scales associated with the magnetic field and temperature.

5.1. General Structure of Fermion Two-point Function in a Hot Magnetised Medium

5.1.1. General Structure of the Fermion Self-Energy

In a hot magnetized medium, the general structure of the fermion self-energy can indeed be written as a 4×4 matrix in Dirac space, which is also a Lorentz scalar. The fermion self-energy in a hot magnetized medium depends on the three key four-vectors: the fermion momentum P, the heat bath velocity u, and the magnetic field direction n. These vectors introduce anisotropies and symmetry-breaking effects, leading to a more complex structure for the fermion self-energy. Indeed, any 4×4 matrix can be expanded in terms of a set of 16 basis matrices: $\{\mathbb{1}, \gamma_5, \gamma_\mu, \gamma_\mu\gamma_5, \sigma_{\mu\nu}\}$, which are the unit matrix, the four γ-matrices, the six $\sigma_{\mu\nu}$ matrices, the four $\gamma_5\gamma_\mu$ matrices and finally γ_5. So, the general structure can be written [65] as

$$\Sigma(P) = -\alpha\mathbb{1} - \beta\gamma_5 - a\slashed{P} - b\slashed{u} - c\slashed{n} - a'\gamma_5\slashed{P} - b'\gamma_5\slashed{u} - c'\gamma_5\slashed{n}$$

$$- h\,\sigma_{\mu\nu}P^{\mu}P^{\nu} - h'\sigma_{\mu\nu}u^{\mu}u^{\nu} - \kappa\,\sigma_{\mu\nu}n^{\mu}n^{\nu} - d\,\sigma_{\mu\nu}P^{\mu}u^{\nu} - d'\sigma_{\mu\nu}n^{\mu}P^{\nu} - \kappa'\sigma_{\mu\nu}u^{\mu}n^{\nu}\,, \tag{5.3}$$

where various coefficients are known as structure functions. We note that the combinations involving $\sigma_{\mu\nu}$ (the antisymmetric part of the gamma matrices) do not appear in the loop expansion of the self-energy at any order. This is due to the antisymmetric nature of $\sigma_{\mu\nu}$, which implies that any term involving it would vanish when contracted with symmetric tensors formed from the momentum, velocity, and background field directions used in constructing the self-energy. Also in a chirally invariant theory, the terms $\alpha \mathbb{1}$ and $\gamma_5 \beta$ as their presence would explicitly break chiral symmetry. The term $\gamma_5 \slashed{P}$ would appear in the self-energy if fermions interact with an axial vector[9].

By dropping those in (5.3) for chirally symmetric theory, one can now write

$$\Sigma(P) = -a\,\slashed{P} - b\,\slashed{u} - c\,\slashed{n} - b'\gamma_5\,\slashed{u} - c'\gamma_5\,\slashed{n}. \tag{5.4}$$

To highlight the significance of the fermion propagator in a hot magnetized medium, the expression in (3.97) encodes some essential information about the interaction of fermions with the external magnetic field [65]. Below, we examine the form of the propagator in Eq. (3.97) in the presence of a background magnetic field. Since fermion propagator is 4×4 matrix, an additional contribution $(\slashed{P}_{\shortparallel} + m_f)i\gamma_1\gamma_2$ appears which supplements the usual vacuum term $(\alpha'\slashed{P}, \alpha'(P^2)$ is a Lorentz invariant structure function) for a chirally symmetric theory. For a chirally symmetric theory, this new contribution can also be written in terms of the background electromagnetic field strength tensor $F^{\mu\nu}$ as

$$i\gamma_1\gamma_2\slashed{P}_{\shortparallel}\,B \;=\; -\gamma_5 P^{\mu}\tilde{F}_{\mu\nu}\gamma^{\nu}, \tag{5.5}$$

This expression explicitly encodes the magnetic field's effect on the fermion propagator and reflects how the external field modifies the propagator's structure.

The form of a free fermion propagator in a chirally symmetric theory, in the presence of a background magnetic field alone, can be written as $(\alpha'\slashed{P} + \delta'\gamma_5 P^{\mu}\tilde{F}_{\mu\nu}\gamma^{\nu})$, where δ' is a structure coefficient that arises due to the magnetic field. In contrast, if the fermion propagates only in a thermal medium (without a magnetic field), the vacuum structure is modified by the thermal background as $\alpha'\slashed{P} + \beta'\slashed{u})$. In the case where the fermion propagates in a hot magnetized medium, the combined effects of temperature and magnetic field lead to a propagator structure, which can be written as a modification of (5.5) as

$$i\gamma_1\gamma_2\slashed{P}_{\shortparallel} = -\gamma_5\left[(P.n)\,\slashed{u} - (P.u)\,\slashed{n}\right], \tag{5.6}$$

which suggests that $c\slashed{n}$ should not appear in the fermion self-energy [10] and the most general form of the fermion self-energy for a hot magnetised medium becomes

$$\Sigma(P) = -a\,\slashed{P} - b\slashed{u} - b'\gamma_5\,\slashed{u} - c'\gamma_5\,\slashed{n}. \tag{5.7}$$

For a fermion propagating in vacuum, the parameters simplify to $b = b' = c' = 0$ and the self-energy takes the form $\Sigma(P) = -a\slashed{P}$. When the fermion propagates in a pure magnetic field (with no heat bath), $a \neq 0$, $b = 0$, while the structure functions b' and c' depend only on the external magnetic field, as will be shown later. On the other hand, when the fermion propagates in a thermal medium (without a magnetic field), both $a \neq 0$, $b \neq 0$ but both b' and c' vanish, since there are no thermo-magnetic corrections in the absence of the magnetic field, as will also be demonstrated later.

Next, we define the *right-chiral* projection operator, $\mathcal{P}_+$ and the *left chiral* projection operator $\mathcal{P}_-$, respectively,

---

[9]Chiral and axial symmetries cannot both be preserved in the presence of gauge interactions due to the axial anomaly. A choice must be made about which symmetry is to be preserved For a chirally invariant theory this term drops out. Also the use of γ_5 in a Lagrangian introduces parity violation,as it is not invariant under parity transformations.

[10]We have checked that even if one keeps $c\slashed{n}$, the coefficient c becomes zero in one-loop order in the weak field approximation.

defined as:

$$\mathcal{P}_+ = \frac{1}{2}\left(\mathbb{1} + \gamma_5\right),$$ (5.8a)

$$\mathcal{P}_- = \frac{1}{2}\left(\mathbb{1} - \gamma_5\right),$$ (5.8b)

which satisfy the usual properties of projection operator:

$$\mathcal{P}_\pm^2 = \mathcal{P}_\pm, \quad \mathcal{P}_+\,\mathcal{P}_- = \mathcal{P}_-\,\mathcal{P}_+ = 0, \quad \mathcal{P}_+ + \mathcal{P}_- = \mathbb{1}, \quad \mathcal{P}_+ - \mathcal{P}_- = \gamma_5.$$ (5.9)

Using the chirality projection operators, the general structure of the self-energy in (5.7) can be casted in the following form

$$\Sigma(P) = -\mathcal{P}_+\,\mathcal{\cancel{C}}\,\mathcal{P}_- - \mathcal{P}_-\,\mathcal{\cancel{D}}\,\mathcal{P}_+,$$ (5.10)

where $\mathcal{\cancel{C}}$ and $\mathcal{\cancel{D}}$ are defined as

$$\mathcal{\cancel{C}} = a\,\cancel{P} + (b + b')\,\cancel{u} + c'\,\cancel{n},$$ (5.11a)

$$\mathcal{\cancel{D}} = a\,\cancel{P} + (b - b')\,\cancel{u} - c'\,\cancel{n}.$$ (5.11b)

From (5.7) one obtains the general form of the various structure functions as

$$a = \frac{1}{4}\,\frac{\mathsf{Tr}\left(\Sigma\cancel{P}\right) - (P.u)\,\mathsf{Tr}\left(\Sigma\cancel{u}\right)}{(P.u)^2 - P^2},$$ (5.12a)

$$b = \frac{1}{4}\,\frac{-(P.u)\,\mathsf{Tr}\left(\Sigma\cancel{P}\right) + P^2\,\mathsf{Tr}\left(\Sigma\cancel{u}\right)}{(P.u)^2 - P^2},$$ (5.12b)

$$b' = -\frac{1}{4}\,\mathsf{Tr}\left(\cancel{u}\Sigma\gamma_5\right),$$ (5.12c)

$$c' = \frac{1}{4}\,\mathsf{Tr}\left(\cancel{n}\Sigma\gamma_5\right),$$ (5.12d)

which are also Lorentz scalars . Beside T and B, they would also depend on three Lorentz scalars defined by

$$\omega \equiv P^\mu u_\mu,$$ (5.13a)

$$p^3 \equiv -P^\mu n_\mu = p_z\,,$$ (5.13b)

$$p_\perp \equiv \left[(P^\mu u_\mu)^2 - (P^\mu n_\mu)^2 - (P^\mu P_\mu)\right]^{1/2}.$$ (5.13c)

Since $P^2 = \omega^2 - p_\perp^2 - p_z{}^2$, we may interpret ω, $p_\perp$, p_z as Lorentz invariant energy, transverse momentum, longitudinal momentum respectively.

5.1.2. Effective Fermion Propagator

The inverse of the effective fermion propagator is represented diagramatically in Fig. 5.1 and is given by Dyson-Schwinger equation which reads from (4.34) as

$$S^{*\,-1}(P) = \cancel{P} - \Sigma(P)\,.$$ (5.14)

and the fermion propagator reads from (4.35) as

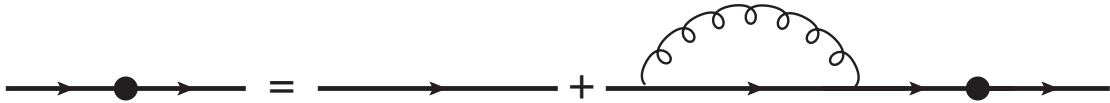$$S^*(P) = \frac{1}{\cancel{P} - \Sigma(P)}\,,$$ (5.15)

Figure 5.1: Diagramatic representation of the Dyson-Schwinger equation for one-loop effective fermion propagator.

Using (5.10) the inverse fermion propagator can be written as

$$S^{*\,-1}(P) = \mathcal{P}_+\left[(1 + a(p_0, |\vec{p}|))\cancel{P} + (b(p_0, |\vec{p}|) + b'(p_0, p_\perp, p_z))\,\cancel{u} + c'(p_0, |\vec{p}|)\cancel{n}\right]\mathcal{P}_-$$

49

$$+ \mathcal{P}_- \left[(1 + a(p_0, |\vec{p}|)) \not{P} + (b(p_0, |\vec{p}|) - b'(p_0, p_\perp, p_z)) \not{u} - c'(p_0, |\vec{p}|) \not{n} \right] \mathcal{P}_+$$

$$= \mathcal{P}_+ \not{L} \mathcal{P}_- + \mathcal{P}_- \not{R} \mathcal{P}_+ \, , \tag{5.16}$$

where $\not{L}$ and $\not{R}$ can be obtained from two four vectors given by

$$L^\mu(p_0, p_\perp, p_z) = \mathcal{A}(p_0, |\vec{p}|) P^\mu + \mathcal{B}_+(p_0, p_\perp, p_z) u^\mu + c'(p_0, |\vec{p}|) n^\mu, \tag{5.17a}$$

$$R^\mu(p_0, p_\perp, p_z) = \mathcal{A}(p_0, |\vec{p}|) P^\mu + \mathcal{B}_-(p_0, p_\perp, p_z) u^\mu - c'(p_0, |\vec{p}|) n^\mu \, , \tag{5.17b}$$

with

$$\mathcal{A}(p_0, |\vec{p}|) = 1 + a(p_0, |\vec{p}|), \tag{5.18a}$$

$$\mathcal{B}_\pm(p_0, p_\perp, p_z) = b(p_0, |\vec{p}|) \pm b'(p_0, p_\perp, p_z) \, . \tag{5.18b}$$

Using (5.16) in (5.15), the propagator can now be written as

$$S^*(P) = \mathcal{P}_- \frac{\not{L}}{L^2} \mathcal{P}_+ + \mathcal{P}_+ \frac{\not{R}}{R^2} \mathcal{P}_- \, , \tag{5.19}$$

where we have used the properties of the projection operators $\mathcal{P}_\pm \gamma^\mu = \gamma^\mu \mathcal{P}_\mp$, $\mathcal{P}_\pm^2 = \mathcal{P}_\pm$, and $\mathcal{P}_+ \mathcal{P}_- = \mathcal{P}_- \mathcal{P}_+ = 0$. It can be checked that $S^*(P) S^{*-1}(P) = \mathcal{P}_+ + \mathcal{P}_- = \mathbb{1}$. Also we have

$$L^2 = L^\mu L_\mu = (\mathcal{A}p_0 + \mathcal{B}_+)^2 - \left[(\mathcal{A}p_z + c')^2 + \mathcal{A}^2 p_\perp^2 \right] = L_0^2 - |\vec{L}|^2 \, , \tag{5.20a}$$

$$R^2 = R^\mu R_\mu = (\mathcal{A}p_0 + \mathcal{B}_-)^2 - \left[(\mathcal{A}p_z - c')^2 + \mathcal{A}^2 p_\perp^2 \right] = R_0^2 - |\vec{R}|^2 \, , \tag{5.20b}$$

where we have used $u^2 = 1$, $n^2 = -1$, $u \cdot n = 0$, $P \cdot u = p_0$, and $P \cdot n = -p_z$. Note that we have suppressed the functional dependencies of L, R, $\mathcal{A}$, $\mathcal{B}_\pm$ and c' and would bring them back whenever necessary.

For the lowest Landau Level (LLL), $l = 0 \Rightarrow p_\perp = 0$, and these relations reduce to

$$L_{LLL}^2 = (\mathcal{A}p_0 + \mathcal{B}_+)^2 - (\mathcal{A}p_z + c')^2 = L_0^2 - L_z^2 \, , \tag{5.21a}$$

$$R_{LLL}^2 = (\mathcal{A}p_0 + \mathcal{B}_-)^2 - (\mathcal{A}p_z - c')^2 = R_0^2 - R_z^2 \, . \tag{5.21b}$$

The poles of the effective propagator, given by $L^2 = 0$ and $R^2 = 0$, determine the quasi-particle dispersion relations in a hot magnetized medium. These lead to a total of four collective modes with positive energy – two from $L^2 = 0$ and two from $R^2 = 0$. The detailed discussion of these dispersion properties will be addressed later.

In absence of magnetic field ($B = 0$), $b' = c' = 0$ and $\not{L} = \not{R}$. Then, the effective fermion propagator in a non-magnetised thermal medium can be written from (5.19) as

$$S^*(P) = \frac{\not{L}}{L^2} \bigg|_{B=0} = \frac{(1+a)\not{P} + b\not{u}}{[(1+a)p_0 + b]^2 - (1+a)P^2} \, . \tag{5.22}$$

One can obtain the following quantities in rest frame of heat bath from Ref. [112] as

$$(1+a)\not{P} + b\not{u} = \frac{1}{2}(\gamma_0 + \vec{\gamma} \cdot \hat{\boldsymbol{p}})\mathcal{D}_+ + \frac{1}{2}(\gamma_0 - \vec{\gamma} \cdot \hat{\boldsymbol{p}})\mathcal{D}_- \, , \tag{5.23a}$$

$$[(1+a)p_0 + b]^2 - (1+a)P^2 = [(1+a)(\omega - p) + b] \, [(1+a)(\omega + p) + b] = \mathcal{D}_+ \mathcal{D}_- \, , \tag{5.23b}$$

where

$$\mathcal{D}_\pm(p, \omega) = (1+a)(\omega \mp p) + b. \tag{5.24}$$

Using (5.23a) and (5.23b) in (5.22), one finally obtains the effective fermion propagator in a non-magnetised thermal medium as

$$S^\star(P) = \frac{1}{2} \frac{(\gamma_0 - \vec{\gamma} \cdot \hat{\boldsymbol{p}})}{\mathcal{D}_+(\omega, p)} + \frac{1}{2} \frac{(\gamma_0 + \vec{\gamma} \cdot \hat{\boldsymbol{p}})}{\mathcal{D}_-(\omega, p)} \, , \tag{5.25}$$

which agrees with (4.45).

5.2. General Structure of Gauge Boson Two Point Function in a Hot Magnetised Medium

We have discussed in previous subsections 5.1 that in presence of nontrivial background, *e.g.*, heat bath and magnetic field, the boost and rotational symmetries of the system are broken. In the presence of both finite temperature and a finite magnetic field B, the gauge boson self-energy would acquires a more complex covariant structure due to the combined effects of thermal and magnetic backgrounds. Now, the four-vectors and tensors available to form the general covariant structure of the gauge boson self-energy are P^μ, $g^{\mu\nu}$, the electromagnetic field tensor $F^{\mu\nu}$ and it's dual $\tilde{F}^{\mu\nu}$, the four velocity of the heat bath, u^μ and a new four vector given in (5.2) that defines the direction of the magnetic field n^μ.

5.2.1. Tensor decomposition

For a hot magnetized medium, the available Lorentz vectors P^μ, u^μ and n^μ along with metric tensor $g^{\mu\nu}$, can be used to construct a set of seven symmetric basis tensors, namely $P^\mu P^\nu$, $P^\mu n^\nu + n^\mu P^\nu$, $n^\mu n^\nu$, $P^\mu u^\nu + u^\mu P^\nu$, $u^\mu u^\nu$, $u^\mu n^\nu + n^\mu u^\nu$ and $g^{\mu\nu}$. These basis tensors respect the symmetries and constraints of the system and are formed by combining these four-vectors and the metric tensor in a symmetric way. These seven tensors reduce to four because of constraints provided by the gauge invariance condition in (4.56). Below we obtain [66] the four basis tensors[11].

We first form the transverse four momentum and the transverse metric tensor as

$$P_\perp^\mu = P^\mu - (P \cdot u)u^\mu + (P \cdot n)n^\mu$$
$$= P^\mu - p_0 u^\mu + p^3 n^\mu = P^\mu - P_\parallel^\mu, \tag{5.26a}$$

$$g_\perp^{\mu\nu} = g^{\mu\nu} - u^\mu u^\nu + n^\mu n^\nu = g^{\mu\nu} - g_\parallel^{\mu\nu}, \tag{5.26b}$$

where

$$P_\parallel^\mu = p_0 u^\mu - p^3 n^\mu, \tag{5.27a}$$

$$P_\parallel^2 = P_\parallel^\mu P_\mu^\parallel = p_0^2 - p_3^2, \tag{5.27b}$$

$$g_\parallel^{\mu\nu} = u^\mu u^\nu - n^\mu n^\nu, \tag{5.27c}$$

$$P_\perp^\mu P_\mu^\perp = P_\perp^2 = P^2 - p_0^2 + p_3^2 = P^2 - P_\parallel^2 = -p_\perp^2, \tag{5.27d}$$

where $P^2 = P_\parallel^2 + P_\perp^2 = P_\parallel^2 - p_\perp^2$, $P_\parallel^2 = p_0^2 - p_3^2$ and $p_\perp^2 = p_1^2 + p_2^2$. We further note that the three independent Lorentz scalars are p_0, p^3 and $P_\perp^2$.

We take $B^{\mu\nu}$ in (4.63b) as one of projection tensors in hot magnetized system. Now $A^{\mu\nu}A_{\mu\nu} = 2$ indicates that it is a combination of two mutually orthogonal projection tensors, which yields two degenerate transverse modes for gauge boson in heat bath. Projection of $A^{\mu\nu}$ along magnetic field direction n^μ is given as

$$\bar{n}^\mu = A^{\mu\nu} n_\nu. \tag{5.28}$$

So we can construct another second rank tensor orthogonal to both P^μ and $B^{\mu\nu}$ as,

$$Q^{\mu\nu} = \frac{\bar{n}^\mu \bar{n}^\nu}{\bar{n}^2}. \tag{5.29}$$

We, now, construct the third projection tensor $R^{\mu\nu}$, with a constraint such that the sum of $R^{\mu\nu}$, $B^{\mu\nu}$ and $Q^{\mu\nu}$ gives the vacuum projection operator $V^{\mu\nu}$ as

$$R^{\mu\nu} = V^{\mu\nu} - B^{\mu\nu} - Q^{\mu\nu} = A^{\mu\nu} - Q^{\mu\nu} = g_\perp^{\mu\nu} - \frac{P_\perp^\mu P_\perp^\nu}{P_\perp^2}. \tag{5.30}$$

---

[11]We note here that a set of four different basis tensors were used in Refs. [67, 223–225].

It can be checked easily that all the projection tensors satisfy the following properties,

$$P_\mu Z^{\mu\nu} = 0, \tag{5.31a}$$

$$Z^{\mu\lambda} Z^\nu_\lambda = Z^{\mu\nu}, \tag{5.31b}$$

$$Z^{\mu\nu} Z_{\mu\nu} = 1. \tag{5.31c}$$

where $Z = B, R, Q$. The three projection tensors are orthogonal to each other:

$$Z^{\mu\nu} Y_{\mu\nu} = 0, \tag{5.32a}$$

where $Z \neq Y$ and $Y = B, R, Q$. Now we construct the fourth tensor as

$$N^{\mu\nu} = \frac{\bar{u}^\mu \bar{n}^\nu + \bar{u}^\nu \bar{n}^\mu}{\sqrt{\bar{u}^2}\sqrt{\bar{n}^2}}, \tag{5.33}$$

which satisfies the following properties

$$N^{\mu\rho} N_{\rho\nu} = B^\mu_\nu + Q^\mu_\nu, \tag{5.34a}$$

$$B^{\mu\rho} N_{\rho\nu} + N^{\mu\rho} B_{\rho\nu} = N^\mu_\nu \ , \ Q^{\mu\rho} N_{\rho\nu} + N^{\mu\rho} Q_{\rho\nu} = N^\mu_\nu, \tag{5.34b}$$

$$R^{\mu\rho} N_{\rho\nu} = N^{\mu\rho} R_{\rho\nu} = 0. \tag{5.34c}$$

5.2.2. Vector gauge boson self-energy

Now, one can write a general covariant structure of gauge boson self-energy as

$$\Pi^{\mu\nu} = bB^{\mu\nu} + cR^{\mu\nu} + dQ^{\mu\nu} + aN^{\mu\nu}, \tag{5.35}$$

where b, c, d and a are four Lorentz-invariant form factors associated with the four basis tensors. Note that (5.35) can also be expressed as

$$\Pi^{\mu\nu} = bB^{\mu\nu} + cA^{\mu\nu} + (d - c)Q^{\mu\nu} + aN^{\mu\nu} \tag{5.36}$$

This particular decomposition of the self-energy in terms of four tensor basis is exactly same that has been used in Ref. [205, 226] which, however were then applied for different perspectives.

The (00) components of the constituent tensors are given by

$$B_{00} = \bar{u}^2, \tag{5.37a}$$

$$R_{00} = 0, \tag{5.37b}$$

$$Q_{00} = 0, \tag{5.37c}$$

$$N_{00} = 0, \tag{5.37d}$$

$$\Pi_{00} = bB_{00} = b\bar{u}^2. \tag{5.37e}$$

Using these information, we obtain the form factors as

$$b = B^{\mu\nu} \Pi_{\mu\nu}, \tag{5.38a}$$

$$c = R^{\mu\nu} \Pi_{\mu\nu}, \tag{5.38b}$$

$$d = Q^{\mu\nu} \Pi_{\mu\nu}, \tag{5.38c}$$

$$a = \frac{1}{2} N^{\mu\nu} \Pi_{\mu\nu}. \tag{5.38d}$$

In absence of the magnetic field by comparing with the known general form of finite temperature self-energy in (4.64), as

$$\Pi_T A_{\mu\nu} + \Pi_L B_{\mu\nu} = b_0 B_{\mu\nu} + c_0 R_{\mu\nu} + d_0 Q_{\mu\nu} + a_0 N_{\mu\nu}, \tag{5.39}$$

one can write

$$b_0 = \Pi_L, \tag{5.40a}$$

$$c_0 = d_0 = \Pi_T, \tag{5.40b}$$

$$a_0 = 0. \tag{5.40c}$$

where we used the fact that $R_{\mu\nu} + Q_{\mu\nu} = A_{\mu\nu}$.

5.2.3. Gauge boson propagator

The inverse of the general gauge boson propagator following Dyson-Schwinger equation is given in (4.67) and the free propagator is given in (4.68). In covariant gauge the inverse of the gauge boson propagator in vacuum reads [109, 112, 113] as

$$\left(\mathcal{D}^0\right)^{-1}_{\mu\nu} = -P^2 g_{\mu\nu} + \frac{\xi-1}{\xi} P_\mu P_\nu, \tag{5.41}$$

where ξ is the gauge parameter. From (5.30) one can write

$$P_\mu P_\nu = P^2 \left[g_{\mu\nu} - (B_{\mu\nu} + R_{\mu\nu} + Q_{\mu\nu}) \right]. \tag{5.42}$$

and using this in (5.41), we get

$$\left(\mathcal{D}^0\right)^{-1}_{\mu\nu} = \frac{P^2}{\xi} g_{\mu\nu} + P^2 \frac{\xi-1}{\xi} (B_{\mu\nu} + R_{\mu\nu} + Q_{\mu\nu}). \tag{5.43}$$

From (5.43) and (5.35) we can now readily get the Dyson-Schwinger equation from (4.67) as

$$\mathcal{D}^{-1}_{\mu\nu} = -\frac{P^2}{\xi} g_{\mu\nu} - \left(P_m^2 + b\right) B_{\mu\nu} - \left(P_m^2 + c\right) R_{\mu\nu} - \left(P_m^2 + d\right) Q_{\mu\nu} - a N_{\mu\nu}, \tag{5.44}$$

where

$$P_m^2 = P^2 \frac{\xi-1}{\xi}. \tag{5.45}$$

The inverse of (5.44) can be written as

$$\mathcal{D}_{\mu\rho} = \alpha P_\mu P_\rho + \beta B_{\mu\rho} + \gamma R_{\mu\rho} + \delta Q_{\mu\rho} + \sigma N_{\mu\rho}, \tag{5.46}$$

along with

$$\delta^\nu_\mu = \mathcal{D}_{\mu\rho} \left(\mathcal{D}^{-1}\right)^{\rho\nu}$$
$$-\delta^\nu_\mu = \alpha \frac{P^2}{\xi} P_\mu P^\nu + \left[\frac{\beta P^2}{\xi} + \beta(P_m^2 + b) + \sigma a\right] B^\nu_\mu$$
$$+ \left[\frac{\delta P^2}{\xi} + \delta(P_m^2 + d) + \sigma a\right] Q^\nu_\mu + \left[\frac{\gamma P^2}{\xi} + \gamma(P_m^2 + c)\right] R^\nu_\mu$$
$$+ \left[\beta a + \sigma(P_m^2 + d) + \frac{\sigma P^2}{\xi}\right] \frac{\bar{u}_\mu \bar{n}^\nu}{\sqrt{\bar{u}^2}\sqrt{\bar{n}^2}} + \left[\delta a + \sigma(P_m^2 + b) + \frac{\sigma P^2}{\xi}\right] \frac{\bar{n}_\mu \bar{u}^\nu}{\sqrt{\bar{u}^2}\sqrt{\bar{n}^2}}. \tag{5.47}$$

Now, we write down the explicit forms of various tensors:

$$B^\nu_\mu = \frac{1}{P^2(P^2 - \omega^2)} \left[P^4 u_\mu u^\nu + \omega^2 P_\mu P^\nu - \omega P^2 (P_\mu u^\nu + u_\mu P^\nu)\right], \tag{5.48a}$$

$$A^\nu_\mu = \frac{1}{P^2 - \omega^2} \left[(P^2 - \omega^2)(\delta^\nu_\mu - u_\mu u^\nu) - P_\mu P^\nu - \omega^2 u_\mu u^\nu + \omega (P_\mu u^\nu + u_\mu P^\nu)\right], \tag{5.48b}$$

$$Q^\nu_\mu = \frac{1}{(P^2 - \omega^2)^2 \bar{n}^2} \left[(P^2 - \omega^2)^2 n_\mu n^\nu - (P \cdot n)(P^2 - \omega^2)(P_\mu n^\nu + n_\mu P^\nu) + \omega^2 (P \cdot n)^2 u_\mu u^\nu\right.$$
$$\left. + (P.n)^2 P_\mu P^\nu + \omega(P \cdot n)(P^2 - \omega^2)(u_\mu n^\nu + n_\mu u^\nu) - \omega(P \cdot n)(P^2 - \omega^2)(P_\mu u^\nu + u_\mu P^\nu)\right], \tag{5.48c}$$

$$R^\nu_\mu = A^\nu_\mu - Q^\nu_\mu$$
$$= \delta^\nu_\mu - \left[1 + \frac{\omega^2}{P^2 - \omega^2} + \frac{\omega^2(P \cdot n)^2}{\bar{n}^2(P^2 - \omega^2)^2}\right] u_\mu u^\nu - \frac{1}{P^2 - \omega^2} \left[1 + \frac{(P \cdot n)^2}{\bar{n}^2(P^2 - \omega^2)}\right] P_\mu P^\nu - \frac{1}{\bar{n}^2} n_\mu n^\nu$$

53

$$+ \frac{1}{P^2 - \omega^2} \left[\omega + \frac{\omega (P \cdot n)^2}{\bar{n}^2 (P^2 - \omega^2)} \right] (P_\mu u^\nu + u_\mu P^\nu) + \frac{(P \cdot n)}{\bar{n}^2 (P^2 - \omega^2)} (P_\mu n^\nu + n_\mu P^\nu)$$

$$- \frac{\omega (P \cdot n)}{\bar{n}^2 (P^2 - \omega^2)} (u_\mu n^\nu + n_\mu u^\nu) \,, \tag{5.48d}$$

$$\frac{\bar{u}_\mu \bar{n}^\nu}{\sqrt{\bar{u}^2} \sqrt{\bar{n}^2}} = \frac{1}{\sqrt{\bar{u}^2} \sqrt{\bar{n}^2}} \left[(P^2 - \omega^2) u_\mu n^\nu - (P \cdot n) u_\mu P^\nu + \omega (P \cdot n) u_\mu u^\nu - \frac{\omega (P^2 - \omega^2)}{P^2} P_\mu n^\nu \right.$$

$$\left. + \frac{\omega (P \cdot n)}{P^2} P_\mu P^\nu - \frac{\omega^2 (P \cdot n)}{P^2} P_\mu u^\nu \right] \,, \tag{5.48e}$$

$$\frac{\bar{n}_\mu \bar{u}^\nu}{\sqrt{\bar{u}^2} \sqrt{\bar{n}^2}} = \frac{1}{\sqrt{\bar{u}^2} \sqrt{\bar{n}^2}} \left[(P^2 - \omega^2) n_\mu u^\nu - (P \cdot n) P_\mu u^\nu + \omega (P \cdot n) u_\mu u^\nu - \frac{\omega (P^2 - \omega^2)}{P^2} n_\mu P^\nu \right.$$

$$\left. + \frac{\omega (P \cdot n)}{P^2} P_\mu P^\nu - \frac{\omega^2 (P \cdot n)}{P^2} u_\mu P^\nu \right] \,, \tag{5.48f}$$

where

$$\bar{u}^2 = \bar{u}^\mu \bar{u}_\mu = \left(u^\mu - \frac{\omega}{P^2} P^\mu \right) \left(u_\mu - \frac{\omega}{P^2} P_\mu \right) = \frac{P^2 - \omega^2}{P^2} \,, \tag{5.49a}$$

$$\bar{n}^2 = \bar{n}^\mu \bar{n}_\mu = A^{\mu\alpha} n_\alpha A_{\mu\sigma} n^\sigma = - \frac{1}{(P^2 - \omega^2)^2} \left[(P^2 - \omega^2)^2 + (P \cdot n)^2 P^2 \right] \,. \tag{5.49b}$$

Using (5.48a) to (5.48f) in (5.47) and equating different coefficients from both sides yield the following conditions:

$$\text{Coefficient of } P_\mu P^\nu : \quad \alpha = -\frac{\xi}{P^4}, \tag{5.50a}$$

$$\text{Coefficient of } u_\mu u^\nu : \quad \frac{\beta P^2}{\xi} + \beta (P_m^2 + b) + \sigma a = -1, \tag{5.50b}$$

$$\text{Coefficient of } n_\mu n^\nu : \quad \frac{\delta P^2}{\xi} + \delta (P_m^2 + d) + \sigma a = -1, \tag{5.50c}$$

$$\text{Coefficient of } \delta_\mu^\nu : \quad \frac{\gamma P^2}{\xi} + \gamma (P_m^2 + c) = -1, \tag{5.50d}$$

$$\text{Coefficient of } P_\mu n^\nu : \quad \beta a + \sigma (P_m^2 + d) + \frac{\sigma P^2}{\xi} = 0, \tag{5.50e}$$

$$\text{Coefficient of } n_\mu P^\nu : \quad \delta a + \sigma (P_m^2 + b) + \frac{\sigma P^2}{\xi} = 0. \tag{5.50f}$$

Solving these equations, one gets

$$\alpha = -\frac{\xi}{P^4}, \tag{5.51a}$$

$$\beta = -\frac{P^2 + d}{(P^2 + b)(P^2 + d) - a^2}, \tag{5.51b}$$

$$\gamma = -\frac{1}{P^2 + c}, \tag{5.51c}$$

$$\delta = -\frac{P^2 + b}{(P^2 + b)(P^2 + d) - a^2}, \tag{5.51d}$$

$$\sigma = \frac{a}{(P^2 + b)(P^2 + d) - a^2}. \tag{5.51e}$$

Now, using these the general covariant structure of the gauge boson propagator in covariant gauge can finally be obtained from (5.46) as

$$\mathcal{D}_{\mu\nu} = -\frac{\xi P_\mu P_\nu}{P^4} - \frac{(P^2 + d) B_{\mu\nu}}{(P^2 + b)(P^2 + d) - a^2} - \frac{R_{\mu\nu}}{P^2 + c} - \frac{(P^2 + b) Q_{\mu\nu}}{(P^2 + b)(P^2 + d) - a^2}$$

$$+ \frac{a N_{\mu\nu}}{(P^2 + b)(P^2 + d) - a^2}. \tag{5.52}$$

We recall that the breaking of boost invariance due to finite temperature leads to two modes (degenerate transverse mode and plasmino). Now, the breaking of the rotational invariance in presence of magnetic field lifts the degeneracy of the transverse modes which introduces an additional mode in the hot medium. These three dispersive modes of gauge boson can be seen from the poles of (5.52). The poles $(P^2 + b)(P^2 + d) - a^2 = 0$, lead to two dispersive modes. We call one mode

n^+ with energy ω_{n^+} and the other one n^- with energy ω_{n^-}. The pole $P^2 + c = 0$ leads to the third dispersive mode c with energy ω_c. We will discuss about these dispersive modes in details later for both strong and weak field approximation.

When we turn off the magnetic field, the general structure of the propagator in a non-magnetized thermal bath can be obtained by putting $b_0 = \Pi_L$, $c_0 = d_0 = \Pi_T$, $a_0 = 0$ and $A_{\mu\nu} = R_{\mu\nu} + Q_{\mu\nu}$ as

$$\mathcal{D}_{\mu\nu} = -\frac{\xi P_\mu P_\nu}{P^4} - \frac{B_{\mu\nu}}{P^2 + \Pi_L} - \frac{A_{\mu\nu}}{P^2 + \Pi_T}. \tag{5.53}$$

which agrees with the known result [109, 112, 113] given in (4.69).

5.3. Limiting Consideration

In this subsection we note some important points which will be required for computation of various quantities in thermo-magnetic medium.

1. In non-central heavy-ion collisions (HIC), the generated magnetic field arises due to the motion of charged nuclei. The strength and time dependence [227, 228] of this field are key factors influencing the evolution of the quark-gluon plasma (QGP) and other observables. To simplify the treatment of such a rapidly changing field, it is common to assume a constant background magnetic field under specific conditions. This allows for analytic progress in calculations, focusing on the dominant effects while capturing essential physical features. Incorporating a magnetic field into a hot medium introduces an additional scale that significantly affects the dynamics of the system. Alongside the fermion mass m_f and the temperature T, the magnetic field strength B becomes a crucial scale. Below, we outline the relevant domains of scales and their implications:

   a) Strong Field Approximation: Indeed, the strength of the magnetic field generated in non-central HIC is extremely high. The value of $|eB| \sim 15 m_\pi^2$, where e is the electronic charge, m_π is the mass of a pion, corresponds to a magnetic field strength of the order of 10^{18} Gauss. This is much larger than the temperature T and m_f typically encountered in the LHC at CERN [29]. Also in the dense sector, magnetars, which are a type of neutron star (NS), are indeed known to possess extremely strong magnetic fields. These fields are one of the defining characteristics of magnetars and can be much stronger than those in typical neutron stars. [21, 22, 229]. The effect of this strong enough magnetic field can be incorporated via a simplified Lowest Landau Level (LLL) approximation in which fermions are basically confined within the LLL. In the strong field approximation the scale hierarchy is $m_f < T < \sqrt{|eB|}$, where the loop momentum $K \sim T$ within HTL approximation.

   b) Weak Field Approximation: The magnetic field generated during the HIC is expected to decay rapidly over time, typically on the timescale of the collision. This allows for a simplified treatment of the problem, where we can often work within a weak-field approximation, with a scale hierarchy, $\sqrt{|eB|} < m_f < T$. The weak field approximation simplifies the modeling of the hot, magnetized QGP by allowing the magnetic field to be treated as a perturbation that does not significantly alter the dominant thermal effects. This leads to a manageable situation where one can calculate the impact of the magnetic field on thermodynamic quantities, dispersion relations, and transport phenomena in a systematic manner.

2. We would consider $m_f = 5$ MeV for two light quark flavors u and d.

3. We choose a frame of reference as shown in Fig. 5.2 in which one considers the external momentum of the vector
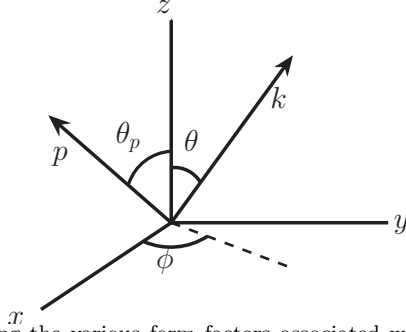
Figure 5.2: Choice of reference frame for computing the various form factors associated with the general structure of gauge boson 2-point functions. The magnetic field is along z-direction.

boson in xz plane[12] with $0 < \theta_p < \pi/2$. So one can write

$$P^\mu = (p_0, p\sin\theta_p, 0, p\cos\theta_p), \tag{5.54}$$

and then loop momenta

$$K^\mu = (k_0, k\sin\theta\cos\phi, k\sin\theta\sin\phi, k\cos\theta). \tag{5.55}$$

5.3.1. Scale hierarchies in weak field approximation

The presence of magnetic field $q_f B$ introduces another scale in addition to the thermal scales gT and T. In weak field approximation one can have two hierarchies of scales:

(i) When $\sqrt{q_f B}$ is the smallest scale compared to temperature and quark mass, one can work with a hierarchy of scales $\sqrt{q_f B} < m_f < T$ and $\sqrt{q_f B}$ can be treated as perturbation. In this domain the Schwinger propagator for a fermion in weak field approximation [230, 231] up to an $\mathcal{O}[(q_f B)^2]$ is obtained by expanding the sum over all Landau levels in (3.101). Now combining (3.101) and (5.6) the fermion propagator in background magnetic field reads as

$$
\begin{aligned}
S_m^w(k) &= \frac{\slashed{K} + m_f}{K^2 - m_f^2}(q_f B)^0 - (q_f B)\frac{(\gamma_5\{(K\cdot n)\slashed{u} - (K\cdot u)\slashed{n}\} - i\gamma_1\gamma_2 m_f)}{(K^2 - m_f^2)^2} \\
&\quad - 2(q_f B)^2\left[\frac{\{(K\cdot u)\slashed{u} - (K\cdot n)\slashed{n}\} - \slashed{K}}{(K^2 - m_f^2)^3} - \frac{k_\perp^2(\slashed{K} + m_f)}{(K^2 - m_f^2)^4}\right] + \mathcal{O}\left[(q_f B)^3\right],
\end{aligned} \tag{5.56}
$$

which is a perturbative series of $q_f B$. In $q_f B \to 0$, the thermo-magnetic correction vanishes. Alternatively, the thermo-magnetic effects are obtained as higher order perturbative corrections to the nonmagnetized part [i.e., HTL part as $(q_f B)^0$]. This means that for each given order in $q_f B$ in a perturbative series, one can use HTL approximation within the scale hierarchy $\sqrt{q_f B} < gT < T$ to obtain the desired order of coupling.

(ii) When quark mass m_f is the smallest scale compared to temperature and magnetic field, one may work with a hierarchy $m_f < \sqrt{q_f B} < T$ by considering m_f as perturbation for a given order of $q_f B$. In this hierarchy m_f in fermion propagator is either set to be zero or expanded in m_f for a given order of $q_f B$.

As discussed above, we will be working here only with the hierarchy[13] $\sqrt{q_f B} < m_f < T$.

---

[12] However, it is possible to consider a general reference frame with $P_\mu = (p_0, p_1, p_2, p_3)$, and the final results would remain invariant under the choice of reference frame. This invariance holds because the anisotropy induced by the external magnetic field along the z-direction breaks the equivalence between $p_\perp$ and p_3 while p_1 and p_2 remain indistinguishable. To simplify the calculations, we adopt a specific choice for the reference frame in this analysis.

[13] Performing calculations with the alternative hierarchy constitutes an independent problem in its own right, requiring a separate and

5.4. Collective Behaviour of Fermion in Thermo-Magnetic QCD medium

5.4.1. Computations of quark self-energy and structure functions in one-loop in a weak field approximation

Here, we present the computations of the various structure functions in (5.12a) to (5.12d) in 1-loop order (Fig.5.3) in a weak field and HTL approximations following the imaginary time formalism. In Fig.5.3 the modified quark propagator
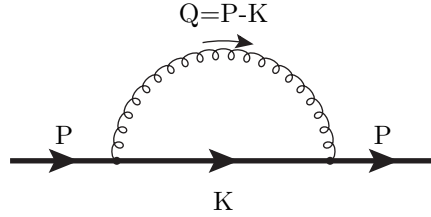

Figure 5.3: Displays the one loop fermion self-energy in a hot magnetized medium.

(bold line) due to background magnetic field is given in (5.58). Since glouns are chargeless, their propagators do not change in presence of magnetic field. The gluon propagator in Feynman gauge, is given as[65, 112, 113, 230]

$$D_{ab}^{\mu\nu}(Q) = -i\delta_{ab}\frac{g^{\mu\nu}}{Q^2}. \tag{5.57}$$

We note that we would like to explore the fermion spectrum in a hot magnetised background in the limit $m_f^2 < q_f B < T^2$. In this domain the fermion propagator is obtained by expanding the sum over all Landau levels in powers of $q_f B$ in (5.56).Now first order in $q_f B$ reads [65, 230] as

$$S(K) = \frac{\slashed{K}}{K^2 - m_f^2} - \frac{\gamma_5\left[(K.n)\,\slashed{u} - (K.u)\,\slashed{n}\right]}{(K^2 - m_f^2)^2}(q_f B) + \mathcal{O}[(q_f B)^2]$$

$$= S_1^{B=0}(K) + S_2^{B\neq 0}(K) + \mathcal{O}\left[(q_f B)^2\right], \tag{5.58}$$

where the fermion mass in the numerator has been neglected in the weak field domain, $m_f^2 < (q_f B) < T^2$.

The one-loop quark self-energy upto $\mathcal{O}(|q_f B|)$ can be written as

$$\Sigma(P) = g^2\,C_F\,T\sum_{\{K\}}\gamma_\mu\left(\frac{\slashed{K}}{K^2 - m_f^2} - \frac{\gamma_5\left[(K \cdot n)\,\slashed{u} - (K \cdot u)\,\slashed{n}\right]}{(K^2 - m_f^2)^2}q_f B\right)\gamma^\mu\,\frac{1}{(P \cdot K)^2}$$

$$\simeq \Sigma^{B=0}(P,T) + \Sigma^{B\neq0}(P,T) \equiv \Sigma^0 + \Sigma^B. \tag{5.59}$$

where g is the QCD coupling constant, $C_F = 4/3$ is the Casimir invariant of $SU(3)$ group, T is the temperature of the system. The $\{K\}$ is fermionic freequency sum with $k_0 = (2n+1)i\pi T$. The first term is the thermal bath contribution in absence of magnetic field ($B = 0$) whereas the second one is from the magnetised thermal bath.

Using (5.59) in (5.12a) and (5.12b), the structure functions a and b, respectively, become

$$a(p_0, |\vec{p}|) = \frac{1}{4}\frac{\mathsf{Tr}\left(\Sigma^0\,\slashed{P}\right) - (P.u)\,\mathsf{Tr}\left(\Sigma^0\slashed{u}\right)}{(P \cdot u)^2 - P^2}, \tag{5.60a}$$

$$b(p_0, |\vec{p}|) = \frac{1}{4}\frac{-(P.u)\,\mathsf{Tr}\left(\Sigma^0\,\slashed{P}\right) + P^2\,\mathsf{Tr}\left(\Sigma^0\slashed{u}\right)}{(P \cdot u)^2 - P^2}, \tag{5.60b}$$

where the contributions coming from Σ^B vanish due to the trace of odd number of γ-matrices. Following the well known results in Ref. [112, 113, 115], one can write

$$a(p_0, |\vec{p}|) = -\frac{m_{th}^2}{|\vec{p}|^2}Q_1\left(\frac{p_0}{|\vec{p}|}\right), \tag{5.61a}$$

$$b(p_0, |\vec{p}|) = \frac{m_{th}^2}{|\vec{p}|}\left[\frac{p_0}{|\vec{p}|}Q_1\left(\frac{p_0}{|\vec{p}|}\right) - Q_0\left(\frac{p_0}{|\vec{p}|}\right)\right], \tag{5.61b}$$

detailed analysis tailored to that framework.

where the Legendre functions of the second kind read as

$$Q_0(x) = \frac{1}{2} \ln\left(\frac{x+1}{x-1}\right), \tag{5.62a}$$

$$Q_1(x) = x\, Q_0(x) - 1 = \frac{x}{2} \ln\left(\frac{x+1}{x-1}\right) - 1, \tag{5.62b}$$

and the thermal mass. [108, 112, 113, 115] of the quark is given as

$$m_{th}^2 = C_F \frac{g^2 T^2}{8}. \tag{5.63}$$

The thermal part of the self-energy in (5.59) becomes

$$\Sigma^{B=0}(P,T) \equiv \Sigma^0(P,T) = g^2\, C_F\, T \sum_{\{K\}} \gamma_\mu \frac{\slashed{K}}{K^2 - m^2} \gamma^\mu \frac{1}{(P-K)^2}$$

$$= -a(p_0, |\vec{p}|)\slashed{P} - b(p_0, |\vec{p}|)\slashed{u}. \tag{5.64}$$

Again using (5.59) in (5.12c) and (5.12d), the structure functions b' and c', respectively, become

$$b' = -\frac{1}{4}\, \mathsf{Tr}(\slashed{u}\gamma_5 \Sigma^B), \tag{5.65a}$$

$$c' = \frac{1}{4}\, \mathsf{Tr}(\slashed{n}\gamma_5 \Sigma^B), \tag{5.65b}$$

where the contributions coming from Σ^0 vanish due to the trace of odd number of γ-matrices. For computing the above thermo-magnetic structure functions, one needs to use the following two traces:

$$\mathsf{Tr}\left[\slashed{u}\gamma_5\gamma_\mu\gamma_5\left[(K\cdot n)\slashed{u} - (K\cdot u)\slashed{n}\right]\gamma^\mu\right] = 8\,(K\cdot n), \tag{5.66a}$$

$$\mathsf{Tr}\left[\slashed{n}\gamma_5\gamma_\mu\gamma_5\left[(K\cdot n)\slashed{u} - (K\cdot u)\slashed{n}\right]\gamma^\mu\right] = 8\,(K\cdot u). \tag{5.66b}$$

With this one can obtain

$$b' = 2\,g^2\, C_F\, T\, q_f\, B \sum_{\{K\}} (K\cdot n)\, \Delta_F^2(K)\, \Delta_B(P-K), \tag{5.67a}$$

$$c' = -2\,g^2\, C_F\, T\, q_f\, B \sum_{\{K\}} (K\cdot u)\, \Delta_F^2(K)\, \Delta_B(P-K), \tag{5.67b}$$

where the boson and fermion propagators in Saclay representation are given in subsec 4.1.4 and then we perform the frequency sum using Saclay Method.

Now following HTL approximation in presence of magnetic field [54, 232] the (5.67a) and (5.67b) are simplified as [65]

$$b' = -4\,g^2\, C_F\, M^2(T, m_f, q_f B) \int \frac{d\Omega}{4\pi} \frac{\hat{K}\cdot n}{P\cdot \hat{K}}, \tag{5.68a}$$

$$c' = 4\,g^2\, C_F\, M^2(T, m_f, q_f B) \int \frac{d\Omega}{4\pi} \frac{\hat{K}\cdot u}{P\cdot \hat{K}}. \tag{5.68b}$$

Using the results of the HTL angular integrations [233]

$$\int \frac{d\Omega}{4\pi} \frac{\hat{K}\cdot u}{P\cdot \hat{K}} = \frac{1}{|\vec{p}|} Q_0\left(\frac{p^0}{|\vec{p}|}\right), \tag{5.69a}$$

$$\int \frac{d\Omega}{4\pi} \frac{\hat{K}\cdot n}{P\cdot \hat{K}} = -\frac{p^3}{|\vec{p}|^2} Q_1\left(\frac{p^0}{|\vec{p}|}\right), \tag{5.69b}$$

the thermo-magnetic structures functions become [65]

$$b' = 4g^2\, C_F\, M^2(T, m_f, q_f B) \frac{p^3}{|\vec{p}|^2} Q_1\left(\frac{p^0}{|\vec{p}|}\right), \tag{5.70a}$$

$$c' = 4g^2\, C_F\, M^2(T, m_f, q_f B) \frac{1}{|\vec{p}|} Q_0\left(\frac{p^0}{|\vec{p}|}\right), \tag{5.70b}$$

with the magnetic mass is obtained as

$$M^2(T, m_f, q_f B) = \frac{q_f B}{16\pi^2} \left[\ln(2) - \frac{T}{m_f}\frac{\pi}{2}\right]. \tag{5.71}$$

We note here that for $m_f \to 0$, the magnetic mass diverges but it can be regulated by the the thermal mass m_{th} in (5.63) as is done in Refs. [232, 233]. Then the domain of applicability becomes $m_{th}^2(\sim g^2 T^2) < q_f B < T^2$ instead of $m_f^2 < q_f B < T^2$.

The thermo-magnetic part of the self-energy in (5.59) becomes

$$\Sigma^{B\neq 0}(P,T) \equiv \Sigma^B(P,T) = -g^2\, C_F\, T\, q_f\, B \sum_{\{K\}} \gamma_\mu \frac{\gamma_5\left[(K\cdot n)\slashed{u} - (K\cdot u)\slashed{n}\right]}{(K^2 - m_f^2)^2}\gamma^\mu \frac{1}{(P-K)^2}$$

$$= -b'(p_0,|\vec{p}|)\gamma_5\slashed{u} - c'(p_0,|\vec{p}|)\gamma_5\slashed{n}. \tag{5.72}$$

Now combining (5.64), (5.72) and (5.59), the general structure of quark self-energy in hot magnetised QCD becomes

$$\Sigma(p_0,|\vec{p}|) = -a(p_0,|\vec{p}|)\slashed{P} - b(p_0,|\vec{p}|)\slashed{u} - \gamma_5 b'(p_0,|\vec{p}|)\slashed{u} - \gamma_5 c'(p_0,|\vec{p}|)\slashed{n}. \tag{5.73}$$

which agrees quite well with the general structure as discussed in (5.7) and also with results directly calculated in Refs. [54, 232, 233].

5.4.2. Transformation properties of structure functions and propagator

First, we outline some transformation properties of the various structure functions as obtained in (5.61a), (5.61b), (5.70a) and (5.70b).

1. Under the transformation $\vec{p} \to -\vec{p} = (p_\perp, -p_z)$:

$$a(p_0, |-\vec{p}|) = a(p_0, |\vec{p}|), \tag{5.74a}$$

$$b(p_0, |-\vec{p}|) = b(p_0, |\vec{p}|), \tag{5.74b}$$

$$b'(p_0, p_\perp, -p_z) = -b'(p_0, p_\perp, p_z), \tag{5.74c}$$

$$c'(p_0, |-\vec{p}|) = c'(p_0, |\vec{p}|). \tag{5.74d}$$

2. For $p_0 \to -p_0$:

$$a(-p_0, |\vec{p}|) = a(p_0, |\vec{p}|), \tag{5.75a}$$

$$b(-p_0, |\vec{p}|) = -b(p_0, |\vec{p}|), \tag{5.75b}$$

$$b'(-p_0, p_\perp, p_z) = b'(p_0, p_\perp, p_z), \tag{5.75c}$$

$$c'(-p_0, |\vec{p}|) = -c'(p_0, |\vec{p}|). \tag{5.75d}$$

3. For $P \to -P = (-p_0, -\vec{p})$:

$$a(-p_0, |-\vec{p}|) = a(p_0, |\vec{p}|), \tag{5.76a}$$

$$b(-p_0, |-\vec{p}|) = -b(p_0, |\vec{p}|), \tag{5.76b}$$

$$b'(-p_0, p_\perp, -p_z) = -b'(p_0, p_\perp, p_z), \tag{5.76c}$$

$$c'(-p_0, |-\vec{p}|) = -c'(p_0, |\vec{p}|). \tag{5.76d}$$

We have used the fact that $Q_0(-x) = -Q_0(x)$ and $Q_1(-x) = Q_1(x)$.

Now based on the above we also note down the transformation properties of those quantities appearing in the propagator: .

1. For $\mathcal{A}$:

$$\mathcal{A}(p_0, p_\perp, p_z) \xrightarrow{\vec{p} \to -\vec{p}} \mathcal{A}(p_0, p_\perp, p_z), \tag{5.77a}$$

$$\mathcal{A}(p_0, p_\perp, p_z) \xrightarrow{p_0 \to -p_0} \mathcal{A}(p_0, p_\perp, p_z), \tag{5.77b}$$

$$\mathcal{A}(p_0, p_\perp, p_z) \xrightarrow[\vec{p} \to -\vec{p}]{p_0 \to -p_0} \mathcal{A}(p_0, p_\perp, p_z). \tag{5.77c}$$

2. For $\mathcal{B}_\pm$:

$$\mathcal{B}_\pm(p_0, p_\perp, p_z) \xrightarrow{\vec{p} \to -\vec{p}} \mathcal{B}_\mp(p_0, p_\perp, p_z), \tag{5.78a}$$

$$\mathcal{B}_\pm(p_0, p_\perp, p_z) \xrightarrow{p_0 \to -p_0} -\mathcal{B}_\mp(p_0, p_\perp, p_z), \tag{5.78b}$$

$$\mathcal{B}_\pm(p_0, p_\perp, p_z) \xrightarrow[\vec{p} \to -\vec{p}]{p_0 \to -p_0} -\mathcal{B}_\pm(p_0, p_\perp, p_z). \tag{5.78c}$$

Using the above transformation properties, it can be shown that $\not{L}$, $\not{R}$, L^2 and R^2, respectively given in (5.17a), (5.17b), (5.20a) and (5.20b) transform as

$$\not{L}(p_0, p_\perp, p_z) \xrightarrow{\vec{p} \to -\vec{p}} \mathcal{A}(p_0, |\vec{p}|)(p_0\gamma^0 + \vec{p} \cdot \vec{\gamma}) + \mathcal{B}_-(p_0, p_\perp, p_z)\not{u} + c'(p_0, |\vec{p}|)\not{u}, \tag{5.79a}$$

$$\not{R}(p_0, p_\perp, p_z) \xrightarrow{\vec{p} \to -\vec{p}} \mathcal{A}(p_0, |\vec{p}|)(p_0\gamma^0 + \vec{p} \cdot \vec{\gamma}) + \mathcal{B}_+(p_0, p_\perp, p_z)\not{u} - c'(p_0, |\vec{p}|)\not{u}, \tag{5.79b}$$

$$L^2(p_0, p_\perp, p_z) \xrightarrow{\vec{p} \to -\vec{p}} R^2(p_0, p_\perp, p_z), \tag{5.79c}$$

$$R^2(p_0, p_\perp, p_z) \xrightarrow{\vec{p} \to -\vec{p}} L^2(p_0, p_\perp, p_z), \tag{5.79d}$$

and

$$\not{L}(p_0, p_\perp, p_z) \xrightarrow[\vec{p} \to -\vec{p}]{p_0 \to -p_0} -\not{L}(p_0, p_\perp, p_z), \tag{5.80a}$$

$$\not{R}(p_0, p_\perp, p_z) \xrightarrow[\vec{p} \to -\vec{p}]{p_0 \to -p_0} -\not{R}(p_0, p_\perp, p_z), \tag{5.80b}$$

$$L^2(p_0, p_\perp, p_z) \xrightarrow[\vec{p} \to -\vec{p}]{p_0 \to -p_0} L^2(p_0, p_\perp, p_z), \tag{5.80c}$$

$$R^2(p_0, p_\perp, p_z) \xrightarrow[\vec{p} \to -\vec{p}]{p_0 \to -p_0} R^2(p_0, p_\perp, p_z). \tag{5.80d}$$

Now we are in a position to check the transformation properties of the effective propagator under some of the discrete symmetries:

Chirality

Under chirality the fermion propagator transform as [234]

$$S(p_0, \vec{p}) \longrightarrow -\gamma_5 \, S(p_0, \vec{p}) \, \gamma_5. \tag{5.81}$$

The effective propagator, $S^*(p_0, p_\perp, p_z)$, in (5.19) transforms under chirality as

$$-\gamma_5 \, S^*(p_0, p_\perp, p_z) \, \gamma_5 = -\gamma_5 \mathcal{P}_- \frac{\not{L}(p_0, p_\perp, p_z)}{L^2(p_0, p_\perp, p_z)} \mathcal{P}_+ \gamma_5 - \gamma_5 \mathcal{P}_+ \frac{\not{R}(p_0, p_\perp, p_z)}{R^2(p_0, p_\perp, p_z)} \mathcal{P}_- \gamma_5$$

$$= \mathcal{P}_+ \frac{\not{L}(p_0, p_\perp, p_z)}{L^2(p_0, p_\perp, p_z)} \mathcal{P}_+ + \mathcal{P}_- \frac{\not{R}(p_0, p_\perp, p_z)}{R^2(p_0, p_\perp, p_z)} \mathcal{P}_-$$

$$= S^*(p_0, p_\perp, p_z), \tag{5.82}$$

which satisfies (6.8) and indicates that it is chirally invariant.

Reflection

Under reflection the fermion propagator transforms [234] as

$$S(p_0, \vec{p}) \longrightarrow S(p_0, -\vec{p}). \tag{5.83}$$

The effective propagator, $S^*(p_0, p_\perp, p_z)$, in (5.19) transforms under reflection as

$$S^*(p_0, p_\perp, -p_z) = \mathcal{P}_- \frac{\not{L}(p_0, p_\perp, -p_z)}{L^2(p_0, p_\perp, -p_z)} \mathcal{P}_+ + \mathcal{P}_+ \frac{\not{R}(p_0, p_\perp, -p_z)}{R^2(p_0, p_\perp, -p_z)} \mathcal{P}_-$$

$$= \mathcal{P}_- \frac{\mathcal{A}(p_0, |\vec{p}|)(p_0\gamma^0 + \vec{p} \cdot \vec{\gamma}) + \mathcal{B}_-(p_0, p_\perp, p_z)\not{u} + c'(p_0, |\vec{p}|)\not{u}}{R^2(p_0, p_\perp, p_z)} \mathcal{P}_+$$

$$+ \mathcal{P}_+ \frac{\mathcal{A}(p_0, |\vec{p}|)(p_0\gamma^0 + \vec{p} \cdot \vec{\gamma}) + \mathcal{B}_+(p_0, p_\perp, p_z)\not{u} - c'(p_0, |\vec{p}|)\not{u}}{L^2(p_0, p_\perp, p_z)} \mathcal{P}_-$$

$$\neq S^*(p_0, p_\perp, p_z). \tag{5.84}$$

However, now considering the rest frame of the heat bath, $u^\mu = (1,0,0,0)$, and the background magnetic field along z-direction, $n^\mu = (0,0,0,1)$, one can write (5.84) as

$$S^*(p_0, p_\perp, -p_z) = \mathcal{P}_- \frac{\mathcal{A}(p_0, |\vec{p}|)(p_0\gamma^0 + \vec{p}\cdot\vec{\gamma}) + \mathcal{B}_-(p_0, p_\perp, p_z)\gamma_0 - c'(p_0, |\vec{p}|)\gamma^3}{R^2(p_0, p_\perp, p_z)} \mathcal{P}_+$$

$$+ \mathcal{P}_+ \frac{\mathcal{A}(p_0, |\vec{p}|)(p_0\gamma^0 + \vec{p}\cdot\vec{\gamma}) + \mathcal{B}_+(p_0, p_\perp, p_z)\gamma_0 + c'(p_0, |\vec{p}|)\gamma^3}{L^2(p_0, p_\perp, p_z)} \mathcal{P}_-$$

$$\neq S^*(p_0, p_\perp, p_z). \tag{5.85}$$

As seen in both cases the reflection symmetry is violated as we will see later while discussing the dispersion property of a fermion.

Parity

Under parity a fermion propagator transforms [234] as

$$S(p_0, \vec{p}) \longrightarrow \gamma_0 \, S(p_0, -\vec{p}) \, \gamma_0. \tag{5.86}$$

The effective propagator, $S^*(p_0, p_\perp, p_z)$, in (5.19) under parity transforms as

$$\gamma_0 \, S^*(p_0, p_\perp, -p_z) \, \gamma_0 = \gamma_0 \mathcal{P}_- \frac{\not{L}(p_0, p_\perp, -p_z)}{L^2(p_0, p_\perp, -p_z)} \mathcal{P}_+ \gamma_0 + \gamma_0 \mathcal{P}_+ \frac{\not{R}(p_0, p_\perp, -p_z)}{R^2(p_0, p_\perp, -p_z)} \mathcal{P}_- \gamma_0$$

$$= \mathcal{P}_+ \gamma_0 \frac{\not{L}(p_0, p_\perp, -p_z)}{R^2(p_0, p_\perp, p_z)} \gamma_0 \mathcal{P}_- + \mathcal{P}_- \gamma_0 \frac{\not{R}(p_0, p_\perp, -p_z)}{L^2(p_0, p_\perp, p_z)} \gamma_0 \mathcal{P}_+$$

$$\neq S^*(p_0, p_\perp, p_z), \tag{5.87}$$

which does not obey (5.86), indicating that the effective propagator in general frame of reference is not parity invariant due to the background medium.

However, now considering the rest frame of the heat bath, $u^\mu = (1,0,0,0)$, and the background magnetic field along z-direction, $n^\mu = (0,0,0,1)$, one can write (5.87) by using (5.79a), (5.79b) and $\gamma_0 \gamma^i = -\gamma^i \gamma_0$ as

$$\gamma_0 \, S^*(p_0, p_\perp, -p_z) \, \gamma_0 = \mathcal{P}_+ \frac{\not{R}(p_0, p_\perp, p_z)}{R^2(p_0, p_\perp, p_z)} \mathcal{P}_- + \mathcal{P}_- \frac{\not{L}(p_0, p_\perp, p_z)}{L^2(p_0, p_\perp, p_z)} \mathcal{P}_+$$

$$= S^*(p_0, p_\perp, p_z), \tag{5.88}$$

which indicates that the propagator is parity invariant in the rest frame of the magnetised heat bath. We note that other discrete symmetries can also be checked but leave them on the readers.

5.4.3. Modified Dirac equation

For General Case

The effective propagator that satisfy the modified Dirac equation with spinor U is given by

$$\left(\mathcal{P}_+ \not{L} \mathcal{P}_- + \mathcal{P}_- \not{R} \mathcal{P}_+\right) U = 0. \tag{5.89}$$

Using the chiral basis

$$\gamma_0 = \begin{pmatrix} 0 & \mathbb{1} \\ \mathbb{1} & 0 \end{pmatrix}, \qquad \vec{\gamma} = \begin{pmatrix} 0 & \vec{\sigma} \\ -\vec{\sigma} & 0 \end{pmatrix}, \qquad \gamma_5 = \begin{pmatrix} -\mathbb{1} & 0 \\ 0 & \mathbb{1} \end{pmatrix}, \qquad U = \begin{pmatrix} \psi_L \\ \psi_R \end{pmatrix}, \tag{5.90}$$

one can write (5.89) as

$$\begin{pmatrix} 0 & \sigma \cdot R \\ \bar{\sigma} \cdot L & 0 \end{pmatrix} \begin{pmatrix} \psi_L \\ \psi_R \end{pmatrix} = 0, \tag{5.91}$$

where ψ_R and ψ_L are two component Dirac spinors with $\sigma \equiv (1, \vec{\sigma})$ and $\bar{\sigma} \equiv (1, -\vec{\sigma})$, respectively. One can obtain nontrivial solutions with the condition

$$\det \begin{pmatrix} 0 & \sigma \cdot R \\ \bar{\sigma} \cdot L & 0 \end{pmatrix} = 0$$

$$\det[L \cdot \bar{\sigma}] \det[R \cdot \sigma] = 0$$

$$L^2 R^2 = 0. \tag{5.92}$$

We note that for a given p_0 $(= \omega)$, either $L^2 = 0$, or $R^2 = 0$, but not both of them are simultaneously zero. This implies that i) when $L^2 = 0$, $\psi_R = 0$; ii) when $R^2 = 0$, $\psi_L = 0$. These dispersion conditions are same as obtained from the poles of the effective propagator in (5.19) as obtained in subsec. 5.1.2.

1. For $R^2 = 0$ but $L^2 \neq 0$, the right chiral equation is given by

$$(R \cdot \sigma) \, \psi_R = 0. \tag{5.93}$$

Again $R^2 = 0 \Rightarrow R_0 = \pm|\vec{R}| = \pm\sqrt{R_x^2 + R_y^2 + R_z^2}$ and the corresponding dispersive modes are denoted by $R^{(\pm)}$. So the solutions of (5.93) are

(i) $R_0 = |\vec{R}|$; mode $R^{(+)}$; $U_{R^{(+)}} = \sqrt{\dfrac{|\vec{R}| + R_z}{2|\vec{R}|}} \begin{pmatrix} 0 \\ 0 \\ 1 \\ \frac{R_x + iR_y}{|\vec{R}| + R_z} \end{pmatrix} = \begin{pmatrix} 0 \\ \psi_R^{(+)} \end{pmatrix}$, $\qquad$ (5.94a)

(ii) $R_0 = -|\vec{R}|$; mode $R^{(-)}$; $U_{R^{(-)}} = -\sqrt{\dfrac{|\vec{R}| + R_z}{2|\vec{R}|}} \begin{pmatrix} 0 \\ 0 \\ \frac{R_x - iR_y}{|\vec{R}| + R_z} \\ -1 \end{pmatrix} = \begin{pmatrix} 0 \\ \psi_R^{(-)} \end{pmatrix}$. $\qquad$ (5.94b)

2. For $L^2 = 0$ but $R^2 \neq 0$, the left chiral equation is given by

$$(L \cdot \bar{\sigma}) \, \psi_L = 0, \tag{5.95}$$

where $L^2 = 0$ implies two conditions; $L_0 = \pm|\vec{L}| = \pm\sqrt{L_x^2 + L_y^2 + L_z^2}$ and the corresponding dispersive modes are denoted by $L^{(\pm)}$. The two solutions of (5.95) are obtained as

(i) $L_0 = |\vec{L}|$; mode $L^{(+)}$; $U_{L^{(+)}} = -\sqrt{\dfrac{|\vec{L}| + L_z}{2|\vec{L}|}} \begin{pmatrix} \frac{L_x - iL_y}{|\vec{L}| + L_z} \\ -1 \\ 0 \\ 0 \end{pmatrix} = \begin{pmatrix} \psi_L^{(+)} \\ 0 \end{pmatrix}$, $\qquad$ (5.96a)

(i) $L_0 = -|\vec{L}|$; mode $L^{(-)}$; $U_{L^{(-)}} = \sqrt{\dfrac{|\vec{L}| + L_z}{2|\vec{L}|}} \begin{pmatrix} 1 \\ \frac{L_x + iL_y}{|\vec{L}| + L_z} \\ 0 \\ 0 \end{pmatrix} = \begin{pmatrix} \psi_L^{(-)} \\ 0 \end{pmatrix}$. $\qquad$ (5.96b)

We note here that $\psi_L^{(\pm)}$ and $\psi_R^{(\pm)}$ are only chiral eigenstates but neither the spin nor the helicity eigenstates.

For lowest Landau level (LLL)

1. For $R^2_{LLL} = 0$ in (5.21b) indicates that $R_0 = \pm R_z$, $R_x = R_y = 0$. The two solutions obtained, respectively, in (A.5) and (A.6) in Appendix A are given as

$$\text{(i)} \ R_0 = R_z; \qquad \text{mode } R^{(+)}; \qquad U_{R^{(+)}} = \begin{pmatrix} 0 \\ 0 \\ 1 \\ 0 \end{pmatrix} = \begin{pmatrix} 0 \\ \chi_+ \end{pmatrix}. \tag{5.97a}$$

$$\text{(ii)} \ R_0 = -R_z; \qquad \text{mode } R^{(-)}; \qquad U_{R^{(-)}} = \begin{pmatrix} 0 \\ 0 \\ 0 \\ 1 \end{pmatrix} = \begin{pmatrix} 0 \\ \chi_- \end{pmatrix}, \tag{5.97b}$$

where $\chi_+ = \begin{pmatrix} 1 \\ 0 \end{pmatrix}$ and $\chi_- = \begin{pmatrix} 0 \\ 1 \end{pmatrix}$.

2. For LLL, $L^2_{LLL} = 0$ in (5.21a) indicates that $L_0 = \pm L_z$, $L_x = L_y = 0$. The two solutions obtained, respectively, in (A.7) and (A.8) in Appendix A are given as

$$\text{(i)} \ L_0 = L_z; \qquad \text{mode } L^{(+)}; \qquad U_{L^{(+)}} = \begin{pmatrix} 0 \\ 1 \\ 0 \\ 0 \end{pmatrix} = \begin{pmatrix} \chi_- \\ 0 \end{pmatrix}, \tag{5.98a}$$

$$\text{(i)} \ L_0 = -L_z; \qquad \text{mode } L^{(-)}; \qquad U_{L^{(-)}} = \begin{pmatrix} 1 \\ 0 \\ 0 \\ 0 \end{pmatrix} = \begin{pmatrix} \chi_+ \\ 0 \end{pmatrix}. \tag{5.98b}$$

The spin operator along the z direction is given by

$$\Sigma^3 = \sigma^{12} = \frac{i}{2}\left[\gamma^1, \gamma^2\right] = i\,\gamma^1\gamma^2 = \begin{pmatrix} \sigma^3 & 0 \\ 0 & \sigma^3 \end{pmatrix}, \tag{5.99}$$

where σ with single index denotes Pauli spin matrices whereas that with double indices denote generator of Lorentz group in spinor representation. Now,

$$\Sigma^3\, U_{R^{(\pm)}} = \begin{pmatrix} \sigma^3 & 0 \\ 0 & \sigma^3 \end{pmatrix}\begin{pmatrix} 0 \\ \chi_\pm \end{pmatrix} = \begin{pmatrix} 0 \\ \sigma^3\chi_\pm \end{pmatrix} = \pm\begin{pmatrix} 0 \\ \chi_\pm \end{pmatrix} = \pm\, U_{R^{(\pm)}}, \tag{5.100}$$

$$\Sigma^3\, U_{L^{(\pm)}} = \begin{pmatrix} \sigma^3 & 0 \\ 0 & \sigma^3 \end{pmatrix}\begin{pmatrix} \chi_\mp \\ 0 \end{pmatrix} = \begin{pmatrix} \sigma^3\chi_\mp \\ 0 \end{pmatrix} = \mp\begin{pmatrix} \chi_\mp \\ 0 \end{pmatrix} = \mp\, U_{L^{(\pm)}}. \tag{5.101}$$

So, the modes $L^{(-)}$ and $R^{(+)}$ have spins along the direction of magnetic field whereas $L^{(+)}$ and $R^{(-)}$ have spins opposite to the direction of magnetic field. Now we discuss the helicity eigenstates of the various modes in LLL. The helicity operator is defined as

$$\mathcal{H}_{\vec{p}} = \hat{\mathbf{p}} \cdot \vec{\Sigma}. \tag{5.102}$$

When a particle moves along $+z$ direction, $\hat{\mathbf{p}} = \hat{\mathbf{z}}$ and when it moves along $-z$ direction, $\hat{\mathbf{p}} = -\hat{\mathbf{z}}$.
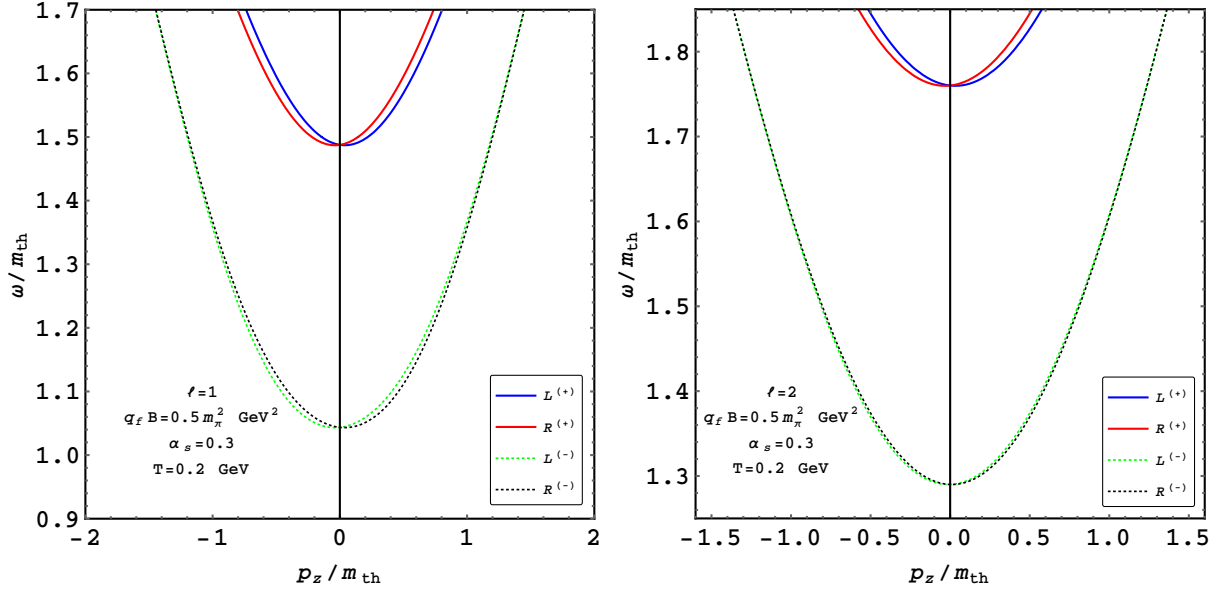
Figure 5.4: Dispersion plots for higher Landau level, $l \neq 0$ in the presence of a thermal and magnetized medium. The energy ω and momentum p_z are iscaled with the thermal mass m_{th} for convenience.

Thus

$$\mathcal{H}_{\vec{p}} = \begin{cases} \Sigma^3, & \text{for} \quad p_z > 0, \\ -\Sigma^3, & \text{for} \quad p_z < 0. \end{cases} \tag{5.103}$$

Thus,

$$\mathcal{H}_{\vec{p}} \, U_{R(\pm)} = \begin{cases} \pm U_{R(\pm)}, & \text{for} \quad p_z > 0, \\ \mp U_{R(\pm)}, & \text{for} \quad p_z < 0. \end{cases} \tag{5.104}$$

and

$$\mathcal{H}_{\vec{p}} \, U_{L(\pm)} = \begin{cases} \mp U_{L(\pm)}, & \text{for} \quad p_z > 0, \\ \pm U_{L(\pm)}, & \text{for} \quad p_z < 0. \end{cases} \tag{5.105}$$

5.4.4. Dispersion and collective behaviour of quark in weak field approximation

In presence of magnetic field, the component of momentum transverse to the magnetic field is Landau quantised and takes discrete values given by $p_\perp^2 = 2l|q_f B|$, where l is a given Landau levels. In presence of pure background magnetic field and no heat bath $(T = 0)$, the Dirac equation gives rise a dispersion relation (see section 2) as

$$E^2 = p_z^2 + m_f^2 + (2\,\nu + 1)\, q_f\, |Q| B - q_f\, Q\, B\, \sigma\,, \tag{5.106}$$

where $\nu = 0, 1, 2, \cdots$, $Q = \pm 1$, $\sigma = +1$ for spin up and $\sigma = -1$ for spin down. The solutions are classified by energy eigenvalues

$$E_l^2 = p_z^2 + m_f^2 + 2\,l\,q_f\,B\,. \tag{5.107}$$

where one can define

$$2\,l = (2\,\nu + 1)\,|Q| - Q\,\sigma\,. \tag{5.108}$$

Now, we examine the dispersion properties of fermions in a hot magnetized medium. In the general case (for higher Landau levels, $l \neq 0$), the dispersion curves are obtained by solving $L^2 = 0$ and $R^2 = 0$ numerically, as given in equations (5.20a) and (5.20b). The roots of the equation $L_0 = \pm|\vec{L}| \Rightarrow L_0 \mp |\vec{L}| = 0$, which leads to $L^{(\pm)}$ with energy $\omega_{L(\pm)}$. Similarly,
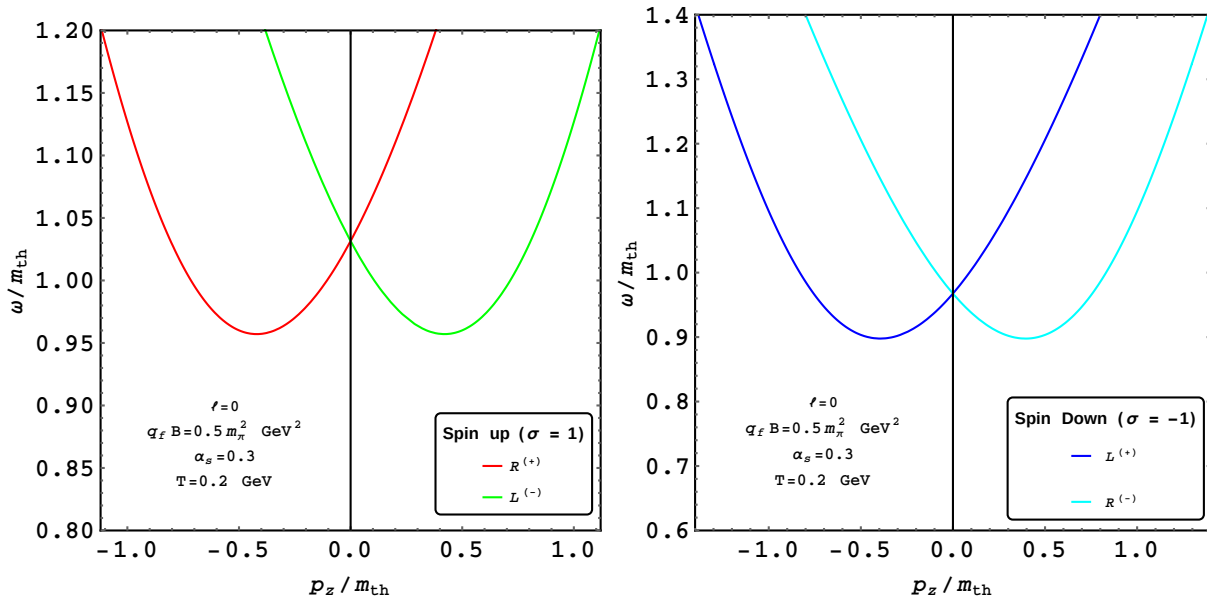
Figure 5.5: Same as Fig. 5.4 but for LLL, $l = 0$. For details see the text.

the roots of $R_0 = \pm|\vec{R}| \Rightarrow R_0 \mp |\vec{R}| = 0$, are denoted by $R^{(\pm)}$ with energy $\omega_{R^{(\pm)}}$. The corresponding eigenstates are derived in equations (5.96a), (5.96b), (5.94a), and (5.94b) in subsection 5.4.3. We have chosen $T = 0.2$ GeV, $\alpha_s = 0.3$ and $q_f B = 0.5 m_\pi^2$, where m_π is the pion mass. In Fig. 5.4, the dispersion curves for higher Landau levels are presented, showing that all four modes can propagate for a given choice of Q. This occurs because the corresponding states for these modes are neither spin nor helicity eigenstates, as discussed in subsection 5.4.3. Additionally, we note that negative energy modes exist but are not shown here.

At LLL, $l = 0$ implies $p_\perp = 0$, and the roots of $R_0 = \pm R_z$ give rise to two right-handed modes, $R^{(\pm)}$, with energy $\omega_{R^{(\pm)}}$, whereas those for $L_0 = \pm L_z$ produce [14] two left-handed modes, $L^{(\pm)}$ with energy $\omega_{L^{(\pm)}}$. The analytic solutions for the dispersion relations in LLL are presented in Appendix B, revealing four different modes, with the corresponding eigenstates derived in subsection 5.4.3. Now at LLL we discuss two possibilities below:

(i) For a positively charged fermion with $Q = 1$, $\sigma = 1$ implies $\nu = 0$ and $\sigma = -1$ implies $\nu = -1$. It is important to note that ν can never be negative, which means that modes with $Q = 1$ and $\sigma = -1$ (spin down) cannot propagate in LLL. The right-handed mode $R^{(+)}$ and the left handed mode $L^{(-)}$, both with spin up as shown in subsection 5.4.3, will propagate in LLL for $p_z > 0$. The $R^{(+)}$ mode, which has a chirality to helicity ratio of $+1$, is a quasiparticle, whereas the $L^{(-)}$ left-handed mode, with a chirality to helicity ratio of -1, is known as a plasmino (hole). However, for $p_z < 0$, the right-handed mode flips to a plasmino (hole) as its chirality to helicity ratio becomes -1, while the left-handed mode becomes a particle as its chirality to helicity ratio becomes $+1$. The dispersion behaviour of these two modes is shown in the left panel of Fig. 5.5, starting at the mass $m^{*-}_{LLL}\big|_{p_z=0}$, as given in equation (B.9).

(ii) for negatively charged fermion $Q = -1$, $\sigma = 1$ implies $\nu = -1$ and $\sigma = -1$ implies $\nu = 0$. Thus, the modes with $Q = -1$ and $\sigma = +1$ (spin up) cannot propagate in LLL. However, the modes $L^{(+)}$ and $R^{(-)}$ have spin down as found in subsec. 5.4.3 will propagate in LLL. Their dispersion are shown in the right panel of Fig. 5.5 which begin

---

[14]A general note for left-handed modes at LLL is that at small p_z, L_z is negative for LLL and becomes positive after a moderate value of p_z. This causes the left-handed modes $L^{(+)}$ and $L^{(-)}$ to flip in LLL compared to those in higher Landau levels. For further details, see Appendix B.

at mass m_{LLL}^{*+} as given in (B.9). For $p_z > 0$ the mode $L^{(+)}$ has helicity to chirality ratio $+1$ whereas $R^{(-)}$ has that of -1 and vice-versa for $p_z < 0$.
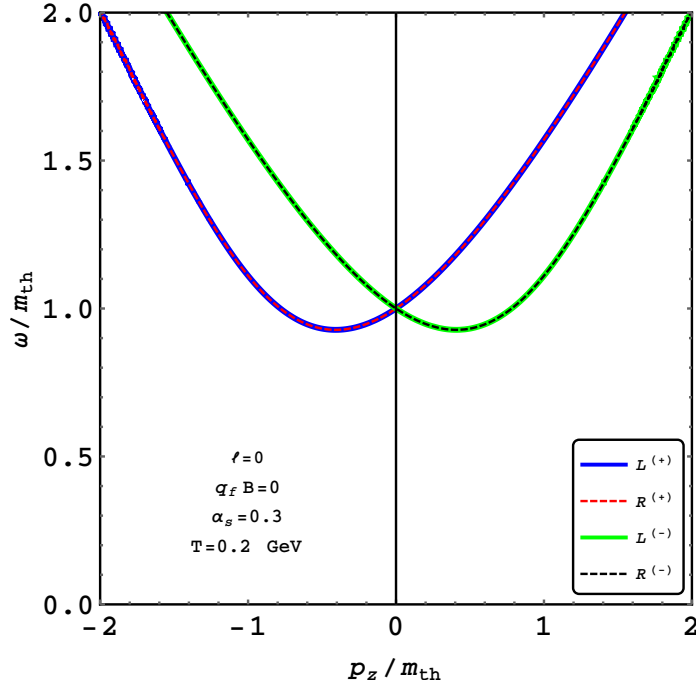

Figure 5.6: The dispersion relations in a thermal medium are described by the poles of HTL propagator in absence of magnetic field, *i.e.*, $B = 0$.

In the absence of a background magnetic field ($B = 0$), the left-handed $L^{(+)}$ and right-handed $R^{(+)}$ fermions merge, as do the left-handed $L^{(-)}$ and right-handed $R^{(-)}$ fermions. This results in degenerate, chirally symmetric modes, with dispersion curves starting at m_{th}. In this scenario, the system recovers the standard HTL result [112, 113, 155], featuring quasiparticle and plasmino modes in a heat bath, as shown in Fig. 5.6.

As seen in the dispersion plots (Figs. 5.4 and 5.5), the left- and right-handed modes remain degenerate at $p_z = 0$ in the presence of a magnetic field. However, at non-zero $|p_z|$, these modes separate, leading to a chiral asymmetry while preserving chiral invariance, as discussed in subsection 5.4.2. Additionally, as highlighted in subsection 5.4.2, the fermion propagator breaks reflection symmetry in the medium, a feature clearly illustrated in all the dispersion plots presented above.

5.4.5. Computation one-loop quark self-energy and form factors in strong field approximation

Since we will be working in strong field approximation, we confine ourselves in the lowest Landau level (LLL). In the LLL the transverse component of the momentum, $P_\perp = 0$. Thus, P^μ reduces to $P_\parallel^\mu$. $P_\parallel^\mu$ can be written as a linear combination of u^μ and n^μ. In the chiral limit the general structure of fermion self-energy in lowest Landau level can be written from Eq. (5.7) as

$$\Sigma(p_0, p_3) \;=\; -a\slashed{u} - b\slashed{n} - c\gamma_5\slashed{u} - d\gamma_5\slashed{n}, \tag{5.109}$$

where $\slashed{u} = \gamma_0$ and $\slashed{n} = \gamma^3 n_3 = \gamma^3$. Now, the various form factors can be obtained from Eqs. (5.12a) to (5.12d) as

$$a = -\frac{1}{4}\mathsf{Tr}[\Sigma\slashed{u}], \tag{5.110a}$$

66

$$b = \frac{1}{4}\text{Tr}[\Sigma \not{n}], \tag{5.110b}$$

$$c = -\frac{1}{4}\text{Tr}[\gamma_5 \Sigma \not{u}], \tag{5.110c}$$

$$d = \frac{1}{4}\text{Tr}[\gamma_5 \Sigma \not{n}]. \tag{5.110d}$$

Finally using the chirality projectors we can express the general structure of the fermion self-energy as,

$$\Sigma(P) = \mathcal{P}_R \not{A} \mathcal{P}_L + \mathcal{P}_L \not{B} \mathcal{P}_R, \tag{5.111}$$

where

$$\not{A} = -(a+c)\not{u} - (b+d)\not{n}, \tag{5.112a}$$

$$\not{B} = -(a-c)\not{u} - (b-d)\not{n}, \tag{5.112b}$$

$$\mathcal{P}_R = \frac{1}{2}(1 + \gamma_5), \tag{5.112c}$$

$$\mathcal{P}_L = \frac{1}{2}(1 - \gamma_5). \tag{5.112d}$$

Using the modified fermion propagator in strong field approximation one can straight way write down the quark self-energy in Feynman gauge from Fig. 5.7 as

$$\Sigma(P) \quad = \quad -ig^2 C_F \int \frac{d^4 K}{(2\pi)^4} \gamma_\mu S(K) \gamma^\mu \Delta(K - P), \tag{5.113}$$

where the unmodified gluonic propagator is given as

$$\Delta(K - P) = \frac{1}{(k_0 - p_0)^2 - (k - p)^2} = \frac{1}{(K - P)_\parallel^2 - (k - p)_\perp^2}. \tag{5.114}$$

and the modified fermion propagator in LLL is given by

$$iS(K) = ie^{-k_\perp^2/q_f B} \frac{\not{K}_\parallel + m_f}{K_\parallel^2 - m_f^2}(1 - i\gamma_1\gamma_2). \tag{5.115}$$
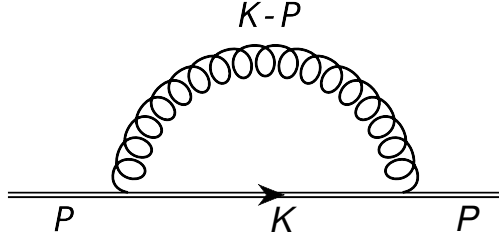

Figure 5.7: The self-energy diagram for a quark in the strong magnetic field approximation is depicted. In this diagram, the double line represents the modified quark propagator, which accounts for the effects of the strong magnetic field.

Now, the thermo-magnetic self-energy $\Sigma(P)$ can be written from Eq. (5.113) as [55]

$$-\Sigma(P) \quad = \quad -ig^2 C_F \int \frac{d^4 K}{(2\pi)^4} e^{-k_\perp^2/q_f B} \gamma_\mu \frac{(\not{K}_\parallel + m_f)}{(K_\parallel^2 - m_f^2)}(1 - i\gamma_1\gamma_2)\,\gamma^\mu \Delta(K - P)$$

$$\Sigma(P) \quad = \quad ig^2 C_F \int \frac{d^4 K}{(2\pi)^4} e^{-k_\perp^2/q_f B} \gamma_\mu \not{K}_\parallel (1 - i\gamma_1\gamma_2)\,\gamma^\mu \tilde{\Delta}_\parallel(K)\Delta(K - P)$$

$$\quad = \quad 2g^2 C_F \sum_{\{K\}}\!\!\!\!\!\!\int e^{-k_\perp^2/q_f B}\left[(1 + i\gamma_1\gamma_2)\,\not{K}_\parallel\right] \tilde{\Delta}_\parallel(K)\Delta(K - P), \tag{5.116}$$

where

$$\tilde{\Delta}_\parallel(K) = \frac{1}{k_0^2 - k_3^2} \tag{5.117}$$

Also at finite temperature, the loop integration measure is replaced by

$$\int \frac{d^4 K}{(2\pi)^4} \longrightarrow iT \sum_{\{k_0\}}\int \frac{d^3 k}{(2\pi)^3} \longrightarrow iT \sum_{\{k_0\}}\int \frac{dk_3}{2\pi}\int \frac{d^2 k_\perp}{(2\pi)^2} \quad . \tag{5.118}$$

Now the expressions of form factors for a particular flavor f become [55]

$$a = -\frac{1}{4}\mathsf{Tr}[\Sigma\slashed{\psi}] \quad = \quad -\frac{2g^2 C_F}{4}\sum_{\{K\}}\!\!\!\!\!\!\!\!\!\!\!\!\!\!\!\!\!\fint e^{-\frac{k_\perp^2}{q_f B}}\mathsf{Tr}\left[(1+i\gamma_1\gamma_2)\slashed{k}_{\shortparallel}\slashed{\psi}\right]\tilde{\Delta}_{\shortparallel}(K)\Delta(K-P)$$

$$= \quad -2g^2 C_F\sum_{\{K\}}\!\!\!\!\!\!\!\!\!\!\!\!\!\!\fint e^{-\frac{k_\perp^2}{q_f B}}k^0\tilde{\Delta}_{\shortparallel}(K)\Delta(K-P), \tag{5.119}$$

$$b = \frac{1}{4}\mathsf{Tr}[\Sigma\slashed{\eta}] \quad = \quad \frac{2g^2 C_F}{4}\sum_{\{K\}}\!\!\!\!\!\!\!\!\!\!\!\!\!\!\fint e^{-\frac{k_\perp^2}{q_f B}}\mathsf{Tr}\left[(1+i\gamma_1\gamma_2)\slashed{k}_{\shortparallel}\slashed{\eta}\right]\tilde{\Delta}_{\shortparallel}(K)\Delta(K-P)$$

$$= \quad 2g^2 C_F\sum_{\{K\}}\!\!\!\!\!\!\!\!\!\!\!\!\!\!\fint e^{-\frac{k_\perp^2}{q_f B}}k^3\tilde{\Delta}_{\shortparallel}(K)\Delta(K-P), \tag{5.120}$$

$$c = -\frac{1}{4}\mathsf{Tr}[\gamma_5\Sigma\slashed{\eta}] \quad = \quad -\frac{2g^2 C_F}{4}\sum_{\{K\}}\!\!\!\!\!\!\!\!\!\!\!\!\!\!\fint e^{-\frac{k_\perp^2}{q_f B}}\mathsf{Tr}\left[\gamma_5(1+i\gamma_1\gamma_2)\slashed{k}_{\shortparallel}\slashed{\eta}\right]\tilde{\Delta}_{\shortparallel}(K)\Delta(K-P)$$

$$= \quad -2g^2 C_F\sum_{\{K\}}\!\!\!\!\!\!\!\!\!\!\!\!\!\!\fint e^{-\frac{k_\perp^2}{q_f B}}k^3\tilde{\Delta}_{\shortparallel}(K)\Delta(K-P), \tag{5.121}$$

$$d = \frac{1}{4}\mathsf{Tr}[\gamma_5\Sigma\slashed{\psi}] \quad = \quad \frac{2g^2 C_F}{4}\sum_{\{K\}}\!\!\!\!\!\!\!\!\!\!\!\!\!\!\fint e^{-\frac{k_\perp^2}{q_f B}}\mathsf{Tr}\left[\gamma_5(1+i\gamma_1\gamma_2)\slashed{k}_{\shortparallel}\slashed{\psi}\right]\tilde{\Delta}_{\shortparallel}(K)\Delta(K-P)$$

$$= \quad 2g^2 C_F\sum_{\{K\}}\!\!\!\!\!\!\!\!\!\!\!\!\!\!\fint e^{-\frac{k_\perp^2}{q_f B}}k^0\tilde{\Delta}_{\shortparallel}(K)\Delta(K-P). \tag{5.122}$$

From the above four expression it can be noted that $b = -c$ and $d = -a$.

Transverse momentum of fermion becomes zero i.e. $P_\perp = 0$ in LLL. Thus effective fermion propagator can be written using Dyson-Schwinger equation [55] as,

$$S_{\text{eff}}(P_{\shortparallel}) = \frac{1}{\slashed{P}_{\shortparallel} - \Sigma}. \tag{5.123}$$

Subsequently the inverse fermion propagator can be written as

$$S_{\text{eff}}^{-1}(P) = \slashed{P}_{\shortparallel} - \Sigma \tag{5.124}$$

$$= \mathcal{P}_R \slashed{L}\mathcal{P}_L + \mathcal{P}_L \slashed{R}\mathcal{P}_R, \tag{5.125}$$

where

$$\slashed{L} = \slashed{P} + (a+c)\slashed{\psi} + (b+d)\slashed{\eta}, \tag{5.126}$$

$$\slashed{R} = \slashed{P} + (a-c)\slashed{\psi} + (b-d)\slashed{\eta}. \tag{5.127}$$

Now the effective propagator can be written as,

$$S_{\text{eff}}(P_{\shortparallel}) = \mathcal{P}_R\frac{\slashed{R}}{R^2}\mathcal{P}_L + \mathcal{P}_L\frac{\slashed{L}}{L^2}\mathcal{P}_R. \tag{5.128}$$

We have,

$$L^2 = (p_0 + (a+c))^2 - (p_3 - (b+d))^2, \tag{5.129}$$

$$R^2 = (p_0 + (a-c))^2 - (p_3 - (b-d))^2. \tag{5.130}$$

Now putting $a = -d$ and $b = -c$, one gets

$$L^2 = p_0^2 - p_3^2 + 2(a-b)(p_0 - p_3) = (p_0 - p_3)(p_0 + p_3 + 2(a-b)), \tag{5.131}$$

$$R^2 = p_0^2 - p_3^2 + 2(a+b)(p_0 + p_3) = (p_0 + p_3)(p_0 - p_3 + 2(a+b)). \tag{5.132}$$

Various discrete symmetries of the effective two point functions are discussed in details in Ref. [65]. The form factors are

calculated as [55]

$$a = -d = -\frac{g^2 C_F}{4\pi^2}\left[\sum_f q_f B \frac{p_0}{p_0^2 - p_3^2}\ln 2 - \sum_f (q_f B)^2 \frac{\zeta'(-2)}{2T^2}\frac{p_0(p_0^2 + p_3^2)}{(p_0^2 - p_3^2)^2}\right], \tag{5.133}$$

$$\begin{aligned}
b &= -c = \frac{g^2 C_F}{4\pi^2}\left[\sum_f q_f B \frac{p_3}{p_0^2 - p_3^2}\ln 2 - \sum_f q_f B \frac{p_3}{2T^2}\zeta'(-2)\right.\\
&\quad \left. - \sum_f (q_f B)^2 \frac{\zeta'(-2)}{T^2}\frac{p_0^2 p_3}{(p_0^2 - p_3^2)^2}\right].
\end{aligned} \tag{5.134}$$

Magnetic mass is found [55] by taking dynamic limit of R^2 and L^2 in Eq (.5.128), i.e., $R^2|_{p\to 0, p_0=0} = L^2|_{p\to 0, p_0=0}$ and is given by

$$M_{\mathrm{sfa}}^2 = \frac{g^2 C_F}{4\pi^2 T^2}\left(\sum_f (q_f B)\, T^2 \ln 4 - \sum_f (q_f B)^2 \zeta'(-2)\right). \tag{5.135}$$

One can notice that the magnetic mass is dependent on both magnetic field and temperature.

5.4.6. Dispersion and collective behaviour of a fermion in a strong field approximation

We now explore the dispersion properties of fermions in a strong and hot magnetized medium. The dispersion relations are obtained by numerically solving $L^2 = 0$ and $R^2 = 0$ as described in Eq. (5.128). These solutions yield four modes: two from $L^2 = 0$ and two from $R^2 = 0$. In the LLL approximation, however, only two modes are allowed [65], as discussed in section 2. One is an L-mode with energy ω_L corresponding to a positively charged fermion with spin up, while the other is an R-mode with energy ω_R for a negatively charged fermion with spin down. The dispersion curves for these modes are presented in Fig. 5.8. In this approximation, the transverse momentum vanishes, effectively reducing the system to two dimensions. At large p_z, both modes approach the behavior of free particles. It is also evident that the presence of the magnetic field breaks reflection symmetry[65].
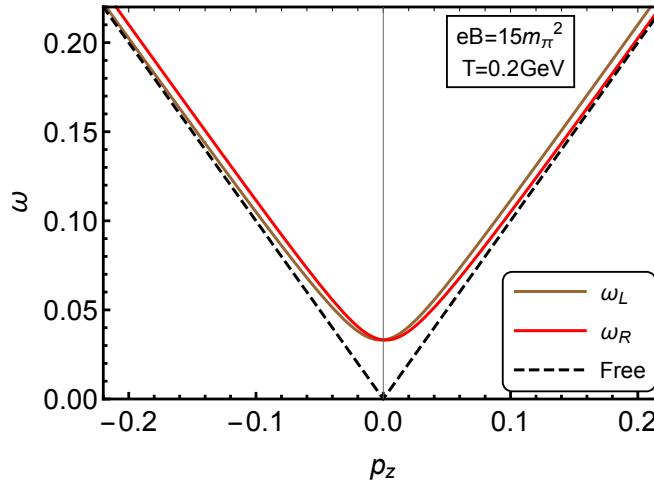

Figure 5.8: The dispersion relation of a fermion in the presence of a strong magnetic field is significantly modified due to Landau quantization and the anisotropic nature of the medium.

5.5. Collective Behaviour of Gauge Boson in Thermo-Magnetic QCD Medium

In this section we would like discuss the dispersion and collective behaviour of gluon both in strong field and weak field approximation in a a thermo-magnetic medium.

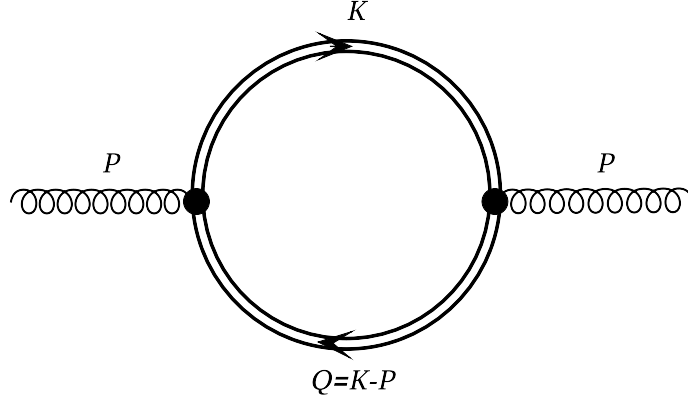### 5.5.1. One loop gluon self-energy, form factors and Debye mass in a strong field approximation

Figure 5.9: The gluon polarization tensor in the limit of strong field approximation.

In the limit of a very strong external magnetic field, $eB \to \infty$, all the Landau levels with $n \geq 1$ are pushed to infinity, leaving only the Lowest Landau Level (LLL) with $n = 0$. Under this LLL approximation in the strong field regime, the fermion propagator simplifies to the following form as

$$iS_m^s(K) = ie^{-k_\perp^2/|q_f B|} \ \frac{\slashed{K}_{\shortparallel} + m_f}{K_{\shortparallel}^2 - m_f^2}(1 - i\gamma_1\gamma_2), \tag{5.136}$$

where K represents the fermionic four-momentum, and we have utilized the properties of the generalized Laguerre polynomials, where $L_n \equiv L_n^0$ and $L_{-1}^\alpha = 0$. In the strong field approximation, or LLL, where $eB \gg k_\perp^2$, an effective dimensional reduction occurs, simplifying the system from $(3+1)$-dimensional to $(1+1)$-dimensional dynamics.

Now in the strong field limit the self-energy (Fig. 5.9) can be computed as

$$-\Pi_{\mu\nu}^s(P) = \sum_f \frac{ig^2}{2} \int \frac{d^4K}{(2\pi)^4} \mathsf{Tr}\left[\gamma_\mu S_m^s(K)\gamma_\nu S_m^s(Q)\right]$$

$$= \sum_f \frac{ig^2}{2} \int \frac{d^2k_\perp}{(2\pi)^2} \exp\left(\frac{-k_\perp^2 - q_\perp^2}{|q_f B|}\right) \int \frac{d^2K_{\shortparallel}}{(2\pi)^2} \mathsf{Tr}\left[\gamma_\mu \frac{\slashed{K}_{\shortparallel} + m_f}{K_{\shortparallel}^2 - m_f^2}(1 - i\gamma_1\gamma_2)\gamma_\nu \frac{\slashed{Q}_{\shortparallel} + m_f}{Q_{\shortparallel}^2 - m_f^2}(1 - i\gamma_1\gamma_2)\right] \tag{5.137}$$

where s indicates that the quantities are evaluated in the strong field approximation, and Tr denotes the Dirac trace. For simplicity, color indices have been omitted. It is evident that the longitudinal and transverse components are fully decoupled, allowing the Gaussian integration over the transverse momenta to be performed straightforwardly, yielding:

$$\Pi_{\mu\nu}^s(P) = -\sum_f i \ e^{-p_\perp^2/2|q_f B|} \ \frac{g^2|q_f B|}{2\pi} \int \frac{d^2K_{\shortparallel}}{(2\pi)^2} \frac{\mathcal{S}_{\mu\nu}^s}{(K_{\shortparallel}^2 - m_f^2)(Q_{\shortparallel}^2 - m_f^2)}$$

$$= \sum_f e^{-p_\perp^2/2|q_f B|} \frac{g^2|q_f B|}{2\pi} \ T \sum_{k_0} \int \frac{dk_3}{2\pi} \frac{\mathcal{S}_{\mu\nu}^s}{(K_{\shortparallel}^2 - m_f^2)(Q_{\shortparallel}^2 - m_f^2)}, \tag{5.138}$$

with the tensor structure $\mathcal{S}_{\mu\nu}^s$ that originates from the Dirac trace is

$$\mathcal{S}_{\mu\nu}^s = K_\mu^{\shortparallel} Q_\nu^{\shortparallel} + Q_\mu^{\shortparallel} K_\nu^{\shortparallel} - g_{\mu\nu}^{\shortparallel}\left((K \cdot Q)_{\shortparallel} - m_f^2\right), \tag{5.139}$$

where the Lorentz indices μ and ν are restricted to longitudinal values because of dimensional reduction to $(1+1)$ dimension and forbids to take any transverse values. Now we use Eq. (5.27a) and Eq. (5.27c) to rewrite $S_{\mu\nu}$ as

$$\mathcal{S}_{\mu\nu}^s = (k_0 u_\mu - k_3 n_\mu)(q_0 u_\nu - q_3 n_\nu) + (q_0 u_\mu - q_3 n_\mu)(k_0 u_\nu - k_3 n_\nu) - (u_\mu u_\nu - n_\mu n_\nu)\left((k \cdot q)_{\shortparallel} - m_f^2\right)$$

$$= u_\mu u_\nu \left(k_0 q_0 + k_3 q_3 + m_f^2\right) + n_\mu n_\nu \left(k_0 q_0 + k_3 q_3 - m_f^2\right) - (u_\mu n_\nu + n_\mu u_\nu)(k_0 q_3 + k_3 q_0). \tag{5.140}$$

First we evaluate the form factors in Eqs. (5.38a), (5.38b) , (5.38c) and (5.38d) in strong field approximation [66] as

$$c = R^{\mu\nu}(\Pi_{\mu\nu}^g + \Pi_{\mu\nu}^s) = c_{YM} + c_s = -\frac{C_A g^2 T^2}{3} \frac{1}{2}\left[\frac{p_0^2}{p^2} - \frac{P^2}{p^2}\mathcal{T}_P(p_0, p)\right] \text{ where } c_s = 0, \tag{5.141a}$$

$$b = B^{\mu\nu}(\Pi^g_{\mu\nu} + \Pi^s_{\mu\nu}) = b_{YM} + \frac{u^\mu u^\nu}{\bar{u}^2}\Pi^s_{\mu\nu} = b_{YM} + b_s$$

$$= -\frac{C_A g^2 T^2}{3\bar{u}^2}[1 - \mathcal{T}_P(p_0, p)] + \sum_f e^{-p_\perp^2/2|q_f B|} \; \frac{g^2|q_f B|}{2\pi\bar{u}^2} \; T\sum_{k_0}\int\frac{dk_3}{2\pi}\frac{k_0 q_0 + k_3 q_3 + m_f^2}{(K_\parallel^2 - m_f^2)(Q_\parallel^2 - m_f^2)}, \tag{5.141b}$$

$$d = d_{YM} + Q^{\mu\nu}\Pi^s_{\mu\nu} = d_{YM} + d_s$$

$$= -\frac{C_A g^2 T^2}{3}\frac{1}{2}\left[\frac{p_0^2}{p^2} - \frac{P^2}{p^2}\mathcal{T}_P(p_0, p)\right] - \sum_f e^{-p_\perp^2/2|q_f B|}\frac{g^2|q_f B|}{2\pi}\frac{p_\perp^2}{p^2} \; T\sum_{k_0}\int\frac{dk_3}{2\pi}\frac{k_0 q_0 + k_3 q_3 - m_f^2}{(K_\parallel^2 - m_f^2)(Q_\parallel^2 - m_f^2)}, \tag{5.141c}$$

$$a = \frac{1}{2}N^{\mu\nu}(\Pi^g_{\mu\nu} + \Pi^s_{\mu\nu}) = \frac{1}{2}N^{\mu\nu}\Pi^s_{\mu\nu} = a_s, \text{ where } a_{YM} = 0, \tag{5.141d}$$

where $\Pi^g_{\mu\nu}$ is the Yang-Mills(YM) contribution from ghost and gluon loop which remains unaffected in presence of magnetic field and can be written as

$$\Pi^g_{\mu\nu}(P) = \frac{N_c g^2 T^2}{3}\int\frac{d\Omega}{2\pi}\left(\frac{p_0 \hat{K}_\mu \hat{K}_\nu}{\hat{K}\cdot P} - g_{\mu 0}g_{\nu 0}\right). \tag{5.142}$$

Now, combining Eq. (5.141b) and the HTL approximation [66, 113, 119] one can have

$$b_s \approx \sum_f e^{-p_\perp^2/2|q_f B|}\frac{g^2|q_f B|}{2\pi\bar{u}^2} T\sum_{k_0}\int\frac{dk_3}{2\pi}\left[\frac{1}{(K_\parallel^2 - m_f^2)} + \frac{2\left(k_3^2 + m_f^2\right)}{(K_\parallel^2 - m_f^2)(Q_\parallel^2 - m_f^2)}\right]$$

$$= -\sum_f e^{-p_\perp^2/2|q_f B|}\frac{g^2|q_f B|}{2\pi\bar{u}^2}\int\frac{dk_3}{2\pi}\left[-\frac{n_F(E_{k_3})}{E_{k_3}} + \left\{\frac{n_F(E_{k_3})}{E_{k_3}} + \frac{p_3 k_3}{E_{k_3}}\frac{\partial n_F(E_{k_3})}{\partial k_3}\left(\frac{p_3 k_3/E_{k_3}}{p_0^2 - p_3^2(k_3/E_{k_3})^2}\right)\right\}\right]$$

$$= -\sum_f e^{-p_\perp^2/2|q_f B|}\frac{g^2|q_f B|}{2\pi\bar{u}^2}\int\frac{dk_3}{2\pi}\frac{p_3 k_3}{E_{k_3}}\frac{\partial n_F(E_{k_3})}{\partial E_{k_3}}\left(\frac{p_3 k_3/E_{k_3}}{p_0^2 - p_3^2(k_3/E_{k_3})^2}\right). \tag{5.143}$$

Using Eq. (5.141b),(5.143) in Eq. (5.37e) one also can directly calculate the Debye screening mass in QCD [66] as

$$(m_D^2)_s = -\Pi_{00}|_{p_0=0,\; \boldsymbol{p}\to 0} = -\bar{u}^2 b|_{p_0=0,\; \boldsymbol{p}\to 0} = m_D^2 + \sum_f(\delta m_{D,f}^2)_s = m_D^2 - \sum_f\frac{g^2|q_f B|}{2\pi}\int\frac{dk_3}{2\pi}\frac{\partial n_F(E_{k_3})}{\partial E_{k_3}}$$

$$= \frac{g^2 N_c T^2}{3} + \sum_f\frac{g^2|q_f B|}{2\pi T}\int_{-\infty}^{\infty}\frac{dk_3}{2\pi} n_F(E_{k_3})\left(1 - n_F(E_{k_3})\right). \tag{5.144}$$

which reduces to the expression of QED Debye mass calculated in Refs. [71, 235] without QCD factors where three distinct scales $(m_f^2, T^2$ and $eB)$ were clearly evident for massive quarks.

Now using Eq. (5.144) in Eq. (5.143) along with $E_{k_3} \sim k_3$, the form factor b can be expressed [66] in terms of m_D as

$$b = -\frac{C_A g^2 T^2}{3\bar{u}^2}[1 - \mathcal{T}_P(p_0, p)] + \sum_f e^{-p_\perp^2/2|q_f B|}\left(\frac{\delta m_{D,f}}{\bar{u}}\right)^2\frac{p_3^2}{p_0^2 - p_3^2}. \tag{5.145}$$

The form factor d then becomes [66]

$$d \approx -\frac{C_A g^2 T^2}{3}\frac{1}{2}\left[\frac{p_0^2}{p^2} - \frac{P^2}{p^2}\mathcal{T}_P(p_0, p)\right] - \sum_f e^{-p_\perp^2/2|q_f B|}\left(\frac{\delta m_{D,f}}{\bar{u}}\right)^2\frac{p_3^2}{p_0^2 - p_3^2}. \tag{5.146}$$

The form factor d_s can be calculated [66] as

$$d_s = Q^{\mu\nu}\Pi^s_{\mu\nu},$$

$$\approx \sum_f i\; e^{-p_\perp^2/2|q_f B|}\frac{g^2|q_f B|}{2\pi}\frac{p_\perp^2}{p^2}\int\frac{d^2 K_\parallel}{(2\pi)^2}\left[\frac{\left(k_0^2 + k_3^2 - m_f^2\right)}{(K_\parallel^2 - m_f^2)(Q_\parallel^2 - m_f^2)}\right],$$

$$\approx -\sum_f e^{-p_\perp^2/2|q_f B|}\; \delta m_{D,f}^2\frac{p_\perp^2}{p^2}\frac{p_3^2}{p_0^2 - p_3^2} \tag{5.147}$$

for $k_3 \sim E_{k_3}$. Now using (5.147) in (5.141c), the form factor d can be written as

$$d \approx -\frac{C_A g^2 T^2}{3}\frac{1}{2}\left[\frac{p_0^2}{p^2} - \frac{P^2}{p^2}\mathcal{T}_P(p_0, p)\right] - \sum_f e^{-p_\perp^2/2|q_f B|}\; \delta m_{D,f}^2\frac{p_\perp^2}{p^2}\frac{p_3^2}{p_0^2 - p_3^2}, \tag{5.148}$$

where $p_3 = p\cos\theta_p$ and $p_\perp = p\sin\theta_p$ as given in Eq. (5.54).

Also

$$
\begin{aligned}
2a = N^{\mu\nu}\Pi^s_{\mu\nu} &= -\sum_f i\, e^{-p_\perp^2/2|q_f B|}\,\frac{g^2|q_f B|}{2\pi\sqrt{\bar{u}^2}\sqrt{\bar{n}^2}}\int \frac{d^2 K_{\shortparallel}}{(2\pi)^2}\left[\frac{-2\frac{\bar{u}\cdot n}{\bar{u}^2}\left(k_0^2+k_3^2+m_f^2\right)+4k_0 k_3}{(K_{\shortparallel}^2-m_f^2)(Q_{\shortparallel}^2-m_f^2)}\right] \\
&= -\sum_f e^{-p_\perp^2/2|q_f B|}\,\frac{g^2|q_f B|}{2\pi\sqrt{\bar{u}^2}\sqrt{\bar{n}^2}}\int \frac{dk_3}{2\pi}\left[-2\frac{\bar{u}\cdot n}{\bar{u}^2}\frac{\partial n_F(E_{k_3})}{\partial E_{k_3}}\frac{p_3^2 k_3^2/E_{k_3}^2}{\left(p_0^2-p_3^2 k_3^2/E_{k_3}^2\right)}\right. \\
&\qquad\left. +\frac{2\partial n_F(E_{k_3})}{\partial E_{k_3}}\frac{p_0 p_3 k_3^2/E_{k_3}^2}{\left(p_0^2-p_3^2 k_3^2/E_{k_3}^2\right)}\right] \\
&\approx -\sum_f 2\, e^{-p_\perp^2/2|q_f B|}\,\frac{\sqrt{\bar{n}^2}}{\sqrt{\bar{u}^2}}\delta m_{D,f}^2\,\frac{p_0 p_3}{p_0^2-p_3^2},
\end{aligned}
\tag{5.149}
$$

where $\bar{n}^2=-p_\perp^2/p^2=-\sin^2\theta_p$ and $\bar{u}^2=-p^2/P^2$.

Also in the strong field approximation, $|eB|>T^2>m_f^2$, one can neglect the quark mass m_f, to get an analytic expression of Debye mass [66] as

$$
\begin{aligned}
(m_D^2)_s &= \frac{g^2 N_c T^2}{3}+\sum_f \frac{g^2|q_f B|}{2\pi T}\int_{-\infty}^{\infty}\frac{dk_3}{2\pi}\,n_F(k_3)\left(1-n_F(k_3)\right) \\
&= \frac{g^2 N_c T^2}{3}+\sum_f \frac{g^2|q_f B|}{4\pi^2} \\
&= m_D^2+\sum_f(\delta m_{D,f}^2)_s \\
&= m_D^2+(\delta m_D^2)_s,
\end{aligned}
\tag{5.150}
$$

5.5.2. Dispersion and collective behaviour of gluon in strong field

As discussed after Eq. (5.52), the dispersion relations for gluon in strong field approximation with LLL read [66] as

$$
P^2+c=0,
\tag{5.151a}
$$

$$
(P^2+b)(P^2+d)-a^2=(P^2-\omega_n^+)(P^2-\omega_n^-)=0,
\tag{5.151b}
$$

with

$$
\omega_{n+}=\frac{-b-d+\sqrt{(b-d)^2+4a^2}}{2},
\tag{5.152a}
$$

$$
\omega_{n-}=\frac{-b-d-\sqrt{(b-d)^2+4a^2}}{2},
\tag{5.152b}
$$

where the form factors are given, respectively, in Eqs. (5.141a), (5.145), (5.148) and (5.149).

The solutions of the three dispersion relations are referred to as the c-mode, n^+-mode and n^--mode, with corresponding energies ω_c, ω_{n+} and ω_{n-}, respectively. The dispersion plot for these gluon modes in the strong field approximation is presented in Fig. 5.10 for $|eB|=20m_\pi^2$, $T=0.2$GeV, and three propagation angles: $\theta_p=0$, $\pi/4$ and $\pi/2$. A coupling constant dependent on both the magnetic field and temperature [54] was used in the analysis. Notably, since $c_s=0$, c-mode remains unaffected by the magnetic field and propagates like the HTL transverse mode, regardless of the propagation angle, as shown in Fig.5.10. This behaviour can be understood as follows: in the strong field approximation, an effective dimensional reduction occurs from $(3+1)$ to $(1+1)$ dimensions in the Lowest Landau Level (LLL). Fermions at the LLL can only move along the direction of the external magnetic field. The electric field associated with the c-mode remains transverse to the external magnetic field, regardless of the gluon's propagation angle. Consequently, the fermions are unaffected by gluon excitations [224], leading to a vanishing quark loop contribution ($c_s=0$).

At $\theta_p=0$, the form factor a vanishes since it is proportional to $\sin\theta_p\cos\theta_p$. In this scenario, the n^- and c modes
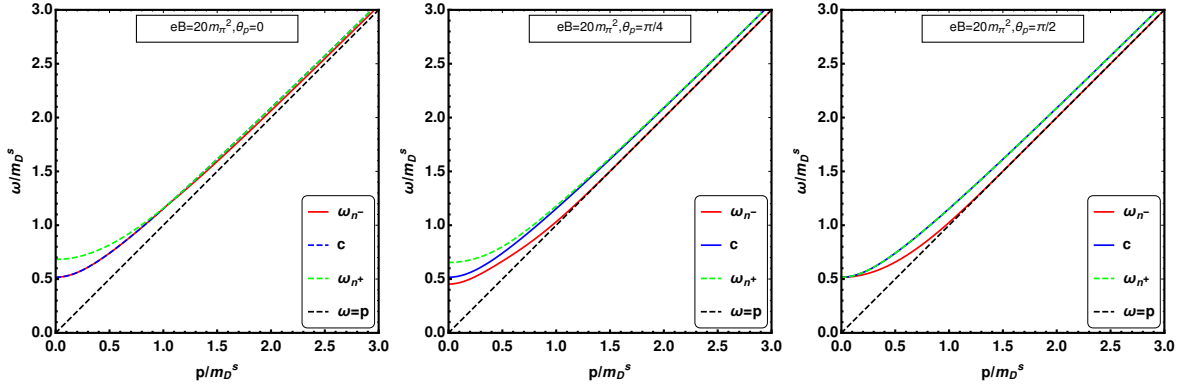
Figure 5.10: The plot illustrates the dispersion relations of the three modes (n^-, c, and n^+ modes) of a gauge boson in the strong field approximation for different propagation angles $\theta_p = 0, , \pi/4, , \pi/2$ at $eB = 20m_\pi^2$ and $T = 0.2$ GeV. The curve $\omega = p$ represents the light cone.

become degenerate, as their form factors align with the HTL transverse polarization function Π_T, excluding the quark loop contribution. This is because the form factor d in Eq. (5.148) is proportional to $\sin^2\theta_p \cos^2\theta_p$, which also vanishes at $\theta_p = 0$. As a result, both the n^- and c-modes coincide with the HTL transverse dispersion, as seen in the left panel of Fig. 5.10. This behavior can be understood as follows: when the gluon propagates along the direction of the external magnetic field ($\theta_p = 0$), the two transverse modes become rotationally symmetric about the magnetic field, leading to their degeneracy. The corresponding electric fields of the n^- and c modes remain perpendicular to the external magnetic field. Since fermions in the LLL can only move along the magnetic field, these transverse electric fields cannot excite them [224], resulting in a vanishing quark loop contribution, as noted earlier. In addition to these two transverse modes, a longitudinal excitation n^+ also exists at $\theta_p = 0$.

At an intermediate propagation angle, such as $\theta_p = \pi/4$, the degeneracy of the transverse modes is lifted, as shown in the middle panel of Fig.5.10. In this case, both transverse and longitudinal modes can excite fermions since their associated electric fields are no longer orthogonal to the external magnetic field. As the propagation angle increases, the pole corresponding to the n^--mode shifts from the transverse channel and gradually approaches the longitudinal channel [224]. At $\theta_p = \pi/2$,, the form factor a in Eq. (5.149) and the quark contribution to the form factor d in Eq. (5.148) vanish due to their dependence on θ_p. Consequently, the n^--mode merges with the HTL longitudinal mode, while then^+ mode merges with the c-mode. This behaviour is depicted in the right panel of Fig. 5.10.

5.5.3. One loop gluon self-energy, form factors and Debye mass in a weak field approximation

The fermion propagator in a weak magnetic field, *i.e.*, $\sqrt{|eB|} < (K \sim T)$ and m_f, can be written up to $\mathcal{O}[(eB)^2]$ as

$$
\begin{aligned}
iS_m^w(K) &= i\frac{\slashed{K} + m_f}{K^2 - m_f^2} + i\,(q_f B)\frac{(\gamma_5\{(K\cdot n)\slashed{u} - (K\cdot u)\slashed{n}\} + i\gamma_1\gamma_2 m_f)}{(K^2 - m_f^2)^2} \\
&+ i\,2(q_f B)^2\left[\frac{\{(K\cdot u)\slashed{u} - (K\cdot n)\slashed{n}\} - \slashed{K}}{(K^2 - m_f^2)^3} - \frac{k_\perp^2(\slashed{K} + m_f)}{(K^2 - m_f^2)^4}\right] + \mathcal{O}\left[(eB)^3\right] \\
&= S_0 + S_1 + S_2 + \mathcal{O}[(eB)^3],
\end{aligned}
\tag{5.153}
$$

where S_0 represents the continuum free field propagator in the absence of the external magnetic field B, while S_1 and S_2 are the correction terms of orders $\mathcal{O}[(eB)]$ and $\mathcal{O}[(eB)^2]$ respectively, in the presence of the magnetic field. The contribution to the gluon self-energy due to the quark loop can be derived from the Feynman diagram shown in Fig. 5.11,

and is given by the expression as [66].

$$\Pi_{\mu\nu}^{w,q}(P) \quad = \quad \sum_f \frac{ig^2}{2} \int \frac{d^4K}{(2\pi)^4} \text{Tr}\left[\gamma_\mu S_m^w(K)\gamma_\nu S_m^w(Q)\right]. \tag{5.154}$$
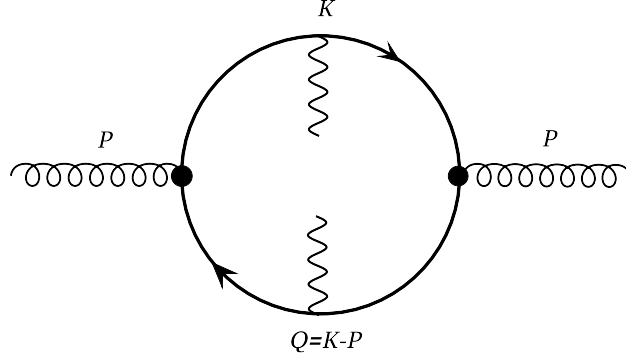

Figure 5.11: The $(eB)^2$ order correction to the gluon polarization tensor ($\delta\Pi_{\mu\nu}^a$) within the weak field approximation.
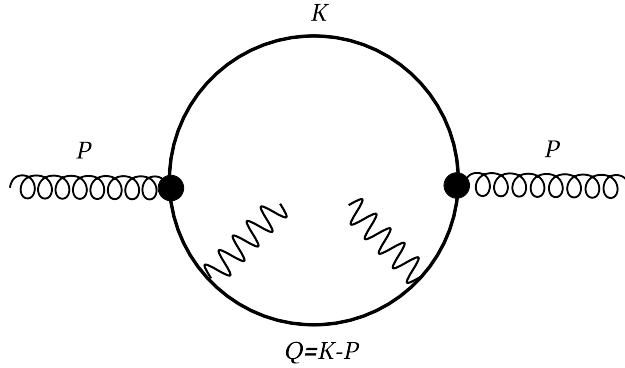

Figure 5.12: The $(eB)^2$ order correction to the gluon polarization tensor ($\delta\Pi_{\mu\nu}^b$) within the weak field approximation.

We have suppressed the colour indices here for convenience. Using Eq.(5.153), the self-energy in the weak field approximation up to $\mathcal{O}[(eB)^2]$, along with the pure Yang-Mills (YM) contribution, the total gluon self-energy in the weak field approximation can be decomposed as [66]

$$\Pi_{\mu\nu}^w(P) = \Pi_{\mu\nu}^g(P) + \Pi_{\mu\nu}^0(P) + \delta\Pi_{\mu\nu}^a(P) + 2\delta\Pi_{\mu\nu}^b(P) + \mathcal{O}[(eB)^3], \tag{5.155}$$

where the first term, $\Pi_{\mu\nu}^g$, represents the YM contribution, which is given in Eq. (5.142). The last three terms in Eq. (5.155) arise from the expansion of the quark loop contribution to the gluon self-energy. The term $\Pi_{\mu\nu}^0$, which involves two S_0, corresponds to the leading-order perturbative term in the absence of the magnetic field B. The remaining two terms are $\mathcal{O}[(eB)^2]$ corrections, as depicted in Fig. 5.11 and Fig. 5.12. However, it is important to note that the $\mathcal{O}[(eB)]$ term vanishes according to Furry's theorem. This is because the expectation value of any odd number of electromagnetic currents must vanish due to charge conjugation symmetry.

Now the second and third terms in Eq. (5.155) can be written as [66]

$$\begin{aligned} \Pi_{\mu\nu}^0(P) \quad &= \quad -\sum_f \frac{ig^2}{2} \int \frac{d^4K}{(2\pi)^4} \text{Tr}\left[\gamma_\mu S_0(K)\gamma_\nu S_0(Q)\right] \\ &= \quad -\sum_f \frac{ig^2}{2} \int \frac{d^4K}{(2\pi)^4} \left[8K_\mu K_\nu - 4K^2 g_{\mu\nu}\right] \frac{1}{(K^2 - m_f^2)(Q^2 - m_f^2)}, \end{aligned} \tag{5.156}$$

$$\delta\Pi^a_{\mu\nu}(P) = -\sum_f \frac{ig^2}{2} \int \frac{d^4K}{(2\pi)^4} \text{Tr}\left[\gamma_\mu S_1(K)\gamma_\nu S_1(Q)\right],$$

$$= -\sum_f \frac{ig^2}{2}(q_f B)^2 \int \frac{d^4K}{(2\pi)^4} \frac{U_{\mu\nu}}{(K^2 - m_f^2)^2(Q^2 - m_f^2)^2}, \tag{5.157}$$

In the numerator, we have neglected the mass of the quark and the external momentum P due to the HTL approximation. The tensor structure of the self-energy correction in the weak field approximation can be written as [66]

$$U_{\mu\nu} = 4(K \cdot u)(Q \cdot u)\left(2n_\mu n_\nu + g_{\mu\nu}\right) + 4(K \cdot n)(Q \cdot n)\left(2u_\mu u_\nu - g_{\mu\nu}\right)$$

$$-4\left[(K \cdot u)(Q \cdot n) + (K \cdot n)(Q \cdot u)\right](u_\mu n_\nu + u_\nu n_\mu) + 4m_f^2 g_{\mu\nu}$$

$$+8m_f^2\left(g_{1\mu}g_{1\nu} + g_{2\mu}g_{2\nu}\right). \tag{5.158}$$

The fourth term in Eq. (5.155) can be written as [66]

$$\delta\Pi^b_{\mu\nu}(P) = -\sum_f \frac{ig^2}{2} \int \frac{d^4K}{(2\pi)^4} \text{Tr}\left[\gamma_\mu S_2(K)\gamma_\nu S_0(Q)\right]$$

$$= -\sum_f ig^2(q_f B)^2 \int \frac{d^4K}{(2\pi)^4}\left[\frac{X_{\mu\nu}}{(K^2 - m_f^2)^3(Q^2 - m_f^2)} - \frac{(K_\parallel^2 - m_f^2)W_{\mu\nu}}{(K^2 - m_f^2)^4(Q^2 - m_f^2)}\right] \tag{5.159}$$

where

$$X_{\mu\nu} = 4\left[(K \cdot u)(u_\mu Q_\nu + u_\nu Q_\mu) - (K \cdot n)(n_\mu Q_\nu + n_\nu Q_\mu)\right.$$

$$+ \left.\left\{(K \cdot n)(Q \cdot n) - (K \cdot u)(Q \cdot u) + m_f^2\right\} g_{\mu\nu}\right], \tag{5.160a}$$

$$W_{\mu\nu} = 4\left(K_\mu Q_\nu + Q_\mu K_\mu\right) - 4\left(K \cdot Q - m_f^2\right)g_{\mu\nu}. \tag{5.160b}$$

1. Computation of form factors and Debye mass of $\mathcal{O}\left[(eB)^0\right]$

In this subsection, we calculate the $\mathcal{O}\left[(eB)^0\right]$ terms in the form factors b, c, d in the weak magnetic field limit which are denoted by b_0, c_0, d_0, respectively.

The form factor b_0 in absence of magnetic field can be written from Eq. (5.37e) as

$$b_0(p_0, p) = \frac{1}{\bar{u}^2}\left[\Pi^g_{00}(P) + \Pi^0_{00}(P)\right]. \tag{5.161}$$

where

$$\Pi^0_{00}(P) = -\sum_f \frac{ig^2}{2} \int \frac{d^4K}{(2\pi)^4}\left[8k_0^2 - 4K^2\right]\frac{1}{(K^2 - m_f^2)(Q^2 - m_f^2)}. \tag{5.162}$$

Using the hard thermal loop (HTL) approximation [66, 108, 113] and performing the frequency sum, one can write

$$\Pi^0_{00}(P) = 2g^2 N_f \int \frac{k^2 dk}{2\pi^2}\frac{dn_F(k)}{dk}\int \frac{d\Omega}{4\pi}\left(1 - \frac{p_0}{P \cdot \hat{K}}\right), \tag{5.163}$$

for $m_f = 0$.

Now the QCD Debye mass in the absence of the magnetic field can directly be obtained using Eq. (5.37e) as

$$m_D^2 = -\Pi^0_{00}\Big|_{\substack{p_0=0 \\ \mathbf{p}\to 0}} = -\bar{u}^2 b_0\Big|_{\substack{p_0=0 \\ \mathbf{p}\to 0}} = \frac{N_c g^2 T^2}{3} - 2N_f g^2 \int \frac{k^2 dk}{2\pi^2}\frac{dn_F(k)}{dk} = \frac{g^2 T^2}{3}\left(N_c + \frac{N_f}{2}\right). \tag{5.164}$$

Using Eq. (5.164) in Eq. (5.163), we get

$$\Pi^0_{00}(P) = -\frac{N_f g^2 T^2}{6}\int \frac{d\Omega}{4\pi}\left(1 - \frac{p_0}{p_0 - \mathbf{p} \cdot \hat{\mathbf{k}}}\right) = -\frac{N_f g^2 T^2}{6}\left(1 - \frac{p_0}{2p}\log\frac{p_0 + p}{p_0 - p}\right), \tag{5.165}$$

where we use $p = \sqrt{p_1^2 + p_3^2}$ as p lies in xz plane as shown Fig. 5.2. The form factor in Eq. (5.161) becomes

$$b_0(p_0, p) = -\frac{m_D^2}{\bar{u}^2}\left(1 - \frac{p_0}{2p}\log\frac{p_0 + p}{p_0 - p}\right), \tag{5.166}$$

which agrees with the HTL longitudinal form factor $\Pi_L(p_0, p)$ [66, 108, 112, 113].

Similarly, we will calculate here the coefficients c_0 and d_0 explicitly.

$$c_0(p_0, p) = R^{\mu\nu}\left[\Pi^g_{\mu\nu}(P) + \Pi^0_{\mu\nu}(P)\right]$$

$$= (\Pi^g)^\mu_\mu(P) + (\Pi^0)^\mu_\mu(P) + \frac{1}{p_\perp^2}\Big[\left(p_0^2 - p_\perp^2\right)\left\{\Pi^g_{00}(P) + \Pi^0_{00}(P)\right\}$$
$$+ p^2\left\{\Pi^g_{33}(P) + \Pi^0_{33}(P)\right\} - 2p_0p_3\left\{\Pi^g_{03}(P) + \Pi^0_{03}(P)\right\}\Big], \tag{5.167}$$

and

$$d_0(p_0, p) = Q^{\mu\nu}\Big[\Pi^g_{\mu\nu}(P) + \Pi^0_{\mu\nu}(P)\Big]$$
$$= -\frac{p^2}{p_\perp^2}\left[\left\{\Pi^g_{33}(P) + \Pi^0_{33}(P)\right\} - \frac{2p_0p_3}{p^2}\left\{\Pi^g_{03}(P) + \Pi^0_{03}(P)\right\}\right.$$
$$\left. + \frac{p_0^2 p_3^2}{p^4}\left\{\Pi^g_{00}(P) + \Pi^0_{00}(P)\right\}\right]. \tag{5.168}$$

Now from Eq. (5.142), we can write [66]

$$\Pi^g_{00}(P) = -\frac{N_c\, g^2 T^2}{3}\left(1 - \frac{p_0}{2p}\log\frac{p_0 + p}{p_0 - p}\right), \tag{5.169}$$

$$\Pi^g_{03}(P) = -\frac{N_c\, g^2 T^2}{3}\frac{p_0 p_3}{p^2}\left(1 - \frac{p_0}{2p}\log\frac{p_0 + p}{p_0 - p}\right), \tag{5.170}$$

$$\Pi^g_{33}(P) = -\frac{N_c\, g^2 T^2}{3}\frac{3p_3^2 - p^2}{p^2}\frac{p_0^2}{2p^2}\left(1 - \frac{p_0}{2p}\log\frac{p_0 + p}{p_0 - p}\right) - \frac{N_c\, g^2 T^2}{3}\frac{p_3^2 - p^2}{2p^2}\frac{p_0}{2p}\log\frac{p_0 + p}{p_0 - p}. \tag{5.171}$$

We note that 00 component from the quark contribution Π^0_{00} is already calculated in Eq. (5.165) and one needs to calculate [66] the remaining two components of $\Pi^0_{\mu\nu}(P)$ which are as follows:

$$\Pi^0_{03}(P) = -\sum_f \frac{ig^2}{2}\int \frac{d^4K}{(2\pi)^4}\frac{8k_0 k_3}{K^2 Q^2} = \frac{N_f g^2 T^2}{6}\int\frac{d\Omega}{4\pi}\frac{p_0 \hat{k}_3}{P\cdot\hat{K}}$$
$$= -\frac{N_f g^2 T^2}{6}\frac{p_0 p_3}{p^2}\left(1 - \frac{p_0}{2p}\log\frac{p_0 + p}{p_0 - p}\right), \tag{5.172}$$

and

$$\Pi^0_{33}(P) = -\sum_f \frac{ig^2}{2}\int\frac{d^4K}{(2\pi)^4}\frac{8k_3^2 + 4K^2}{(K^2 - m_f^2)(Q^2 - m_f^2)} = \frac{N_f g^2 T^2}{6}\int\frac{d\Omega}{4\pi}\frac{p_0 \hat{k}_3^2}{P\cdot\hat{K}}$$
$$= -\frac{N_f g^2 T^2}{6}\frac{3p_3^2 - p^2}{p^2}\frac{p_0^2}{2p^2}\left(1 - \frac{p_0}{2p}\log\frac{p_0 + p}{p_0 - p}\right) + \frac{N_f g^2 T^2}{6}\frac{p_3^2 - p^2}{2p^2}\frac{p_0}{2p}\log\frac{p_0 + p}{p_0 - p}. \tag{5.173}$$

Using the results from Eqs. (5.165), (5.169) - (5.173), $c_0(p_0, p)$ and $d_0(p_0, p)$ become

$$c_0(p_0, p) = d_0(p_0, p) = -\frac{m_D^2}{2p^2}\left[p_0^2 - \left(p_0^2 - p^2\right)\frac{p_0}{2p}\log\frac{p_0 + p}{p_0 - p}\right], \tag{5.174}$$

which agrees with the HTL transverse form factor $\Pi_T(p_0, p)$ [66, 108, 112, 113].

This implies that the zero magnetic field contribution of the fourth form factor a should vanish. Below we obtain the same from Eqs. (5.38d) and (5.156) as [66],

$$a_0 = \frac{1}{2}N^{\mu\nu}\Big[\Pi^g_{\mu\nu} + \Pi^0_{\mu\nu}\Big]$$
$$= \frac{1}{2\sqrt{\bar{u}^2}\sqrt{\bar{n}^2}}\left[u^\mu n^\nu + n^\mu u^\nu - 2\frac{\bar{u}\cdot n}{\bar{u}^2}\bar{u}^\mu\bar{u}^\nu\right]\Big[\Pi^g_{\mu\nu} + \Pi^0_{\mu\nu}\Big]$$
$$= \frac{1}{2\sqrt{\bar{u}^2}\sqrt{\bar{n}^2}}\left[-2\frac{\bar{u}\cdot n}{\bar{u}^2}\Big[\Pi^g_{00} + \Pi^0_{00}\Big] + 2\Big[\Pi^g_{03} + \Pi^0_{03}\Big]\right]$$
$$= 0 \tag{5.175}$$

2. Computation of form factors and Debye mass of $\mathcal{O}\left[(eB)^2\right]$

In this subsection, we calculate the $\mathcal{O}\left[(eB)^2\right]$ coefficients of b, c, d, a which are denoted by b_2, c_2, d_2, a_2, respectively. The form factor b_2, i.e., $\mathcal{O}(eB)^2$ term of the coefficient b, has been computed in as [66],

$$b_2 = \frac{1}{\bar{u}^2}\Big[\delta\Pi^a_{00}(P) + 2\delta\Pi^b_{00}(P)\Big]$$
$$= -\frac{\delta m_D^2}{\bar{u}^2} - \sum_f \frac{g^2(q_f B)^2}{\bar{u}^2\pi^2}\left[\left(g_k + \frac{\pi m_f - 4T}{32 m_f^2 T}\right)(A_0 - A_2)\right.$$

$$+ \left(f_k + \frac{8T - \pi m_f}{128 m_f^2 T} \right) \left(\frac{5 A_0}{3} - A_2 \right) \Bigg]. \tag{5.176}$$

where one obtains [66]

$$f_k = -\sum_{l=1}^{\infty} (-1)^{l+1} \frac{l^2}{16 T^2} K_2 \left(\frac{m_f l}{T} \right), \tag{5.177a}$$

$$g_k = \sum_{l=1}^{\infty} (-1)^{l+1} \frac{l}{4 m_f T} K_1 \left(\frac{m_f l}{T} \right). \tag{5.177b}$$

$$A_0 = \int \frac{d\Omega}{4\pi} \frac{p_0}{P \cdot \hat{K}} = \frac{p_0}{2p} \log \left(\frac{p_0 + p}{p_0 - p} \right), \tag{5.177c}$$

$$A_2 = \int \frac{d\Omega}{4\pi} \frac{c^2 p_0}{P \cdot \hat{K}} = \frac{p_0^2}{2p^2} \left(1 - \frac{3 p_3^2}{p^2} \right) \left(1 - \frac{p_0}{2p} \log \frac{p_0 + p}{p_0 - p} \right) + \frac{1}{2} \left(1 - \frac{p_3^2}{p^2} \right) \frac{p_0}{2p} \log \frac{p_0 + p}{p_0 - p}. \tag{5.177d}$$

and also the Debye screening mass of $\mathcal{O}(eB)^2$ as [66],

$$\delta m_D^2 = -\sum_f \frac{g^2}{3\pi^2} (q_f B)^2 \left[\left(\frac{\partial}{\partial (m_f^2)} \right)^2 + m_f^2 \left(\frac{\partial}{\partial (m_f^2)} \right)^3 \right]$$

$$\times m_f^2 \sum_{l=1}^{\infty} (-1)^{l+1} \left[K_2 \left(\frac{m_f l}{T} \right) - K_0 \left(\frac{m_f l}{T} \right) \right]$$

$$= \frac{g^2}{12\pi^2 T^2} \sum_f (q_f B)^2 \sum_{l=1}^{\infty} (-1)^{l+1} l^2 K_0 \left(\frac{m_f l}{T} \right). \tag{5.178}$$

We obtain $\mathcal{O}(eB)^2$ term of the coefficient c as [66],

$$c_2 = R^{\mu\nu} (\delta \Pi_{\mu\nu}^a + 2 \delta \Pi_{\mu\nu}^b)$$

$$= \sum_f \frac{4 g^2 (q_f B)^2}{3\pi^2} g_k + \sum_f \frac{g^2 (q_f B)^2}{2\pi^2} \left(g_k + \frac{\pi m_f - 4T}{32 m_f^2 T} \right) \times \left[-\frac{7}{3} \frac{p_0^2}{p_\perp^2} + \left(2 + \frac{3}{2} \frac{p_0^2}{p_\perp^2} \right) A_0 \right.$$

$$\left. + \left(\frac{3}{2} + \frac{5}{2} \frac{p_0^2}{p_\perp^2} + \frac{3}{2} \frac{p_3^2}{p_\perp^2} \right) A_2 - \frac{3 p_0 p_3}{p_\perp^2} A_1 - \frac{5}{2} \left(1 - \frac{p_3^2}{p_\perp^2} \right) A_4 - \frac{5 p_0 p_3}{p_\perp^2} A_3 \right], \tag{5.179}$$

where

$$A_1 = \int \frac{d\Omega}{4\pi} \frac{c p_0}{P \cdot \hat{K}} = -\frac{p_0 p_3}{p^2} \left[1 - \frac{p_0}{2p} \log \left(\frac{p_0 + p}{p_0 - p} \right) \right],$$

$$A_3 = \int \frac{d\Omega}{4\pi} \frac{c^3 p_0}{P \cdot \hat{K}} = \frac{p_0}{2p} \frac{p_3}{p} \left(1 - \frac{5}{3} \frac{p_3^2}{p^2} \right) - \frac{3}{2} \frac{p_0}{p} \frac{p_3}{p} \left(1 - \frac{p_0^2}{p^2} - \frac{p_3^2}{p^2} + \frac{5}{3} \frac{p_0^2}{p^2} \frac{p_3^2}{p^2} \right) \left(1 - \frac{p_0}{2p} \log \frac{p_0 + p}{p_0 - p} \right),$$

$$A_4 = \int \frac{d\Omega}{4\pi} \frac{c^4 p_0}{P \cdot \hat{K}} = \frac{3}{8} \left(1 - \frac{p_3^2}{p^2} \right)^2 - \frac{p_0^2}{8 p^2} \left(1 - \frac{5 p_3^2}{p^2} \right)^2 + \frac{5}{3} \frac{p_0^2}{p^2} \frac{p_3^4}{p^4}$$

$$- \frac{3}{8} \left\{ \left(1 - \frac{p_0^2}{p^2} \right)^2 - \frac{2 p_3^2}{p^2} \left(1 - \frac{3 p_0^2}{p^2} \right)^2 + \frac{p_3^4}{p^4} \left(1 - \frac{5 p_0^2}{p^2} \right)^2 + \frac{8 p_0^4}{p^4} \frac{p_3^2}{p^2} \left(1 - \frac{5 p_3^2}{3 p^2} \right) \right\} \left(1 - \frac{p_0}{2p} \log \frac{p_0 + p}{p_0 - p} \right). \tag{5.180a}$$

We calculate the $\mathcal{O}(eB)^2$ term of the coefficient d as

$$d_2 = Q^{\mu\nu} (\delta \Pi_{\mu\nu}^a + 2 \delta \Pi_{\mu\nu}^b) = F_1 + F_2, \tag{5.181}$$

where expressions for F_1 and F_2 can be found as [66].

$$F_1 = \sum_f \frac{g^2 (q_f B)^2 p^2}{\pi^2 p_\perp^2} \left[-g_k \left\{ -\frac{p_0^2 p_3^2}{3 p^4} - \frac{A_0}{4} + \left(\frac{3}{2} + \frac{p_0^2 p_3^2}{p^4} \right) A_2 - \frac{5}{4} A_4 \right\} \right.$$

$$+ \left(\frac{\pi}{32 m_f T} - \frac{1}{8 m_f^2} \right) \left\{ \frac{A_0}{4} - \left(\frac{3}{2} + \frac{p_0^2 p_3^2}{p^4} \right) A_2 + \frac{5}{4} A_4 \right\}$$

$$\left. - f_k \frac{p_0^2 p_3^2}{p^4} \left(\frac{14}{3} - 5 A_0 + A_2 \right) + \frac{p_0^2 p_3^2}{p^4} \frac{8T - \pi m_f}{128 T m_f^2} (5 A_0 - A_2) \right], \tag{5.182}$$

77

$$
\begin{aligned}
F_2 &= \sum_f \frac{2ig^2(q_f B)^2 p^2}{p_\perp^2} \frac{2}{3} \frac{p^0 p^3}{p^2} \int \frac{d^4 K}{(2\pi)^4} \left(-\frac{\partial^2}{\partial\left(m_f^2\right)^2} + k^2\left(1-c^2\right)\frac{\partial^3}{\partial\left(m_f^2\right)^3} \right) \\
&\quad \times \frac{k_0 k c}{(K^2 - m_f^2)(Q^2 - m_f^2)} \\
&= \sum_f \frac{g^2(q_f B)^2}{6\pi^2 m_f T} \frac{p^0 p^3}{p_\perp^2} \frac{1}{1 + \cosh\frac{m_f}{T}} \left(\frac{3A_1}{2} - A_3 \right).
\end{aligned}
\tag{5.183}
$$

The $\mathcal{O}(eB)^2$ term of the coefficient a is calculated as [66].

$$
a_2 = N^{\mu\nu}(\delta\Pi^a_{\mu\nu} + 2\delta\Pi^b_{\mu\nu}) = G_1 + G_2,
\tag{5.184}
$$

where G_1 and G_2 are given as [66].

$$
\begin{aligned}
G_1 &= -\sum_f \frac{4g^2(q_f B)^2}{\sqrt{\bar{u}^2}\sqrt{\bar{n}^2}} \int \frac{k^2 dk}{2\pi^2} \int \frac{d\Omega}{4\pi} \frac{p_0 p_3}{p^2} \left[(-1+c^2)\frac{\partial}{\partial(m_f^2)} - \frac{1}{6}(5-3c^2)m_f^2 \frac{\partial^2}{\partial(m_f^2)^2} \right] \\
&\quad \times \left\{ -\frac{\partial}{\partial\left(m_f^2\right)}\frac{n_F}{E_k}\left(1 - \frac{p_0}{P\cdot\hat{K}}\right) + \frac{n_F}{2E_k^3}\frac{p_0}{P\cdot\hat{K}} \right\} \\
&= -\sum_f \frac{4g^2(q_f B)^2}{\sqrt{\bar{u}^2}\sqrt{\bar{n}^2}} \int \frac{k^2 dk}{2\pi^2} \left[\frac{p_0 p_3}{p^2} \left\{ \left(\frac{2}{3} - A_0 + A_2\right)\frac{\partial^2}{\partial(m_f^2)^2} + \left(\frac{2}{3} - \frac{5A_0}{6} + \frac{A_2}{2}\right)m_f^2\frac{\partial^3}{\partial(m_f^2)^3} \right\} \right. \\
&\quad \left. \times \frac{n_F}{E_k} + \left\{ \left(-A_0 + A_2\right)\frac{\partial}{\partial(m_f^2)} - \frac{1}{6}\left(5A_0 - 3A_2\right)m_f^2\frac{\partial^2}{\partial(m_f^2)^2} \right\}\frac{n_F}{2E_k^3} \right] \\
&= -\sum_f \frac{4g^2(q_f B)^2}{2\pi^2\sqrt{\bar{u}^2}\sqrt{\bar{n}^2}} \left[\frac{p_0 p_3}{p^2} \left\{ \left(\frac{2}{3} - A_0 + A_2\right)g_k + \left(\frac{4}{3} - \frac{5A_0}{3} + A_2\right)f_k \right\} \right. \\
&\quad \left. + \left\{ \left(-A_0 + A_2\right)\frac{\pi m_f - 4T}{32 T m_f^2} - \frac{1}{6}\left(5A_0 - 3A_2\right)\frac{8T - \pi m_f}{64 T m_f^2} \right\} \right].
\end{aligned}
\tag{5.185}
$$

$$
\begin{aligned}
G_2 &= \sum_f \frac{8g^2(q_f B)^2}{\sqrt{\bar{u}^2}\sqrt{\bar{n}^2}} \int \frac{k^2 dk}{2\pi^2} \int \frac{d\Omega}{4\pi} \left[\frac{kc}{6}\frac{\partial^2}{\partial(m_f^2)^2} - \frac{k^3(c-c^3)}{3}\frac{\partial^3}{\partial(m_f^2)^3} \right] \frac{\partial n_F(E_k)}{\partial(m_f^2)}\left(1 - \frac{p_0}{P\cdot\hat{K}}\right) \\
&= -\sum_f \frac{g^2(q_f B)^2}{\sqrt{\bar{u}^2}\sqrt{\bar{n}^2}6\pi^2 m_f T\left(1 + \cosh\frac{m_f}{T}\right)}\left(-5A_1 + 4A_3\right).
\end{aligned}
\tag{5.186}
$$

5.5.4. Dispersion and collective behaviour of gluon in weak field

In weak field approximation the dispersion relation can now be written as

$$
P^2 + c = P^2 + c_0 + c_2 = P^2 + \Pi_T + c_2 = 0,
\tag{5.187a}
$$

$$
\begin{aligned}
(P^2 + b)(P^2 + d) - a^2 &= (P^2 + b_0 + b_2)(P^2 + d_0 + d_2) - a_2^2 = (P^2 + \Pi_L + b_2)(P^2 + \Pi_T - d_2) + a_2^2 \\
&= \left(P^2 - \frac{-b_0 - b_2 - d_0 - d_2 + \sqrt{(b_0 + b_2 - d_0 - d_2)^2 + 4a_2^2}}{2} \right) \\
&\quad \times \left(P^2 - \frac{-b_0 - b_2 - d_0 - d_2 - \sqrt{(b_0 + b_2 - d_0 - d_2)^2 + 4a_2^2}}{2} \right) = 0
\end{aligned}
\tag{5.187b}
$$

which give rise to c, n^+ and n^- dispersive modes with energies ω_c, ω_{n^+} and ω_{n^-} respectively.

In this section, we assume that the magnetic field is the smallest scale and compute all quantities up to $\mathcal{O}[(eB)^2]$. Under this approximation, Eq. (5.187b) simplifies to:

$$
\left(P^2 + b_0 + b_2\right)\left(P^2 + d_0 + d_2\right) = 0.
\tag{5.188}
$$

Since there is no contribution of $\mathcal{O}[(eB)^2]$ from a_2, and it starts contributing only at $\mathcal{O}[(eB)^4]$ a_2 can be safely neglected

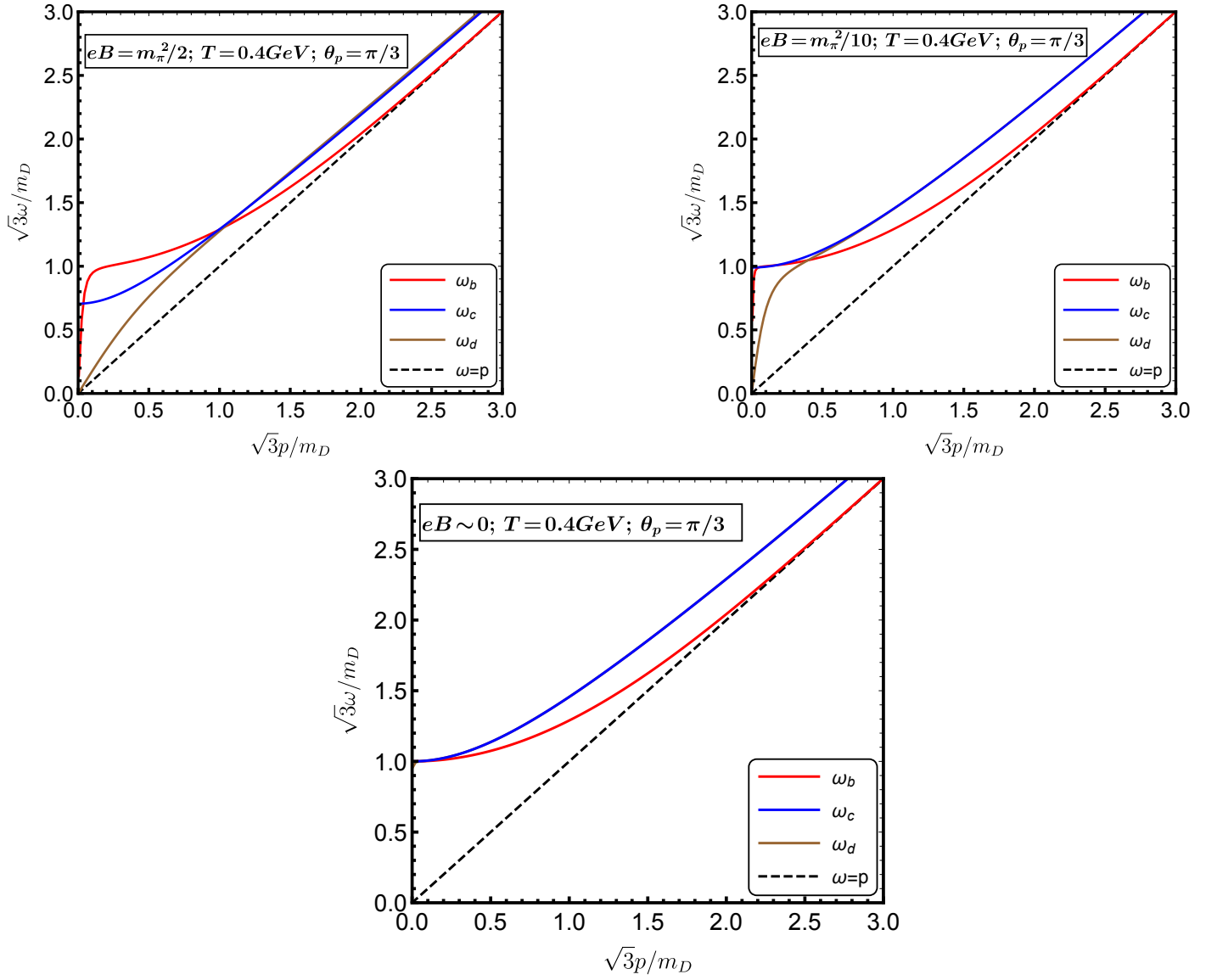Figure 5.13: Gluon dispersion curves for $\theta_p = \pi/3$ with varying magnetic field strength $eB = m_\pi^2/2,\ \ m_\pi^2/10\ $ and $\mathrm{m}_\pi^2/800$ (approximating to zero) for $N_f = 2$.

in the weak field approximation. Therefore, the dispersion relation in the weak field approximation can be written as [66]

$$P^2 + b = 0, \tag{5.189a}$$

$$P^2 + c = 0, \tag{5.189b}$$

$$P^2 + d = 0, \tag{5.189c}$$

where the respective dispersive modes are denoted by b-,c-,d-mode. The dispersion relations are scaled by the plasma frequency of a non-magnetized medium, $\omega_p = m_D/\sqrt{3}$ where m_D^2 is given by Eq. (5.164). As observed, three distinct modes arise when a gluon propagates through a hot magnetized medium. The magnetized plasmon mode, with energy ω_b, results from the form factor b, while the two transverse modes, with energies ω_c and ω_d originate from the form factors c and d, respectively. The application of a magnetic field breaks the degeneracy of the transverse modes that would be present in a purely thermal medium.
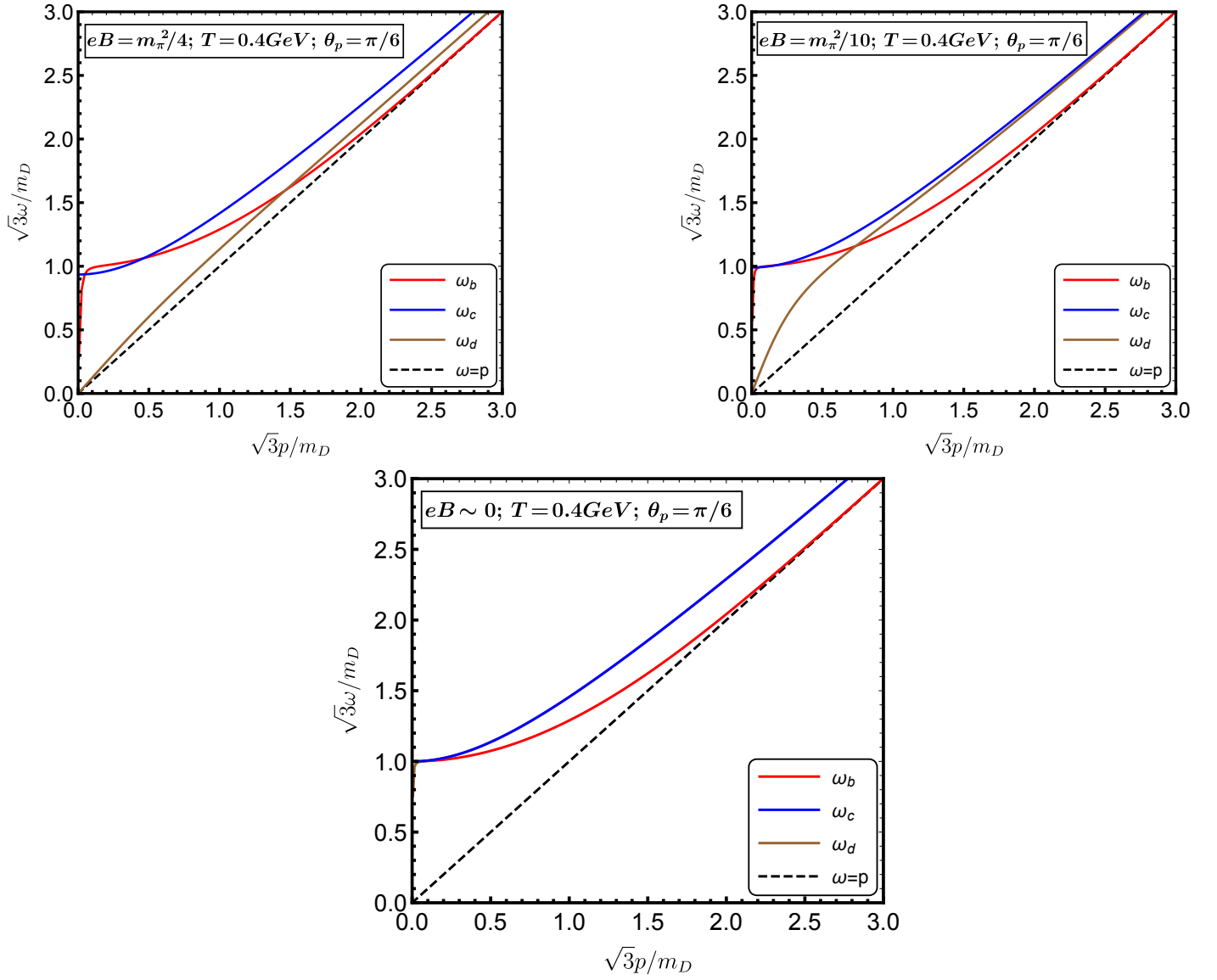
Figure 5.14: Gluon dispersion curves for $\theta_p = \pi/6$ with varying magnetic field strength $eB = m_\pi^2/4$, $m_\pi^2/10$ and $m_\pi^2/800$ (approximating to zero) for $N_f = 2$.

The dispersion curves for gluons are shown in Fig. 5.13, where the gluon propagates at an angle $\theta_p = \pi/3$ relative to the direction of the magnetic field. We have considered three different values for the magnetic field: $|eB| = m_\pi^2/2$, $m_\pi^2/10$ and $m_\pi^2/800$ (which approximates to 0). For a given magnetic field strength, such as $|eB| = m_\pi^2/2$, two modes (the b-mode and d-mode) exhibit a vanishing plasma frequency, while the c-mode retains a finite plasma frequency. The zero plasma frequency for the b-mode and d-mode could be an artefact of the weak field approximation used in the series expansion of the Schwinger propagator, as shown in Eq (5.153). In this approximation, the propagator is expanded in powers of eB, assuming eB is the smallest scale. This expansion imposes a restriction on the momentum p, which is valid only when $p \gtrsim \sqrt{eB}$. Therefore, in the limit $p \to 0$ with a non-zero eB (even if small), p becomes the lowest scale, causing Eq. (5.153) to no longer hold. Specifically, for the d-mode at very small magnetic fields, the dispersion curve abruptly drops to zero at $p = 0$. This occurs because the condition $p \gtrsim \sqrt{eB}$ is violated when taking the $p \to 0$ limit before the $eB \to 0$ limit. However, if the $eB \to 0$ limit is taken first, the situation changes: in this case, considering $eB = 0$ recovers the two HTL dispersive modes for gluon propagation. In Fig. 5.14 we have also displayed the dispersion

of gluon when it propagates at an angle $\theta_p = \pi/6$.

5.6. Debye mass in a magnetized hot and dense medium

The electromagnetic Debye mass in the presence of a hot magnetized medium was calculated in [66, 71, 235]. Here, we extend the approach of Ref. [235] to include QCD effects, incorporating the influence of color-charged and chemical potential of fermions in a hot and dense magnetized medium. Using Eq.(23) of Ref. [235] we can straightaway write down

$$\left(m_D^B\right)^2\Big|_{\text{QED}} = \frac{-\alpha T}{\sqrt{\pi}} eB \int_0^\infty du\sqrt{u} \int_{-1}^1 dv \sum_{l=-\infty}^\infty \exp\left\{-u\left(m^2 + W_l^2\right)\right\} \coth \bar{u} \left(2W_l^2 - \frac{1}{u}\right), \tag{5.190}$$

where u/v, l and α represent respectively the proper time, Landau levels and QED coupling constant with $W_l = (2l + 1)\pi T - i\mu$ at finite chemical potential. Now, the Poisson resummation [235] of the Landau levels is represented as

$$\sum_{l=-\infty}^\infty \exp^{-a(l-z)^2} = \left(\frac{\pi}{a}\right)^{1/2} \sum_{l=-\infty}^\infty \exp^{-\pi^2 l^2/a - 2i\pi zl}. \tag{5.191}$$

Taking derivative in both side with respect to a, we obtain

$$\sum_{l=-\infty}^\infty e^{-a(l-z)^2} (l-z)^2 = \frac{1}{2a}\left(\frac{\pi}{a}\right)^{1/2} \sum_{l=-\infty}^\infty \exp^{-\pi^2 l^2/a - 2i\pi zl} - \frac{\pi^{5/2}}{a^{5/2}} \sum_{l=-\infty}^\infty l^2 \exp^{-\pi^2 l^2/a - 2i\pi zl}. \tag{5.192}$$

Using Eqs. (5.191) and (5.192), we can write

$$\sum_{l=-\infty}^\infty \exp\left(-uW_l^2\right) \left(2W_l^2 - \frac{1}{u}\right) = \sum_{l=-\infty}^\infty e^{-4u\pi^2 T^2 (l-i\hat{\mu}+1/2)^2} \left(8\pi^2 T^2 \left(l - i\hat{\mu} + 1/2\right)^2 - \frac{1}{u}\right),$$

$$= \sum_{l=-\infty}^\infty e^{-a(l-z)^2} \frac{1}{u}\left(2a\left(l - z\right)^2 - 1\right),$$

$$= -\frac{2\pi^{5/2}}{a^{3/2}u} \sum_{l=-\infty}^\infty l^2 \exp^{-\pi^2 l^2/a - 2i\pi zl}, \tag{5.193}$$

with $a = 4u\pi^2 T^2$, $z = i\hat{\mu} - 1/2$, $\hat{\mu}$ being $\mu/2\pi T$. So, Eq. (5.193) becomes

$$\sum_{l=-\infty}^\infty \exp\left(-uW_l^2\right) \left(2W_l^2 - \frac{1}{u}\right) = -\frac{1}{4\sqrt{\pi}T^3 u^{5/2}} \sum_{l=-\infty}^\infty l^2 \exp^{-l^2/4uT^2 - 2\pi\hat{\mu}l} e^{i\pi l},$$

$$= \frac{1}{4\sqrt{\pi}T^3 u^{5/2}} \sum_{l=-\infty}^\infty (-1)^{l+1} l^2 \exp^{-l^2/4uT^2 - 2\pi\hat{\mu}l},$$

$$= \frac{1}{4\sqrt{\pi}T^3 u^{5/2}} \sum_{l=-\infty}^\infty (-1)^{l+1} l^2 e^{-l^2/4uT^2} \left(e^{-2\pi\hat{\mu}l} + e^{2\pi\hat{\mu}l}\right),$$

$$= \frac{1}{2\sqrt{\pi}T^3 u^{5/2}} \sum_{l=-\infty}^\infty (-1)^{l+1} l^2 \cosh\left(2\pi\hat{\mu}l\right) e^{-l^2/4uT^2}. \tag{5.194}$$

Using Eq. (5.194) in Eq. (5.190), we get

$$\left(m_D^B\right)^2\Big|_{\text{QED}} = \frac{\alpha eB}{\pi T^2} \int_0^\infty \frac{du}{u^2} \coth\left(eBu\right) \exp\left(-um^2\right)$$

$$\times \sum_{l=1}^\infty (-1)^{l+1} l^2 \cosh\left(2\pi\hat{\mu}l\right) \exp\left(-\frac{l^2}{4uT^2}\right). \tag{5.195}$$

Changing the variable from u to $x = l^2/(4uT^2)$, we get

$$\left(m_D^B\right)^2\Big|_{\text{QED}} = \frac{e^2\, eB}{\pi^2 T^2} \int_0^\infty e^{-x} dx \sum_{l=1}^\infty (-1)^{l+1} \coth\left(\frac{eBl^2}{4xT^2}\right) \exp\left(-\frac{m^2 l^2}{4xT^2}\right). \tag{5.196}$$

Extending this to QCD, we derive an expression for the modified Debye mass that accounts for both a finite chemical potential and the presence of an arbitrary magnetic field as

$$\left(m_D^B\right)^2 = \frac{g^2 N_c T^2}{3} + \sum_f \frac{g^2 q_f B}{2\pi^2} \int\limits_0^\infty e^{-x} dx$$
$$\times \sum_{l=1}^\infty (-1)^{l+1} \cosh\left(2l\pi\hat{\mu}\right) \coth\left(\frac{q_f B l^2}{4xT^2}\right) \exp\left(-\frac{m_f^2 l^2}{4xT^2}\right). \tag{5.197}$$

In Eq. (5.197), the first term originates from pure gluonic contributions, a feature absent in the QED case. The second term arises from the quark loop, obtained by substituting m with m_f and e with g. Additionally, a sum over quark flavours is included, incorporating a QCD factor of $\frac{1}{2}\sum_f$ to account for flavour contributions.

In the strong magnetic field regime, where $m_{\text{th}}^2 \sim g^2 T^2 \leq T^2 \leq q_f B$, and considering the LLL approximation while neglecting the current quark mass m_f, Eq. (5.197) simplifies directly to the following form[15]:

$$(m_D^s)^2 = \frac{g^2 N_c T^2}{3} + \sum_f \frac{g^2 q_f B}{4\pi^2}. \tag{5.198}$$

This simplified expression matches the Debye mass in the strong magnetic field limit, as shown in Eq.(5.150). It is derived by evaluating the gluon polarization tensor with the quark propagator in the strong field approximation and subsequently taking the static limit of its zero-zero component[66].
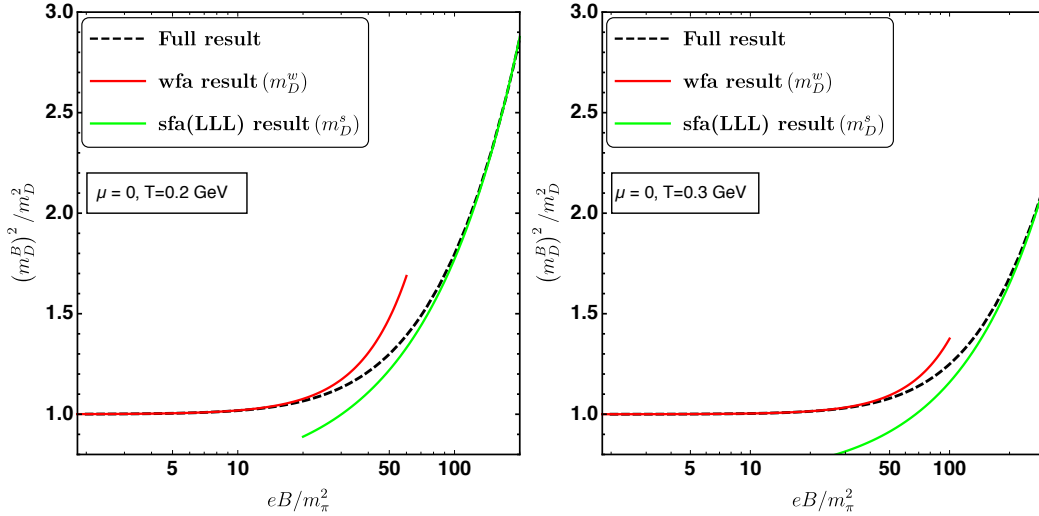

Figure 5.15: Comparison of the scaled one-loop Debye masses in Eqs.(5.197), (5.198) and (5.199) as a function of the scaled magnetic field for $N_f = 3$, $\mu = 0$. Left panel: $T = 200$ MeV, Right panel: $T = 300$ MeV.

In the weak field approximation $(T^2 > m_{\text{th}}^2 > q_f B)$, the square of Debye mass can be obtained from Eq. (5.197) by expanding $\coth\left(q_f B l^2/4xT^2\right)$ as

$$\begin{aligned}(m_D^w)^2 &\simeq \frac{g^2 T^2}{3}\left[\left(N_c + \frac{N_f}{2}\right) + 6N_f\hat{\mu}^2\right] \\ &+ \sum_f \frac{g^2 (q_f B)^2}{12\pi^2 T^2}\sum_{l=1}^\infty (-1)^{l+1} l^2 \cosh\left(2l\pi\hat{\mu}\right) K_0\left(\frac{m_f l}{T}\right) + \mathcal{O}[(q_f B)^4] \\ &= m_D^2 + \delta m_D^2,\end{aligned} \tag{5.199}$$

---

[15] Our fermionic part of Debye mass is different from Ref. [236] by a factor of 2 which was somehow overlooked by the authors of the Ref. [236] in Matsurbara Sum. We also find the same mismatch with the Ref. [237]

where, m_D corresponds to the QCD Debye mass in a hot and dense medium without an external magnetic field, while $K_n(z)$ denotes the modified Bessel function of the second kind. The second term represents the thermo-magnetic correction arising from the weak external magnetic field. It is important to emphasize that Eq.(5.199) holds only for $\mu \leq m_f$, as the infinite sum over l diverges for $\mu > m_f$. Furthermore, the thermo-magnetic contribution in Eq.(5.199) is consistent with the Debye mass expression given in Eq. (5.178) in the absence of a quark chemical potential.

In Fig.5.15, we compare the full expression from Eq.(5.197), the strong field result from Eq.(5.198), and the weak field approximation from Eq.(5.199), all scaled by m_D, as a function of the magnetic field scaled by the squared pion mass. For $T = 200$ MeV, the weak field approximation (red curve) closely matches the full result (dashed line) in the region where $|eB|/m_\pi^2 \leq 10$. Beyond this threshold ($|eB|/m_\pi^2 \geq 10$), significant deviations appear, indicating the breakdown of the weak field approximation. Thus, for $T = 200$ MeV, Eq. (5.199) remains a reliable approximation within the defined weak field domain. Conversely, the LLL result (green line) aligns well with the full expression for $|eB|/m_\pi^2 \geq 70$ at $T = 200$ MeV. The right panel, showing results for $T = 300$ MeV, demonstrates similar behaviour. These plots highlight that the boundaries between the strong ($|eB| > T^2$) and weak ($|eB| < T^2$) field regimes shift with temperature. In the intermediate region, using the full expression would be ideal, though it presents significant computational challenges.

5.7. Strong coupling and scales

The one-loop running coupling which evolves with both the momentum transfer and the magnetic field is recently obtained in Ref. [225] as

$$\alpha_s(\Lambda^2, |eB|) = \frac{\alpha_s(\Lambda^2)}{1 + b_1\,\alpha_s(\Lambda^2) \ln\left(\frac{\Lambda^2}{\Lambda^2 + |eB|}\right)}, \tag{5.200}$$

in the domain $|eB| < \Lambda^2$ where the one-loop running coupling at renormalization scale reads as

$$\alpha_s(\Lambda^2) = \frac{1}{b_1\,\ln\left(\Lambda^2/\Lambda_{\overline{\rm MS}}^2\right)}, \tag{5.201}$$

with $b_1 = \frac{11N_c - 2N_f}{12\pi}$, $\Lambda_{\overline{\rm MS}} = 176$ MeV [238] at $\alpha_s(1.5{\rm GeV}) = 0.326$ for $N_f = 3$. Here, we adopt separate renormalization scales for gluons and quarks: Λ_g and Λ_q, respectively. Their central values are chosen as $\Lambda_g = 2\pi T$ and $\Lambda_q = 2\pi\sqrt{T^2 + \mu^2/\pi^2}$. These scales can vary by a factor of 2 around their central values. The magnetic field strength, meanwhile, must satisfy $|eB| > \Lambda^2$ for the strong field regime and $|eB| < \Lambda^2$ for the weak field, relative to temperature and renormalization scale, as outlined in Sec.5.3.1. The left panel of Fig.5.16 shows the running of α_s with $|eB|$ at the central renormalization scale $\Lambda_g = \Lambda_q = 2\pi T$ GeV for $T = 0.4$ GeV, indicating a gradual increase in α_s within the $|eB| < \Lambda^2$ domain. The right panel of Fig. 5.16 illustrates the running of α_s with temperature for $|eB| = m_\pi^2$, reaffirming the slow variation of α_s with $|eB|$.

5.8. Quark-Gluon Three Point Function

We start by considering the one-loop level 3-point function in a hot magnetized medium as derived in [233], within HTL approximation [112, 113, 119, 239] as

$$\Gamma^\mu(P, K; Q) = \gamma^\mu + \delta\Gamma^\mu_{\rm HTL}(P, K) + \delta\Gamma^\mu_{\rm TM}(P, K), \tag{5.202}$$

where the external four-momentum $Q = P - K$. The 3-point function in this context is an important component in understanding the interactions of gauge bosons in a hot and magnetized environment. The HTL approximation simplifies the calculations by accounting for high-temperature effects, which are relevant in the study of thermal field theory in the
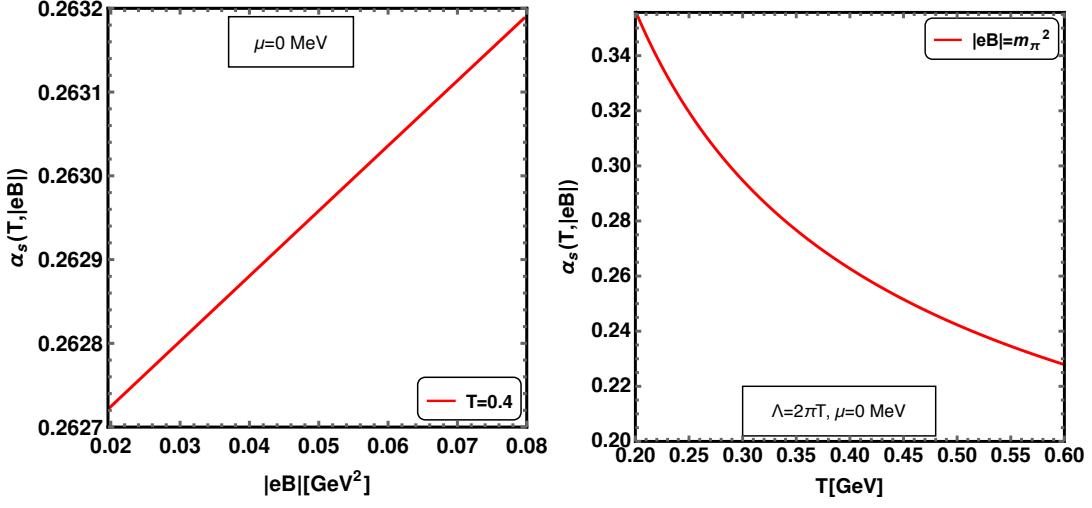
Figure 5.16: Left psnel: variation of the one-loop QCD coupling with weak magnetic field, $|eB|$ for $T = 0.4$GeV. Right panel: variation with temperature, T for $|eB| = m_\pi^2$.

presence of external magnetic fields.

The HTL correction part [113, 119, 150, 239] is given as

$$\delta\Gamma^\mu_{\text{HTL}}(P,K) \;=\; m_{th}^2 G^{\mu\nu}\gamma_\nu = m_{th}^2 \int \frac{d\Omega}{4\pi} \frac{\hat{Y}^\mu \hat{\slashed{Y}}}{(P\cdot\hat{Y})(K\cdot\hat{Y})} = \delta\Gamma^\mu_{\text{HTL}}(-P,-K), \tag{5.203}$$

where $\hat{Y}_\mu = (1,\hat{y})$ is a light like four vector and the thermo-magnetic (TM) correction part [232, 233] is given

$$\delta\Gamma^\mu_{\text{TM}}(P,K) = 4\gamma_5 g^2 C_F M^2 \int \frac{d\Omega}{4\pi} \frac{1}{(P\cdot\hat{Y})(K\cdot\hat{Y})} \left[(\hat{Y}\cdot n)\slashed{u} - (\hat{Y}\cdot u)\slashed{n} \right] \hat{Y}^\mu . \tag{5.204}$$

Now, choosing the temporal component of the thermo-magnetic correction part of the 3-point function and external three momentum $\vec{q} = 0$, we get

$$\delta\Gamma^0_{\text{TM}}(P,K)\big|_{\vec{q}=0} \;=\; \gamma_5 M'^2 \int \frac{d\Omega}{4\pi} \frac{1}{(P\cdot\hat{Y})(K\cdot\hat{Y})} \left[(\hat{Y}\cdot n)\slashed{u} - (\hat{Y}\cdot u)\slashed{n} \right]$$

$$= \; \gamma_5 M'^2 \int \frac{d\Omega}{4\pi} \frac{1}{(P\cdot\hat{Y})(K\cdot\hat{Y})} \left[(\hat{Y}\cdot n)\gamma_0 + (\hat{Y}\cdot u)\gamma^3 \right] \tag{5.205}$$

Along with this following identity:

$$\left(\frac{1}{K\cdot\hat{Y}} - \frac{1}{P\cdot\hat{Y}} \right) \;=\; \frac{Q\cdot\hat{Y}}{(P\cdot\hat{Y})(K\cdot\hat{Y})} = \frac{q_0}{(P\cdot\hat{Y})(K\cdot\hat{Y})},$$

and , (5.69a) and (5.69b), we one finally obtain

$$\delta\Gamma^0_{\text{TM}}(P,K)\big|_{\vec{q}\to} \;=\; \frac{M'^2 p_z}{p^2 q_0}\delta Q_1 \gamma_5\gamma^0 - \frac{M'^2}{p q_0}\delta Q_0 \gamma_5\gamma^3$$

$$= \; -\frac{M'^2}{p q_0} \left[\delta Q_0\, \gamma_5 + \frac{p_z}{p}\,\delta Q_1\, (i\gamma^1\gamma^2) \right] \gamma^3 , \tag{5.206}$$

where $\delta Q_n = Q_n\left(\frac{p_0}{p}\right) - Q_n\left(\frac{k_0}{p}\right)$. We note that this expression matches exactly with the expression obtained in (5.212) from the general structure of fermion self-energy.

Now, we aim to verify the general structure of the temporal 3-point function by leveraging the general form of the self-energy. The $(N+1)$-point functions are connected to the N-point functions through the Ward-Takahashi identity. Specifically, the 3-point function is related to the 2-point function as follows:

$$Q_\mu\Gamma^\mu(P,K;Q) \;=\; S^{-1}(P) - S^{-1}(K) = \slashed{P} - \slashed{K} - \Sigma(P) + \Sigma(K)$$

$$= \; \underbrace{(\slashed{P} - \slashed{K})}_{\text{Free}} - \underbrace{\left(\Sigma^{B=0}(P,T) - \Sigma^{B=0}(K,T)\right)}_{\text{Thermal or HTL correction}} - \underbrace{\left(\Sigma^{B\neq0}(P,T) - \Sigma^{B\neq0}(K,T)\right)}_{\text{Thermo-magnetic correction}}$$

$$
\begin{aligned}
= \quad & \slashed{Q} + a(p_0, |\vec{p}|)\slashed{P} + b(p_0, |\vec{p}|)\slashed{u} - a(k_0, |\vec{k}|)\slashed{K} - b(k_0, |\vec{k}|)\slashed{u} + b'(p_0, p_\perp, p_z)\gamma_5\slashed{u} \\
& + c'(p_0, p_\perp, p_z)\gamma_5\slashed{u} - b'(k_0, k_\perp, k_z)\gamma_5\slashed{u} - c'(k_0, k_\perp, k_z)\gamma_5\slashed{u} \,,
\end{aligned}
\tag{5.207}
$$

where $Q = P - K$. To confirm the general structure of the self-energy in Eq.(5.7) in relation to the inverse propagator in Eq.(5.14), we now proceed to derive the temporal component of the 3-point function. This is done by setting $\vec{q} = 0$; $\vec{p} = \vec{k}$ and $p = k$.

Using (5.61a), (5.61b), (5.70a) and (5.70b), we can obtain

$$
\begin{aligned}
\Gamma^0(P, K; Q)\big|_{\vec{q}=0} = \quad & \gamma_0 \underbrace{- \frac{m_{th}^2}{pq_0}\delta Q_0\,\gamma^0 + \frac{m_{th}^2}{pq_0}\delta Q_1\,(\hat{p}\cdot\vec{\gamma})}_{\text{Thermal or HTL correction}} \\
& \underbrace{- \frac{M'^2}{pq_0}\left[\delta Q_0\,\gamma_5 + \frac{p_z}{p}\delta Q_1\,\left(i\gamma^1\gamma^2\right)\right]\gamma^3}_{\text{Thermo-magnetic correction}} \\
= \quad & \gamma^0 + \delta\Gamma^0_{\text{HTL}}(P, K; Q) + \delta\Gamma^0_{\text{TM}}(P, K; Q) \,,
\end{aligned}
\tag{5.208}
$$

with

$$
\gamma_5\gamma^0 = -i\gamma^1\gamma^2\gamma^3 \,,
$$
$$
M'^2 = 4\,C_F\,g^2\,M^2(T, m, q_f B)\,,
\tag{5.209a}
$$

It is important to emphasize that the thermo-magnetic (TM) correction $\delta\Gamma^0_{\text{TM}}$ matches exactly with with the result obtained from direct calculation in (5.206). Furthermore, this result is consistent with the HTL 3-point function [232, 233] in the absence of a background magnetic field, which can be recovered by setting $B = 0 \Rightarrow M' = 0$ as

$$
\begin{aligned}
\Gamma^0_{\text{HTL}}(P, K; Q)\big|_{\vec{q}=0} = \quad & \left[1 - \frac{m_{th}^2}{pq_0}\delta Q_0\right]\gamma^0 + \frac{m_{th}^2}{pq_0}\delta Q_1\,(\hat{p}\cdot\vec{\gamma}) \\
= \quad & \gamma^0 + \delta\Gamma^0_{\text{HTL}}(P, K; Q)\,,
\end{aligned}
\tag{5.210}
$$

where all components, i.e., $(0, 1, 2, 3)$, are relevant for pure thermal background. This alignment validates the correction's accuracy and its agreement with established results in the context of thermal field theory, confirming the consistency of the approach.

In the absence of the heat bath, by setting $T = 0 \Rightarrow$ we have $m_{th} = 0$ and $M'^2 = 4\,C_F\,g^2\,M^2(T = 0, m, q_f, B)$. Under these conditions, the temporal 3-point function in Eq. (5.208) simplifies to:

$$
\begin{aligned}
\Gamma^0_B(P, K; Q)\big|_{\vec{q}=0} = \quad & \gamma^0 \underbrace{- \frac{M'^2}{pq_0}\left[\delta Q_0\,\gamma_5 + \frac{p_z}{p}\delta Q_1\,(i\gamma^1\gamma^2)\right]\gamma^3}_{\text{Pure magnetic correction}} \\
= \quad & \gamma^0 + \delta\Gamma^0_M(P, K; Q)\,.
\end{aligned}
\tag{5.211}
$$
$$
\tag{5.212}
$$

We observe that in the case of a pure background magnetic field without a heat bath, the gauge boson is aligned along the direction of the magnetic field. Consequently, there is no polarization in the transverse direction. As a result, only the longitudinal components (i.e, the (0,3)-components) of the 3-point function will be relevant for the pure background magnetic field, in contrast to the case of a pure thermal background as described in Eq. (5.210).

5.9. Two Quark-Two Gluon Four Point Function

The one-loop level two quark-two gluon 4-point function in a hot magnetised medium in [233] within HTL approximation as

$$
\Gamma^{\mu\nu}(P_1, P_2, Q_1) = \delta\Gamma^{\mu\nu}_{\text{HTL}}(P_1, P_2, Q_1) + \delta\Gamma^{\mu\nu}_{\text{TM}}(P_1, P_2, Q_1),
\tag{5.213}
$$

where the first term is HTL contribution and the second term is the thermo-magnetic correction in presence of magnetic field. The HTL contribution is obtained in Ref. [113, 233] as

$$\delta\Gamma^{\mu\nu}_{\text{HTL}}(P_1, P_2, Q_1) = -m^2_{th} \int \frac{d\Omega}{2\pi} \frac{\hat{Y}^\mu \hat{Y}^\nu \hat{\slashed{Y}}}{[(P_1+Q_1)\cdot\hat{Y}][(P_2-Q_1)\cdot\hat{Y}]} \left[\frac{1}{P_1\cdot\hat{Y}} + [\frac{1}{P_2\cdot\hat{Y}}\right], \tag{5.214}$$

We note that (5.214) reproduces QED 4-point vertex [113] when one replaces the thermal quark mass m_{th} by electron thermal mass. The 4-point HTL vertex in (5.214) satisfies Ward identity with HTL 3-point functions as

$$Q_{1\mu}\delta\Gamma^{\mu\nu}_{\text{HTL}}(P_1, P_2, Q_1) = \delta\Gamma^\nu_{\text{HTL}}(P_1, P_2-Q_1) - \delta\Gamma^\nu_{\text{HTL}}(P_1+Q_1, P_2). \tag{5.215}$$

The thermo-magnetic contribution to 4-point function is recently obtained in Ref. [233] as

$$\begin{aligned}
\delta\Gamma^{\mu\nu}_{\text{TM}}(P_1, P_2, Q_1) = &\; 4i\gamma_5 g^2 M' \int \frac{d\Omega}{2\pi} \left[\frac{1}{P_1\cdot\hat{Y}} + [\frac{1}{P_2\cdot\hat{Y}}\right] \frac{1}{[(P_1+Q_1)\cdot\hat{Y}][(P_2-Q_1)\cdot\hat{Y}]} \\
&\times \Big[\left\{ \left(\hat{Y}\cdot b\right)\left(\hat{Y}^\mu u^\nu + \hat{Y}^\nu u^\mu\right) - \left(\hat{Y}\cdot u\right)\left(\hat{Y}^\mu b^\nu + \hat{Y}^\nu b^\mu\right) \right\} \slashed{K} \\
&+ \hat{Y}^\mu \hat{Y}^\nu \left\{ \left(\hat{Y}\cdot b\right)\slashed{u} - \left(\hat{Y}\cdot u\right)\slashed{b} \right\} \Big].
\end{aligned} \tag{5.216}$$

The 4-point thermo-magnetic vertex in (5.216) satisfies Ward identity with thermo-magnetic 3-point functions as

$$Q_{1\mu}\delta\Gamma^{\mu\nu}_{\text{TM}}(P_1, P_2, Q_1) = \delta\Gamma^\nu_{\text{TM}}(P_1, P_2-Q_1) - \delta\Gamma^\nu_{\text{TM}}(P_1+Q_1, P_2). \tag{5.217}$$

6. Thermodynamics of a Thermo-Magnetic QCD matter

The equation of state (EoS) plays a crucial role in studying the hot and dense QCD matter, specifically the quark-gluon plasma created in relativistic heavy-ion collisions. This is because the EoS governs the thermodynamic properties of the medium and is essential for understanding its behaviour. Additionally, the time evolution of the hot, dense fireball is modeled through hydrodynamics, which relies on the EoS of deconfined QCD matter as an input. In the absence of a magnetic field, the EoS has been systematically calculated using both Lattice QCD (LQCD) methods [240, 241] and Hard Thermal Loop perturbation theory (HTLpt) at various levels: two-loop (next-to-leading order, NLO) [136] and three-loop (next-to-NLO, NNLO) [131–135, 139, 140] for finite temperature and chemical potential. In contrast, the expansion dynamics of a thermo-magnetic medium is governed by magneto-hydrodynamics [242, 243], which requires a thermo-magnetic EoS as input. Given the significance of this, a systematic determination of the EoS for a magnetized hot QCD medium is vital. Some efforts in LQCD have been made in Ref. [244], though these are limited to a temperature range of 100–300 MeV. This section will focus on the thermodynamics of thermo-magnetic QCD matter.

The total thermodynamic free energy up to one-loop order in HTLpt, in the presence of a background magnetic field B, can be expressed as:

$$F = F_q + F_g + F_0 + \Delta\mathcal{E}^0_T + \Delta\mathcal{E}^B_T \tag{6.1}$$

where, F_q and F_g represent the contributions to the free energy from quarks and gluons, respectively, which will be calculated in the presence of the magnetic field using the HTL approximation. F_0 refers to the tree-level contribution arising solely due to the constant magnetic field. It is given by

$$F_0 \rightarrow \frac{1}{2}B^2 + \Delta\mathcal{E}^{B^2}_0, \tag{6.2}$$

where $\Delta\mathcal{E}^{B^2}_0$ is a counter term of $\mathcal{O}[(q_f B)^2]$ from vacuum as we will see later. The $\Delta\mathcal{E}_T$ is a counter term independent of magnetic field (viz. $\mathcal{O}[(q_f B)^0 T^4]$)as

$$\Delta\mathcal{E}^0_T = \Delta\mathcal{E}^{\text{HTL}}_T + \Delta\mathcal{E}_T, \tag{6.3}$$

where $\Delta\mathcal{E}^{\text{HTL}}_T$ is the HTL counter term [139, 140]. The counter term $\Delta\mathcal{E}_T$ emerges due to the quark loop in the gluonic

two-point function in the presence of a magnetic field. However, the magnetic field dependence cancels out explicitly from both the numerator and the denominator, as will be demonstrated later. Additionally, the counter term $\Delta \mathcal{E}_T^B$ is of order $\mathcal{O}[(q_f B)T^2]$ and $\mathcal{O}[(q_f B)^3/T^2]$.

The pressure of a system is defined as

$$P = -F. \tag{6.4}$$

We also note the QCD Casimir numbers are $C_A = N_c$, $d_A = N_c^2 - 1$, $d_F = N_c N_f$ and $C_F = (N_c^2 - 1)/2N_c$ where N_c is the number of color and N_f is the number of quark flavour.

The quark free energy can be written as [54, 112],

$$F_q = -d_F \sum_{\{p_0\}} \!\!\!\!\!\! \oint \frac{d^3 p}{(2\pi)^3} \ln\left(\det[S^{-1}(P)]\right). \tag{6.5}$$

The partition function for a gluon can generally be written in Euclidean space [54, 112] as

$$\mathcal{Z}_g = \mathcal{Z} \mathcal{Z}^{\text{ghost}}, \quad \mathcal{Z} = N_\xi \prod_{n,\boldsymbol{p}} \sqrt{\frac{(2\pi)^D}{\det D_{\mu\nu,E}^{-1}}}, \quad \mathcal{Z}^{\text{ghost}} = \prod_{n,\boldsymbol{p}} P_E^2. \tag{6.6}$$

In this expression, the product over $\boldsymbol{p}$ represents the summation over spatial momentum, while the product over n corresponds to the discrete Bosonic Matsubara frequencies ($\omega_n = 2\pi n\beta$; $with n = 0, 1, 2, \cdots$) due to the Euclidean time formalism. Here, D denotes the space-time dimension of the theory. The quantity $D_{\mu\nu,E}^{-1}$ is the inverse gauge boson propagator in Euclidean space, with $P_E^2 = \omega_n^2 + p^2$ being the square of the four-momentum. $N_\xi = 1/(2\pi\xi)^{D/2}$ is the normalization factor that arises from the introduction of a Gaussian integral at each spatial location, where averaging is done over the gauge condition function with width ξ the gauge fixing parameter. The gluon free energy can now be written as [54, 112]

$$F_g = -d_A \frac{T}{V} \ln \mathcal{Z}_g = d_A \left[\frac{1}{2} \sum_{P_E} \!\!\!\!\! \oint \ln\left[\det\left(D_{\mu\nu,E}^{-1}(P_E)\right)\right] - \sum_{P_E} \!\!\!\!\! \oint \ln P_E^2 \right]. \tag{6.7}$$

We note that the presence of the normalization factor N_ξ eliminates the gauge dependence explicitly.

Now, the second-order QNS is defined as

$$\chi = -\frac{\partial^2 F}{\partial \mu^2}\bigg|_{\mu=0} = \frac{\partial^2 P}{\partial \mu^2}\bigg|_{\mu=0} = \frac{\partial n}{\partial \mu}\bigg|_{\mu=0}. \tag{6.8}$$

This represents the measure of the variance or fluctuation in the net quark number. One can also calculate the covariance between two conserved quantities when the quark flavors have different chemical potentials. Alternatively, one may choose other bases depending on the system, such as the net baryon number $\mathcal{B}$, net charge $\mathcal{Q}$, and strangeness number $\mathcal{S}$, or $\mathcal{B}$, $\mathcal{Q}$ and the third component of the isospin $\mathcal{I}_3$. In our case, we assume the strangeness and charge chemical potentials are zero. Additionally, we consider the same chemical potential for all flavors, which leads to vanishing off-diagonal quark number susceptibilities. Consequently, the net second-order baryon number susceptibility is related to the second-order quark number susceptibility as $\chi_B = \frac{1}{3}\chi$. The chiral condensate is defined as

$$\langle \bar{q}q \rangle = \frac{\text{Tr}[\bar{q}q\, e^{-\beta \text{H}}]}{\text{Tr}[e^{-\beta \text{H}}]} = \frac{\partial \Omega}{\partial m_f}, \tag{6.9}$$

where H is the Hamiltonian of the system. $\Omega = -\frac{T}{V} \ln Z$ is the thermodynamic potential where Z is the partition function of a quark-antiquark gas. Quark condensate also can be written using quark propagator as

$$\langle \bar{q}q \rangle = -N_c N_f \sum_{\{P\}} \!\!\!\!\! \oint \text{Tr}\left[S(P)\right], \tag{6.10}$$

where N_c and N_f are the numbers of quark colors and flavors respectively. Susceptibility is the measure of the response of a system to small external force. Chiral susceptibility is a measure of the response of the chiral condensate to small changes in the current quark mass m_f. It quantifies how the chiral symmetry breaking (or the chiral condensate) is

affected by changes in the quark mass. The chiral susceptibility is defined as

$$\chi_c = -\frac{\partial \langle \bar{q}q \rangle}{\partial m_f}\bigg|_{m_f=0}. \tag{6.11}$$

This susceptibility captures the sensitivity of the condensate to changes in the quark mass, which is particularly relevant near the phase transition where chiral symmetry restoration occurs. A larger chiral susceptibility suggests that the chiral condensate is more responsive to changes in the quark mass, and in the context of QCD, it is closely related to the critical temperature for chiral symmetry restoration in hot QCD matter.

6.1. Thermodynamics in Weak Field Approximation

6.1.1. One loop quark free energy in presence of a weakly magnetized medium

Based on the general form of the quark self-energy[16] in Eq.(5.7), and assuming a weak external magnetic field aligned with the z (or third direction), the inverse of the effective quark propagator from Eq.(5.14) can be written as follows:

$$\begin{aligned}
S_{\text{eff}}^{-1} &= \not{P} - \Sigma(P) = \not{P} + \mathcal{A}\not{P} + \mathcal{B}\not{u} + \mathcal{B}'\gamma_5\not{u} + \mathcal{C}'\gamma_5\not{n} \\
&= \mathcal{C}(p_0, p_\perp, p_3)p_0\gamma_0 - \mathcal{D}(p_0, p_\perp, p_3)p_i\gamma_i + \mathcal{B}'(p_0, p_\perp, p_3)\gamma_5\gamma_0 + \mathcal{C}'(p_0, p_\perp, p_3)\gamma_5\gamma_3.
\end{aligned} \tag{6.12}$$

Here

$$\mathcal{C}(p_0, p_\perp, p_3) = 1 + \mathcal{A}(p_0, p_\perp, p_3) + \frac{\mathcal{B}(p_0, p_\perp, p_3)}{p_0} = 1 - \mathcal{A}'(p_0, p_\perp, p_3), \tag{6.13a}$$

$$\mathcal{D}(p_0, p_\perp, p_3) = 1 + \mathcal{A}(p_0, p_\perp, p_3), \tag{6.13b}$$

with

$$\mathcal{A}(p_0, p_\perp, p_3) = -\frac{m_{\text{th}}^2}{p^2}\int\frac{d\Omega}{4\pi}\frac{\boldsymbol{p}\cdot\hat{\boldsymbol{k}}}{p_0 - \boldsymbol{p}\cdot\hat{\boldsymbol{k}}} = \frac{m_{\text{th}}^2}{p^2}\left[1 - \mathcal{T}_P\right], \tag{6.14a}$$

$$\mathcal{A}'(p_0, p_\perp, p_3) = \frac{m_{\text{th}}^2}{p_0}\int\frac{d\Omega}{4\pi}\frac{1}{p_0 - \boldsymbol{p}\cdot\hat{\boldsymbol{k}}} = \frac{m_{\text{th}}^2}{p_0^2}\mathcal{T}_P, \tag{6.14b}$$

$$\mathcal{B}'(p_0, p_\perp, p_3) = -m_{\text{eff}}^2\int\frac{d\Omega}{4\pi}\frac{\hat{k}_3}{p_0 - \boldsymbol{p}\cdot\hat{\boldsymbol{k}}} = \frac{m_{\text{eff}}^2\,p_3}{p^2}\left[1 - \mathcal{T}_P\right], \tag{6.14c}$$

$$\mathcal{C}'(p_0, p_\perp, p_3) = m_{\text{eff}}^2\int\frac{d\Omega}{4\pi}\frac{1}{p_0 - \boldsymbol{p}\cdot\hat{\boldsymbol{k}}} = \frac{m_{\text{eff}}^2}{p_0}\mathcal{T}_P, \tag{6.14d}$$

where we have written the coefficients in terms of

$$\mathcal{T}_P = \int\frac{d\Omega}{4\pi}\frac{p_0}{p_0 - \boldsymbol{p}\cdot\hat{\boldsymbol{k}}}. \tag{6.15}$$

This expression represents an integral defined as the angular average over $\angle\boldsymbol{p}, \hat{\boldsymbol{k}}$. For simplicity, the arguments of all structure functions will be omitted from now on.

The determinant of Eq. (6.12) can be calculated as

$$\begin{aligned}
\det\left[S_{\text{eff}}^{-1}\right] &= (\mathcal{C}^2 p_0^2 - \mathcal{D}^2 p^2 + \mathcal{B}'^2 - \mathcal{C}'^2)^2 - 4(p_0\mathcal{B}'\mathcal{C} + p_3\mathcal{C}'\mathcal{D})^2 \\
&= A_0^2 - A_s^2.
\end{aligned} \tag{6.16}$$

By combining Eqs. (6.5) and (6.16), the one-loop quark free energy in the presence of a weak magnetic field under the HTL approximation takes the form [54]:

$$F_q = -N_c\sum_f\int\frac{d^4P}{(2\pi)^4}\ln\left(A_0^2 - A_s^2\right) = -2N_cN_f\int\frac{d^4P}{(2\pi)^4}\ln\left(P^2\right) - N_c\sum_f\int\frac{d^4P}{(2\pi)^4}\ln\left(\frac{A_0^2 - A_s^2}{P^4}\right)$$

---

[16]Different notation is used here for various structure functions.

$$= -\frac{7\pi^2 T^4 N_c N_f}{180} \left(1 + \frac{120}{7}\hat{\mu}^2 + \frac{240}{7}\hat{\mu}^4\right) - N_c \sum_f \int \frac{d^4 P}{(2\pi)^4} \ \ln\left[\frac{(A_0 + A_s)(A_0 - A_s)}{P^4}\right]. \tag{6.17}$$

Now the argument of the logarithm in Eq. (6.17) can be simplified using Eq. (6.16) as

$$\frac{(A_0 + A_s)(A_0 - A_s)}{P^4} = 1 + 2\left(\frac{\mathcal{A}'(\mathcal{A}' - 2)p_0^2 - \mathcal{A}(\mathcal{A} + 2)p^2 + \mathcal{B}'^2 - \mathcal{C}'^2}{P^2}\right)$$

$$+ \frac{\left(\mathcal{A}'(\mathcal{A}' - 2)p_0^2 - \mathcal{A}(\mathcal{A} + 2)p^2 + \mathcal{B}'^2 - \mathcal{C}'^2\right)^2 - 4(\mathcal{B}'\mathcal{C}\ p_0 + \mathcal{C}'\mathcal{D}\ p_3)^2}{P^4}. \tag{6.18}$$

In the-high temperature limit, the logarithmic term in Eq. (6.17) can be expanded in a series of coupling constants g retaining contributions up to $\mathcal{O}(g^4)$ as outlined in Ref. [54]:

$$\ln\left[\frac{(A_0 + A_s)(A_0 - A_s)}{P^4}\right] = 2\left(\frac{\mathcal{A}'^2 p_0^2 - \mathcal{A}^2 p^2 + \mathcal{B}'^2 - \mathcal{C}'^2 - 2\mathcal{A}' p_0^2 - 2\mathcal{A} p^2}{P^2}\right)$$

$$- 4\left(\frac{\left(\mathcal{A}' p_0^2 + \mathcal{A} p^2\right)^2 + (\mathcal{B}' p_0 + \mathcal{C}' p_3)^2}{P^4}\right) + \mathcal{O}(g^6), \tag{6.19}$$

with

$$(\mathcal{B}'^2 - \mathcal{C}'^2) = m_{\text{eff}}^4 \left[\frac{p_3^2}{p^4} + \frac{\mathcal{T}_P^2 p_3^2}{p^4} - \frac{\mathcal{T}_P^2}{p_0^2} - \frac{2\mathcal{T}_P p_3^2}{p^4}\right], \tag{6.20}$$

$$(\mathcal{B}' p_0 + \mathcal{C}' p_3)^2 = m_{\text{eff}}^4 \left[\frac{p_0^2 p_3^2}{p^4}\left(1 + \mathcal{T}_P^2 - 2\mathcal{T}_P\right) + \frac{\mathcal{T}_P^2}{p_0^2} p_3^2 + \frac{2p_3^2}{p^2}\left(\mathcal{T}_P - \mathcal{T}_P^2\right)\right], \tag{6.21}$$

$$(\mathcal{A}' p_0^2 + \mathcal{A} p^2) = m_{\text{th}}^2, \tag{6.22}$$

$$(\mathcal{A}'^2 p_0^2 - \mathcal{A}^2 p^2) = m_{\text{th}}^4 \left[\frac{\mathcal{T}_P^2}{p_0^2} - \frac{(1 - \mathcal{T}_P)^2}{p^2}\right]. \tag{6.23}$$

Also we note that

$$m_{\text{th}}^2 = \frac{g^2 C_F T^2}{8}\left(1 + 4\hat{\mu}^2\right), \tag{6.24a}$$

$$m_{\text{eff}}^2 = 4g^2 C_F M_{B,f}^2(T, \mu, m_f, q_f B) ; \quad M_B^2 = \sum_f M_{B,f}^2(T, \mu, m_f, q_f B). \tag{6.24b}$$

The magnetic mass[17] for a given flavor f is given as

$$M_{B,f}^2 = \frac{q_f B}{16\pi^2}\left[-\frac{1}{4}\aleph(z) - \frac{\pi T}{2m_f} - \frac{\gamma_E}{2}\right], \tag{6.26}$$

where $\hat{\mu} = \mu/2piT$ and the function $\aleph(z)$ is defined as

$$\aleph(z) = -2\gamma_E - 4\ln 2 + 14\zeta(3)\hat{\mu}^2 - 62\zeta(5)\hat{\mu}^4 + 254\zeta(7)\hat{\mu}^6 + \mathcal{O}(\hat{\mu}^8), \tag{6.27a}$$

$$\aleph(1, z) = -\frac{1}{12}\left(\ln 2 - \frac{\zeta'(-1)}{\zeta(-1)}\right) - (1 - 2\ln 2 - \gamma_E)\hat{\mu}^2 - \frac{7}{6}\zeta(3)\hat{\mu}^4 + \frac{31}{15}\zeta(5)\hat{\mu}^6 + \mathcal{O}(\hat{\mu}^8) \tag{6.27b}$$

In the limit of vanishing current quark mass ($m_f \to 0$), the magnetic mass in Eq. (6.26) exhibits a divergence. To address this issue, a regularization scheme has been employed, following the approach described in Refs. [107, 245], by introducing a mass cutoff equivalent to the fermion's thermal mass m_{th} the fermion. So, up to $\mathcal{O}(g^4)$ the one-loop quark free energy is obtained Ref. [54] as,

$$F_q = N_c N_f \left[-\frac{7\pi^2 T^4}{180}\left(1 + \frac{120}{7}\hat{\mu}^2 + \frac{240}{7}\hat{\mu}^4\right)\right.$$

---

[17]For finite chemical potential, the expression for f_1 a well-known fermionic function (also presented in Eq.(34) of Ref.[232]), is modified to account for the presence of the chemical potential. The updated form is given by:

$$f_1(y) = -\frac{1}{2}\ln\left(\frac{y}{4\pi}\right) + \frac{1}{4}\aleph(z) + \cdots. \tag{6.25}$$

This modification is evident in the expression for the magnetic mass in Eq.(6.26). At zero chemical potential, the magnetic mass simplifies to the following form[232]: $M_{B,f}^2 = \frac{q_f B}{16\pi^2}\left[\ln 2 - \frac{\pi T}{2m_f}\right]$.

$$
+ \quad \frac{m_{\text{th}}^2 T^2}{6} \left(1 + 12\hat{\mu}^2\right) + 4m_{\text{th}}^4 \left[\left(\frac{\pi^2}{3} - 2\right)\epsilon\right] \sum_{\{P\}} \frac{1}{P^4} \Bigg]
$$

$$
+ \quad N_c \sum_f m_{\text{eff}}^4 \left[\frac{2\pi^2}{9} + \left(\frac{4\zeta(3)}{3} - \frac{8}{3} - \frac{2\pi^2}{27}\right)\epsilon\right] \sum_{\{P\}} \frac{1}{P^4},
$$

$$
= \quad N_c N_f \left[-\frac{7\pi^2 T^4}{180}\left(1 + \frac{120}{7}\hat{\mu}^2 + \frac{240}{7}\hat{\mu}^4\right) + \frac{m_{\text{th}}^2 T^2}{6}\left(1 + 12\hat{\mu}^2\right) + \frac{m_{\text{th}}^4}{12\pi^2}\left(\pi^2 - 6\right)\right]
$$

$$
+ \quad N_c \sum_f \frac{m_{\text{eff}}^4}{16}\left(\frac{2}{9\epsilon} + \frac{1}{27}\left(12\ln\frac{\hat{\Lambda}}{2} - 6\aleph(z) + \frac{36\zeta(3)}{\pi^2} - 2 - \frac{72}{\pi^2}\right)\right)\Bigg],
$$

$$
= \quad N_c N_f \left[-\frac{7\pi^2 T^4}{180}\left(1 + \frac{120\hat{\mu}^2}{7} + \frac{240\hat{\mu}^4}{7}\right) + \frac{g^2 C_F T^4}{48}\left(1 + 4\hat{\mu}^2\right)\left(1 + 12\hat{\mu}^2\right)\right.
$$

$$
+ \frac{g^4 C_F^2 T^4}{768\pi^2}\left(1 + 4\hat{\mu}^2\right)^2\left(\pi^2 - 6\right) + \frac{g^4 C_F^2}{27 N_f} M_B^4\left(12\ln\frac{\hat{\Lambda}}{2} - 6\aleph(z) + \frac{36\zeta(3)}{\pi^2}\right.
$$

$$
\left.\left. -2 - \frac{72}{\pi^2}\right)\right] + \frac{2N_c g^4 C_F^2}{9\epsilon} M_B^4. \tag{6.28}
$$

It is important to observe that the $\mathcal{O}[g^2]$ term in Eq. (6.28) does not receive any magnetic corrections. Magnetic contributions only emerge at $\mathcal{O}[g^4]$, corresponding to $\mathcal{O}[(q_f B)^2]$. Additionally, the thermo-magnetic correction to the quark free energy in a weak magnetic field exhibits a $\mathcal{O}(1/\epsilon)$divergence, arising from the HTL approximation. To obtain a finite result, an appropriate counter term is required, which will be addressed in a later discussion.

6.1.2. One loop gluon free energy in presence of a weakly magnetized medium

The determinant of inverse of gluon propagator in Euclidean space can be obtained from Eq. (5.44) as

$$
\det\left(D_{\mu\nu,E}^{-1}(P_E)\right) = -\frac{P_E^2}{\xi}\left(-P_E^2 + c\right)\left\{\left(-P_E^2 + b\right)\left(-P_E^2 + d\right) - a^2\right\}
$$

$$
= -\frac{P_E^2}{\xi}\left(-P_E^2 + c\right)\left(-P_E^2 + \frac{b + d + \sqrt{(b-d)^2 + 4a^2}}{2}\right)
$$

$$
\times\left(-P_E^2 + \frac{b + d - \sqrt{(b-d)^2 + 4a^2}}{2}\right), \tag{6.29}
$$

with four eigenvalues: $-P_E^2/\xi$, $\left(-P_E^2 + c\right)$, $\left(-P_E^2 + \frac{b+d+\sqrt{(b-d)^2+4a^2}}{2}\right)$ and $\left(-P_E^2 + \frac{b+d-\sqrt{(b-d)^2+4a^2}}{2}\right)$. We note here that instead of a two fold degenerate transverse mode $(-P_E^2 + \Pi_T)$ in thermal medium as discussed earlier in subsection 5.2.3, now one has two distinct transverse modes, $(-P_E^2 + c)$ and $(-P_E^2 + d)$ as a does not contribute in $\mathcal{O}(eB)^2$ but starts contributing in $\mathcal{O}(eB)^4$ onwards. Using Eq. (6.29) in Eq. (6.7), the one-loop gluon free energy for hot magnetized medium is given by

$$
F_g = (N_c^2 - 1)\left[\mathcal{F}_g^1 + \mathcal{F}_g^2 + \mathcal{F}_g^3\right], \tag{6.30}
$$

where

$$
\mathcal{F}_g^1 = \frac{1}{2}\sum_{P_E} \ln\left(1 - \frac{b + d + \sqrt{(b-d)^2 + 4a^2}}{2P_E^2}\right), \tag{6.31a}
$$

$$
\mathcal{F}_g^2 = \frac{1}{2}\sum_{P_E} \ln\left(-P_E^2 + c\right), \tag{6.31b}
$$

$$
\mathcal{F}_g^3 = \frac{1}{2}\sum_{P_E} \ln\left(-P_E^2 + \frac{b + d - \sqrt{(b-d)^2 + 4a^2}}{2}\right). \tag{6.31c}
$$

Since we are considering small (weak) magnetic field approximation and intend to calculate all the quantities up to $O(eB)^2$, Eq.(6.31a),(6.31b),(6.31c) can be approximated as

$$\mathcal{F}_g^1 = \frac{1}{2} \sum_{P_E} \ln\left(1 - \frac{b}{P_E^2}\right), \tag{6.32a}$$

$$\mathcal{F}_g^2 = \frac{1}{2} \sum_{P_E} \ln\left(-P_E^2 + c\right), \tag{6.32b}$$

$$\mathcal{F}_g^3 = \frac{1}{2} \sum_{P_E} \ln\left(-P_E^2 + d\right). \tag{6.32c}$$

The different structure functions are derived in subsections 5.5.1 and 5.5.3, respectively, for the strong and weak field approximations. Thus the total gluonic free energy F_g is obtained in Ref. [54] as

$$
\begin{aligned}
F_g = &-\frac{d_A \pi^2 T^4}{45}\left[1 - \frac{15}{2}\hat{m}_D^2 + 30(\hat{m}_D^w)^3 + \frac{45}{8}\hat{m}_D^4\left(2\ln\frac{\hat{\Lambda}}{2} - 7 + 2\gamma_E + \frac{2\pi^2}{3}\right)\right] \\
&+ d_A\left[-\frac{m_D^2 \delta m_D^2}{(4\pi)^2}\left(\frac{\Lambda}{4\pi T}\right)^{2\epsilon}\left(\frac{1}{2\epsilon} + \ln 2 + \gamma_E\right) + \sum_f \frac{g^2(q_f B)^2}{(12\pi)^2}\frac{T^2}{m_f^2}\left(\frac{\Lambda}{4\pi T}\right)^{2\epsilon}\left[\frac{1}{\epsilon} + 4.97\right.\right. \\
&+ 3\hat{m}_D^2\left\{\frac{1 - \ln 2}{\epsilon^2} + \frac{1}{\epsilon}\left(\frac{7}{2} - \frac{\pi^2}{6} - \ln^2(2) - 2\gamma_E(\ln 2 - 1)\right) + 4.73\right\}\Big] \\
&- \sum_f \frac{g^2(q_f B)^2}{(12\pi)^2}\frac{\pi T}{32 m_f}\left(\frac{\Lambda}{4\pi T}\right)^{2\epsilon}\left[\left\{\frac{3}{8\epsilon^2} + \frac{1}{\epsilon}\left(\frac{21}{8} + \frac{3}{4}\frac{\zeta'(-1)}{\zeta(-1)} + \frac{27}{4}\ln 2\right) + 43.566\right.\right. \\
&+ \frac{3}{4}\hat{m}_D^2\left[\frac{1}{\epsilon^2}\left(5\pi^2 - \frac{609}{10} + \frac{114\ln 2}{5}\right) + \frac{1}{\epsilon}\left(30\zeta(3) - \frac{5779}{75} + \frac{121}{6}\pi^2 + \frac{114}{5}\ln^2(2)\right.\right. \\
&+ \frac{468}{25}\ln 2 + \gamma_E\left(10\pi^2 - \frac{609}{5} + \frac{228}{5}\ln 2\right)\Big) + 106.477\Big]\Big\} + \frac{8}{3\pi}\left\{\frac{3\ln 2 - 4}{2\epsilon} - 3.92\right. \\
&+ 3\hat{m}_D^2\left[\frac{1}{40\epsilon^2}\left(11 + 5\pi^2 - 92\ln 2\right) + \frac{1}{\epsilon}\left(\frac{3}{4}\zeta(3) + \frac{1557}{200} - \frac{\pi^2}{3} - \frac{23}{10}\ln^2(2)\right.\right. \\
&- \frac{168}{25}\ln 2 + \gamma_E\left(\frac{11}{20} + \frac{\pi^2}{4} - \frac{23}{5}\ln 2\right)\Big) - 1.86\Big]\Big\}\Big]\Big],
\end{aligned}
\tag{6.33}
$$

where we have also added the HTL counterterm [136] as given in Eq. (6.35), the scaled thermal Debye mass $\hat{m}_D = m_D/2\pi T$ and and the scaled thermo-magnetic Debye mass $\hat{m}_D^w = m_D^w/2\pi T$ in weak magnetic field as given in Eq. (5.199). The gluonic free energy, dependent on the magnetic field, exhibits both $\mathcal{O}(1/\epsilon)$ (UV) and $\mathcal{O}(1/\epsilon^2)$ (collinear and UV) divergences. These magnetic field-dependent divergences present in Eqs.(6.28) and (6.33) can be eliminated [11] by redefining the magnetic field contribution in the tree-level free energy F_0 in Eq. (6.1).

6.1.3. Total free energy and pressure in weak field approximation

1. Free energy

The total one-loop free energy of a weakly magnetized hot medium can be expressed using Eq. (6.1) as follows:

$$F = F_q + F_g + F_0 + \Delta\mathcal{E}_0. \tag{6.34}$$

The quark component of the free energy, F_q, includes both the HTL part (which is independent of the magnetic field) and the thermo-magnetic correction, as derived in Eq. (6.28). Similarly, the gluonic part consists of the HTL term as well as the thermo-magnetic correction. The $\Delta\mathcal{E}_0$ is the HTL counterterm given [136] as

$$\Delta\mathcal{E}_0 = \frac{d_A}{128\pi^2\epsilon}m_D^4, \tag{6.35}$$

As mentioned in the previous section, the divergences associated with the external magnetic field B in Eqs. (6.28) and (6.33) can be eliminated by modifying the magnetic field contribution in the tree-level free energy, following the procedure described in[11], as [54].

$$
\begin{aligned}
F_0 &= \frac{B^2}{2} \rightarrow \frac{B^2}{2}\left[1 - \frac{4N_c g^4 C_F^2}{9\epsilon}\frac{M_B^4}{B^2} + \frac{m_D^2 \delta m_D^2}{\epsilon(4\pi)^2 B^2} - \sum_f \frac{g^2 q_f^2}{(12\pi)^2}\frac{2T^2}{m_f^2}\left[\frac{1}{\epsilon}\right.\right. \\
&+ \left. 3\hat{m}_D^2\left\{\frac{1-\ln 2}{\epsilon^2} + \frac{1}{\epsilon}\left(\frac{7}{2} - \frac{\pi^2}{6} - \ln^2(2) - 2\left(\gamma_E + \ln\frac{\hat{\Lambda}}{2}\right)(\ln 2 - 1)\right)\right\}\right] \\
&+ \sum_f \frac{g^2 q_f^2}{(12\pi)^2}\frac{\pi T}{16 m_f}\left[\left\{\frac{3}{8\epsilon^2} + \frac{1}{\epsilon}\left(\frac{21}{8} + \frac{3}{4}\frac{\zeta'(-1)}{\zeta(-1)} + \frac{27}{4}\ln 2 + \frac{3}{4}\ln\frac{\hat{\Lambda}}{2}\right)\right.\right. \\
&+ \frac{3}{4}\hat{m}_D^2\left[\frac{1}{\epsilon^2}\left(5\pi^2 - \frac{609}{10} + \frac{114\ln 2}{5}\right) + \frac{1}{\epsilon}\left(30\zeta(3) - \frac{5779}{75} + \frac{121}{6}\pi^2 + \frac{114}{5}\ln^2(2)\right.\right. \\
&+ \left. \frac{468}{25}\ln 2 + \left(\gamma_E + \ln\frac{\hat{\Lambda}}{2}\right)\left(10\pi^2 - \frac{609}{5} + \frac{228}{5}\ln 2\right)\right)\bigg]\bigg\} + \frac{8}{3\pi}\left\{\frac{3\ln 2 - 4}{2\epsilon}\right. \\
&+ 3\hat{m}_D^2\left[\frac{1}{40\epsilon^2}\left(11 + 5\pi^2 - 92\ln 2\right) + \frac{1}{\epsilon}\left(\frac{3}{4}\zeta(3) + \frac{1557}{200} - \frac{\pi^2}{3} - \frac{23}{10}\ln^2(2)\right.\right. \\
&- \left.\left.\left.\left.\left. \frac{168}{25}\ln 2 + \left(\gamma_E + \ln\frac{\hat{\Lambda}}{2}\right)\left(\frac{11}{20} + \frac{\pi^2}{4} - \frac{23}{5}\ln 2\right)\right)\right]\right\}\right]\right].
\end{aligned}
$$

(6.36)

So, the renormalized total free energy [54] becomes

$$
F = F_q^r + F_g^r
$$

(6.37)

where,

$$
\begin{aligned}
F_q^r &= N_c N_f\left[-\frac{7\pi^2 T^4}{180}\left(1 + \frac{120\hat{\mu}^2}{7} + \frac{240\hat{\mu}^4}{7}\right) + \frac{g^2 C_F T^4}{48}\left(1 + 4\hat{\mu}^2\right)\left(1 + 12\hat{\mu}^2\right)\right. \\
&+ \frac{g^4 C_F^2 T^4}{768\pi^2}\left(1 + 4\hat{\mu}^2\right)^2\left(\pi^2 - 6\right) + \frac{g^4 C_F^2}{27 N_f}M_B^4\left(12\ln\frac{\hat{\Lambda}}{2} - 6\aleph(z) + \frac{36\zeta(3)}{\pi^2}\right. \\
&- \left.\left. 2 - \frac{72}{\pi^2}\right)\right],
\end{aligned}
$$

(6.38)

and

$$
\begin{aligned}
\frac{F_g^r}{d_A} &= -\frac{\pi^2 T^4}{45}\left[1 - \frac{15}{2}\hat{m}_D^2 + 30(\hat{m}_D^w)^3 + \frac{45}{8}\hat{m}_D^4\left(2\ln\frac{\hat{\Lambda}}{2} - 7 + 2\gamma_E + \frac{2\pi^2}{3}\right)\right] \\
&- \pi^2 T^4 \hat{m}_D^2 \delta\hat{m}_D^2\left(\gamma_E + \ln\hat{\Lambda}\right) + \sum_f \frac{g^2(q_f B)^2}{(12\pi)^2}\frac{T^2}{m_f^2}\left[4.97 + 2\ln\frac{\hat{\Lambda}}{2}\right. \\
&+ 3\hat{m}_D^2\left\{2(1 - \ln 2)\ln^2\frac{\hat{\Lambda}}{2} + 2\left(\frac{7}{2} - \frac{\pi^2}{6} - \ln^2(2) - 2\gamma_E(\ln 2 - 1)\right)\ln\frac{\hat{\Lambda}}{2} + 4.73\right\}\bigg] \\
&- \sum_f \frac{g^2(q_f B)^2}{(12\pi)^2}\frac{\pi T}{32 m_f}\left[\left\{\frac{3}{4}\ln^2\frac{\hat{\Lambda}}{2} + 2\ln\frac{\hat{\Lambda}}{2}\left(\frac{21}{8} + \frac{3}{4}\frac{\zeta'(-1)}{\zeta(-1)} + \frac{27}{4}\ln 2\right) + 43.566\right.\right. \\
&+ \frac{3}{4}\hat{m}_D^2\left[2\ln^2\frac{\hat{\Lambda}}{2}\left(5\pi^2 - \frac{609}{10} + \frac{114\ln 2}{5}\right) + 2\ln\frac{\hat{\Lambda}}{2}\left(30\zeta(3) - \frac{5779}{75} + \frac{121}{6}\pi^2 + \frac{114}{5}\ln^2(2)\right.\right. \\
&+ \left.\left. \frac{468}{25}\ln 2 + \gamma_E\left(10\pi^2 - \frac{609}{5} + \frac{228}{5}\ln 2\right)\right) + 106.477\right]\bigg\} + \frac{8}{3\pi}\left\{(3\ln 2 - 4)\ln\frac{\hat{\Lambda}}{2} - 3.92\right. \\
&+ 3\hat{m}_D^2\left[\frac{1}{20}\ln^2\frac{\hat{\Lambda}}{2}\left(11 + 5\pi^2 - 92\ln 2\right) + 2\ln\frac{\hat{\Lambda}}{2}\left(\frac{3}{4}\zeta(3) + \frac{1557}{200} - \frac{\pi^2}{3} - \frac{23}{10}\ln^2(2)\right.\right.
\end{aligned}
$$

$$- \frac{168}{25}\ln 2 + \gamma_E \left(\frac{11}{20} + \frac{\pi^2}{4} - \frac{23}{5}\ln 2\right)\bigg) - 1.86\bigg]\bigg\}\bigg]. \tag{6.39}$$

2. Pressure

The pressure of hot and dense QCD matter in one-loop HTLpt, considering the presence of a weak magnetic field, can now be directly expressed from the one-loop free energy as follows:

$$P(T, \mu, B, \Lambda) = -F(T, \mu, B, \Lambda), \tag{6.40}$$

whereas the ideal gas limit of the pressure [54] reads as

$$P_{\text{Ideal}}(T, \mu) = \frac{B^2}{2} + N_c N_f \frac{7\pi^2 T^4}{180} \left(1 + \frac{120}{7}\hat{\mu}^2 + \frac{240}{7}\hat{\mu}^4\right) + (N_c^2 - 1)\frac{\pi^2 T^4}{45}. \tag{6.41}$$

6.1.4. Result within high temperature expansion in weak field approximation

Now, we discuss the main results in weak field approximation. In Fig. 6.1, we show the temperature dependence of the scaled pressure compared to the ideal gas value for hot and dense magnetized QCD matter in one-loop HTLpt within the weak field approximation. The results are presented for various magnetic field strengths: $|eB| = 0, , m_\pi^2/2, , m_\pi^2, ,$ and, $3m_\pi^2/2$. The left panel of Fig.6.1 shows the pressure for zero chemical potential, $\mu = 0$, while the right panel corresponds to $\mu = 0.3$ GeV. For $|eB| = 0$, we recover the standard one-loop HTLpt pressure, as noted in previous works [125–127, 137, 148, 149, 246–248]. Both plots reveal that the pressure at low temperatures ($T < 0.8$ GeV) is significantly influenced by the presence of the magnetic field. However, at high temperatures ($T \geq 0.8$ GeV), the pressure becomes almost independent of the magnetic field, as the temperature dominates and the weak field approximation ($|eB| < m_{\text{th}}^2 < T^2$) holds.
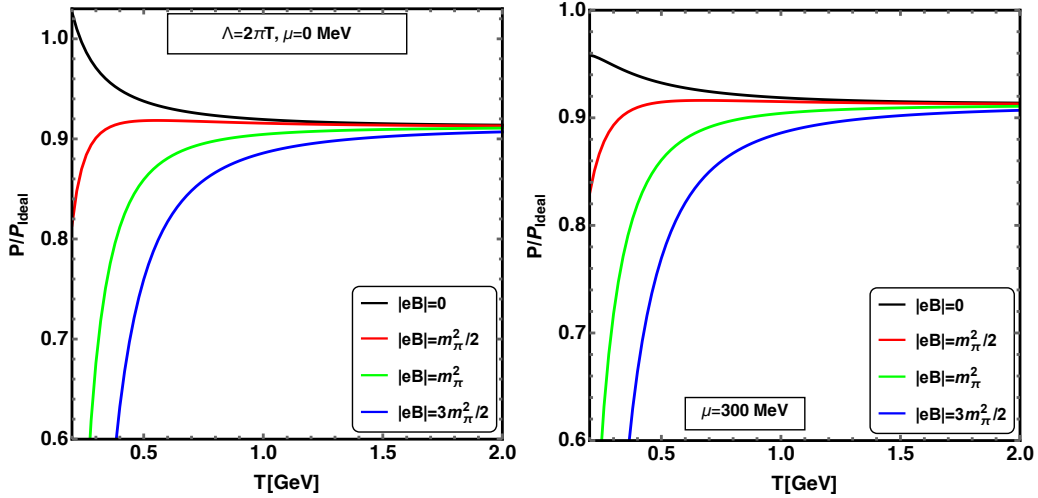
Figure 6.1: The left panel depicts the variation of the scaled one-loop pressure with temperature for $N_f = 2$ at $\mu = 0$, while the right panel shows the same variation for $\mu = 300$ MeV. Both panels illustrate the behaviour under weak magnetic fields of varying strengths: $|eB| = 0$, $m_\pi^2/2$, m_π^2, and $3m_\pi^2/2$. In the right panel, where $\mu \neq 0$, the renormalization scales are set as defined in Sec. 5.7 of the text.

Additionally, we highlight a challenge encountered with HTLpt for $|eB| = 0$. The one-loop HTLpt expansion leads to overcounting of certain contributions in strong coupling (g), as the loop expansion and coupling expansion are asymmetrical in HTLpt. This asymmetry results in an infinite series in g at each loop order. At leading order in HTLpt, only the perturbative coefficients for g^0 and g^3 are correctly obtained, and higher-order terms in g are introduced at each
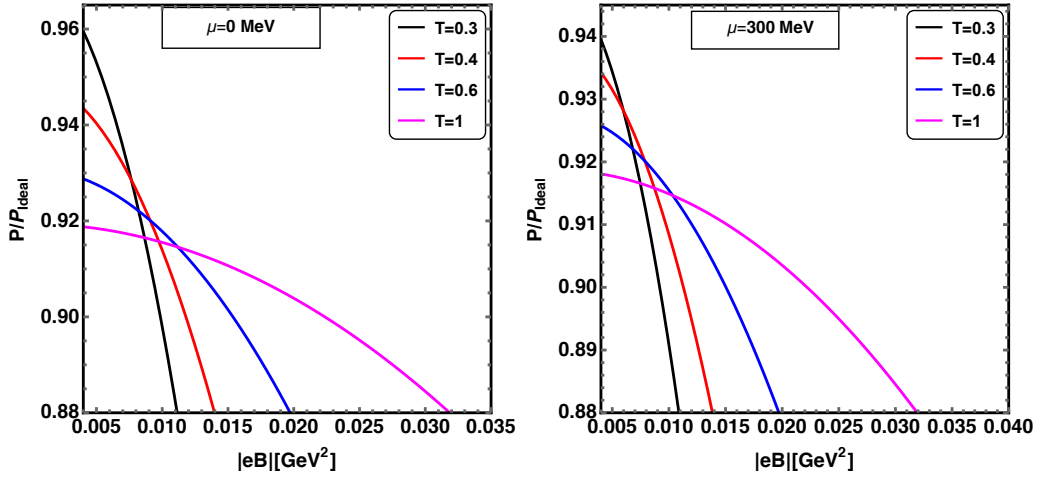
Figure 6.2: The left panel illustrates the variation of the scaled one-loop pressure with respect to $|eB|$ for $N_f = 2$ at $\mu = 0$, while the right panel presents the corresponding variation for $\mu = 300$ MeV. The plots are generated at temperatures $T = 0.3, 0.4, 0.6,$ and 1 GeV. The renormalization scales employed in the calculations are defined in Sec. 5.7 of the text.

subsequent loop level. This issue can be corrected by extending the calculation to higher loop orders [128, 129, 131–136, 139, 140, 233?]. Moreover, we observe that the pressure is slightly lower in the presence of a non-zero chemical potential (right panel) compared to when $\mu = 0$, for a given $|eB|$.

From Fig. 6.2, it is evident that as the temperature T increases, the slope of the curve becomes smaller. This reinforces the idea that, within the weak field approximation, the impact of the magnetic field reduces as the temperature rises. It implies that at low temperatures, the magnetic field has a significant effect, but at higher temperatures, its influence becomes increasingly insignificant.
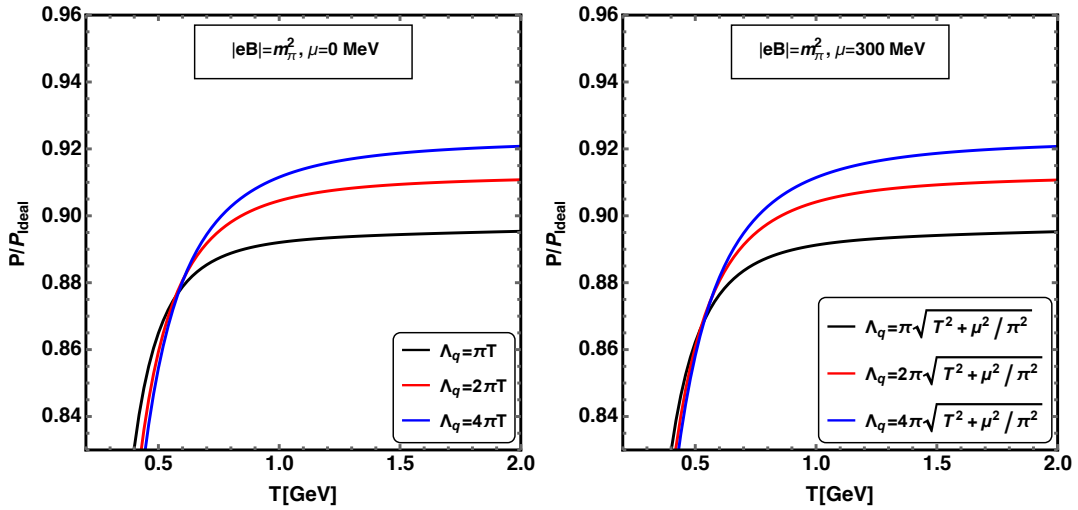
Figure 6.3: The plots illustrate the variation of the scaled one-loop pressure with temperature for $N_f = 2$. The left panel corresponds to $\mu = 0$, while the right panel shows results for $\mu = 300$ MeV. The pressure is evaluated in the presence of a weak magnetic field of strength $eB = m_\pi^2$. The calculations consider different renormalization scales for gluons: $\Lambda_g = \pi T, 2\pi T,$ and $4\pi T$, are considered, and the renormalization scale for quarks is specified in the inset.

To examine the sensitivity to the renormalization scale $\Lambda_{q,g}$, we show in Fig. 6.3 the temperature dependence of the scaled one-loop pressure in the presence of a constant weak magnetic field, while varying $\Lambda_{q,g}$ by a factor of two around its central value for both zero and finite chemical potential. The results reveal a moderate dependence on the renormalization scale
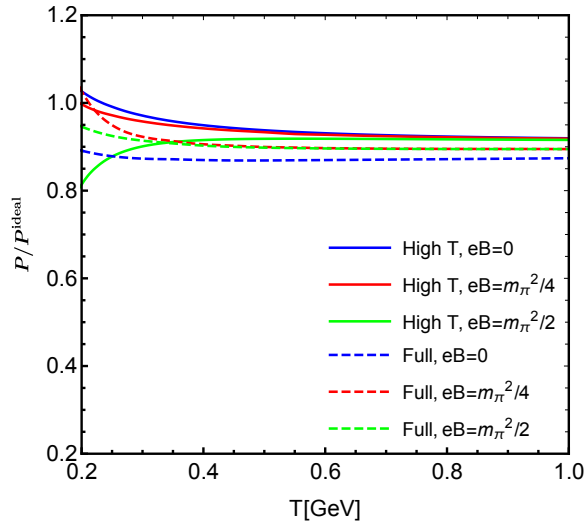
Figure 6.4: The plots present a comparison of the pressure of QCD matter computed with and without employing the high-temperature expansion for different magnetic field strengths: $eB = 0$, $m_\pi^2/4$, and $m_\pi^2/2$, with $N_f = 2$. Calculations labeled as "Full" correspond to those performed without applying the high-temperature expansion.

$\Lambda_{q,g}$. To further minimize the renormalization scale-dependent uncertainty, higher-loop calculations and log resummation may be required.

6.1.5. Comparison of high temperature expansion with full results

In this section, we aim to justify our use of the high-temperature expansion by comparing the results obtained with and without this approximation, within the framework of HTL perturbation theory. The full numerical results are given in Appendix D of Ref [54]. Figure 6.4 presents a comparison of the scaled pressure of QCD matter computed using both methods for different magnetic field strengths. The solid lines correspond to the results from the high-temperature expansion, while the dashed lines represent the results without it. As seen in the figure, the two sets of results are nearly identical for a given field strength, with noticeable differences only at low temperatures. This confirms that the high-temperature expansion offers an accurate analytical expression for the pressure. While this expansion is not strictly part of HTL perturbation theory, it is particularly useful for higher-order loops, as it avoids the complex calculations involved with quasiparticle poles and Landau damping. The high-temperature expansion has been widely used in the literature for HTL at leading, next-to-leading, and next-to-next-to-leading orders. In a similar manner, we apply this approximation here in the presence of a magnetic field, and the following results are based on this approach.

6.1.6. Quark number susceptibility in weak field approximation

The renormalized quark-gluon free energy in weak field approximation is given in Eq. (6.37) along with quark one is given in Eq. (6.38) and the gluon one is given Eq. (6.39). In Ref. [56], the second-order quark number susceptibility (QNS) in the weak field limit is derived by relating the free energy or pressure, as outlined in Eq. (6.8). This method provides a calculation of the QNS, reflecting how the system's response to quark number fluctuations is modified by the presence of a weak magnetic field. The second-order QNS of free quarks and gluons in a thermal environment can be written as:

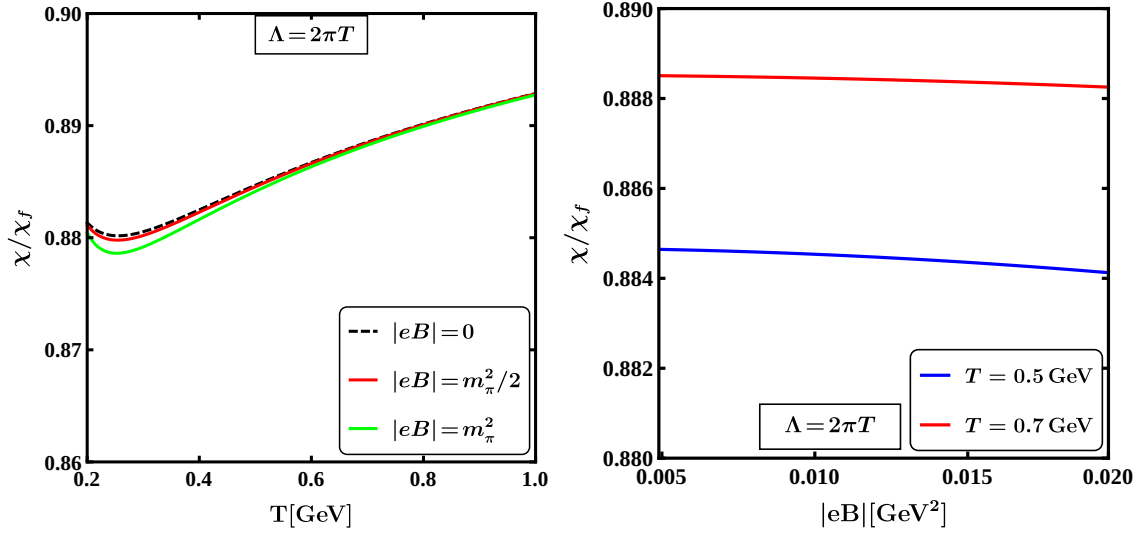$$\chi_f = \frac{1}{3} N_c N_f T^2. \tag{6.42}$$

Figure 6.5: The plots illustrate the variation of the second-order QNS, scaled by its thermal free-field value, as a function of temperature (left panel) and magnetic field strength (right panel). These results are shown for a fermion mass of $m_f = 5$ MeV and $N_f = 3$.
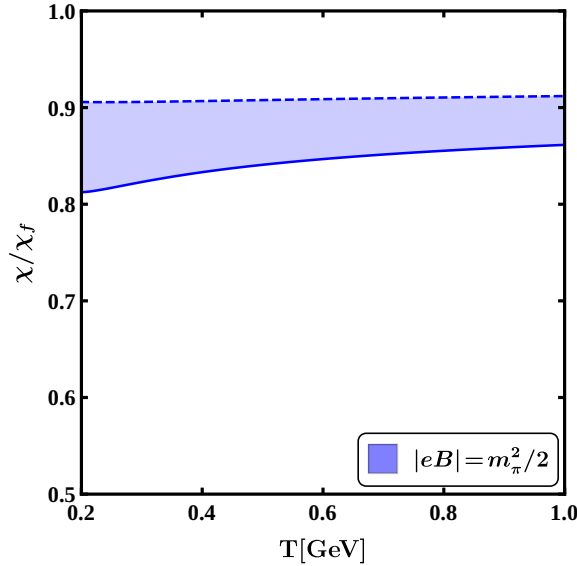

Figure 6.6: The plots depict the sensitivity of the second-order QNS, scaled by the free field value,scaled by its free-field value, to the choice of renormalization scale in the presence of a weak magnetic field for $N_f = 3$. The dashed curves correspond to the renormalization scale $\Lambda = \pi T$, while the solid curves represent $\Lambda = 4\pi T$.

The left panel of Fig. 6.5 depicts the variation of the scaled second-order QNS with temperature for various magnetic field strengths, employing a central renormalization scale of $\Lambda = 2\pi T$. The weak field influence acts as a minor adjustment to the thermal medium, with the second-order QNS in the weak field case being nearly identical to that in the thermal medium. As temperature increases, the value of the second-order QNS rises and approaches the free field value at sufficiently high temperatures. The effect of the magnetic field on the second-order QNS is more pronounced at lower temperatures. As seen in the right panel of Fig. 6.5, the second-order QNS gradually decreases as the magnetic field strength increases. In Fig. 6.6, the dependence of the second-order weak field QNS on the renormalization scale is investigated by varying the scale within a factor of two around the central value $\Lambda = 2\pi T$.

6.1.7. Chiral susceptibility in weak field approximation

We examine a magnetized QCD medium in the weak magnetic field limit, where we assume the hierarchy of scales, $\sqrt{|q_f B|} < m_{\text{th}} \sim gT < T$. Treating $q_f B$ as a small perturbation, the Schwinger propagator for a fermion in the presence of a weak magnetic field can be expanded and expressed up to $\mathcal{O}[(q_f B)^2]$ from Eq. (5.56) as

$$
\begin{aligned}
S(K) &= \frac{\slashed{K} + m_f}{K^2 - m_f^2} + i\gamma^1\gamma^2 \frac{\slashed{K}_\parallel + m_f}{(K^2 - m_f^2)^2}(q_f B) + 2\left[\frac{\{(K \cdot u)\slashed{u} - (K \cdot n)\slashed{n}\} - \slashed{K}}{(K^2 - m_f^2)^3} - \frac{k_\perp^2(\slashed{K} + m_f)}{(K^2 - m_f^2)^4} \right](q_f B)^2 \\
&\quad + \mathcal{O}\left[(q_f B)^3\right] \\
&= S_0 + S_1 + S_2 + \mathcal{O}[(q_f B)^3].
\end{aligned}
\tag{6.43}
$$

We can express the chiral condensate for a free fermion in a weak magnetic field up to $\mathcal{O}[(q_f B)^2]$ using Eq. (6.43) as follows:

$$
\begin{aligned}
\langle \bar{q}q \rangle_f &= -N_c N_f \sum_{\{P\}} \text{Tr}\left[S_0(P) + S_1(P) + S_2(P) \right], \\
&= -4m_f N_c N_f \sum_{\{P\}} \left[\frac{1}{P^2 - m_f^2} - 2(q_f B)^2 \frac{p_\perp^2}{(P^2 - m_f^2)^4} \right].
\end{aligned}
\tag{6.44}
$$

The chiral susceptibility for a free fermion in the presence of a weak magnetic field is computed in Ref. [57] using the definition provided in Eq. (6.11) as

$$
\begin{aligned}
\chi_c = -\frac{\partial \langle \bar{q}q \rangle}{\partial m_f}\bigg|_{m_f = 0} &= 4N_c N_f \sum_{\{P\}} \left[\frac{1}{P^2} - 2(q_f B)^2 \frac{p_\perp^2}{(P^2)^4} \right] \\
&= \frac{N_c N_f}{6} T^2 \left[1 + 12\hat{\mu}^2 - (q_f B)^2 \frac{\beth(z)}{16\pi^4 T^4} \right],
\end{aligned}
\tag{6.45}
$$

where $\hat{\mu} = \mu/2\pi T$. μ is the quark chemical potential. The $\beth(z)$ is given as

$$
\beth(z) = -4\left[7\zeta(3) - 186\zeta(5)\hat{\mu}^2 + 1905\zeta(7)\hat{\mu}^4 - 14308\zeta(9)\hat{\mu}^6 \right] + \mathcal{O}(\hat{\mu}^8).
\tag{6.46}
$$

Based on the Dyson-Schwinger equation, the effective inverse propagator for a massive fermion can be expressed as [57]

$$
S_{\text{eff}}^{-1} = \slashed{P} - m_f \mathbb{1} - \Sigma.
\tag{6.47}
$$

where the general covariant form of the fermion self-energy in the presence of a weak thermo-magnetic field is provided in Eq. (5.7). Using Eq. (5.7), the form of the inverse propagator for a massive fermion in a thermo-magnetic medium can be expressed as

$$
S_{\text{eff}}^{-1}(P) = (1+a)\slashed{P} + b\slashed{u} + c'\gamma_5\slashed{u} + d'\gamma_5\slashed{n} - m_f \mathbb{1}.
\tag{6.48}
$$

To calculate the chiral susceptibility in the presence of a weak magnetic field, we need the effective fermion propagator, as outlined in Eqs. (6.10) and (6.11). This requires inverting Eq.(6.48) to obtain the effective fermion propagator. In the massless case, the inversion of the effective inverse propagator is straightforward, leading to a general form for the effective propagator expressed in terms of $\slashed{P}$, $\slashed{u}$, $\gamma_5\slashed{u}$, and $\gamma_5\slashed{n}$. For the massive case, where the propagator involves Dirac matrices like $\slashed{P}$, $\slashed{u}$, $\gamma_5\slashed{u}$, $\gamma_5\slashed{n}$, and $\mathbb{1}$, we apply a method used in Refs. [57, 249] to derive the structure of the effective propagator.

To compute the inverse of a matrix R, we start by selecting a matrix R. Multiplying R with R, we obtain a new matrix U defined as

$$
U = MR.
\tag{6.49}
$$

The inverse of the matrix M can now be expressed as

$$
M^{-1} = RU^{-1}.
\tag{6.50}
$$

In this scenario, we aim to determine the inverse of the matrix S_{eff}^{-1}. To simplify the process, it is crucial to select R such that the resulting U from Eq. (6.49) takes on a particularly straightforward form. This strategic choice of R ensures that inverting U becomes a manageable task, ultimately facilitating the computation of the inverse of the target matrix S_{eff}^{-1}.

Thus we choose R as

$$R \;=\; (1+a)\,\slashed{P} + b\,\slashed{u} - c'\gamma_5\,\slashed{u} - d'\gamma_5\,\slashed{n} - m_f\mathbb{I}. \tag{6.51}$$

From Eqs. (6.48) and (6.49), we have

$$U = S_{\text{eff}}^{-1}R \;=\; \alpha\,\slashed{P} + \beta\,\slashed{u} + \delta\,\gamma_5 + \lambda\,\mathbb{I}, \tag{6.52}$$

where

$$\begin{aligned}
\alpha &= -2(1+a)\,m_f,\\
\beta &= -2b\,m_f,\\
\delta &= 2((1+a)c'p_0 + bc' + (1+a)d'p_3),\\
\lambda &= (1+a)^2P^2 + b^2 + c'^2 - d'^2 + m_f^2 + 2(1+a)bp_0.
\end{aligned} \tag{6.53}$$

We can now easily invert the matrix U to get

$$U^{-1} \;=\; \frac{1}{N^2}(\alpha\,\slashed{P} + \beta\,\slashed{u} + \delta\,\gamma_5 - \lambda\,\mathbb{I}), \tag{6.54}$$

where

$$N^2 \;=\; \alpha^2 P^2 + 2\alpha\beta p_0 + \beta^2 + \delta^2 - \lambda^2. \tag{6.55}$$

Using Eq. (6.50), the effective fermion propagator S_{eff} can be expressed as

$$S_{\text{eff}} \;=\; RU^{-1} = \left((1+a)\,\slashed{P} + b\,\slashed{u} - c'\gamma_5\,\slashed{u} - d'\gamma_5\,\slashed{n} - m_f\,\mathbb{I}\right)\frac{\alpha\,\slashed{P} + \beta\,\slashed{u} + \delta\,\gamma_5 - \lambda\,\mathbb{I}}{\alpha^2 P^2 + 2\alpha\beta p_0 + \beta^2 + \delta^2 - \lambda^2}. \tag{6.56}$$

The dispersion relation for a massive fermion in a weakly magnetized thermal medium is determined by equating the denominator of the effective propagator to zero. This equation defines the relationship between the fermion's energy and momentum under the influence of both the thermal environment and the magnetic field. Using the effective quark propagator given in Eq. (6.56), the chiral condensate $\langle\bar{q}q\rangle$ is expressed as

$$\begin{aligned}
\langle\bar{q}q\rangle &= -N_c\,N_f \sum_{\{P\}}\!\!\!\!\!\!\diagdown\;\; \mathsf{Tr}[S_{\text{eff}}(P)]\\
&= 4m_f N_c\,N_f \sum_{\{P\}}\!\!\!\!\!\!\diagdown\;\; \frac{(1+a)^2\,P^2 + 2(1+a)\,b\,p_0 + b^2 + d'^2 - c'^2 - m_f^2}{\alpha^2 P^2 + 2\alpha\beta p_0 + \beta^2 + \delta^2 - \lambda^2}.
\end{aligned} \tag{6.57}$$

The chiral susceptibility in the massless limit can be determined from Eq. (6.57) as

$$\begin{aligned}
\chi_c &= -\frac{\partial\langle\bar{q}q\rangle}{\partial m_f}\Bigg|_{m_f=0}\\
&= -4N_c\,N_f \sum_{\{P\}}\!\!\!\!\!\!\diagdown\;\; \frac{(1+a)^2\,P^2 + 2(1+a)\,b\,p_0 + b^2 + d'^2 - c'^2}{4\Big[(1+a)c'\,p_0 + bc' + (1+a)d'\,p_3\Big]^2 - \Big[(1+a)^2P^2 + b^2 + c'^2 - d'^2 + 2(1+a)\,b\,p_0\Big]^2},
\end{aligned} \tag{6.58}$$

where the expressions of various structure functions are calculated in Ref. [57].

Using the structure functions the expression for the chiral susceptibility [57] as

$$\begin{aligned}
\chi_c &= \frac{N_c N_f}{6}T^2\Bigg[1 + 12\hat{\mu}^2 + \frac{3}{\pi^2}\left(\frac{\Lambda}{4\pi T}\right)^{2\epsilon}\left(\frac{1}{\epsilon} - \aleph(z)\right)\frac{m_{\text{th}}^2}{T^2}\\
&\quad + \frac{1}{\pi^2}\left(\frac{\Lambda}{4\pi T}\right)^{2\epsilon}\left(\frac{1}{\epsilon} + \frac{4}{3} - \aleph(z)\right)\frac{m_{\text{eff}}'^2}{T^2} + \frac{\beth(z)}{32\pi^4}\left(\pi^2 - 6\right)\frac{m_{\text{th}}^4}{T^4} - \frac{\beth(z)}{24\pi^4}\left(\pi^2 - 6\right)\frac{m_{\text{eff}}^4}{T^4}\Bigg].
\end{aligned} \tag{6.59}$$

We note that the logarithmic divergence comes from the thermal part. A new divergence appears in presence of the

magnetic field. One canrenormalize the chiral susceptibility within $\overline{MS}$ renormalization scheme using the following counter term [57] as

$$\Delta\chi_c^{counter} = -\frac{N_cN_f}{6\pi^2\epsilon}\left(3m_{\text{th}}^2 + m_{\text{eff}}'^2\right).$$ (6.60)

The renormalized chiral susceptibility is obtained as [57]

$$
\begin{aligned}
\chi_c =& \frac{N_cN_f}{6}T^2\left[1 + 12\hat{\mu}^2 + \frac{3}{\pi^2}\left(2\ln\hat{\Lambda} - 2\ln 2 - \aleph(z)\right)\frac{m_{\text{th}}^2}{T^2}\right.\\
&+ \frac{1}{3\pi^2}\left(4 - 3\aleph(z) + 6\ln\hat{\Lambda} - 6\ln 2\right)\frac{m_{\text{eff}}'^2}{T^2} + \frac{\beth(z)}{32\pi^4}\left(\pi^2 - 6\right)\frac{m_{\text{th}}^4}{T^4} - \frac{\beth(z)}{24\pi^4}\left(\pi^2 - 6\right)\frac{m_{\text{eff}}^4}{T^4}\bigg],
\end{aligned}
$$ (6.61)

with $\hat{\Lambda} = \Lambda/2\pi T$ and $\hat{\mu} = \mu/2\pi T$. The result obtained is fully analytic in the presence of both chemical potential and weak magnetic field. It is important to note that Eq.(6.61) contains terms of order $\mathcal{O}[(q_f B)^0]$ and $\mathcal{O}[(q_f B)^2]$. The $\mathcal{O}[(q_f B)^0]$ term reproduces the thermal chiral susceptibility without chemical potential, as derived in Ref. [151]. On the other hand, the $\mathcal{O}[(q_f B)^2]$ terms represent the thermo-magnetic corrections to the thermal chiral susceptibility. To obtain the results, we take into account the magnetic field-dependent running coupling, as discussed in subsection 5.7.
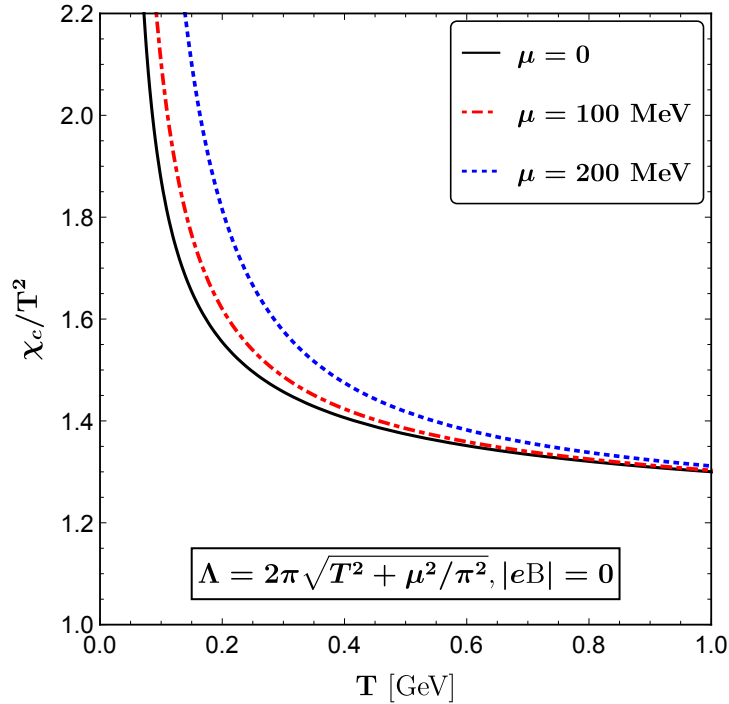
Figure 6.7: The plot shows the variation of chiral susceptibility, scaled by T^2, as a function of temperature for chemical potentials 0, 100, and 200 MeV in the absence of an external magnetic field.

In Fig.6.7, the temperature dependence of the chiral susceptibility, scaled by temperature squared, is shown for both zero and non-zero quark chemical potentials in the absence of a magnetic field. The impact of the quark chemical potential is more noticeable at low temperatures, as seen in the figure. A similar plot for the thermal QCD medium at zero chemical potential was presented in Ref.[151]. At lower temperatures, the chiral susceptibility increases sharply for both zero and non-zero chemical potentials. However, this increase does not indicate a chiral phase transition; rather, it arises due to the temperature-dependent behaviour of the coupling constant and the chosen renormalization scale, as explained in Ref. [151]. At high temperatures, the chiral susceptibility approaches the free-field value.
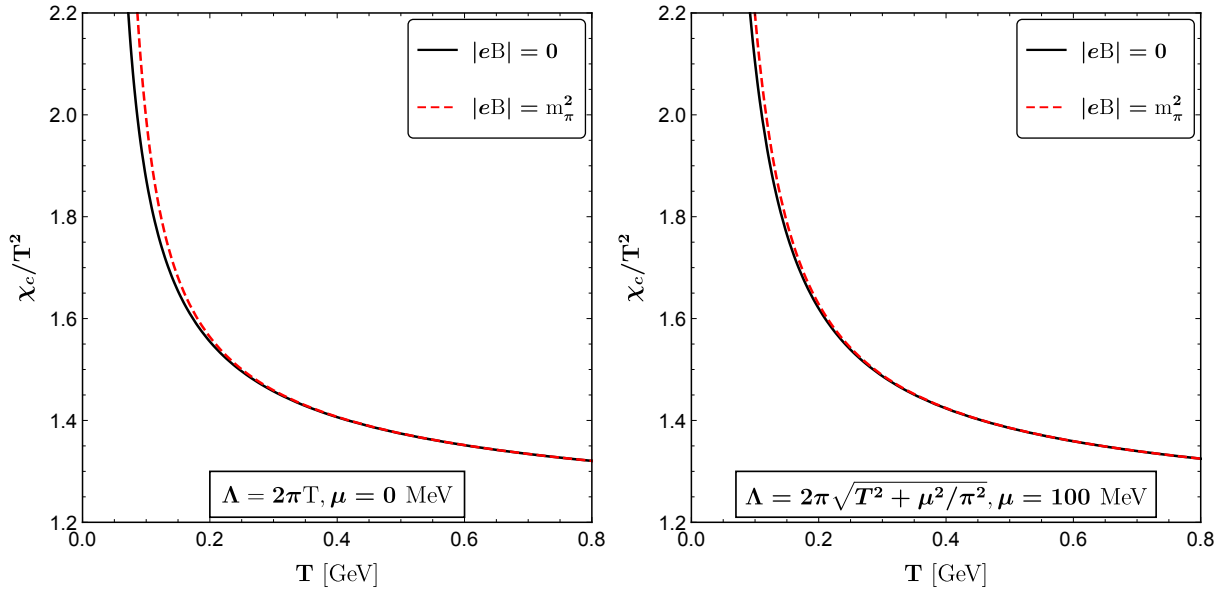
Figure 6.8: The plots illustrate the variation of chiral susceptibility, scaled by T^2, as a function of temperature T for two magnetic field strengths, $|eB| = 0$ and $|eB| = m_\pi^2$. The left panel corresponds to a quark chemical potential $\mu = 0$ MeV, while the right panel shows the results for $\mu = 100$ MeV.

Figure 6.8 presents the variation of chiral susceptibility scaled with temperature squared as a function of temperature for both zero and finite magnetic fields. The left panel shows the impact of a weak magnetic field on the chiral susceptibility at zero quark chemical potential, while the right panel illustrates the same for finite quark chemical potential. In the low-temperature regime, the chiral susceptibility is slightly higher in the presence of a magnetic field compared to the thermal medium. However, since we are considering a weak magnetic field, the increase in susceptibility due to the field is modest. As the temperature rises, the influence of the magnetic field diminishes, with temperature eventually dominating the behaviour. It is important to note that the scale hierarchy for a weakly magnetized medium is satisfied for temperatures above approximately $T > 0.14$ GeV, as we have chosen $|eB| = m_\pi^2 = 0.14^2$ GeV^2 in Fig. 6.8. Therefore, the weak field and HTL approximations hold true at high temperatures. This aligns with our analysis, as we are calculating the chiral susceptibility of the medium within the perturbative regime.

Figure 6.9 clearly illustrates the impact of the magnetic field, showing how the scaled chiral susceptibility varies with the magnetic field at a fixed temperature of $T = 200$ MeV. It is observed that the chiral susceptibility increases gradually with the magnetic field, both with and without the presence of chemical potential.

Figure 6.10 demonstrates the sensitivity of the chiral susceptibility to the renormalization scale in the presence of a constant weak magnetic field. In this figure, the chiral susceptibility scaled by T^2 is plotted against temperature for both zero (left panel) and finite (right panel) chemical potential. The renormalization scale, Λ, is varied by a factor of 2 around its central value $2\pi\sqrt{T^2 + \mu^2/\pi^2}$.

It is important to note that the HTL approximation remains valid above the phase transition temperature, where the scale hierarchy $\sqrt{|q_f B|} < gT < T$ is preserved. In the plots, we have displayed the chiral susceptibilities at low temperatures primarily to highlight the steep increase observed in the curves.
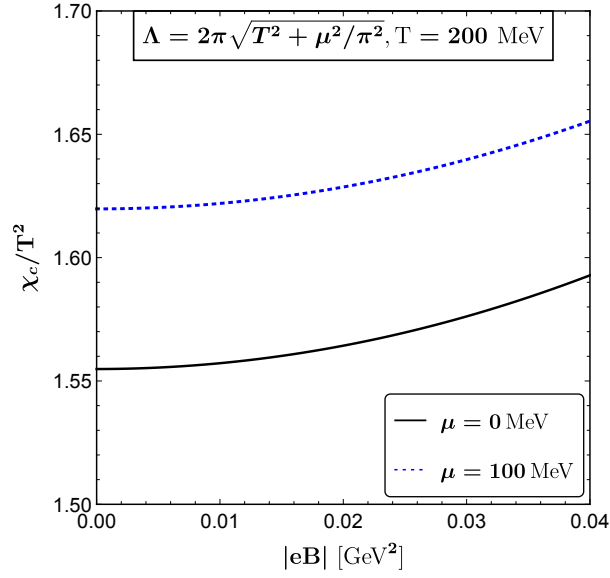
Figure 6.9: The plots depict the scaled chiral susceptibility as a function of the magnetic field strength $|eB|$ at temperatures $T = 0.2$ GeV. Results are shown for two quark chemical potentials: $\mu = 0$ MeV and $\mu = 100$ MeV.
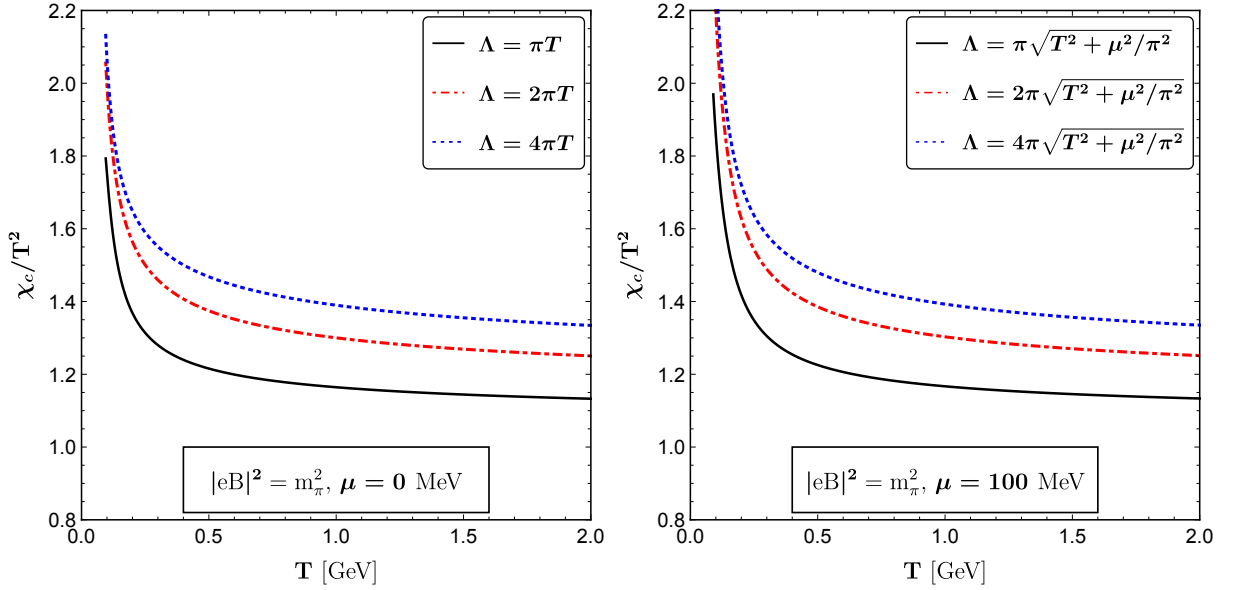

Figure 6.10: The chiral susceptibility, scaled by T^2, is shown as a function of temperature for a magnetic field strength of $|eB| = m_\pi^2$, with varying renormalization scales.

6.2. Thermodynamics in Strong Field Approximation

6.2.1. One loop quark free energy in presence of a strongly magnetized medium

The inverse of the effective quark propagator in the strong field approximation can be expressed by combining Eq.(5.125) and Eq.(5.109) as follows

$$
\begin{aligned}
S_{\text{eff}}^{-1} = \slashed{P}_{\shortparallel} + \Sigma &= (p_0 + a)\slashed{u} + (b - p_3)\slashed{n} + c\gamma_5\slashed{u} + d\gamma_5\slashed{n} \\
&= (p_0 + a)\gamma^0 + (b - p_3)\gamma^3 + c\gamma_5\gamma^0 + d\gamma_5\gamma^3.
\end{aligned}
\tag{6.62}
$$

101

Now we evaluate the determinant as,

$$
\det[S_{\text{eff}}^{-1}] = \left((b+c-p_3)^2 - (a+d+p_0)^2 \right)\left((-b+c+p_3)^2 - (a-d+p_0)^2 \right)
$$

$$
= (p_0^2 - p_3^2)\left((p_0+2a)^2 - (p_3-2b)^2 \right) = P_{\shortparallel}^2 \left(P_{\shortparallel}^2 + 4ap_0 + 4bp_3 + 4a^2 - 4b^2 \right)
$$

$$
= P_{\shortparallel}^4 \left(1 + \frac{4a^2 - 4b^2 + 4ap_0 + 4bp_3}{P_{\shortparallel}^2} \right), \tag{6.63}
$$

where we have used $d = -a$ and $c = -b$.

So Eq. (6.5) becomes

$$
F_q = -d_F \sum_{\{p_0\}}\!\!\!\!\!\!\!\!\!\!\int \frac{d^3p}{(2\pi)^3} \ln\left[P_{\shortparallel}^4 \left(1 + \frac{4a^2 - 4b^2 + 4ap_0 + 4bp_3}{P_{\shortparallel}^2} \right) \right]
$$

$$
= -2d_F \sum_{\{p_0\}}\!\!\!\!\!\!\!\!\!\!\int \frac{d^3p}{(2\pi)^3} \ln P_{\shortparallel}^2 - d_F \sum_{\{p_0\}}\!\!\!\!\!\!\!\!\!\!\int \frac{d^3p}{(2\pi)^3} \ln\left[1 + \frac{4a^2 - 4b^2 + 4ap_0 + 4bp_3}{P_{\shortparallel}^2} \right]
$$

$$
= F_q^{\text{ideal}} + F_q', \tag{6.64}
$$

where free energy of free quarks [53]

$$
F_q^{\text{ideal}} = -2d_F \sum_{\{p_0\}}\!\!\!\!\!\!\!\!\!\!\int \frac{d^3p}{(2\pi)^3} \ln P_{\shortparallel}^2 = -2d_F \sum_f \frac{q_f B}{(2\pi)^2} \sum_{\{p_0\}}\!\!\!\!\!\!\!\!\!\!\int dp_3 \ln P_{\shortparallel}^2
$$

$$
= -d_F \sum_f \frac{q_f B T^2}{12}, \tag{6.65}
$$

and

$$
F_q' = -d_F \sum_{\{p_0\}}\!\!\!\!\!\!\!\!\!\!\int \frac{d^3p}{(2\pi)^3} \ln\left[1 + \frac{4a^2 - 4b^2 + 4ap_0 + 4bp_3}{P_{\shortparallel}^2} \right]
$$

$$
= -d_F \sum_{\{p_0\}}\!\!\!\!\!\!\!\!\!\!\int \frac{d^3p}{(2\pi)^3} \left[\frac{4(ap_0+bp_3)}{P_{\shortparallel}^2} + \frac{4\left(a^2 P^2 - b^2 P^2 - 2a^2 p_0^2 - 2b^2 p_3^2 - 4abp_0 p_3 \right)}{P_{\shortparallel}^4} + \mathcal{O}(g^6) \right]. \tag{6.66}
$$

Here, we have retained terms up to $\mathcal{O}(g^4)$ to derive the analytic expression for the free energy. The expansion used above is valid under the condition $g^2(q_f B/T^2) < 1$, which can be interpreted as $(q_f B)/T^2 \gtrsim 1$ and $g \ll 1$.

Since, in the strong field approximation, the fermion is assumed to be in the LLL, Eq. (6.66) simplifies to:

$$
F_q' = -d_F \sum_f \frac{q_f B}{(2\pi)^2} \sum_{\{p_0\}}\!\!\!\!\!\!\!\!\!\!\int dp_3 \left[\frac{4(ap_0+bp_3)}{P_{\shortparallel}^2} + \frac{4\left(a^2 P^2 - b^2 P^2 - 2a^2 p_0^2 - 2b^2 p_3^2 - 4abp_0 p_3 \right)}{P_{\shortparallel}^4} + \mathcal{O}(g^6) \right]. \tag{6.67}
$$

. The quark free energy up to $\mathcal{O}(g^4)$ has been derived in Ref. [55] as

$$
F_q = -d_F \sum_f \frac{q_f B T^2}{12} - 4d_F \sum_f \frac{(q_f B)^2}{(2\pi)^2} \frac{g^2 C_F}{4\pi^2} \left(\frac{\Lambda}{4\pi T} \right)^{2\epsilon} \left[\frac{1}{8\epsilon}\left(4\ln 2 - q_f B \frac{\zeta'(-2)}{T^2} \right) \right.
$$

$$
+ \frac{1}{24576}\left\{ 12288 \ln 2(3\gamma_E + 4\ln 2 - \ln\pi) + \frac{256\zeta[3]}{\pi^4 T^2}\left(2\pi^4 T^2 - 3g^2 C_F(q_f B)\ln 2 \right) \right.
$$

$$
+ 3\pi^2(q_f B)(2 + 3\gamma_E + 4\ln 2 - \ln\pi) \Big) - \frac{8g^2 C_F}{\pi^6 T^4}(q_F B)^2 \zeta[3]^2(4 + 105\ln 2)
$$

$$
\left.\left. + \frac{7245 g^2 C_F}{\pi^8 T^6}(q_F B)^3 \zeta[3]^3 \right\}\right]
$$

$$
= -d_F \sum_f \frac{q_f B T^2}{12} - 4d_F \sum_f \frac{(q_f B)^2}{(2\pi)^2} \frac{g^2 C_F}{4\pi^2} \left[\frac{1}{8\epsilon}\left(4\ln 2 - q_f B \frac{\zeta'(-2)}{T^2} \right) + \frac{1}{24576} \right.
$$

$$
\left\{ 12288 \ln 2 \left(3\gamma_E + 2\ln\hat{\Lambda} + \ln 4 - \ln\pi \right) + \frac{256\zeta[3]}{\pi^4 T^2}\left(-3C_F g^2 q_f B \ln 2 \right) \right.
$$

102

$$+6\pi^2 q_f B \ln \hat{\Lambda} + 3\pi^2 q_f B(2 + 3\gamma_E + \ln 4 - \ln \pi) + 2\pi^4 T^2\Big) - \frac{8g^2 C_F}{\pi^6 T^4}(q_f B)^2$$

$$\times \zeta[3]^2(4 + 105\ln 2) + \frac{7245 g^2 C_F}{\pi^8 T^6}(q_f B)^3 \zeta[3]^3\Bigg\}\Bigg], \tag{6.68}$$

where $\hat{\Lambda} = \Lambda/2\pi T$. The quark free energy has $\mathcal{O}[(q_f B)^2/\epsilon]$ and $\mathcal{O}[(q_f B)^3/T^2\epsilon]$ divergences.

6.2.2. One loop gluon free energy in presence of a strongly magnetized medium

The determinant of inverse of gluon propagator in Euclidean space can be obtained from Eq. (5.44) as

$$\det\left(D_{\mu\nu,E}^{-1}(P_E)\right) \;=\; -\frac{P_E^2}{\xi}\left(-P_E^2 + c\right)\left(-P_E^2 + b\right)\left(-P_E^2 + d\right), \tag{6.69}$$

with four eigenvalues: $-P_E^2/\xi$, $\left(-P_E^2 + c\right)$, $\left(-P_E^2 + d\right)$, and $\left(-P_E^2 + b\right)$. In contrast to the previously discussed two-fold degenerate transverse mode $(-P_E^2 + \Pi_T)$ in thermal medium (as mentioned in subsection 5.2.3), we now have two distinct transverse modes: $(-P_E^2 + c)$ and $(-P_E^2 + d)$ as a does not contribute in $\mathcal{O}(eB)^2$ but starts contributing in $\mathcal{O}(eB)^4$ onwards. By substituting Eq. (6.69) into Eq. (6.7), we can express the one-loop gluon free energy for hot magnetized medium is given by

$$F_g = (N_c^2 - 1)\left[\mathcal{F}_g^1 + \mathcal{F}_g^2 + \mathcal{F}_g^3\right], \tag{6.70}$$

where

$$\mathcal{F}_g^1 = \frac{1}{2}\sum_{P_E}\!\!\!\!\!\!\!\int \ln\left(1 - \frac{b}{P_E^2}\right), \tag{6.71a}$$

$$\mathcal{F}_g^2 = \frac{1}{2}\sum_{P_E}\!\!\!\!\!\!\!\int \ln\left(-P_E^2 + c\right), \tag{6.71b}$$

$$\mathcal{F}_g^3 = \frac{1}{2}\sum_{P_E}\!\!\!\!\!\!\!\int \ln\left(-P_E^2 + d\right). \tag{6.71c}$$

The different structure functions are derived in subsection 5.5.3 within the strong field approximation. In this approximation, where $m_f^2 < T^2 < q_f B$, the expressions for the various contributions to the gluon free energy in the Lowest Landau Level (LLL) can be obtained from Eqs. (6.70). By combining Eqs.(6.71a), (6.71b), and (6.71c) with Eq.(6.70), we can express the total one-loop free energy, expanded up to $\mathcal{O}[g^4]$, as

$$F_g \;\approx\; d_A\left[\sum_{P}\!\!\!\!\!\!\!\int \ln\left(-P^2\right) - \frac{b + c + d}{2P^2} - \frac{b^2 + c^2 + d^2}{4P^4}\right], \tag{6.72}$$

where the expansion is performed to derive an analytical expression for the free energy, which is valid under the condition $g^2(q_f B/T^2) < 1$. This condition can be interpreted as $(q_f B)/T^2 \gtrsim 1$ and $g \ll 1$.

The one-loop gluon free energy's hard contribution in a strongly magnetized thermal medium is derived in Ref. [55] as:

$$\begin{aligned}
F_g^{\text{hard}} &= \frac{d_A}{(4\pi)^2}\Bigg[\frac{1}{\epsilon}\Bigg\{-\frac{1}{8}\left(\frac{C_A g^2 T^2}{3}\right)^2 + \frac{g^4 T^4}{96}\sum_{f_1,f_2}\frac{q_{f_1}B}{q_{f_2}B} + \frac{N_f^2 g^4 T^4}{96} + \frac{C_A N_f g^4 T^4}{36}\\
&\quad - \sum_{f_1,f_2}\frac{g^4(q_{f_1}B)(q_{f_2}B)}{64\pi^4} + N_f\sum_f\frac{g^4 T^2 q_f B}{32\pi^2} - \sum_f\frac{1}{4\pi^2}\frac{C_A g^4 T^2 q_f B}{6}(1 + \ln 2)\Bigg\}\\
&\quad - \frac{16\pi^4 T^4}{45} + \frac{2C_A g^2 \pi^2 T^4}{9} + \frac{1}{12}\left(\frac{C_A g^2 T^2}{3}\right)^2\left(8 - 3\gamma_E - \pi^2 + 4\ln 2 - 3\ln\frac{\hat{\Lambda}}{2}\right)
\end{aligned}$$

$$
\begin{aligned}
+ \ & \frac{N_f \pi^2 T^2}{2} \left(\frac{g^2}{4\pi^2}\right)^2 \sum_f q_f B \left(\frac{2\zeta'(-1)}{\zeta(-1)} - 1 + 2\ln\hat\Lambda\right) + \left(N_f^2 + \sum_{f_1,f_2} \frac{q_{f_1} B}{q_{f_2} B}\right) \\
\times \ & \frac{g^4 T^4}{32} \left(\frac{2}{3}\ln\frac{\hat\Lambda}{2} - \frac{60\zeta'[4]}{\pi^4} - \frac{1}{18}(25 - 12\gamma_E - 12\ln 4\pi)\right) - \frac{1}{2}\left(\frac{g^2}{4\pi^2}\right)^2 \\
\times \ & \sum_{f_1,f_2} q_{f_1} B q_{f_2} B \left(\ln\frac{\hat\Lambda}{2} + \gamma_E + \ln 2\right) - \frac{C_A N_f g^4 T^4}{36}\left(1 - 2\frac{\zeta'(-1)}{\zeta(-1)} - 2\ln\frac{\hat\Lambda}{2}\right) \\
- \ & \sum_f \frac{C_A g^4 T^2 q_f B}{144\pi^2}\left(\pi^2 - 4 + 12\ln\frac{\hat\Lambda}{2} - 2\ln 2\left(6\gamma_E + 4 + 3\ln 2 - 6\ln\frac{\hat\Lambda}{2}\right) + 12\gamma_E\right)\Bigg].
\end{aligned}
$$
(6.73)

As observed, F_g^{hard} exhibits a $\mathcal{O}(1/\epsilon)$ divergence, which arises both from the HTL approximation and from the thermomagnetic contributions.

We obtain the soft contribution to the gluon free energy by considering soft gluon momentum, where $P \sim gT$ and $p_0 = 0$,

$$
F_g^{\text{soft}} \approx d_A\left[-\frac{(m_D^s)^3 T}{12\pi} + \mathcal{O}[\epsilon]\right],
$$
(6.74)

where the Debye mass in strong field is given in Eq. 5.198.

The total gluonic contribution becomes

$$
F_g = F_g^{\text{hard}} + F_g^{\text{soft}}.
$$
(6.75)

6.2.3. Renormalized free energy in a strong field approximation

By combining Eq. (6.1) and Eq. (6.75), the one-loop free energy of deconfined QCD matter in a strong magnetic field can be written as

$$
F = F_q + F_g^{\text{hard}} + F_g^{\text{soft}} + F_0 + \Delta\mathcal{E}_T^0 + \Delta\mathcal{E}_T^B.
$$
(6.76)

The expression exhibits $\mathcal{O}[1/\epsilon]$ divergences at different orders of $(q_f B)$. To handle the $\mathcal{O}[(q_f B)^2]$ divergences in the free energy, we regularize by redefining the tree-level free energy term $B^2/2$ as [55]

$$
F_0 = \frac{B^2}{2} \ \rightarrow \ \frac{B^2}{2} \underbrace{+ 4d_F \sum_f \frac{(q_f B)^2}{(2\pi)^2}\frac{g^2 C_F}{4\pi^2}\frac{\ln 2}{2\epsilon} + \frac{d_A}{(4\pi)^2}\sum_{f_1,f_2}\frac{g^4 q_{f_1} B q_{f_2} B}{64\pi^4\epsilon}}_{\Delta\mathcal{E}^{B^2}}
$$

$$
\rightarrow \ \frac{B^2}{2} + \Delta\mathcal{E}^{B^2}.
$$
(6.77)

The remaining divergences of $\mathcal{O}[(q_f B)^0 T^4]$, $\mathcal{O}[T^2(q_f B)]$, and $\mathcal{O}[(q_f B)^3/T^2]$ are renormalized by introducing appropriate counter terms. Specifically, the $\mathcal{O}[(q_f B)^0 T^4]$ divergences are regulated by adding counterterms as follows

$$
\begin{aligned}
\Delta\mathcal{E}_T^0 &= \Delta\mathcal{E}_T^{\text{HTL}} + \Delta\mathcal{E}_T \\
&= \underbrace{d_A\frac{m_D^4}{128\pi^2\epsilon}}_{\Delta\mathcal{E}_T^{\text{HTL}}} \underbrace{- \frac{d_A}{(4\pi)^2}\left[\frac{g^4 T^4}{96\epsilon}\sum_{f_1,f_2}\frac{q_{f_1} B}{q_{f_2} B} + \frac{N_f^2 g^4 T^4}{96\epsilon} + \frac{C_A N_f g^4 T^4}{36\epsilon}\right]}_{\Delta\mathcal{E}_T},
\end{aligned}
$$
(6.78)

where m_D represents the Debye screening mass in the HTL approximation. The divergences of $\mathcal{O}[T^2(q_f B)]$ and $\mathcal{O}[(q_f B)^3/T^2]$ are then controlled by adding suitable counter terms as follows

$$
\Delta\mathcal{E}_T^B = -4d_F\sum_f\frac{(q_f B)^3}{(2\pi)^2}\frac{g^2 C_F}{4\pi^2}\frac{\zeta'(-2)}{8T^2\epsilon} - \frac{d_A}{(4\pi)^2\epsilon}\left[\frac{N_f g^4 T^2}{32\pi^2}\sum_f q_f B\right.
$$

$$-\sum_f \frac{1}{4\pi^2} \frac{C_A g^4 T^2 q_f B}{6} (1 + \ln 2) \Bigg].$$
(6.79)

Now using Eqs. (6.68), (6.73), (6.74), (6.77), (6.78) and (6.79) in Eq. (6.76), the renormalized one-loop quark-gluon free energy in the presence of a strong magnetic field is given by:

$$F = F_q^r + F_g^r + \frac{B^2}{2},$$
(6.80)

where renormalized quark free enrgy F_q^r is given by

$$
\begin{aligned}
F_q^r &= -d_F \sum_f \frac{q_f B T^2}{12} - 4 d_F \sum_f \frac{(q_f B)^2}{(2\pi)^2} \frac{g^2 C_F}{4\pi^2} \Bigg[\frac{1}{24576} \Big\{ 12288 \ln 2 \big(3\gamma_E \\
&\quad + 2 \ln \hat{\Lambda} + \ln 16\pi \big) + \frac{256\zeta[3]}{\pi^4 T^2} \Big(-3 C_F g^2 q_f B \ln 2 + 6\pi^2 q_f B \ln \hat{\Lambda} + 3\pi^2 q_f B \\
&\quad (2 + 3\gamma_E + \ln 16\pi) + 2\pi^4 T^2 \Big) - \frac{8 g^2 C_F}{\pi^6 T^4} (q_f B)^2 \zeta[3]^2 (4 + 105 \ln 2) \\
&\quad + \frac{7245 g^2 C_F}{\pi^8 T^6} (q_f B)^3 \zeta[3]^3 \Big\} \Bigg],
\end{aligned}
$$
(6.81)

and the renormalized total gluon free energy containing both hard and soft contributions is given as

$$
\begin{aligned}
F_g^r &= \frac{d_A}{(4\pi)^2} \Bigg[-\frac{16\pi^4 T^4}{45} + \frac{2 C_A g^2 \pi^2 T^4}{9} + \frac{1}{12} \left(\frac{C_A g^2 T^2}{3} \right)^2 \Big(8 - 3\gamma_E - \pi^2 + 4 \ln 2 \\
&\quad -3 \ln \frac{\hat{\Lambda}}{2} \Big) + \frac{N_f \pi^2 T^2}{2} \left(\frac{g^2}{4\pi^2} \right)^2 \sum_f q_f B \left(\frac{2\zeta'(-1)}{\zeta(-1)} - 1 + 2 \ln \hat{\Lambda} \right) \\
&\quad + \left(N_f^2 + \sum_{f_1, f_2} \frac{q_{f_1} B}{q_{f_2} B} \right) \frac{g^4 T^4}{32} \left(\frac{2}{3} \ln \frac{\hat{\Lambda}}{2} - \frac{60\zeta'[4]}{\pi^4} - \frac{1}{18} (25 - 12\gamma_E - 12 \ln 4\pi) \right) \\
&\quad - \frac{1}{2} \left(\frac{g^2}{4\pi^2} \right)^2 \sum_{f_1, f_2} q_{f_1} B q_{f_2} B \left(\ln \frac{\hat{\Lambda}}{2} + \gamma_E + \ln 2 \right) - \frac{C_A N_f g^4 T^4}{36} \left(1 - 2 \frac{\zeta'(-1)}{\zeta(-1)} \right) \\
&\quad - 2 \ln \frac{\hat{\Lambda}}{2} \Big) - \sum_f \frac{C_A g^4 T^2 q_f B}{144\pi^2} \left(\pi^2 - 4 + 12 \ln \frac{\hat{\Lambda}}{2} - 2 \ln 2 \Big(6\gamma_E + 4 + 3 \ln 2 \right. \\
&\quad \left. - 6 \ln \frac{\hat{\Lambda}}{2} \right) + 12\gamma_E \Big) \Bigg] - \frac{d_A (m_D^s)^3 T}{12\pi}.
\end{aligned}
$$
(6.82)

6.2.4. Anisotropic pressure of deconfined QCD matter in a strong magnetic field

1. Longitudinal and transverse pressure

In a thermal background, the QCD pressure can be derived from the system's free energy, and it is typically isotropic. However, in the presence of a thermo-magnetic background, an additional extensive parameter arises due to the external magnetic field, B. In such a scenario, the free energy can be expressed as:

$$\mathcal{F}(T, V, B) = E^{\text{total}} - TS - eB \cdot \mathcal{M},$$

where $\mathcal{M}$ is the magnetization. The free energy density for a system confined within a finite spatial volume V is expressed as

$$F = \mathcal{F}/V = \epsilon^{\text{total}} - Ts - eB \cdot M,$$
(6.83)

where ϵ^{total} is total the energy density and the entropy density is given by

$$s = -\frac{\partial F}{\partial T},$$
(6.84)

and the magnetization density is expressed as

$$M = -\frac{\partial F}{\partial(eB)} \tag{6.85}$$

and the total energy density is expressed as $\epsilon^{\text{total}} = \epsilon + \epsilon^{\text{field}}$, where ϵ is the energy density of the medium and $\epsilon^{\text{field}} = eB \cdot M$. In the presence of a strong magnetic field, the spatial geometry becomes anisotropic, leading to different pressures in the directions parallel and perpendicular to the magnetic field [250]. The longitudinal and transverse pressures are given as

$$P_z = -F, \ \ P_\perp = -F - eB \cdot M = P_z - eB \cdot M. \tag{6.86}$$

2. Pressure of ideal quark and gluon gas in a strong magnetic field

The free energy of an ideal quark-gluon gas in absence of magnetic field is given as

$$F_T^{\text{ideal}} = -d_F \frac{7\pi^2 T^4}{180} - d_A \frac{\pi^2 T^4}{45}, \tag{6.87}$$

and the corresponding pressure reads as

$$\begin{aligned} P_T^{\text{i}} \equiv P_T^{\text{ideal}} &= d_F \frac{7\pi^2 T^4}{180} + d_A \frac{\pi^2 T^4}{45} \\ &\equiv (P_T^q)^{\text{i}} + (P_T^g)^{\text{i}}. \end{aligned} \tag{6.88}$$

The free energy of a ideal quark-gluon gas in presence of magnetic field is given by

$$\begin{aligned} F^{\text{ideal}} &= F_q^{\text{ideal}} + F_g^{\text{ideal}} \\ &= -d_F \sum_f (q_f B) \frac{T^2}{12} - d_A \frac{\pi^2 T^4}{45}. \end{aligned} \tag{6.89}$$

As seen the magnetic field affects quarks but not gluons, making the ideal quark-gluon gas pressure anisotropic. The ideal longitudinal pressure. The ideal longitudinal pressure is given by

$$P_z^{\text{i}} \equiv P_z^{\text{ideal}} = -F^{\text{ideal}} = d_F \sum_f (q_f B) \frac{T^2}{12} + d_A \frac{\pi^2 T^4}{45} \equiv (P_z^q)^{\text{i}} + (P_z^g)^{\text{i}}. \tag{6.90}$$

The magnetization of the ideal quark-gluon gas is calculated using the following expression given in Eq. (6.85) as

$$\begin{aligned} M^{\text{ideal}} &= -\frac{\partial F^{\text{ideal}}}{\partial(eB)} \\ &= d_F \sum_f \frac{q_f T^2}{12}. \end{aligned} \tag{6.91}$$

As found, the magnetization of an ideal quark-gluon gas in the LLL remains independent of the magnetic field in the presence of a strong magnetic field. In the LLL, positively charged particles with spin up align along the direction of the magnetic field, while negatively charged particles with spin down align oppositely. Due to this spin alignment, the system naturally minimizes its free energy with respect to the magnetic field eB. Consequently, even if the magnetic field is increased, the spin alignment does not change, leading to a constant magnetization for a given temperature T. However, as the temperature increases, thermal motion along the field direction can lead to an increase in magnetization, even though the spin alignment itself remains unchanged.

Now, the ideal transverse pressure of the quark-gluon gas can be expressed using Eq. (6.86) as

$$P_\perp^{\text{i}} \equiv P_\perp^{\text{ideal}} = d_A \frac{\pi^2 T^4}{45} \tag{6.92}$$

We observe that the transverse pressure of the ideal magnetized quark-gluon gas remains independent of the magnetic field and matches the ideal gluon pressure. As noted earlier, gluons are not influenced by the magnetic field and contribute to this isotropic pressure. In contrast, quarks only have momenta along the z-direction in the LLL and thus contribute exclusively to the longitudinal pressure.

6.2.5. Results in strong field approximation

We considered a magnetic field-dependent one-loop strong coupling as discussed in subsection 5.7. For the ideal quark-gluon gas, gluons are unaffected by the magnetic field, while quarks are strongly influenced. In Fig. 6.11, we show the variation of the ideal quark pressure $(P_z^q)^{\mathrm{i}}$ from Eq. (6.90) in the presence of a magnetic field, and $(P_T^q)^{\mathrm{i}}$ from Eq. (6.88) in its absence, as a function of temperature. The ideal quark pressure $(P_z^q)^{\mathrm{i}}$ in the presence of a magnetic field is proportional to $(eB)T^2$, whereas in the absence of a magnetic field, $(P_T^q)^{\mathrm{i}}$ is proportional to T^4. At low temperatures, T^2 dominates for a given magnetic field, while at high temperatures, T^4 takes over, resulting in a crossing point at an intermediate temperature, as seen in Fig. 6.11. Additionally, the ideal longitudinal pressure increases linearly with an increasing magnetic field, consistent with Eq. (6.90).
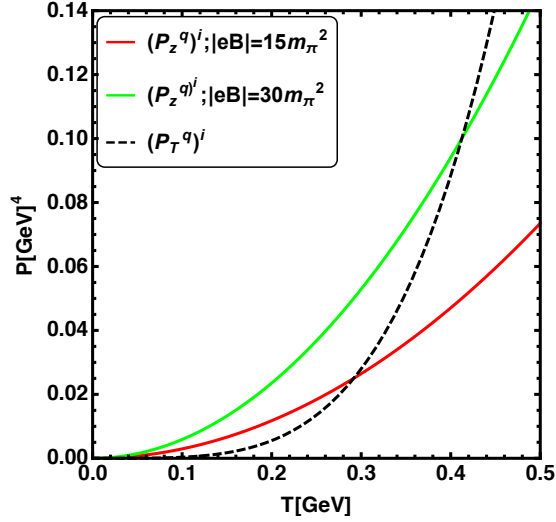
Figure 6.11: The variation of ideal quark pressure with and without a magnetic field as a function of temperature is shown.
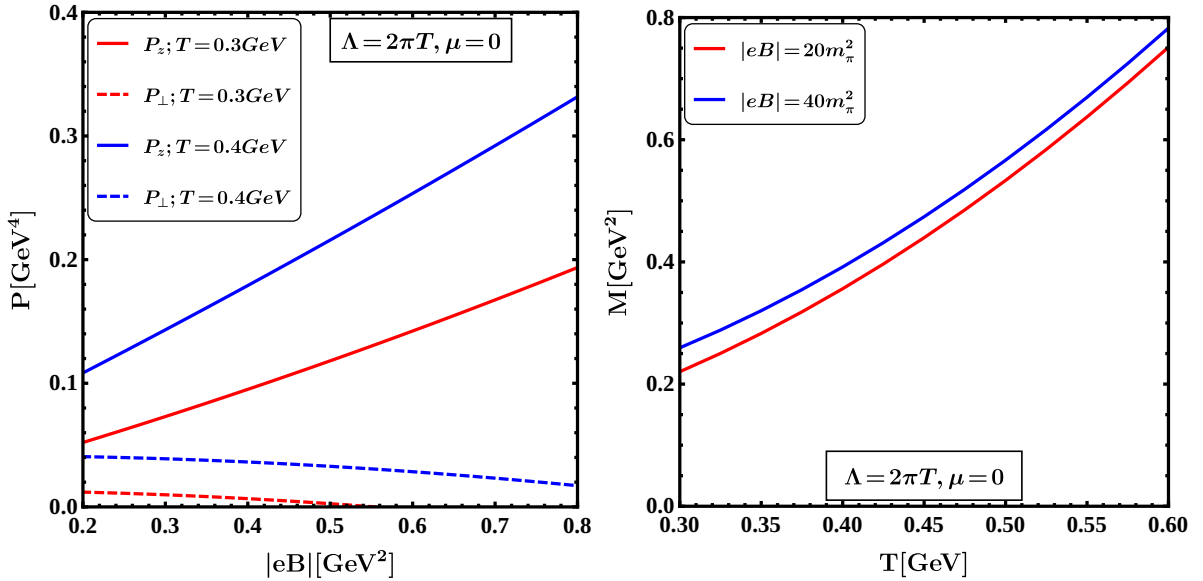
Figure 6.12: The variation of the longitudinal and transverse pressures at $\mu = 0$ with magnetic field is illustrated in the left panel. In the right panel, the magnetization as a function of temperature is shown for $N_f = 3$.

In the left panel of Fig. 6.12, the variation of longitudinal and transverse pressure with the strength of the magnetic field at $\mu = 0$ is shown. It is evident that the longitudinal pressure (the pressure along the direction of the magnetic field) of the magnetized QGP increases as the magnetic field strength increases, while the transverse pressure exhibits the opposite behaviour. This suggests that the system tends to elongate along the longitudinal direction and compress along the transverse direction under a high magnetic field.

In the right panel of Fig. 6.12, the magnetization of the system is plotted as a function of temperature. A positive magnetization indicates paramagnetism in the strongly magnetized QCD medium, which aligns with recent lattice calculations [244]. While the qualitative trends of pressure and magnetization shown in Fig. 6.12 match the lattice results from Ref. [244], there are quantitative discrepancies. These arise because the calculation here only captures the correct perturbative coefficients up to g^0 and g^3 in the leading order HTLpt framework. To achieve a complete result up to $\mathcal{O}(g^5)$, one would need to go beyond one-loop calculations.
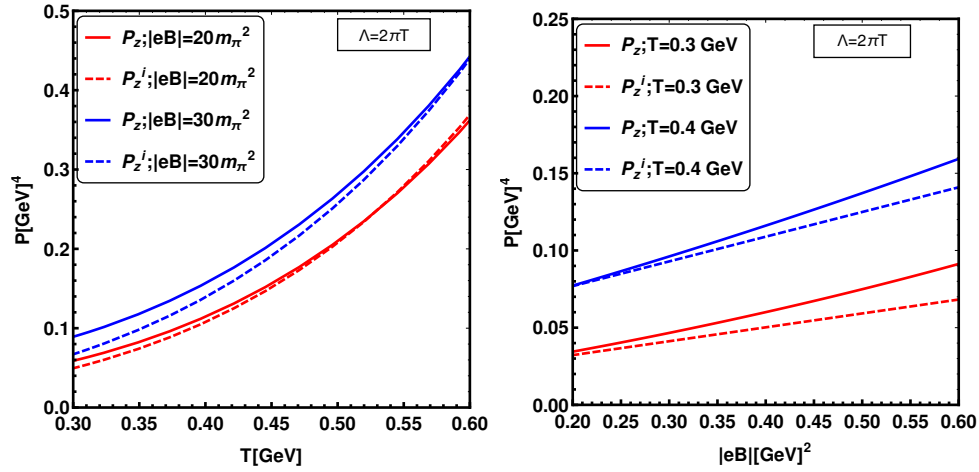
Figure 6.13: The left panel displays the variation of one-loop longitudinal pressure as a function of temperature for different values of magnetic field, with $N_f = 3$ and the central value of the renormalization scale, $\Lambda = 2\pi T$. The right panel shows the variation of the same pressure as a function of magnetic field at different temperatures. Dashed curves represent the ideal longitudinal pressure.

The left panel of Fig. 6.13 compares the 1-loop longitudinal pressure (solid curve) with the ideal pressure (dashed curve) for different values of field strength as a function of temperature. The right panel shows the same comparison but with magnetic field strength for various temperatures. In both cases, the 1-loop pressure increases with both temperature and field strength. However, the 1-loop interacting pressure is higher than the ideal pressure in both panels. This enhancement is due to the fact that, at 1-loop order, both the effective quark two-point function and the effective gluon two-point function containing the quark loop are strongly influenced by the magnetic field, contributing to the additional pressure compared to the ideal case. For a given magnetic field, this enhancement is more pronounced in the temperature range of 300-500 MeV, as seen from the scaled pressure with the ideal pressure ($P_z/P_z^{\rm i}$) in the left panel of Fig. 6.14. However, this enhancement diminishes with increasing temperature and approaches the ideal value at high temperatures. For a given temperature, the ratio ($P_z/P_z^{\rm i}$) increases with the strength of the magnetic field, as $P_z^{\rm i}$ has a linear dependence on eB, while P_z has a higher power dependence on eB.

The magnetization of an ideal quark-gluon gas in the presence of a magnetic field has already been discussed in subsection 6.2.4. Now, the magnetization of an interacting quark-gluon system is calculated using Eq. (6.85) and it is
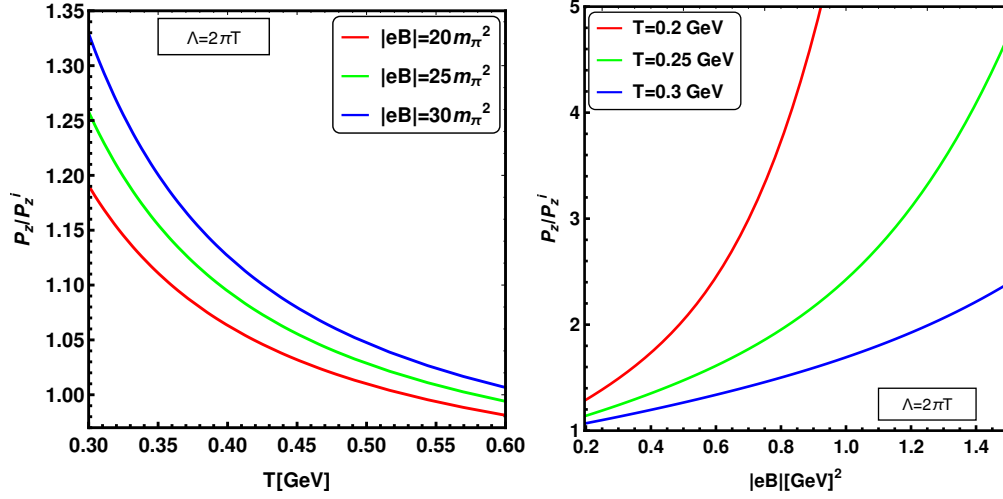
Figure 6.14: The left panel shows the variation of the one-loop longitudinal pressure scaled with the ideal longitudinal pressure as a function of temperature for different values of magnetic field, with $N_f = 3$. The right panel displays the variation of the same pressure as a function of magnetic field at different temperatures.

proportional to $[aT^2 + b(eB) + c(eB)^2/T^2 + d(eB)^3/T^4 + f(eB)^4/T^6]$. This formula is plotted in Fig. 6.15. For a given value of eB, at low temperatures, the terms with $1/T^n$ for $n = 2, 4, 6$ dominate, but are limited by the scale gT. In contrast, at higher temperatures, the T^2 terms become more significant, as shown in the left panel of Fig. 6.15. Unlike an ideal quark-gluon gas, the magnetization of an interacting quark-gluon system increases with the strength of the magnetic field, which is evident from the right panel[18] of Fig. 6.15. This trend matches with lattice QCD results [251]. In the strong magnetic field approximation, where $g^2T^2 < T^2 < eB$, the magnetization achieves positive values ranging from $0 < M < 1$. Therefore, in the presence of a strong magnetic field, the deconfined QCD matter exhibits a paramagnetic nature (i.e., the magnetization aligns parallel to the magnetic field direction) [251]. As the magnetization increases in the strong field limit, it also boosts the pressure along the field direction, specifically the longitudinal direction. This, in turn, significantly influences the transverse pressure.

The one-loop transverse pressure is calculated using Eq. (6.86). From this equation and the left panel of Fig 6.16, it is clear that the one-loop transverse pressure increases with temperature but shows a similar trend to the longitudinal pressure (left panel of Fig. 6.13), though it is lower in magnitude. The dashed lines represent the ideal transverse pressure, which remains independent of the magnetic field as indicated by Eq. (6.92). For a high magnetic field, the pressure starts off at a lower value compared to the ideal gas, especially at low T, and then crosses over. This behaviour is also evident in the right panel of Fig 6.16,, where the transverse pressure is displayed as a function of magnetic field for two different temperatures. The dashed lines here also indicate the ideal transverse pressure, which remains unaffected by the magnetic field. The transverse pressure for the interacting case is given by Eq. (6.86) as $P_\perp = P_z - eB \cdot M$. For a given temperature, its variation is relatively slow (or almost unchanged) with a lower magnetic field due to the competition between P_z and eBM. As the magnetization M increases steadily with the magnetic field (right panel of Fig. 6.15), the transverse pressure, $P_\perp$, tends to decrease, dropping below the ideal gas value and may even become negative for low T at high magnetic fields. This suggests that the system may compress in the transverse direction [251].

---

[18]The magnetization increases with the magnetic field even when the fermions are confined to the LLL due to the interactions present.
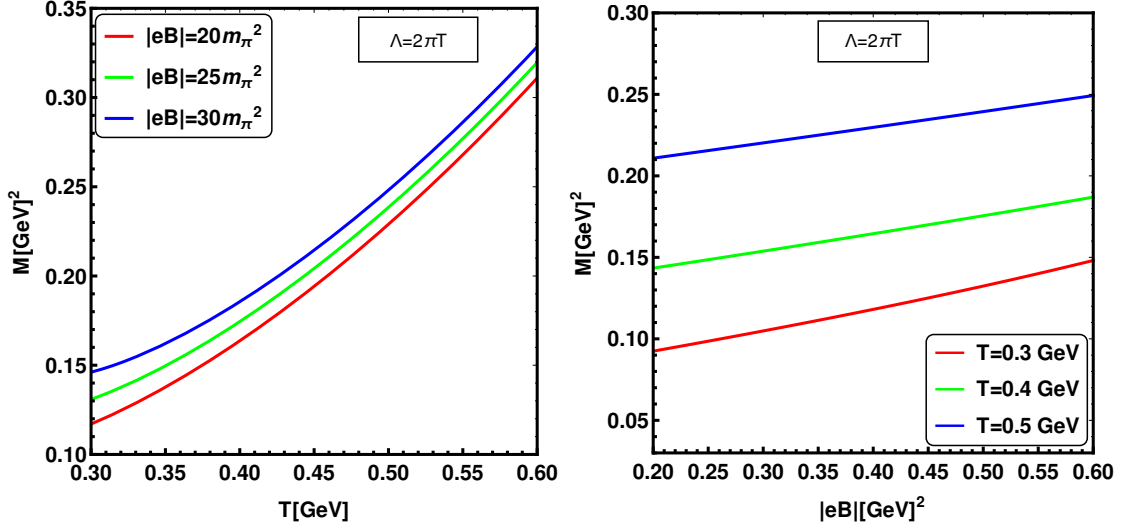
Figure 6.15: The left panel shows the variation of magnetization with temperature for different magnetic field strengths whereas the right panel displays the variation as a function of magnetic field for various temperatures.
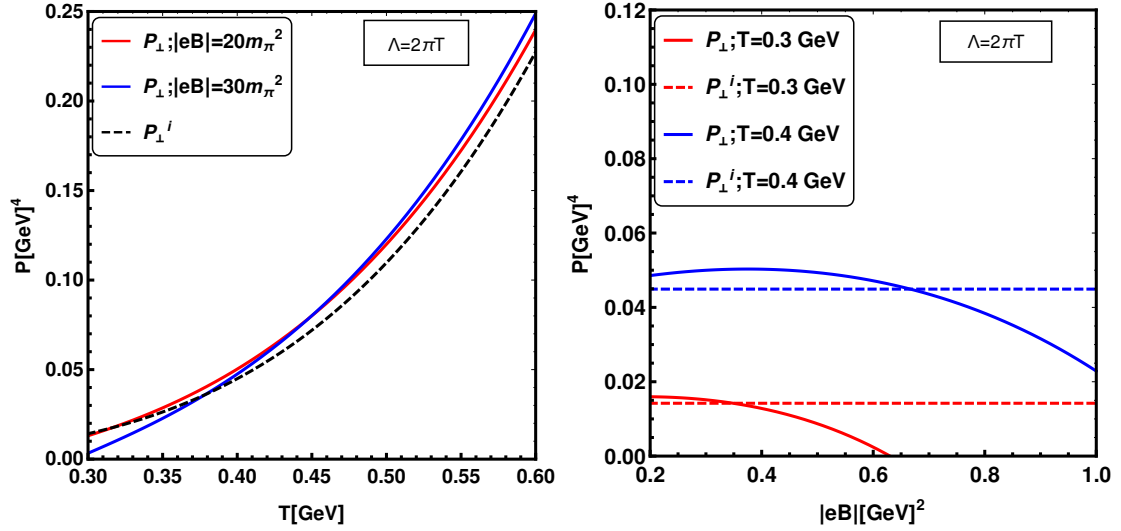

Figure 6.16: The one-loop transverse pressure is shown in terms of temperature for different magnetic field strengths in the left panel, and as a function of magnetic field for various temperatures in the right panel. The dashed curves denote the ideal transverse pressure.

6.2.6. Quark number susceptibility in strong field approximation

The renormalized free energy in a strong field is derived in Eq.(6.80). The renormalized quark free energy for $\mu = 0$ is given in Eq.(6.82). The extension to a finite chemical potential, μ, is presented in Ref. [56] as

$$
\begin{aligned}
F_q^r &= -d_F \sum_f \frac{q_f B T^2}{6}\Big(1 + 12\hat{\mu}^2\Big) + 4d_F \sum_f \frac{g^2 C_F (q_f B)^2}{(2\pi)^4}\left[-\ln 2 \ln \frac{\hat{\Lambda}}{2} - \frac{3\gamma_E \ln 2}{2} \right. \\
&+ \ln 2 \ln \pi - \frac{1}{2}\ln 2 \ln 16\pi + \frac{g^2 C_F (q_f B)}{4\pi^2}\frac{63 \ln 2^2 \zeta(3)}{72\pi^2 T^2} - \frac{g^2 C_F (q_f B)}{4\pi^2}\frac{217(q_f B)^2 \zeta(5)}{36864\pi^4 T^6} \\
&\times \Big(\gamma_E + 2\ln 2 - 12\ln G\Big)^2 + \frac{7\hat{\mu}^2}{2}\zeta(3)\ln \frac{\hat{\Lambda}}{2} + \frac{\hat{\mu}^2}{288T^2}\left\{ \frac{7\zeta(3)g^2 C_F (q_f B)}{4\pi^2} \right. \\
&\times \Big(3 + 3\gamma_E + 4\ln 2 - 36\ln G\Big)^2 + 504 T^2 \zeta(3)\Big(3\gamma_E + 8\ln 2 - \ln \pi\Big) - \frac{36\ln 2}{\pi^2}\frac{g^2 C_F (q_f B)}{4\pi^2} \\
&\times \Big(49\zeta(3)^2 + 186\ln 2\zeta(5)\Big)\Big\} - \frac{7(q_f B)^2 \hat{\mu}^2}{184320\pi^2 T^6}\frac{g^2 C_F (q_f B)}{4\pi^2}\left\{ -31\zeta(5)\Big(-15 + 15\gamma_E + 16\ln 2\Big) \right.
\end{aligned}
$$

$$\times \quad \left(\gamma_E + 2\ln 2 - 12\ln G\right) - \frac{48825}{\pi^4}\zeta(3)^2\zeta(5) - \frac{9525\zeta(7)}{\pi^2}\left(\gamma_E + 2\ln 2 - 12\ln G\right)^2$$

$$+ \quad 55800\zeta(5)\zeta'(-3)\left(\gamma_E + 2\ln 2 - 12\ln G\right)\Bigg\} - \frac{31\hat{\mu}^4}{2}\zeta(5)\ln\frac{\hat{\Lambda}}{2} + \frac{\hat{\mu}^4}{4320\pi^2 T^2}\Bigg\{ - 1080\pi^2 T^2$$

$$\times \quad \left(98\zeta(3)^2 + 31\zeta(5)\left(3\gamma_E + 8\ln 2 - \ln\pi\right)\right) - \frac{g^2 C_F(q_f B)}{4\pi^2}\left(14\pi^4\zeta(3)\left(15\gamma_E + 16\ln 2\right)\right.$$

$$\times \quad \left(3 + 3\gamma_E + 4\ln 2 - 36\ln G\right) - 46305\zeta(3)^3 + 2790\pi^2\zeta(5)\left(3 + 3\gamma_E - 4\ln 2 - 36\ln G\right)^2$$

$$- \quad 820260\ln 2\zeta(3)\zeta(5) - 1028700\ln 2^2\zeta(7) - 25200\pi^4\zeta(3)\zeta'(-3)\left(3 + 3\gamma_E + 4\ln 2 - 36\ln G\right)\Bigg)\Bigg\}$$

$$- \quad \frac{\hat{\mu}^4(q_f B)^2}{331776 T^6}\frac{g^2 C_F(q_f B)}{4\pi^2}\Bigg\{\frac{10897740}{\pi^6}\zeta(3)\zeta(5)^2 + \frac{37804725}{\pi^6}\zeta(3)^2\zeta(7) + \frac{2253510\zeta(9)}{\pi^4}$$

$$\times \quad \left(\gamma_E + 2\ln 2 - 12\ln G\right)^2 + \frac{24003}{\pi^2}\zeta(7)\left(\gamma_E + 2\ln 2 - 12\ln G\right)\left(-15 + 15\gamma_E + 16\ln 2\right)$$

$$- \quad 1800\zeta'(-3)\Bigg) + \frac{31\zeta(5)}{100}\Bigg(14175 - 40950\gamma_E + 26775\gamma_E^2 + 68240\gamma_E\ln 2 + 41728\ln 2^2$$

$$+ \quad 151200\ln G - 151200\gamma_E\ln G - 240\ln 2\left(231 + 640\ln G\right) + 3175200\zeta'(-5)$$

$$\times \quad \left(\gamma_E + 2\ln 2 - 12\ln G\right) - 226800\zeta'(-3)\left(-15 + 15\gamma_E + 16\ln 2\right) + 204120000\zeta'(-3)^2\Bigg)\Bigg\}\Bigg] \qquad (6.93)$$

where $\hat{\Lambda} = \Lambda/2\pi T$, $\hat{\mu} = \mu/2\pi T$, with $G \approx 1.2824$ as Glaisher's constant and $\gamma_E \approx 0.5772$ as the Euler-Mascheroni constant. The free energy of ideal quarks in a magnetic field is described in Ref. [53] as

$$F_q^{\text{ideal}} \quad = \quad -2d_F \sum_{\{p_0\}}\!\!\!\!\!\!\!\!\!\!\!\oint \frac{d^3 p}{(2\pi)^3}\ln\left(-P_{\shortparallel}^2\right) = -2d_F \sum_f \frac{q_f B}{(2\pi)^2}\sum_{\{p_0\}}\!\!\!\!\!\!\!\!\!\!\!\oint dp_3 \ln\left(-P_{\shortparallel}^2\right)$$

$$= \quad -d_F \sum_f \frac{q_f B T^2}{6}\left(1 + 12\hat{\mu}^2\right). \qquad (6.94)$$

The renormalized gluon free energy in strong field is given in Eq. (6.82).

As discussed in subsection 6.2.4, the presence of a strong magnetic field induces anisotropy in the pressure of the system, leading to two distinct pressures – one parallel to the magnetic field direction (longitudinal) and another perpendicular to it (transverse). These longitudinal and transverse pressures are specified in Eq. (6.86). Due to this anisotropy, two different second-order transport coefficients are derived from combining Eqs. (6.4) and (6.86): χ_z along the longitudinal direction and $\chi_\perp$ along the transverse direction in the presence of a strong magnetic field. The longitudinal second-order transport coefficient, χ_z, can be obtained from this framework as

$$\chi_z = \left.\frac{\partial^2 P_z}{\partial\mu^2}\right|_{\mu=0}, \qquad (6.95)$$

whereas the transverse one, $\chi_\perp$, can be derived similarly as

$$\chi_\perp = \left.\frac{\partial^2 P_\perp}{\partial\mu^2}\right|_{\mu=0}. \qquad (6.96)$$

The longitudinal pressure for a noninteracting quark-gluon gas in the presence of a strong magnetic field is expressed as

$$P_{sf} = \sum_f N_c N_f\, q_f B\frac{T^2}{6}(1 + 12\hat{\mu}^2) + (N_c^2 - 1)\frac{\pi^2 T^4}{45}. \qquad (6.97)$$

The second-order longitudinal QNS for the ideal quark gluon plasma is is expressed as

$$\chi_{sf} = \sum_f N_c N_f\frac{q_f B}{\pi^2}. \qquad (6.98)$$

The transverse pressure of ideal quark-gluon plasma is given as

$$P_{sf}^{\perp} = (N_c^2 - 1)\frac{\pi^2 T^4}{45}. \qquad (6.99)$$

Thus, the second-order transverse QNS of the ideal quark-gluon plasma vanishes [56].
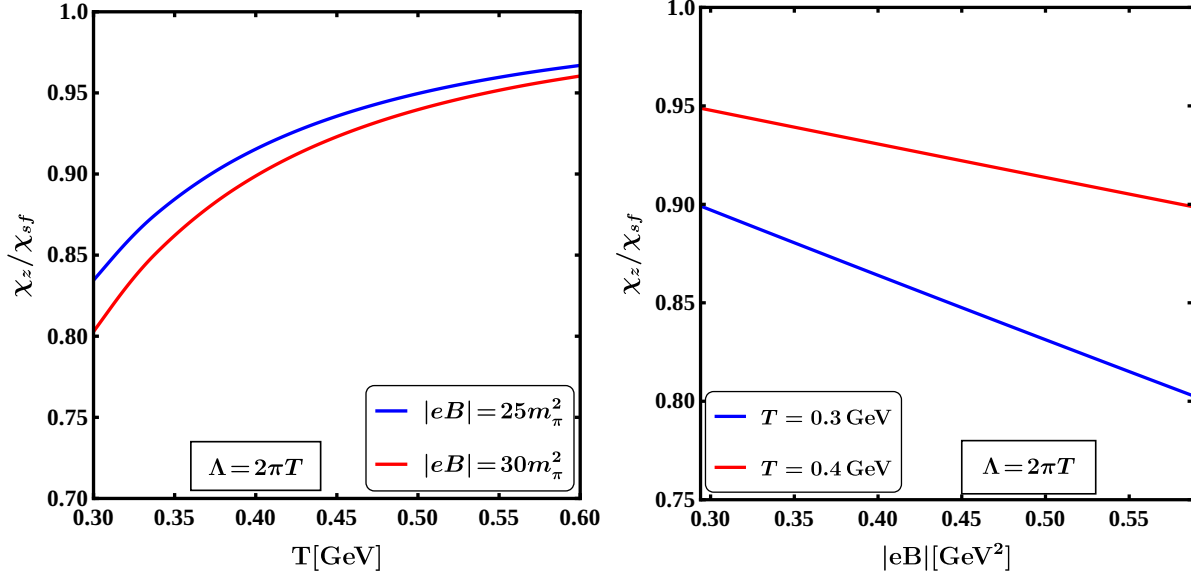

Figure 6.17: The left panel shows the variation of the longitudinal part of the second-order QNS, scaled by its free field value, as a function of temperature in the presence of a strong magnetic field for $N_f = 3$. The right panel illustrates the variation with respect to the strength of the magnetic field for $N_f = 3$.
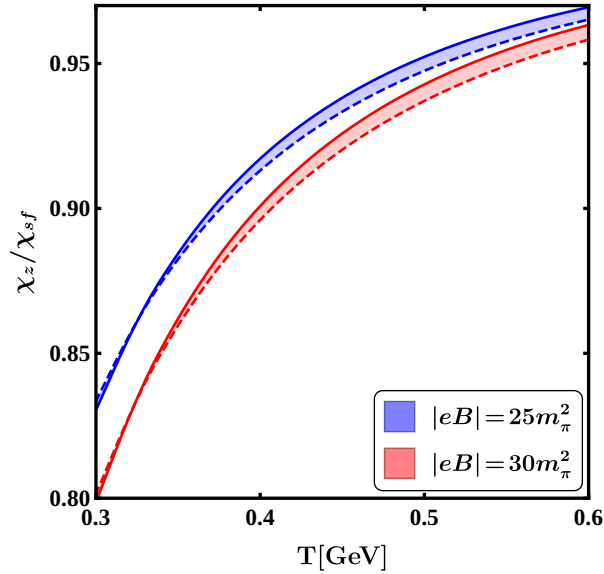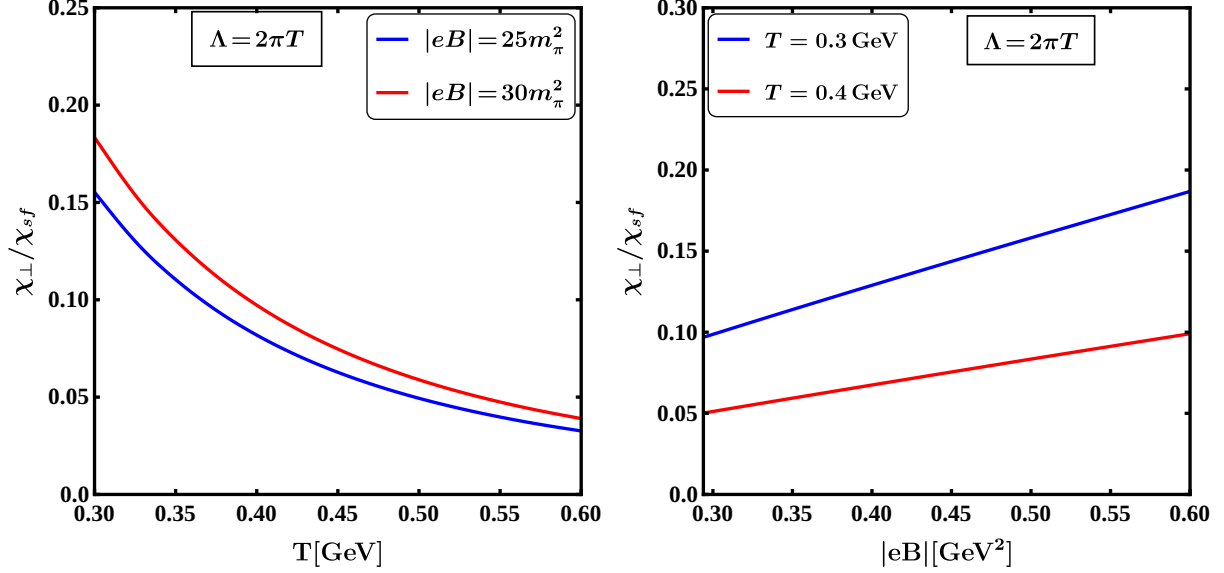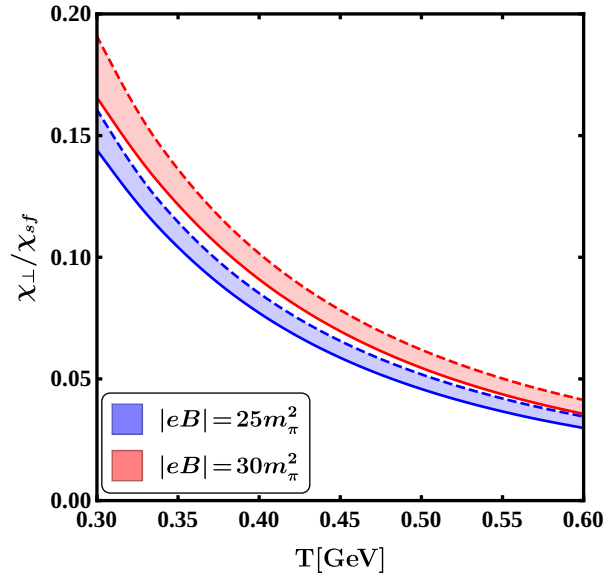

Figure 6.18: The plots depict the sensitivity of the longitudinal part of the second-order QNS scaled with that of free field value in presence of strong magnetic field, to the renormalization scale for $N_f = 3$. The dashed and the continuous curves represent $\Lambda = \pi T$ and $\Lambda = 4\pi T$ respectively.

In the left panel of Fig. 6.17, the variation of the longitudinal second-order QNS with temperature is displayed for two different values of magnetic field strength and the central renormalization scale $\Lambda = 2\pi T$. For a given magnetic field strength, the longitudinal second-order QNS increases with temperature, approaching the free field value at high temperatures. Conversely, for a fixed temperature, the longitudinal second-order QNS decreases as the magnetic field

strength increases, as shown in the right panel of Fig. 6.17 for two distinct temperatures and the central renormalization scale $\Lambda = 2\pi T$.

The QGP pressure and the second-order QNS are both influenced by the choice of the renormalization scale Λ. Fig. 6.18 demonstrates the sensitivity of these results to the renormalization scale. Here, the scale is varied around the central value by a factor of two, spanning from πT to $4\pi T$.

Figure 6.19: The left panel shows the variation of the transverse part of the second-order QNS, scaled by its free field value, as a function of temperature in the presence of a strong magnetic field for $N_f = 3$. The right panel illustrates the variation with respect to the strength of the magnetic field for $N_f = 3$.

Figure 6.20: The plots depict the sensitivity of the transverse QNS, scaled by its free field value in the presence of a strong magnetic field, to the renormalization scale for $N_f = 3$ is shown in Fig. 6.20. The dashed curve represents the case with $\Lambda = \pi T$, while the continuous curve represents $\Lambda = 4\pi T$. .

113

In the left panel of Fig. 6.19, the variation of the transverse second-order QNS with temperature is shown for two different values of magnetic field strength and the central renormalization scale $\Lambda = 2\pi T$. It is observed that the transverse second-order QNS decreases with increasing temperature, indicating a shrinking effect in the transverse direction. Conversely, for a fixed temperature, the transverse second-order QNS increases with an increase in magnetic field strength, as illustrated in the right panel of Fig. 6.19 for two different temperatures and the central renormalization scale $\Lambda = 2\pi T$. This behaviour contrasts with the longitudinal second-order QNS. In Fig. 6.20, the sensitivity of the transverse second-order QNS to the renormalization scale is demonstrated by varying it by a factor of two around the central value, $\Lambda = 2\pi T$.

The second-order quark number susceptibility measures the fluctuation of the net quark number relative to its average value. As the system becomes anisotropic under a strong magnetic field, there are two distinct pressures along the longitudinal and transverse directions relative to the magnetic field. Fig.6.12 illustrates that the magnitude of the longitudinal pressure is greater than that of the transverse pressure, leading to a greater expansion along the longitudinal direction Ref. [55]. Similarly, there are two distinct quark number susceptibilities along the longitudinal and transverse directions. From Eq. (6.98), it is evident that the longitudinal QNS for the ideal quark-gluon plasma in the presence of a strong magnetic field depends solely on the strength of the magnetic field. However, for the interacting quark-gluon plasma, the longitudinal QNS depends on both temperature and magnetic field. This susceptibility increases with temperature and approaches the ideal (non-interacting) QNS at very high temperatures, as demonstrated in Fig. 6.21.

Transverse QNS behaves quite differently from the longitudinal one due to the influence of magnetization. In an ideal quark-gluon plasma, the transverse QNS is zero because only gluons contribute to the transverse pressure. The quarks' momenta are constrained to align with the magnetic field due to dimensional reduction in the presence of a strong magnetic field. Therefore, the transverse pressure solely consists of gluon pressure. When interactions are present, however, the transverse QNS becomes non-zero as the transverse pressure gains contribution from internal quark loops. This transverse QNS gradually diminishes at high temperatures (in the free limit), as illustrated in Fig. 6.21.
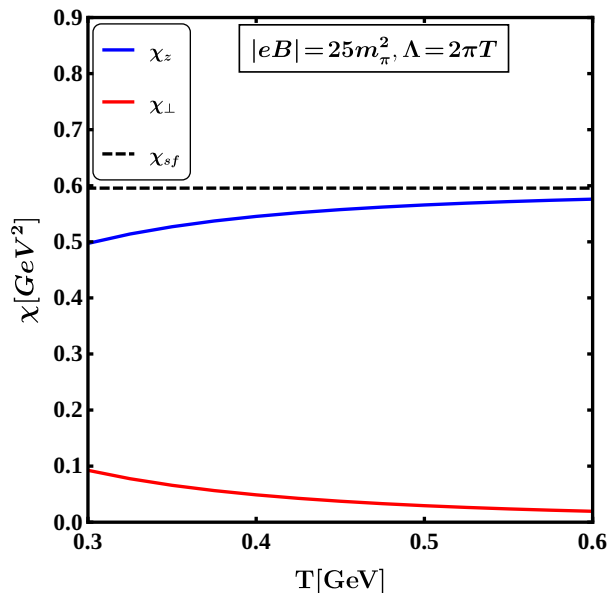

Figure 6.21: The behaviour of longitudinal and transverse QNS with temperature in the presence of a strong magnetic field.

7. Damping Rate in Presence of Thermo-Magnetic Medium

The damping rate γ for a particle in a thermal medium carries a straightforward physical interpretation. Due to continuous interactions with the medium, such a particle (or more precisely, a quasiparticle) does not possess a sharply defined energy level but instead appears as a resonance with a width given by γ. A quasiparticle can only be treated as a genuine physical excitation when γ is much smaller than its energy, allowing it to propagate sufficiently long to produce meaningful physical effects.

In quantum field theory with a thermal background but without a magnetic field, the damping rate of a particle is linked to the imaginary part of its dispersion relation [184, 185]. Additionally, for fermions, the damping rate is connected to the imaginary part of the self-energy [252]. Here, we extend the concept of the damping rate to include a thermo-magnetic medium. Below, we define the damping rates for various types of particles in such a medium.

The damping or interaction rate characterizes the attenuation of a particle over time [184, 185], described by the time evolution of a plane wave $\exp(-i\omega t)$, where ω represents the particle's frequency. As discussed earlier, the particle's dispersion relation indicates that ω generally consists of both real and imaginary components:

$$\omega = \text{Re } \omega + i\text{Im } \omega. \tag{7.1}$$

Now, we define the damping rate as

$$\gamma = -\text{Im } \omega. \tag{7.2}$$

This damping rate quantifies the rate at which the particle's amplitude decreases due to interactions with the medium. Then we write

$$\exp(-i\omega t) = \exp\left(-i\text{Re } \omega t\right) \times \exp\left(-\gamma t\right). \tag{7.3}$$

For a gauge boson, the propagator in the covariant gauge, as obtained in Eq. (5.52), exhibits two degenerate transverse modes and one long-wavelength plasmon mode. The dispersion relations for the longitudinal plasmon mode and the two transverse modes in the weak-field approximation are given, respectively, by Eqs. (5.189a), (5.189b), and (5.189c). The medium-induced longitudinal (plasmon) mode, derived from Eq. (5.189a), does not contribute to the damping rate[19]. The dispersion relations for the two transverse modes of a gauge boson are, respectively, given as

$$P^2 + c = \omega^2 - p^2 + c = 0\,, \tag{7.4a}$$

$$P^2 + d = \omega^2 - p^2 + d = 0\,, \tag{7.4b}$$

where c and d are associated with transverse self-energies of gauge boson and defined in Eq. (5.38b) and Eq. (5.38c). For the case of no overdamping, the damping rates of the transverse gauge boson modes can be obtained, respectively, as

$$\gamma_c = \frac{1}{2\omega(p)}\text{Im } c(\omega, p)\,, \tag{7.5a}$$

$$\gamma_d = \frac{1}{2\omega(p)}\text{Im } d(\omega, p)\,. \tag{7.5b}$$

The damping rates for gauge bosons in the strong field approximation can be derived from the dispersion relations in Eqs. (5.151a) and (5.151b).

For a fermion with mass m_f and four-momentum P, the dispersion relation can be expressed as

$$\not{P} + m_f - \Sigma(E, p) = 0\,, \tag{7.6}$$

---

[19]This is because the longitudinal dispersive mode merges with the light cone at high photon momentum.

where $E = \sqrt{P^2 + M^2}$ is energy and $\Sigma(E, p)$ is self-energy of heavy fermion. Squaring the dispersion relation given in Eq. (7.6) and then taking the trace, one obtains

$$E = \frac{1}{2E} \, \text{Tr} \, \left[(\slashed{P} + m_f) \, \Sigma(E, p) \right] \quad \Rightarrow \quad \gamma(E) = -\text{Im} \, E = -\frac{1}{2E} \, \text{Im} \, \text{Tr} \, \left[(\slashed{P} + m_f) \, \Sigma(E, p) \right], \tag{7.7}$$

where we have neglected Σ^2 term which contributes to higher order.

7.1. Soft Contribution to Hard Photon Damping Rate in Thermo-Magnetic Medium

The tensor structures of $R^{\mu\nu}$ and $Q^{\mu\nu}$ are given as [68]

$$R^{\mu\nu} = \begin{pmatrix} 0 & 0 & 0 & 0 \\ 0 & 0 & 0 & 0 \\ 0 & 0 & -1 & 0 \\ 0 & 0 & 0 & 0 \end{pmatrix}, \quad Q^{\mu\nu} = \begin{pmatrix} 0 & 0 & 0 & 0 \\ 0 & -\cos^2 \theta_p & 0 & \sin \theta_p \cos \theta_p \\ 0 & 0 & 0 & 0 \\ 0 & \sin \theta_p \cos \theta_p & 0 & -\sin^2 \theta_p \end{pmatrix}. \tag{7.8}$$

Using Eq.(7.8) in Eq.(5.38b) and Eq. (5.38c) we can write the form factors σ and δ in weak field approximation as

$$c = -\left(\Pi_0^{22} + \Pi_2^{22} \right), \tag{7.9}$$

$$d = -\cos^2 \theta_p \left(\Pi_0^{11} + \Pi_2^{11} \right) - \sin^2 \theta_p \left(\Pi_0^{33} + \Pi_2^{33} \right) + 2 \sin \theta_p \cos \theta_p \left(\Pi_0^{13} + \Pi_2^{13} \right). \tag{7.10}$$

Combining Eq.(7.5a) with Eq.(7.9) and Eq.(7.5b) with Eq.(7.10), the damping rates become

$$\gamma_c(p) = \frac{1}{2p} \left(\text{Im}\Pi_0^{22} + \text{Im}\Pi_2^{22} \right), \tag{7.11}$$

$$\gamma_d(p) = \frac{1}{2p} \left[\cos^2 \theta_p \left(\text{Im}\Pi_0^{11} + \text{Im}\Pi_2^{11} \right) + \sin^2 \theta_p \left(\text{Im} \, \Pi_0^{33} + \text{Im} \, \Pi_2^{33} \right) \right.$$
$$\left. -2 \sin \theta_p \cos \theta_p \left(\text{Im} \, \Pi_0^{13} + \text{Im} \, \Pi_2^{13} \right) \right] \tag{7.12}$$

The damping rates in Eqs.(7.11) and (7.12) can now be written as

$$\gamma_c(p) = \gamma_{\text{th}}(p) + \gamma_c^B(p), \tag{7.13}$$

$$\gamma_d(p) = \gamma_{\text{th}}(p) + \gamma_d^B(p). \tag{7.14}$$

where γ_{th} is the $\mathcal{O}[(eB)^0]$ contribution or thermal contribution is given as

$$\gamma_{\text{th}}(p) = \frac{1}{2p} \text{Im}\Pi_0^{22} = \frac{1}{2p} \left[\cos^2 \theta_p \text{Im}\Pi_0^{11} + \sin^2 \theta_p \text{Im} \, \Pi_0^{33} - 2 \sin \theta_p \cos \theta_p \text{Im} \, \Pi_0^{13} \right]. \tag{7.15}$$

The thermomagnetic corrections of $\mathcal{O}[(eB)^2]$ are given as

$$\gamma_c^B(p) = \frac{1}{2p} \text{Im}\Pi_2^{22}, \tag{7.16}$$

$$\gamma_d^B(p) = \frac{1}{2p} \left[\cos^2 \theta_p \text{Im}\Pi_2^{11} + \sin^2 \theta_p \text{Im} \, \Pi_2^{33} - 2 \sin \theta_p \cos \theta_p \text{Im} \, \Pi_2^{13} \right]. \tag{7.17}$$

We need to obtain the imaginary parts of 11, 22, 33 and 13 components of the photon self-energy $\Pi^{\mu\nu}$ which are computed in Ref. [68] in details. We note that our convention of the photon self-energy $\Pi^{\mu\nu}$ differs by a minus sign from that in Ref. [68] . Thus, the imaginary parts of 11, 22, 33 and 13 components of the photon self-energy $\Pi^{\mu\nu}$ here will be preceded by a minus sign.

The damping rate of photon in presence of magnetic field depends on the angle, θ_p, between the photon's momentum and the magnetic field. Figure 7.1 illustrates the variation of the damping rate for a hard photon with its propagation angle. It shows an increase in the damping rate with the increasing propagation angle. Notably, the two transverse modes of a hard photon are damped similarly. Due to the weak strength of the magnetic field, the difference in damping rates is minimal. We note that the magnetic correction scales as $\mathcal{O}[(eB)^2]$, and reversing the direction of the magnetic field from z to $-z$ does not affect the result. These two orientations correspond to the propagation angles θ_p and $\pi - \theta_p$, which are
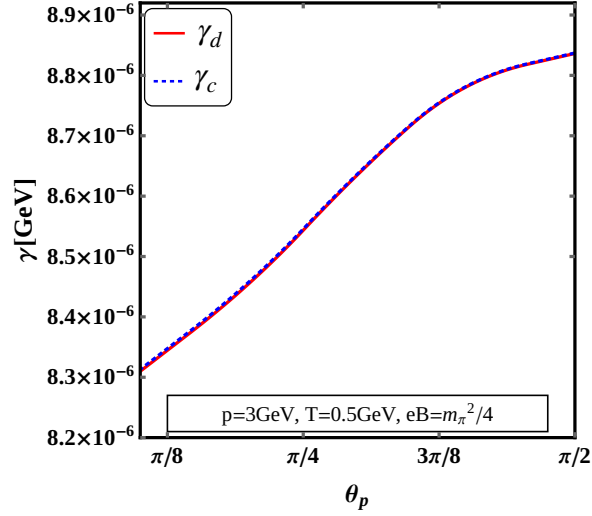
Figure 7.1: A plot of the damping rate of a photon as a function of the propagation angle θ_p for the given parameters $p = 3$ GeV, $T = 0.5$ GeV and $eB = m_\pi^2/4$.

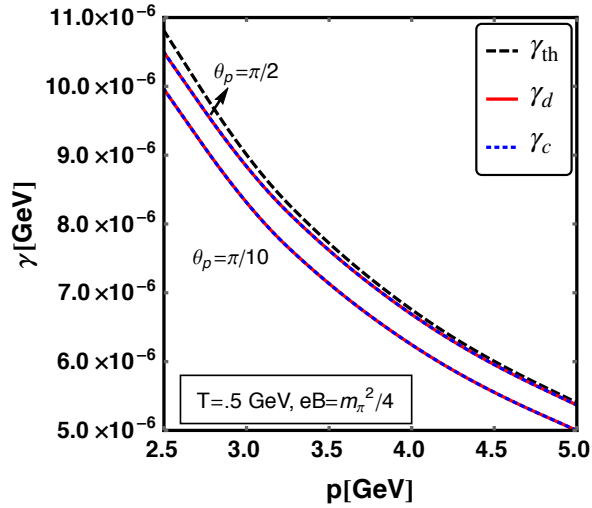identical and lead to the same damping rate for a photon.

Figure 7.2: Plot of damping rate of photon with the energy for the given conditions $T = 0.5$ GeV and $eB = m_\pi^2/4$ at the specified propagation angles $\theta_p = \pi/10$ and $\pi/2$.

In Figure 7.2, we present the damping rate as a function of photon momentum for two propagation angles, $\pi/10$ and $\pi/2$. The soft contribution to the damping rate in a thermal medium matches well with the results reported in Ref. [188]. When considering a thermo-magnetic medium, the soft contribution to the damping rate is reduced compared to the thermal case. For smaller propagation angles, this reduction is more significant than in the thermal medium. As the photon momentum increases, the damping rate approaches the thermal value, suggesting that at higher momenta, the temperature becomes the dominant scale relative to the strength of the magnetic field.

In Figure 7.3, we observe the variation of the damping rate with temperature for a specific momentum and magnetic field, across two propagation angles: $\pi/10$ and $\pi/2$. It is evident that the soft contribution to the damping rate increases with temperature both in thermal and thermomagnetic mediums. For a smaller propagation angle ($\pi/10$), the damping rate is significantly more reduced compared to that of a larger propagation angle ($\pi/2$). This behavior aligns with the
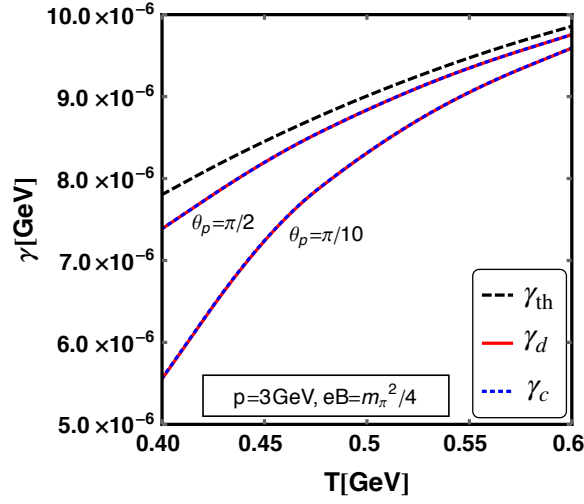
Figure 7.3: A plot of the damping rate of a hard photon as a function of temperature T for the given conditions $p = 3$ GeV and $eB = m_\pi^2/4$, and for the propagation angles $\pi/10$ and $\pi/2$.

trends observed in Figure 7.2, where the damping rate showed different dependencies on the propagation angle.
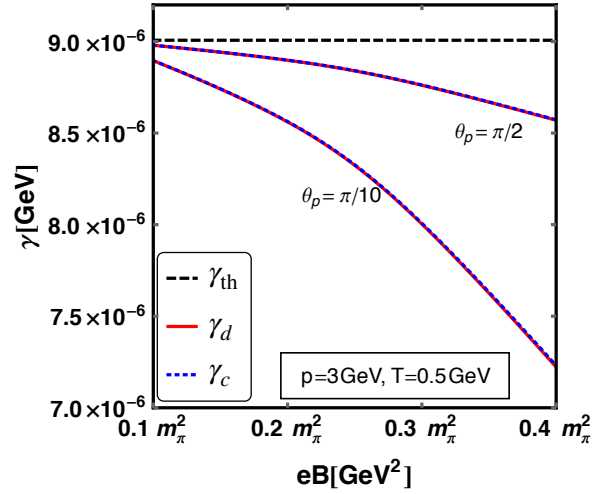
Figure 7.4: Plot of damping rate of the hard photon as a function of the magnetic field strength eB for the conditions $T = 0.5$ GeV and $p = 3$ GeV, and for two propagation angles $\pi/10$ and $\pi/2$.

In Figure 7.4, we observe the variation of the damping rate with the magnetic field strength for specific values of photon momentum and temperature across two propagation angles. The thermal damping rate, represented by the black dashed horizontal line, is independent of the magnetic field strength $(\mathcal{O}[(eB)^0])$. As the magnetic field increases, the thermo-magnetic damping rate decreases. This indicates that higher magnetic fields suppress the damping effect. At smaller propagation angles $(\pi/10)$, photons experience less damping compared to higher propagation angles $(\pi/2)$. This behaviour aligns with the trends observed in Figure 7.2, where the damping rate varies with the propagation angle, showing reduced damping at smaller angles.

In Figure 7.5, we observe the variation of the photon damping rate with the separation scale Λ while maintaining the scale hierarchy $eT \ll \Lambda \ll T$. As the allowed phase space increases with the increase of Λ, the damping rate is also
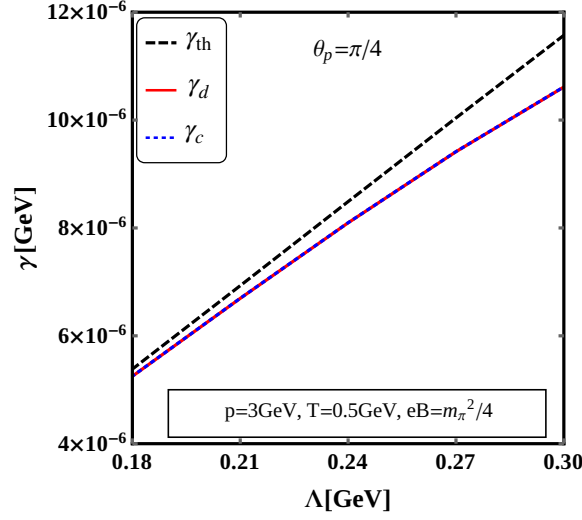
Figure 7.5: Plot of damping rate of photon as a function of Λ for the specified conditions $\theta_p = \pi/4$, $p = 3$ GeV, $T = 0.5$ GeV and $eB = m_\pi^2/4$.

increases with it [20]. The magnetic correction to the thermal damping rate is negative, indicating that the presence of a magnetic field reduces the damping rate compared to the purely thermal case. As Λ increases, the difference between the thermal and thermo-magnetic damping rates widens, reflecting the cumulative effects of the magnetic field and increasing phase space.

7.2. Damping Rate of Fermion in an Arbitrary Magnetic Field

In this subsection we will calculate the damping rate of fermion in a thermal and generalised magnetic field following two approaches. The first one is using imaginary part of the fermion self-energy and the second one is using the poles of the fermion propagators vis-a-vis from the fermion dispersion relation.

7.2.1. Damping rate from imaginary part of the fermion self-energy

he damping rate, as introduced in Ref.[69], is derived using wave functions in coordinate space, building upon the general methodology outlined in Ref.[252]. It is expressed as

$$\gamma_n(p_z) = \frac{1}{2p_0} \int d^4u' \int d^4u \text{Tr} \left[\frac{2\pi\ell^2}{V_\perp} \int dp \sum_s \bar{\Psi}_{n,p,s}(u') \text{Im}\Sigma(u',u) \Psi_{n,p,s}(u) \right], \tag{7.18}$$

where $u = (t,x,y,z)$ and $u' = (t',x',y',z')$ represent space-time coordinates. The factor $1/(2\pi\ell^2)$ i denotes the number of degenerate states per unit area in the transverse plane, excluding spin degeneracy. The total number of these degenerate states is then given by $V_\perp/(2\pi\ell^2)$, where $V_\perp$ is the transverse plane's volume (or area).

By analyzing the fermion wave functions in the presence of a constant magnetic field, one can subsequently derive the result presented in Ref. [69] as

$$\begin{aligned} \gamma_n(p_z) &= \frac{1}{p_0} \left\{ \frac{\delta_{n,0}}{2} \left[p_\parallel^2 \text{Im}(\delta v_{\parallel,n} + s_\perp \tilde{v}_n) - \bar{m}_0 \text{Im}(\delta m_n + s_\perp \tilde{m}_n) \right] \right. \\ &\quad \left. + (1 - \delta_{n,0}) \left[p_\parallel^2 \text{Im}(\delta v_{\parallel,n}) - \bar{m}_0 \text{Im}(\delta m_n) - 2n|qB| \text{Im}(\delta v_{\perp,n}) \right] \right\}, \end{aligned} \tag{7.19}$$

---

[20] However, it's noted that when the hard contribution is added, the damping rate is expected to independent of Λ.

In the final expression, it is assumed that the fermion is on the mass shell, which implies $p_0 = \sqrt{2n|qB| + \bar{m}_0^2 + p_z^2}$. The imaginary parts of the self-energy functions are then provided in Ref. [69] as

$$\mathrm{Im}\left[\delta v_{\parallel,n}^+\right] = \frac{\alpha}{p_\parallel^2}\sum_{n'=0}^{\infty}\sum_{\{s\}}\int q_\perp dq_\perp \mathcal{I}_0^{n,n'-1}\left(\frac{q_\perp^2\ell^2}{2}\right)\frac{\left(s_1 E_{n',k_z^{s'}}p_0 - k_z^{s'}p_z\right)\left[1 - n_F(s_1 E_{n',k_z^{s'}}) + n_B(s_2 E_q)\right]}{s_1 s_2\sqrt{\left[q_\perp^2 - (q_\perp^-)^2\right]\left[q_\perp^2 - (q_\perp^+)^2\right]}}, \quad (7.20)$$

$$\mathrm{Im}\left[\delta v_{\parallel,n}^-\right] = \frac{\alpha}{p_\parallel^2}\sum_{n'=0}^{\infty}\sum_{\{s\}}\int q_\perp dq_\perp \mathcal{I}_0^{n-1,n'}\left(\frac{q_\perp^2\ell^2}{2}\right)\frac{\left(s_1 E_{n',k_z^{s'}}p_0 - k_z^{s'}p_z\right)\left[1 - n_F(s_1 E_{n',k_z^{s'}}) + n_B(s_2 E_q)\right]}{s_1 s_2\sqrt{\left[q_\perp^2 - (q_\perp^-)^2\right]\left[q_\perp^2 - (q_\perp^+)^2\right]}}, \quad (7.21)$$

$$\mathrm{Im}\left[\delta m_n^+\right] = \alpha\bar{m}_0\sum_{n'=0}^{\infty}\sum_{\{s\}}\int q_\perp dq_\perp \left[\mathcal{I}_0^{n,n'}\left(\frac{q_\perp^2\ell^2}{2}\right) + \mathcal{I}_0^{n,n'-1}\left(\frac{q_\perp^2\ell^2}{2}\right)\right]\frac{1 - n_F(s_1 E_{n',k_z^{s'}}) + n_B(s_2 E_q)}{s_1 s_2\sqrt{\left[q_\perp^2 - (q_\perp^-)^2\right]\left[q_\perp^2 - (q_\perp^+)^2\right]}}, \quad (7.22)$$

$$\mathrm{Im}\left[\delta m_n^-\right] = \alpha\bar{m}_0\sum_{n'=0}^{\infty}\sum_{\{s\}}\int q_\perp dq_\perp \left[\mathcal{I}_0^{n-1,n'}\left(\frac{q_\perp^2\ell^2}{2}\right) + \mathcal{I}_0^{n-1,n'-1}\left(\frac{q_\perp^2\ell^2}{2}\right)\right]\frac{1 - n_F(s_1 E_{n',k_z^{s'}}) + n_B(s_2 E_q)}{s_1 s_2\sqrt{\left[q_\perp^2 - (q_\perp^-)^2\right]\left[q_\perp^2 - (q_\perp^+)^2\right]}} \quad (7.23)$$

$$\mathrm{Im}\left[\delta v_{\perp,n}\right] = \frac{\alpha}{2n}\sum_{n'=0}^{\infty}\sum_{\{s\}}\int q_\perp dq_\perp \mathcal{I}_2^{n-1,n'-1}\left(\frac{q_\perp^2\ell^2}{2}\right)\frac{1 - n_F(s_1 E_{n',k_z^{s'}}) + n_B(s_2 E_q)}{s_1 s_2\sqrt{\left[q_\perp^2 - (q_\perp^-)^2\right]\left[q_\perp^2 - (q_\perp^+)^2\right]}}. \quad (7.24)$$

By using the five functions in Eqs. (7.20) through (7.23), one can obtain the spin-average Landau-level dependent values of the parallel velocity and mass as [69]

$$\mathrm{Im}\left[\delta v_{\parallel,n}\right] = \frac{1}{2}\mathrm{Im}\left[\delta v_{\parallel,n}^+ + \delta v_{\parallel,n}^-\right], \quad (7.25)$$

$$\mathrm{Im}\left[\delta m_n\right] = \frac{1}{2}\mathrm{Im}\left[\delta m_n^+ + \delta m_n^-\right]. \quad (7.26)$$

along with the associated spin-splitting functions, i.e.,

$$\mathrm{Im}\left[\tilde{v}_n\right] = \frac{s_\perp}{2}\mathrm{Im}\left[\delta v_{\parallel,n}^+ - \delta v_{\parallel,n}^-\right], \quad (7.27)$$

$$\mathrm{Im}\left[\tilde{m}_n\right] = \frac{s_\perp}{2}\mathrm{Im}\left[\delta m_n^+ - \delta m_n^-\right]. \quad (7.28)$$

As anticipated, all these parameters, including $\mathrm{Im}\left[\delta v_{\perp,n}\right]$, depend on the Landau levels and are functions of the longitudinal momentum p_z.

Substituting Eqs. (7.20) through (7.24) into the general expression for the rate (7.19), the following damping rate for the zeroth Landau level can be derived as

$$\gamma_0(p_z) = \frac{\alpha|qB|}{4p_0}\sum_{n'=0}^{\infty}\sum_{\{s\}}\int d\xi \left[n'\mathcal{I}_0^{0,n'-1}(\xi) - \left(n' + \bar{m}_0^2\ell^2\right)\mathcal{I}_0^{0,n'}(\xi)\right]\frac{\left[1 - n_F(s_1 E_{n',k_z^{s'}}) + n_B(s_2 E_q)\right]}{s_1 s_2\sqrt{(\xi - \xi^-)(\xi - \xi^+)}}, \quad (7.29)$$

where the identity $\xi\mathcal{I}_0^{0,n'-1}(\xi) = n'\mathcal{I}_0^{0,n'}(\xi)$ has been used. The expression for the damping rate in higher Landau levels ($n \geq 1$) is as follows

$$\gamma_n(p_z) = \frac{\alpha|qB|}{4p_0}\sum_{n'=0}^{\infty}\sum_{\{s\}}\int d\xi \left[\mathcal{I}_0^{n,n'-1}(\xi) + \mathcal{I}_0^{n-1,n'}(\xi)\right]\frac{(n + n')\left[1 - n_F(s_1 E_{n',k_z^{s'}}) + n_B(s_2 E_q)\right]}{s_1 s_2\sqrt{(\xi - \xi^-)(\xi - \xi^+)}}$$
$$- \frac{\alpha}{4p_0}\sum_{n'=0}^{\infty}\sum_{\{s\}}\int d\xi \left[\mathcal{I}_0^{n,n'}(\xi) + \mathcal{I}_0^{n-1,n'-1}(\xi)\right]\frac{(n + n' + \bar{m}_0^2\ell^2)\left[1 - n_F(s_1 E_{n',k_z^{s'}}) + n_B(s_2 E_q)\right]}{s_1 s_2\sqrt{(\xi - \xi^-)(\xi - \xi^+)}}. \quad (7.30)$$

In this context, shorthand notations are introduced: $\xi = q_\perp^2\ell^2/2$ and $\xi^\pm = (q_\perp^\pm)^2\ell^2/2$.

The expressions for the damping rates can be rewritten in a form valid for all $n \geq 0$ as follows

$$\gamma_n(p_z) = \frac{\alpha|qB|}{4p_0}\sum_{n'=0}^{\infty}\sum_{\{s\}}\int d\xi \frac{\mathcal{M}_{n,n'}(\xi)\left[1 - n_F(s_1 E_{n',k_z^{s'}}) + n_B(s_2 E_q)\right]}{s_1 s_2\sqrt{(\xi - \xi^-)(\xi - \xi^+)}}, \quad (7.31)$$

wherethe following function has been introduced as

$$\mathcal{M}_{n,n'}(\xi) = -\left(n + n' + \bar{m}_0^2\ell^2\right)\left[\mathcal{I}_0^{n,n'}(\xi) + \mathcal{I}_0^{n-1,n'-1}(\xi)\right] + (n + n')\left[\mathcal{I}_0^{n,n'-1}(\xi) + \mathcal{I}_0^{n-1,n'}(\xi)\right]. \quad (7.32)$$
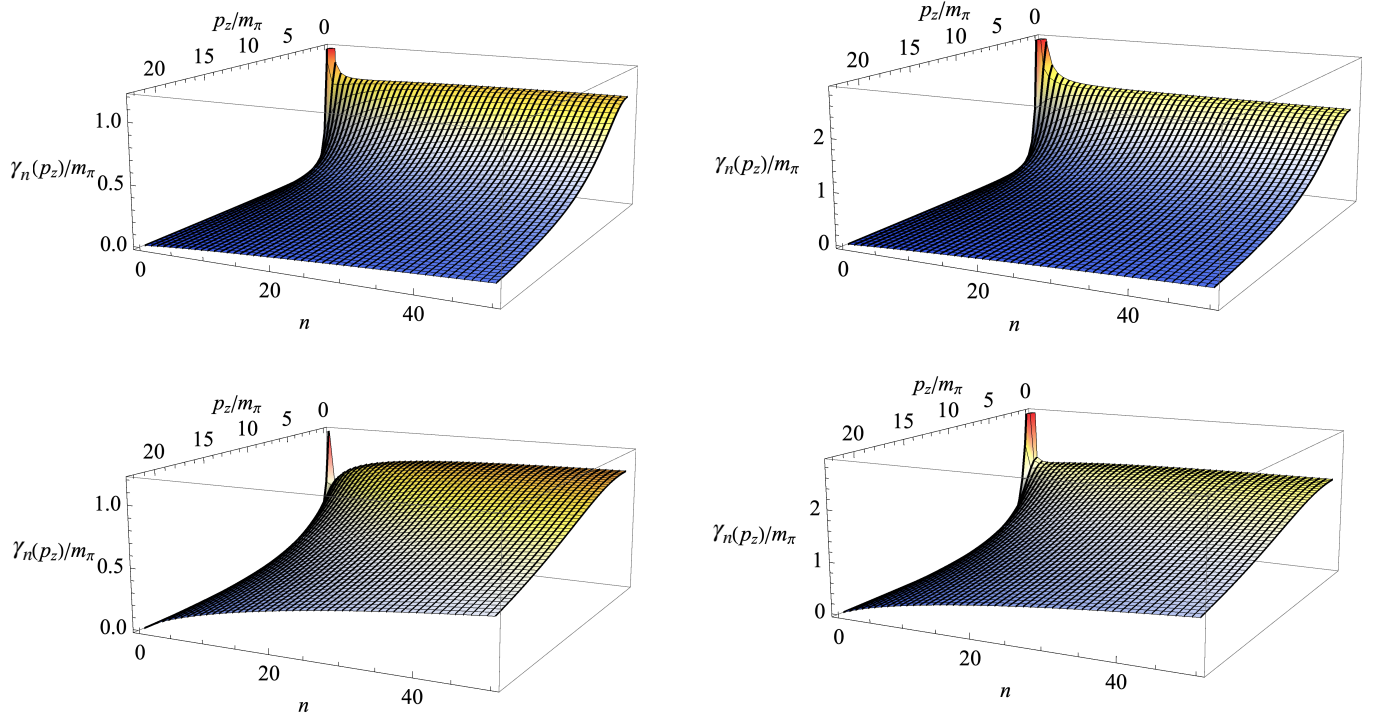
Figure 7.6: The fermion damping rate as a function of the longitudinal momentum p_z and the Landau-level index n is shown in units of the pion mass. Four separate panels display the results for two different temperatures: $T = 200$ MeV (left panels) and $T = 400$ MeV (right panels), and two magnetic fields: $|qB| = (75 \text{ MeV})^2$ (top panels) and $|qB| = (200 \text{ MeV})^2$ (bottom panels).

As can be verified, the damping rate in Eq. (7.31) is a positive definite quantity.

The fermion damping rate described by Eq.(7.31) is shown numerically as a function of the Landau-level index n and the longitudinal momentum p_z in Fig. 7.6. The rate values and p_z are measured in units of the pion mass $m_\pi = 135$ MeV. A QCD coupling constant of $\alpha_s = 1/2$ is used for the calculations. The left panel presents results for a temperature $T = 200$ MeV with two different magnetic fields: $|qB| = (75 \text{ MeV})^2$ (top panels) and $|qB| = (200 \text{ MeV})^2$ (bottom panels). The right panel displays results for a temperature $T = 400$ MeV with the same two magnetic field strengths as mentioned in the left panel. From Fig. 7.6, it is clear that both temperature and magnetic field contribute to an increase in the damping rates. These factors expand the phase space available for transitions to other Landau levels. Specifically, the presence of a magnetic field plays a critical role in initiating the leading-order processes responsible for the damping rate. Without the field, only subleading-order processes influence the fermion damping rate. The enhancement factors resulting from increased temperatures and magnetic fields are not uniform across the Landau-level index n and longitudinal momentum p_z. For instance, raising the temperature from $T = 200$ MeV to $T = 400$ MeV leads to enhancement factors ranging from approximately 2 to 4 across the entire n and p_z region investigated. The most substantial enhancements occur in the low-lying Landau levels at small longitudinal momenta. In contrast, increasing the magnetic field from $|qB| = (75 \text{ MeV})^2$ to $|qB| = (200 \text{ MeV})^2$ results the largest enhancement factors, ranging from 5 to 6, which are observed at high p_z values and low n.

7.2.2. Damping rates from the poles of the propagator

If the full structure of the fermion propagator is known, the fermion damping rate can be determined from the positions of its poles in the complex energy plane. At the leading order in the coupling, the explicit form of the fermion propagator
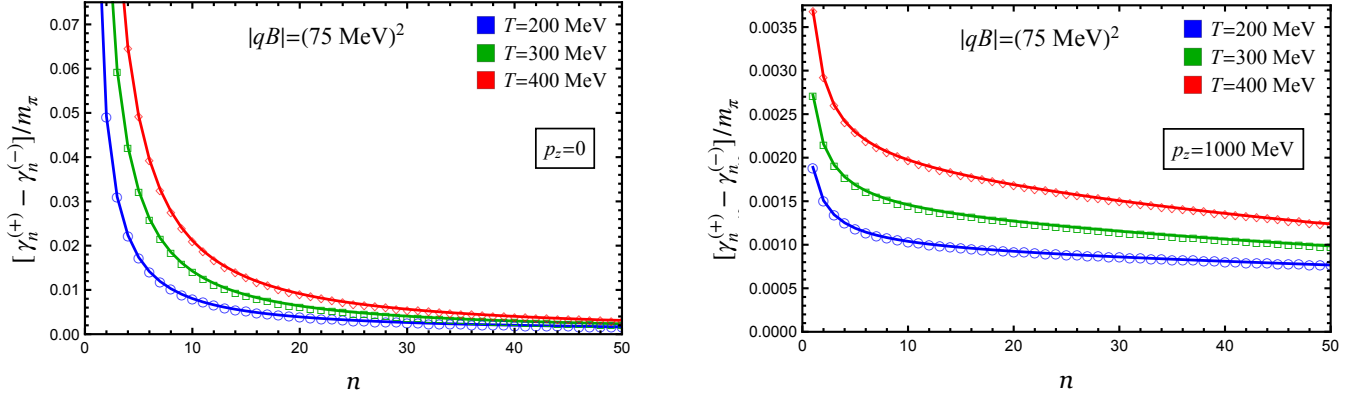
Figure 7.7: The spin-splitting of damping rates as functions of the Landau-level index n is illustrated for two fixed values of the longitudinal momentum: $p_z = 0$ (left panel) and $p_z = 1000$ MeV (right panel). The magnetic field is $|qB| = (75 \text{ MeV})^2$. Each panel shows results for three different temperatures: $T = 200$ MeV (blue), $T = 300$ MeV (green), and $T = 400$ MeV (red).

is outlined in Ref. [69]. The fermion propagator is modified by self-energy functions, and the quasiparticle energies can be extracted from the positions of the poles. Assuming that self-energy corrections are small, the approximate expressions for the (positive) energies are given by Ref. [69] as

$$
p_0^{(\pm)} \simeq \sqrt{2n|qB| + \bar{m}_0^2 + p_z^2}\left(1 + \frac{\bar{m}_0 \delta m_n - (2n|qB| + \bar{m}_0^2)\delta v_{\parallel,n} + 2n|qB|\delta v_{\perp,n} \pm \sqrt{2n|qB| + \bar{m}_0^2}(\bar{m}_0 \tilde{v}_n - \tilde{m}_n)}{2n|qB| + \bar{m}_0^2 + p_z^2}\right) \quad (7.33)
$$

Note that there are two separate branches of solutions represented by $(\pm)$, corresponding to the two spin states. In the free case, these branches were degenerate. However, already at the leading order in coupling, the self-energy corrections $\tilde{v}_n$ and $\tilde{m}_n$ lifts this degeneracy.

Nevertheless, using the imaginary parts of the self-energy functions from Eqs.(7.20) to (7.24), we can determine the leading-order corrections to the imaginary parts of the particle energies, specifically $\text{Im}[\delta p_{0,n}^{(\pm)}]$. Since the $\text{Im}[\delta p_{0,n}^{(\pm)}]$ should coincide up an overall sign with the damping rate, the result is derived in Ref. [69] as

$$
\gamma_n^{(\pm)} \simeq \frac{(2n|qB| + \bar{m}_0^2)\text{Im}[\delta v_{\parallel,n}] - \bar{m}_0\text{Im}[\delta m_n] - 2n|qB|\text{Im}[\delta v_{\perp,n}] \mp \sqrt{2n|qB| + \bar{m}_0^2}(\bar{m}_0\text{Im}[\tilde{v}_n] - \text{Im}[\tilde{m}_n])}{\sqrt{2n|qB| + \bar{m}_0^2 + p_z^2}}. \quad (7.34)
$$

As anticipated, this result highlights that the two spin-split Landau-level states exhibit different damping rates. It is also interesting to observe that the spin-averaged damping rate, defined as $\Gamma_n^{(\text{ave})} \equiv (\Gamma_n^{(+)} + \Gamma_n^{(-)})/2$, matches exactly with the result obtained using a distinct method in the preceding subsection, as shown in Eq. (7.19).

We now examine the spin-splitting effects on the damping rates. Two sets of numerical results are shown in Fig. 7.7. This figure displays the difference between the damping rates for spin-up and spin-down states as functions of the Landau-level index n. The two panels displays the results for the same minimal magnetic field strength, $|qB| = (75 \text{ MeV})^2$, but for two distinct longitudinal momenta: $p_z = 0$ (left panel) and $p_z = 1000$ MeV (right panel). The results for three different temperatures are shown in various colors. The difference in damping rates between the spin-up and spin-down states is generally small, typically a few percent or less of the average rate. However, it can reach up to around 10% in the low-lying Landau levels at small longitudinal momenta. It is also noted that the relative spin splitting diminishes with increasing magnetic field. Therefore, for most practical applications, using the spin-averaged damping rate, $\Gamma_n^{(\text{ave})} \equiv (\Gamma_n^{(+)} + \Gamma_n^{(-)})/2$, as explored in detail in the previous subsection 7.2.1, may be sufficient. This conclusion is further supported by the observation that the systematic uncertainties associated with the one-loop approximation used in the study are likely larger than the effects of spin splitting. Nevertheless, spin splitting represents a qualitatively new feature that can have

a significant impact in strongly magnetized plasmas. Although the differences in the damping rates between spin-split states in each Landau level are relatively small in magnitude, they may still influence certain spin-related phenomena, such as chiral magnetic or chiral separation effects.

8. Electromagnetic Spectral Function and Dilepton Production Rate in Presence of Thermo-Magnetic Medium

Electromagnetically interacting particles, such as real photons and virtual photons (dileptons), serve as effective probes for studying the thermodynamic properties of strongly interacting matter created in ultra-relativistic nucleus-nucleus collisions. Their dual nature is key: electromagnetic interactions are strong enough to produce detectable signals yet weak enough to allow photons and leptons to escape the finite nuclear system without undergoing further interactions. The emission characteristics of real and virtual photons are intrinsically linked to the size of the thermal system they originate from. In large systems, photons are likely to experience rescattering and thermalization, leading to a momentum distribution that adheres to the Planck spectrum. In such cases, the emission rate corresponds to blackbody radiation, depending solely on the temperature and surface area of the emitter, independent of its microscopic details. However, for the much smaller systems typical of heavy-ion collisions – where the size is significantly smaller than the photon mean free path–photons tend to escape without further interactions. Here, the emission rate is determined by the thermal constituent dynamics, which are encoded in the imaginary part of the photon self-energy. Consequently, the photon and dilepton spectra offer valuable insights into the properties and interactions of the thermal constituents from which they originate [253, 254].

In Ref.[255], it was demonstrated that emission rates in a thermalized system can be connected to the electromagnetic current correlation function within a quantum framework, and notably, in a nonperturbative way. More broadly, the production rate of a particle that interacts weakly with the thermal bath constituents (which may themselves strongly interact) can always be formulated in terms of the discontinuities or the imaginary parts of the particle's self-energy[153, 256–260].

In the following, we briefly discuss how the spectral function of photons is related to the emission rates of virtual photons. This connection arises through the discontinuities in the photon self-energy in a thermal medium [153, 257, 258].

The two point current-current correlator, $C_{\mu\nu}(p)$, can be expressed in terms of the photon self-energy, $\Pi_{\mu\nu}(p)$, as follows

$$q_f^2 C_{\mu\nu}(p) = \Pi_{\mu\nu}(p), \tag{8.1}$$

with q_f represents the electric charge of a given quark flavour f. This relationship establishes a link between the fluctuations of the electromagnetic current in a thermal system and the photon self-energy in the quantum field framework.

The electromagnetic spectral representation can be obtained by taking the imaginary part of the current-current correlation function $C_\mu^\mu(p)$ as

$$\rho(p) = \frac{1}{\pi}\mathcal{I}m\, C_\mu^\mu(p) = \frac{1}{\pi}\mathcal{I}m\, \Pi_\mu^\mu(p)/q_f^2. \tag{8.2}$$

The dilepton multiplicity per unit space-time volume is expressed as [257]

$$\frac{dR}{d^4x} = 2\pi e^2 e^{-\beta p_0} L_{\mu\nu}\rho^{\mu\nu}\frac{d^3\vec{q}_1}{(2\pi)^3 E_1}\frac{d^3\vec{q}_2}{(2\pi)^3 E_2}. \tag{8.3}$$

In this context, e represents the electromagnetic coupling constant. The three-momenta and energies of the lepton pair

components are given by $\vec{q}_i$ and E_i, respectively, where $i = 1, 2$. The photonic tensor, or the electromagnetic spectral function in a thermal medium, can be expressed as

$$\rho^{\mu\nu}(p_0, \vec{p}) = -\frac{1}{\pi}\frac{e^{\beta p_0}}{e^{\beta p_0} - 1}\text{Im}\left[D^{\mu\nu}(p_0, \vec{p})\right] \equiv -\frac{1}{\pi}\frac{e^{\beta p_0}}{e^{\beta p_0} - 1}\frac{1}{P^4}\text{Im}\left[\Pi^{\mu\nu}(p_0, \vec{p})\right], \quad (8.4)$$

where 'Im' stands for imaginary part, $\Pi^{\mu\nu}$ corresponds to the two-point current-current correlation function or the self-energy of the photon and $D^{\mu\nu}$ corresponds to the photon propagator. Here we have used the relation [257]

$$D^{\mu\nu}(p_0, \vec{p}) = \frac{1}{P^4}\Pi^{\mu\nu}(p_0, \vec{p}), \quad (8.5)$$

where $P \equiv (p_0, \vec{p})$ is the four momenta of the photon. The leptonic tensor in terms of Dirac spinors is expressed as

$$L_{\mu\nu} = \frac{1}{4}\sum_{\text{spins}}\text{Tr}\left[\bar{u}(Q_2)\gamma_\mu v(Q_1)\bar{v}(Q_1)\gamma_\nu u(Q_2)\right] = Q_{1\mu}Q_{2\nu} + Q_{1\nu}Q_{2\mu} - (Q_1 \cdot Q_2 + m_l^2)g_{\mu\nu}, \quad (8.6)$$

where $Q_1 \equiv (q_0, \vec{q}_1)$ and $Q_2 \equiv (q_0, \vec{q}_2)$ are the four-momenta of the first and second leptons, respectively, and m_l is the mass of the lepton. Incorporating the delta function $\int d^4P\,\delta^4(Q_1 + Q_2 - P) = 1$, the dilepton multiplicity from equation (8.3) can be expressed as

$$\frac{dR}{d^4x} = 2\pi e^2 e^{-\beta p_0}\int d^4P\,\delta^4(Q_1 + Q_2 - P)L_{\mu\nu}\rho^{\mu\nu}\frac{d^3\vec{q}_1}{(2\pi)^3 E_1}\frac{d^3\vec{q}_2}{(2\pi)^3 E_2}. \quad (8.7)$$

Using the identity

$$\int \frac{d^3\vec{q}_1}{E_1}\frac{d^3\vec{q}_2}{E_2}\delta^4(Q_1 + Q_2 - P)\,L_{\mu\nu} = \frac{2\pi}{3}\left(1 + \frac{2m_l^2}{P^2}\right)\sqrt{1 - \frac{4m_l^2}{P^2}}\left(P_\mu P_\nu - P^2 g_{\mu\nu}\right) = \frac{2\pi}{3}F_1(m_l, P^2)\left(P_\mu P_\nu - P^2 g_{\mu\nu}\right), \quad (8.8)$$

the dilepton production rate in (8.7) comes out to be

$$\frac{dR}{d^4x\,d^4P} = \frac{\alpha}{12\pi^4}\frac{n_B(p_0)}{P^2}F_1(m_l, P^2)\,\text{Im}\left[\Pi^\mu_\mu(p_0, \vec{p})\right] = \frac{\alpha}{12\pi^4}\frac{n_B(p_0)}{P^2}F_1(m_l, P^2)\frac{1}{2i}\text{Disc}\left[\Pi^\mu_\mu(p_0, \vec{p})\right], \quad (8.9)$$

where $n_B(p_0) = (e^{p_0/T} - 1)^{-1}$ and $e^2 = 4\pi\alpha$, α is the electromagnetic coupling constant. We have also used the transversality condition $P_\mu\Pi^{\mu\nu} = 0$. The invariant mass of the lepton pair is defined as $M^2 \equiv P^2(= p_0^2 - |\vec{p}|^2 = \omega^2 - |\vec{p}|^2)$. We also note that for massless lepton $(m_l = 0)$ $F_1(m_l, P^2) = 1$. The quantity $\text{Im}\left[\Pi^\mu_\mu(p_0, \vec{p})\right]$ contains important information about the constituents of the thermal bath and is highly relevant. Equation (8.9) provides the widely used result for the dilepton emission rate from a thermal medium. It is crucial to note that this relationship is only valid up to $\mathcal{O}(e^2)$, as it does not account for possible reinteractions of the virtual photon on its way out of the thermal bath. Additionally, the expression neglects the possibility of emitting more than one photon. However, this result remains accurate to all orders in strong interaction.

The electromagnetic spectral function and the dilepton production rate are connected through Equations (8.2) and (8.9). The dilepton production rate can be expressed as

$$\frac{dN}{d^4x\,d^4p} = \frac{\alpha e_e^2}{12\pi^3}\frac{n_B(p_0)}{p^2}F_1(m_l, p^2)\rho. \quad (8.10)$$

Now assuming two-flavor case, $N_f = 2$,

$$e_e^2 = q_f^2 = \frac{5}{9}e^2 = \frac{5 \times 4\pi\alpha}{9}, \quad (8.11)$$

and the dilepton production rate, considering a two-flavor case, can be expressed as

$$\frac{dN}{d^4x\,d^4p} = \frac{5\alpha^2}{27\pi^2}\frac{n_B(p_0)}{p^2}F_1(m_l, p^2)\rho. \quad (8.12)$$

8.1. Electromagnetic Spectral Function in Strong Magnetic Field

In strong field approximation the photon self-energy can be obtained from gluon self-energy in Eq. (8.13) by replacing the strong coupling g by charge q_f and colour N_c of the quark as

$$\Pi_{\mu\nu}(p)\Big|_{sfa} = -iN_c\sum_f e^{-p_\perp^2/2q_f B}\frac{q_f^3 B}{\pi}\int\frac{d^2k_\parallel}{(2\pi)^2}\frac{S_{\mu\nu}}{(k_\parallel^2 - m_f^2)(q_\parallel^2 - m_f^2)}, \quad (8.13)$$

124

with the tensor structure $S_{\mu\nu}$ originating from the Dirac trace, can be expressed as:

$$S_{\mu\nu} = k_\mu^{\shortparallel} q_\nu^{\shortparallel} + q_\mu^{\shortparallel} k_\nu^{\shortparallel} - g_{\mu\nu}^{\shortparallel} \left((k \cdot q)_{\shortparallel} - m_f^2 \right). \tag{8.14}$$

In the context, the Lorentz indices μ and ν are restricted to longitudinal values only, meaning they are confined to the components parallel to the four-momentum vector. This restriction forbids taking any transverse values, which are perpendicular to the direction of momentum transfer.

8.1.1. Vacuum Spectral Function in strong magnetic field

In vacuum, the photon polarization tensor in Eq. (8.13) can be simplified using the Feynman parametrization technique [261]. This technique allows the tensor to be expressed in a more compact form by integrating over Feynman parameters. The structure of the photon polarization tensor then takes the form as

$$\Pi_{\mu\nu}(p) = \left(\frac{p_\mu^{\shortparallel} p_\nu^{\shortparallel}}{p_{\shortparallel}^2} - g_{\mu\nu}^{\shortparallel} \right) \Pi(p^2).$$

The expression for the photon polarization tensor, due to current conservation, directly implies that the two-point function is transverse. This is because the Feynman parametrization technique isolates only the components of the photon's momentum that are perpendicular to its direction of propagation. This ensures that the polarization tensor only captures the transverse components, excluding any longitudinal components. Therefore, the tensor structure remains purely transverse, reflecting the conservation of current in the system. The scalar function $\Pi(p^2)$ is given by,

$$\Pi(P^2) = N_c \sum_f \frac{q_f^3 B}{8\pi^2 m_f^2} e^{-p_\perp^2/2q_f B} \left[4m_f^2 + \frac{8m_f^4}{p_{\shortparallel}^2} \left(1 - \frac{4m_f^2}{p_{\shortparallel}^2} \right)^{-1/2} \ln \frac{\left(1 - \frac{4m_f^2}{p_{\shortparallel}^2} \right)^{1/2} + 1}{\left(1 - \frac{4m_f^2}{p_{\shortparallel}^2} \right)^{1/2} - 1} \right]. \tag{8.15}$$

We observe that the lowest threshold (LT) for a photon to decay into fermion and antifermion is determined by the energy conservation condition, where the photon's momentum squared $p_{\shortparallel}^2 (= \omega^2 - p_3^2) = (m_f + m_f)^2 = 4m_f^2$. Interestingly $\Pi(p^2)$ becomes singular at this threshold in the presence of a magnetic field. This occurs due to the appearance of the pre-factor $\sqrt{1 - 4m_f^2/p_{\shortparallel}^2}$ in the denominator of the second term in Eq. (8.15) as a result of dimensional reduction from $(3+1)$ to $(1+1)$ in the presence of a strong magnetic field. Unlike in the absence of a magnetic field, where a similar pre-factor appears in the numerator, in the presence of the field, it appears in the denominator. The magnetic field thus plays a crucial role in amplifying the singular behaviour of the polarization function near the threshold. Now, we investigate $\Pi(p^2)$ in the following two domains around the LT [71], $p_{\shortparallel}^2 = 4m_f^2$:

1. Region-I $p_{\shortparallel}^2 < 4m_f^2$:   Assuming $a = \sqrt{4m_f^2/p_{\shortparallel}^2 - 1}$, the logarithmic in the second term of (8.15) can be written as

$$\ln \left(\frac{ai+1}{ai-1} \right) = \ln \left(\frac{re^{i\theta_1}}{re^{i\theta_2}} \right) = i(\theta_1 - \theta_2), \tag{8.16}$$

where $r = \sqrt{(1+a^2)}$, $\theta_1 = \arctan(a)$ and $\theta_2 = \arctan(-a)$. In Eq.(8.15), the logarithmic term is purely imaginary; however, the overall polarization function $\Pi(p^2)$ remains real. This is due to the prefactor $\left(1 - 4m_f^2/p_{\shortparallel}^2 \right)^{-1/2}$, which becomes imaginary when $p_{\shortparallel}^2 < 4m_f^2$, effectively canceling the imaginary contribution from the logarithmic term. If we consider the limit $p_{\shortparallel}^2 < 0$, the entire expression also remains real. In this case, the denominator of the logarithmic term, $\sqrt{1 - 4m_f^2/p_{\shortparallel}^2}$, ensuring the absence of any imaginary contributions. Therefore, in the region $p_{\shortparallel}^2 < 4m_f^2$, $\Pi(p^2)$ is purely real, as the conditions eliminate any imaginary contributions from both the logarithmic term and the prefactor.

2. Region-II $p_{\shortparallel}^2 > 4m_f^2$:   In this limit, although the prefactor remains real and well-defined, the denominator in the logarithmic term becomes negative. Consequently, a complex number arises from the logarithmic term, which can be expressed as $\ln(-x) = \ln|x| + i\pi$. As a result, the polarization function acquires both real and imaginary
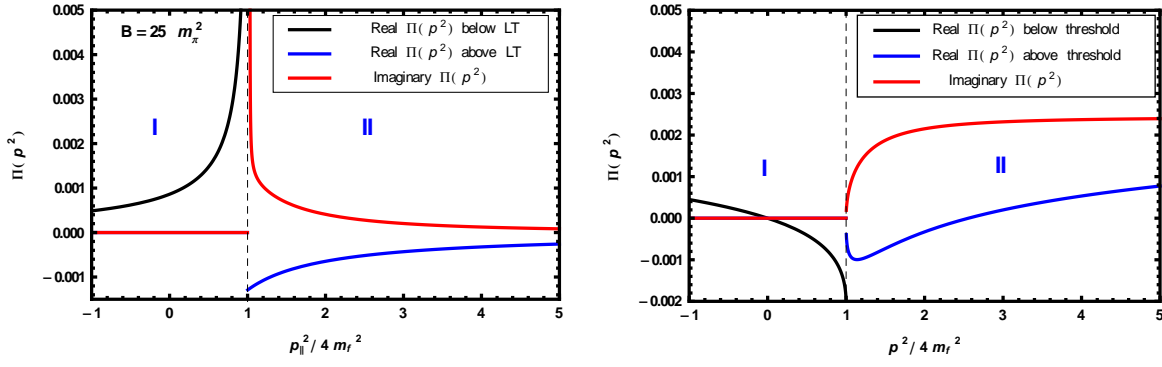
Figure 8.1: The real and imaginary parts of the vacuum polarization function $\Pi(p^2)$ is plotted as a function scaled photon momentum square with respect to LT $4m_f^2$ in various kinematic regions as discussed in the text in presence of a strong magnetic field (left panel) and in absence of a magnetic field (right panel).

components, specifically $\mathcal{R}e\,\Pi(p^2)$ and $\mathcal{I}m\,\Pi(p^2)$. The imaginary part is particularly significant as it plays a crucial role in the analysis of the spectral function and its properties. This contribution provides essential insights into the dynamics of particle interactions and decay processes within the given regime.

Using Eq.(8.2), we extract the vacuum spectral function in the presence of a strong magnetic field as

$$
\rho\Big|_{sfa}^{\text{vacuum}} \;=\; \frac{1}{\pi}\mathcal{I}m\,C_\mu^\mu(p)\Big|_{sfa}^{\text{vacuum}} = N_c \sum_f \frac{q_f B m_f^2}{\pi^2 p_\parallel^2}\, e^{-p_\perp^2/2q_f B}\;\Theta\left(p_\parallel^2 - 4m_f^2\right)\left(1 - \frac{4m_f^2}{p_\parallel^2}\right)^{-1/2}. \tag{8.17}
$$

The imaginary part of $\Pi(p^2)$ is constrained by the LT, $p_\parallel^2 = 4m_f^2$. Below this threshold ($p_\parallel^2 < 4m_f^2$), $\Pi(p^2)$ remains purely real, and there is no electromagnetic spectral contribution in the vacuum under a strong magnetic field, as illustrated in Region I of the left panel of Fig. 8.1. This implies that particle-antiparticle creation does not occur below the LT, as the width of the electromagnetic spectral function vanishes in this regime.

For $p_\parallel^2 > 4m_f^2$, a continuous contribution arises in the real part of $\Pi(p^2)$, depicted by the blue solid line in Region II. While the real part of $\Pi(p^2)$ is continuous both below and above the LT, it exhibits a discontinuity precisely at $p_\parallel^2 = 4m_f^2$. This behaviour highlights the transition in spectral dynamics at the LT, where the interplay of real and imaginary components governs the spectral properties. Though our primary interest lies in the imaginary part, it is worth noting that the real part of is associated with the dispersion properties of the vector boson. This connection has been extensively studied in the absence of a magnetic field in Refs. [156, 262] and in the presence of a magnetic field in Ref.[1]. The imaginary part of the electromagnetic polarization tensor plays a crucial role in determining the system's spectral properties. Beyond the LT ($p_\parallel^2 > 4m_f^2$), there is a continuous nonzero contribution to the electromagnetic spectral function, as given by (8.17), which is represented by a red solid line in Region II of the left panel in Fig. 8.1.

The right panel of Fig. 8.1 illustrates the analytic structure of the vacuum polarization function $\Pi(p^2)$ in absence of a magnetic field. A comparison of the imaginary part of $\Pi(p^2)$ in the absence of a magnetic field with its behaviour in the presence of a strong magnetic field reveals an opposite trend around the lowest threshold. This difference arises due to the effect of dimensional reduction in a strong magnetic field. Consequently, the imaginary part of $\Pi(p^2)$ in the presence of a strong magnetic field leads to a significantly broader photon width, resulting in an enhanced decay into particle-antiparticle pairs. This enhancement is crucial for understanding dilepton production in hot and dense mediums created in heavy-ion collisions.

8.1.2. Thermal spectral function in strong magnetic field

In the previous subsection, we examined aspects of the electromagnetic polarization tensor and its connection to the spectral function in the presence of a strong background magnetic field in vacuum. Now, we extend this analysis to explore the spectral properties of a thermal medium created in heavy-ion collisions under the influence of a strong background magnetic field.

We can simplify by contracting the indices μ and ν in Eq.(8.13), as detailed in [71]

$$\Pi^{\mu}_{\mu}(p)\Big|_{sfa} = -iN_c \sum_f e^{-p_{\perp}^2/2q_f B} \frac{q_f^3 B}{\pi} \int \frac{d^2 k_{\shortparallel}}{(2\pi)^2} \frac{2m_f^2}{(k_{\shortparallel}^2 - m_f^2)(q_{\shortparallel}^2 - m_f^2)}. \tag{8.18}$$

At finite temperature, this can be formulated by replacing the p_0 integral by Matsubara sum as

$$\Pi^{\mu}_{\mu}(\omega, \mathbf{p})\Big|_{sfa} = -iN_c \sum_f e^{-p_{\perp}^2/2q_f B} \frac{2q_f^3 B m_f^2}{\pi} \left(iT \sum_{k_0}\right) \int \frac{dk_3}{2\pi} \frac{1}{(k_{\shortparallel}^2 - m_f^2)(q_{\shortparallel}^2 - m_f^2)}. \tag{8.19}$$

After performing the frequency sum using Saclay method [113, 114] one can write [71]

$$\Pi^{\mu}_{\mu}(\omega, \mathbf{p})\Big|_{sfa} = N_c \sum_f e^{\frac{-p_{\perp}^2}{2q_f B}} \frac{2q_f^3 B m_f^2}{\pi} \int \frac{dk_3}{2\pi} \sum_{l,r=\pm 1} \frac{(1 - n_F(rE_k))(1 - n_F(lE_q))}{4(rl)E_k E_q(p_0 - rE_k - lE_q)} \left[e^{-\beta(rE_k + lE_q)} - 1\right]. \tag{8.20}$$

One can now directly obtain the discontinuity using

$$\text{Disc} \left[\frac{1}{\omega + \sum_i E_i}\right]_{\omega} = -\pi\delta\left(\omega + \sum_i E_i\right), \tag{8.21}$$

which leads to

$$\mathcal{I}m\,\Pi^{\mu}_{\mu}(\omega, \mathbf{p})\Big|_{sfa} = -N_c\pi \sum_f e^{\frac{-p_{\perp}^2}{2q_f B}} \frac{2q_f^3 B m_f^2}{\pi} \int \frac{dk_3}{2\pi} \sum_{l,r=\pm 1} \frac{(1 - n_F(rE_k))(1 - n_F(lE_q))}{4(rl)E_k E_q}$$
$$\times \left[e^{-\beta(rE_k + lE_q)} - 1\right]\delta(\omega - rE_k - lE_q). \tag{8.22}$$

The general form of the delta function in (8.22) corresponds to four processes[21] for $r = \pm 1$ and $l = \pm 1$ as discussed below:

1. For $r = -1$ and $l = -1$, the process corresponds to $\omega < 0$, which violates energy conservation. In this scenario, all quasiparticles possess positive energies.

2. (a) For $r = +1$ and $l = -1$, the process corresponds to, $q \to q\gamma$, where a quark with energy E_k transitions to an energy E_q after emitting a timelike photon of energy ω. (b) For $r = -1$ and $l = 1$ corresponds to a similar situation as (a).Ref. [71] explicitly demonstrates that these processes are prohibited by both phase space and energy conservation. In other words, the production of a timelike photon from the one-loop photon polarization tensor is forbidden due to restrictions imposed by phase space and energy conservation.

3. For $r = 1$ and $s = 1$, the process corresponds to, $q\bar{q} \to \gamma^*$, the annihilation of a quark and a antiquark into a virtual photon, representing the only permitted interactions.

For the last case, the process can be expressed using Eq.(8.22) as

$$\mathcal{I}m\,\Pi^{\mu}_{\mu}(\omega, \mathbf{p})\Big|_{sfa} = N_c\pi \sum_f e^{\frac{-p_{\perp}^2}{2q_f B}} \frac{2q_f^3 B m_f^2}{\pi} \int \frac{dk_3}{2\pi} \delta(\omega - E_k - E_q) \frac{[1 - n_F(E_k) - n_F(E_q)]}{4E_k E_q}. \tag{8.23}$$

Following the k_3 integral outlined in [71], the spectral function in the strong field approximation is ultimately derived according to Eq.(8.2) as

$$\rho\Big|_{sfa} = \frac{1}{\pi}\mathcal{I}m\,C^{\mu}_{\mu}(p)\Big|_{sfa}$$

---

[21] For LLL, these four processes can also be identified from equation (4.19) in Ref. [70] using the Ritus method.

$$= N_c \sum_f \frac{q_f B m_f^2}{\pi^2 p_\parallel^2} \, e^{-p_\perp^2/2q_f B} \, \Theta\left(p_\parallel^2 - 4m_f^2\right) \left(1 - \frac{4m_f^2}{p_\parallel^2}\right)^{-1/2} \left[1 - n_F(p_+^s) - n_F(p_-^s)\right], \qquad (8.24)$$

where

$$p_\pm^s = \frac{\omega}{2} \pm \frac{p_3}{2} \sqrt{\left(1 - \frac{4m_f^2}{p_\parallel^2}\right)}. \qquad (8.25)$$

We observe that the electromagnetic spectral function in the strong field approximation, derived from Eq.(8.24) using the Schwinger method, includes the thermal factor $[1 - n_F(p_+^s) - n_F(p_-^s)]$. This factor appears when a quark and antiquark annihilate into a virtual photon within a thermal medium, representing the only process permitted by the phase space.

The vacuum contribution in the presence of a strong magnetic field can be conveniently isolated from (8.24) as

$$\rho\Big|_{sfa}^{\text{vacuum}} = N_c \sum_f \frac{q_f B m_f^2}{\pi^2 p_\parallel^2} \, e^{-p_\perp^2/2q_f B} \, \Theta\left(p_\parallel^2 - 4m_f^2\right) \left(1 - \frac{4m_f^2}{p_\parallel^2}\right)^{-1/2}, \qquad (8.26)$$

which agrees with that obtained in (8.17).

We highlight some of the notable features of the spectral functions:

(i) In the massless limit of quarks, the electromagnetic spectral function in Eq.(8.24) vanishes due to the presence of the magnetic field, which effectively reduces the system to $(1 + 1)$ dimensions. This feature arises from the symmetry argument and is linked to the CPT invariance of the theory [263]. Physically, this indicates that in $(1 + 1)$ dimensions, an on-shell massless thermal fermion cannot scatter in forward direction.

(ii) The threshold, $p_\parallel^2 = 4m_f^2$, remains unaffected by the strength of the magnetic field and is also independent of T under the condition $q_f B \gg T^2$ in the strong field approximation. Similar to the vacuum case, the spectral function vanishes below this threshold, indicating no pair creation of particle and antiparticle. This is because the polarization tensor is purely real beneath the threshold. Consequently, the energy supplied by the external photon enables the virtual pair in the LLL to become real via photon decay.

(iii) When the photon's longitudinal momentum squared reaches the threshold, $p_\parallel^2 = 4m_f^2$, it intersects with the LLL, causing the spectral strength to diverge due to the factor $\left(1 - 4m_f^2/p_\parallel^2\right)^{-1/2}$. This arises from the dimensional reduction to $(1+1)$ dimensions in the LLL dynamics. The magnetic field induces a dynamical mass generation for the fermions through the mass operator (e.g., chiral condensate), leading to chiral symmetry breaking in the system [1, 264]. Even with the weakest attractive interaction among fermions in $(3+1)$ dimensions, strong fermion pairing occurs in the LLL [1]. A weakly interacting system in the presence of a strong magnetic field can thus be viewed as a strongly correlated system with LLL dynamics that is effectively $(1+1)$ dimensional. Here, m_f is associated with the dynamical mass generated by the condensates [1, 264]. Incorporating this effect through nonperturbative model calculations modifies the longitudinal momentum scale accordingly.

(iv) The spectral strength initially peaks for photon longitudinal momentum $p_\parallel > 2m_f$ due to the effects of dimensional reduction or LLL dynamics. However, as ω increases, it decreases because there are no contributions beyond the LLL in the strong field approximation. To enhance the high-energy behavior of the spectral function, a weak field approximation ($T^2 \gg q_f B$) is necessary.

In Fig. 8.2, the left panel shows the variation of the spectral function with photon energy ω for different values of T, while the right panel displays the variation for different values of the magnetic field. As T increases, the spectral strength in the left panel decreases due to the presence of the thermal weight factor $[1 - n_F(p_+^s) - n_F(p_-^s)]$. The distribution functions $n_F(p_\pm^s)$ increase with T, thereby limiting the available phase space. However, the effect of temperature remains

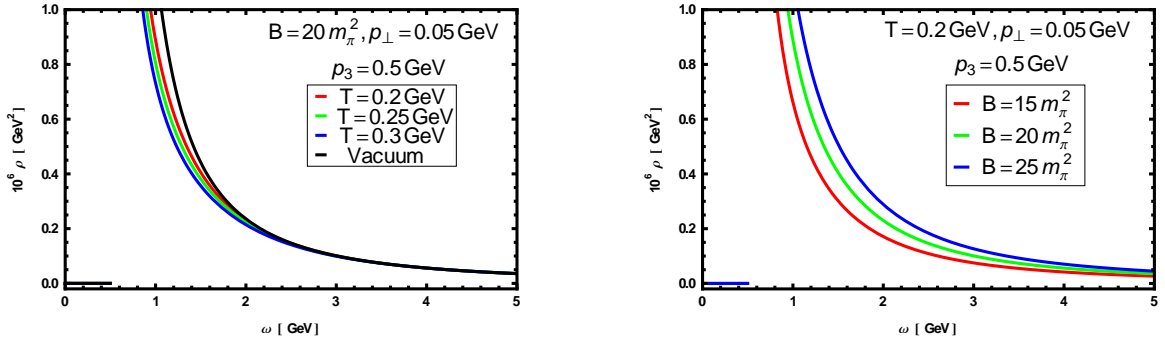Figure 8.2: *Left panel:* The variation of the spectral function with photon energy for varying T, while keeping B, $p_\perp$ and p_3 fixed. *Right panel:* The panel displays the variation of the spectral function for different values of the magnetic field, keeping T, $p_\perp$ and p_3 fixed. The magnetic field values are expressed in terms of the pion mass m_π.
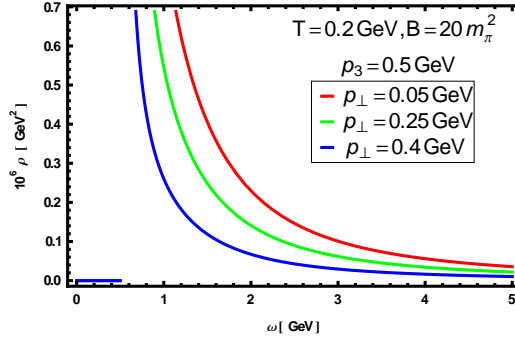

Figure 8.3: The variation of the spectral function with photon energy ω for different transverse momentum values, while keeping B, T and p_3 fixed.

small in the strong field approximation where $q_f B \gg T^2$. In contrast, the spectral strength in the right panel increases with an increase in the magnetic field B, as the spectral function is directly proportional to B.

In Fig. 8.3, the spectral function's variation with photon energy ω is shown for three different values of the transverse momentum $p_\perp$. As the transverse momentum $p_\perp$ increases, the spectral function is found to be exponentially suppressed.

We also consider a special case where the external three-momentum (p) of the photon is zero. In this simplified scenario, the expression for the spectral function can be derived accordingly

$$\rho(\omega)\Big|_{sfa} = \frac{1}{\pi}\mathcal{I}m\ C_\mu^\mu(\omega, \mathbf{p}=0)\Big|_{sfa} = N_c \sum_f \frac{q_f B m_f^2}{\pi^2 \omega^2}\Theta\left(\omega^2 - 4m_f^2\right)\left(1 - \frac{4m_f^2}{\omega^2}\right)^{-1/2}\left[1 - 2n_F\left(\frac{\omega}{2}\right)\right]. \quad (8.27)$$

In Fig.8.4, the same plots are presented as in Fig.8.2, but for the simplified case of zero external three-momentum of the photon. As shown in (8.27), the threshold shifts to the photon energy with $\omega = 2m_f$, resulting in slight changes to the plot shapes. In the following subsec. 8.2, we explore the leading order thermal dilepton rate for a strongly magnetized medium as a spectral property.

8.2. Dilepton rate from QGP in Strong Magnetic Approximation

We first note that dileptons are produced throughout all stages of the hot and dense fireball created in heavy-ion collisions. They originate from the decay of a virtual photon through the annihilation of quark-antiquark pairs in leading order. In non-central heavy-ion collisions, an anisotropic magnetic field is generated in the direction perpendicular to the reaction
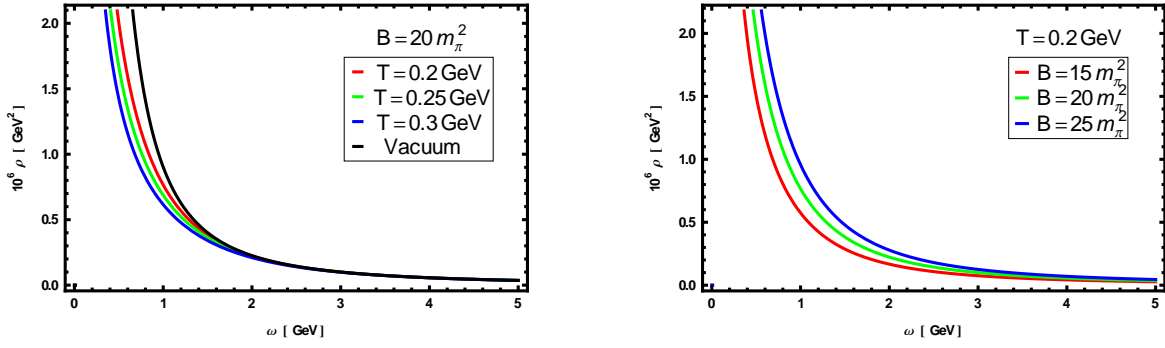
Figure 8.4: Same as Fig. 8.2, but for the special case of zero external three-momentum (p) of the photon.

plane due to the relative motion of the heavy-ions (spectators). This magnetic field can initially be very strong at the time of the collision but then rapidly decreases [227, 228]. Dilepton production in a magnetized hot and dense medium can be analyzed under three different scenarios [17, 70]: (1) only the quarks move within the magnetized medium while the final lepton pairs do not, (2) both quarks and leptons move within the magnetized medium, and (3) only the final lepton pairs move in the magnetic field.

8.2.1. Quarks move in a strong magnetized medium but not the final lepton pairs

We emphasize that the case considered here is both interesting and highly relevant to non-central heavy-ion collisions, particularly for the scenario involving a rapidly decaying magnetic field [227, 228]. This is also applicable to lepton pairs produced late or at the edges of the hot and dense magnetized medium, where they are unaffected by the magnetic field. In this case, only the electromagnetic spectral function $\rho^{\mu\nu}$ in (8.3) will be influenced by the background constant magnetic field, while the leptonic tensor $L_{\mu\nu}$ and the phase space factors remain unchanged. The dilepton rate for massless ($m_l = 0$) leptons can then be expressed from (8.12) as [71]

$$
\begin{aligned}
\frac{dN}{d^4x d^4p} &= = \frac{5\alpha_{\text{em}}^2}{27\pi^2} \frac{n_B(p_0)}{p^2} [\rho(p_{\shortparallel}, p_\perp)]_m \\
&= \frac{5N_c\alpha_{\text{em}}^2}{27\pi^4} n_B(\omega) \sum_f \frac{|q_f B| m_f^2}{p^2 p_{\shortparallel}^2} e^{-p_\perp^2/2|q_f B|} \Theta\left(p_{\shortparallel}^2 - 4m_f^2\right) \left(1 - \frac{4m_f^2}{p_{\shortparallel}^2}\right)^{-1/2} \\
&\quad \times \left[1 - n_F(p_+^s) - n_F(p_-^s)\right],
\end{aligned}
\tag{8.28}
$$

where the electromagnetic spectral function from (8.24) is utilized. The invariant mass of the lepton pair is $M^2 \equiv p^2(\omega^2 - |\mathbf{p}|^2) = \omega^2 - p_3^2 - p_\perp^2 = p_{\shortparallel}^2 - p_\perp^2$.

In Fig. 8.5, the ratio of the dilepton rate in the current scenario under the strong field approximation to that of the perturbative leading order (Born) dilepton rate is shown as a function of the invariant mass. The left panel displays this ratio for finite external photon momentum, while the right panel is for zero external photon momenta. The features of the spectral function discussed earlier are evident in these dilepton rates. The strong field approximation enhances the dilepton rate at very low invariant masses (≤ 100 MeV), but it rapidly decreases at higher invariant masses, similar to the behavior of the spectral function due to the absence of higher Landau levels. To improve the high-mass behaviour of the dilepton rate, a weak field approximation ($q_f B \ll T^2$) is needed. The enhancement seen in the strong field approximation contributes significantly to the dilepton spectra at low invariant masses, although this is beyond the detection capabilities of current heavy-ion collision experiments.
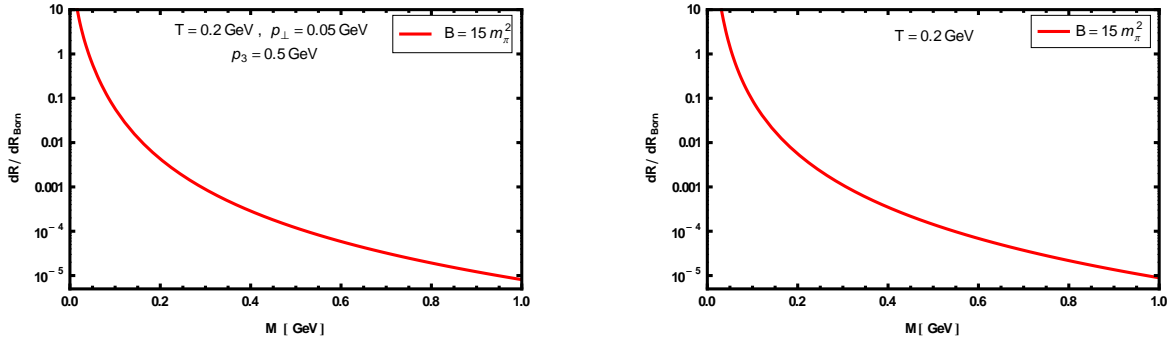
Figure 8.5: The figure displays the ratio of the dilepton rate in the strong magnetic field approximation to the Born rate (perturbative leading order) for both finite (left panel) and zero (right panel) external three-momentum of the photon.

8.2.2. Both quark and lepton move in magnetized medium in strong field approximation

This scenario represents the most general case. To address it, the standard dilepton production rate from (8.12) must be extended to include modifications of the electromagnetic tensor, leptonic tensor, and phase space factors in the presence of a magnetic field. Since our focus is restricted to the Lowest Landau Level (LLL), we summarize below the necessary adjustments to the dilepton production rate [71] specifically for the LLL:

- The phase space factor is altered in the presence of a magnetized medium [265], reflecting the influence of the magnetic field on the dynamics of charged particles, as

$$\frac{d^3\mathbf{q}}{(2\pi)^3 E} \quad \rightarrow \quad \frac{|eB|}{(2\pi)^2} \sum_{n=0}^{\infty} \frac{dq_z}{E}. \tag{8.29}$$

  In this context, the phase space factor undergoes a significant modification due to the presence of a magnetic field. Specifically, $d^2 q_\perp = 2\pi |eB|$, e is the electric charge of the lepton and $\sum_{n=0}^{\infty}$ extends over all LL. However, in the strong magnetic field limit, only the LLL, corresponding to and $n = 0$, contributes. The term $|eB|/(2\pi)^2$ represents the density of states in the transverse direction, which is characteristic of the LLL [1]. This factor encapsulates the effects of dimensional reduction in the magnetized medium, playing a crucial role in determining the modified phase space.

- The electromagnetic spectral function undergoes significant modification in the LLL, as previously discussed.

- In the presence of a constant magnetic field, the fermion spin aligns with the field direction, modifying the standard Dirac spinors $u(q)$ and $v(q)$ in (8.6). These are replaced by $P_n u(\tilde{q})$ and $P_n v(\tilde{q})$, respectively [1, 97], where the modified momentum is $\tilde{q}^\mu = (q^0, 0, 0, q^3)$ and P_n represents the projection operator associated with the nth LL. For LLL, the projection operator simplifies to

$$P_0 = \frac{1 - i\gamma_1\gamma_2}{2}. \tag{8.30}$$

  In the presence of a strong magnetic field, the modification to the leptonic part can be implemented as follows

$$
\begin{aligned}
L^m_{\mu\nu} &= \frac{1}{4} \sum_{\text{spins}} \text{tr}\left[\bar{u}(\tilde{q}_2) P_0 \gamma_\mu P_0 v(\tilde{q}_1) \bar{v}(\tilde{q}_1) P_0 \gamma_\nu P_0 u(\tilde{q}_2)\right] \\
&= \frac{1}{4}\text{tr}\left[(\tilde{\slashed{q}}_1 + m_l)\left(\frac{1 - i\gamma_1\gamma_2}{2}\right)\gamma_\mu\left(\frac{1 - i\gamma_1\gamma_2}{2}\right)(\tilde{\slashed{q}}_2 - m_l)\left(\frac{1 - i\gamma_1\gamma_2}{2}\right)\gamma_\nu\left(\frac{1 - i\gamma_1\gamma_2}{2}\right)\right] \\
&= \frac{1}{2}\left[q^{\shortparallel}_{1\mu}q^{\shortparallel}_{2\nu} + q^{\shortparallel}_{1\nu}q^{\shortparallel}_{2\mu} - ((q_1 \cdot q_2)_{\shortparallel} + m_l^2)(g^{\shortparallel}_{\mu\nu} - g^{\perp}_{\mu\nu} - g_{1\mu}g_{1\nu} - g_{2\mu}g_{2\nu})\right].
\end{aligned}
\tag{8.31}
$$

- Requires an insertion $\int d^2 p^{\shortparallel} \delta^2(q_1^{\shortparallel} + q_2^{\shortparallel} - p^{\shortparallel}) = 1$.

- Replacing $d^2 p^\perp = V^{2/3}\left(\frac{eB}{2\pi}\right)^2$, where V is the volume. This modification introduces a different normalization factor

131

in the dilepton production rate, as detailed in Ref. [70]. $d^2p^\perp = 2\pi|eB|$ and $d^4p = d^2p^\perp d^2p^{||}$.

- Making use of an identity:

$$2\pi|eB|\int\frac{dq_1^z}{E1}\int\frac{dq_2^z}{E2}\ \delta^2(q_1^{||}+q_2^{||}-p^{||})\ L_{\mu\nu}^m = 4\pi\frac{|eB|m_l^2}{(p_{||}^2)^2}\left(1-\frac{4m_l^2}{p_{||}^2}\right)^{-1/2}\left(p_\mu^{||}p_\nu^{||}-p_{||}^2g_{\mu\nu}^{||}\right)$$

$$= \frac{4\pi}{(p_{||}^2)^2}F_2(m_l,p_{||}^2)\left(p_\mu^{||}p_\nu^{||}-p_{||}^2g_{\mu\nu}^{||}\right). \tag{8.32}$$

By incorporating all the modifications discussed—namely, the phase space factor, the electromagnetic spectral function for the Lowest Landau Level (LLL), and the adjustment of the leptonic tensor in the presence of a strong magnetic field,we obtain the dilepton production rate from Eq. (8.3) for LLL as

$$\frac{dN^m}{d^4xd^4p} = \frac{\alpha_{em}e_e^2}{2\pi^3}\frac{n_B(p_0)}{p_{||}^2p^4}F_2(m_l,p_{||}^2)\left(\frac{1}{\pi}\mathcal{I}m\left[C_\mu^\mu(p_{||},p_\perp)\right]\right)_m, \tag{8.33}$$

and for two-flavor case ($N_f = 2$) it becomes

$$\frac{dN^m}{d^4xd^4p} = \frac{10\alpha_{em}^2}{9\pi^2}\frac{n_B(p_0)}{p_{||}^2p^4}\ |eB|m_l^2\left(1-\frac{4m_l^2}{p_{||}^2}\right)^{-1/2}[\rho(p_{||},p_\perp)]_m$$

$$= \frac{10N_c\alpha_{em}^2}{9\pi^4}n_B(\omega)\sum_f\frac{|eB|\,|q_fB|m_f^2m_l^2}{p_{||}^4p^4}\Theta\left(p_{||}^2-4m_l^2\right)\left(1-\frac{4m_l^2}{p_{||}^2}\right)^{-1/2}\Theta\left(p_{||}^2-4m_f^2\right)\left(1-\frac{4m_f^2}{p_{||}^2}\right)^{-1/2}$$

$$\times e^{-p_\perp^2/2|q_fB|}\left[1-n_F(p_+^s)-n_F(p_-^s)\right]. \tag{8.34}$$

It is important to note that the dilepton production rate in Eq. (8.34) scales as $\mathcal{O}[|eB|^2]$ in the presence of a magnetic field B. This scaling arises from the effective dimensional reduction caused by the strong magnetic field [22]. The dimensional reduction in a magnetized hot medium introduces a factor $1/\sqrt{1-4m_l^2/p_{||}^2}$ in the leptonic part $L_{\mu\nu}^m$. This factor contributes an additional threshold condition, $p_{||}^2 \geq 4m_l^2$, alongside the threshold from the electromagnetic part, $p_{||}^2 \geq 4m_f^2$. In a magnetized hot medium, the mass of fermions is influenced by both temperature and magnetic field. The thermal effects [107, 108] are accounted for through thermal QCD and QED, respectively, which introduce corrections to the masses of quarks ($\sim g^2T^2$; g is the QCD coupling) and lepton ($\sim e^2T^2$). Additionally, the magnetic effect is quantized through the LL ($2n|q_fB|$). However, in the LLL ($n = 0$), the magnetic contribution to the mass correction vanishes in the strong field approximation. In this scenario, the dominant effect is the dynamical mass generation due to chiral condensates [1], leading to magnetic field-induced chiral symmetry breaking. The threshold for the dilepton rate will be determined by the effective mass, $\tilde{m} = \max(m_l, m_f)$ as $\Theta\left(p_{||}^2-4\tilde{m}^2\right)$ and the dilepton rate in LLL reads as

$$\frac{dN^m}{d^4xd^4p} = \frac{10N_c\alpha_{em}^2}{9\pi^4}\sum_f\frac{|eB|\,|q_fB|m_f^2m_l^2}{p_{||}^4p^4}\Theta\left(p_{||}^2-4\tilde{m}^2\right)\left(1-\frac{4m_l^2}{p_{||}^2}\right)^{-1/2}\left(1-\frac{4m_f^2}{p_{||}^2}\right)^{-1/2}$$

$$\times e^{-p_\perp^2/2|q_fB|}\,n_B(\omega)\left[1-n_F(p_+^s)-n_F(p_-^s)\right], \tag{8.35}$$

where kinematic factors in the dilepton rate are consistent between the present scenario and those found in Ref. [70]. However, the prefactor $(10/\pi^4)$ and the thermal factor $n_B(\omega)[1-n_F(p_+^s)-n_F(p_-^s)]$ differ from those previously discussed. and the reasons for which are discussed in details earlier. These differences have been outlined in detail earlier, impacting the quantitative comparison of the dilepton rate with the results obtained in Ref. [70]. Furthermore, a comparison with experimental results or the dilepton spectra from Tuchin [17] necessitates a space-time evolution of the dilepton rate in the hot, magnetized medium created during heavy-ion collisions. Proper space-time evolution requires a hydrodynamic framework that accounts for the presence of a magnetic field, which is a complex task and goes beyond the scope of this article.

---

[22] The factor $|eB|$ originates each from both the leptonic part and the electromagnetic spectral function involving quarks.

We also note that for case (3), the production rate requires a modification of the leptonic tensor in a magnetized medium, while the electromagnetic tensor remains unaffected by the presence of the magnetic field. This scenario is relatively rare, and for the sake of brevity, we will not discuss it further here. However, the necessary modifications can still be derived and are straightforward.

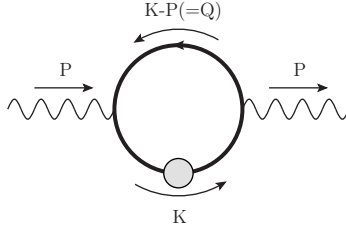## 8.3. Dilepton Rate from QGP in Weak Field Approximation

Figure 8.6: Feynman diagram for the production of the hard dilepton in presence of weak background magnetic field. The internal quarl line with blob corresponds the effective propagator whereas the one without blob is free propagator in presence of magnetic field.

In this subsection we will discuss dilepton production rate in weak field approximation within HTL prescription and the corresponding Feynman diagram is displayed in Fig. 8.6. We know that the dilepton rate in (8.12) is proportional to the spectral representation of photon self-energy. The spectral representation is proportional to imaginary part of the self-energy. From the diagram 8.6 it is clear that the self-energy will contain two quark propagators, one is free given in Eq. (5.56) and the other is the effective one given in Eq. (5.19) and both in presence of weak magnetic field. The spectral representation of free quark propagator has only pole contribution. On the other hand the effective propagator has both pole and discontinuity [65] and thus the spectral representation of effective propagator will have both pole and Landau cut contribution. The dilepton rate will be proportional to the product of two spectral representation of quark propagators, it will then have two different types of contributions. One is pole-pole and the other one is pole-cut contribution. The detailed calculation is available in Ref. [73]. Here will discuss the results only.

The effective quark propagator exhibits four poles, corresponding to different quark modes. These modes, labeled as $q_{L(+)}$, $q_{L(-)}$, $q_{R(+)}$, and $q_{R(-)}$, are associated with frequencies $\omega_{L(+)}$, $\omega_{L(-)}$, $\omega_{R(+)}$, and $\omega_{R(-)}$, respectively. The dispersion relations for these modes are illustrated in Fig. 5.4. The free dispersion $\omega = \sqrt{p_z^2 + p_\perp^2}$ originates from its free propagator. From Fig.5.4, it is evident that the processes of interest involve one hard and one soft quark. This setup utilizes one free (hard) quark propagator in the presence of a magnetic field alongside one resummed thermomagnetic quark propagator (soft) depicted in Fig.8.6. Based on the dispersion plot, the various dilepton production processes can be described as follows: hard quark processes: $qq_{L(+)} \longrightarrow \gamma^* \longrightarrow l^+l^-$, $qq_{L(-)} \longrightarrow \gamma^* \longrightarrow l^+l^-$, $qq_{R(+)} \longrightarrow \gamma^* \longrightarrow l^+l^-$, and $qq_{R(-)} \longrightarrow \gamma^* \longrightarrow l^+l^-$; Soft decay processes: $q_{L(+)} \longrightarrow q\gamma^* \longrightarrow ql^+l^-$, $q_{L(-)} \longrightarrow q\gamma^* \longrightarrow ql^+l^-$, $q_{R(+)} \longrightarrow q\gamma^* \longrightarrow ql^+l^-$, and $q_{R(-)} \longrightarrow q\gamma^* \longrightarrow ql^+l^-$. These processes may not all be allowed due to kinematic restrictions such as energy and momentum conservation. Additionally, soft processes from Landau cut contributions might also play a role in the overall dilepton production.

We note that the soft decay modes primarily contribute to the production of soft dileptons at low energies. These modes are omitted from our considerations as they are not pertinent to the hard dilepton production rate we are interested
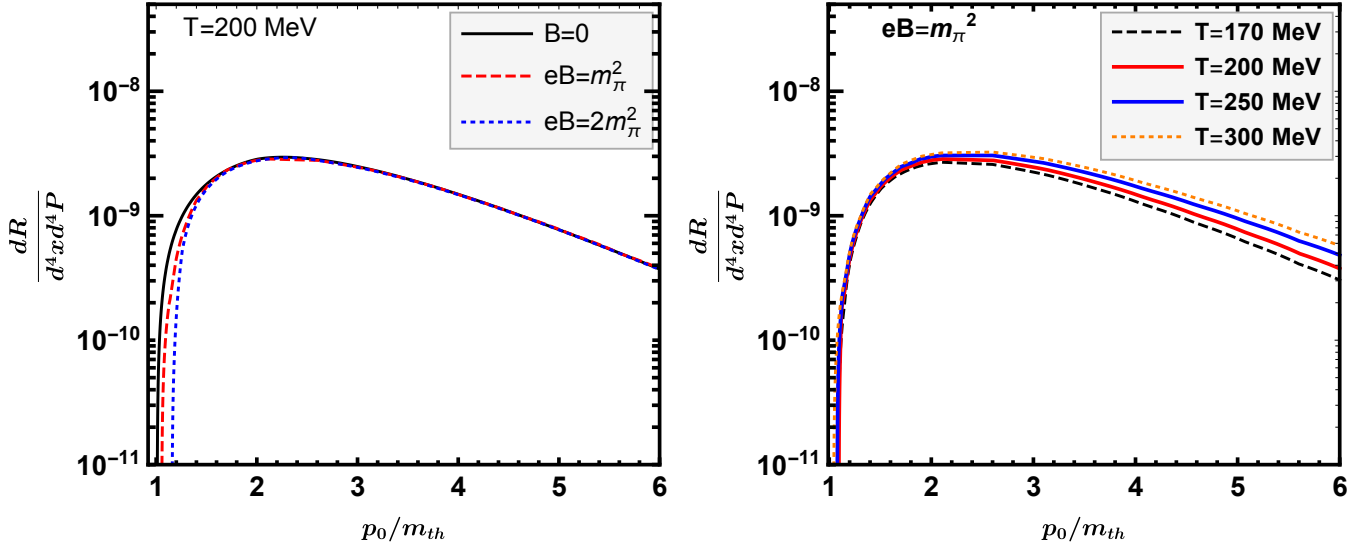
Figure 8.7: The pole-pole contribution of the dilepton production rate as a function of the energy of dilepton in the center-of-mass reference frame at is depicted in the following two scenarios: i) at $T = 200$ MeV with different magnetic field (left panel) and ii) $eB = m_\pi^2$ with different temperature (right panel).

in. Therefore, only the annihilation modes will contribute. In Fig. 8.7, we focus solely on the pole-pole contribution to the dilepton production rate, which is relevant to hard dilepton production. In the left panel, the rate is shown as a function of dilepton energy for $T = 200$ MeVacross different magnetic fields. Without a magnetic field ($eB = 0$), the annihilation process between a hard quark and a soft quark initiates at a dilepton energy $E = m_{th}$, resembling the process $qq_+ \longrightarrow \gamma^* \longrightarrow l^+ l^-$ [73, 113]. When a magnetic field is applied, all four quasiparticle modes,.$\omega_{L(+)}$, $\omega_{L(-)}$, $\omega_{R(+)}$, and $\omega_{R(-)}$, from Fig.5.4 begin to contribute separately to the annihilation process with the hard quark. This results in a slight shift in the energy threshold for dilepton production compared to when there is no magnetic field. The presence of a magnetic field lowers the thermo-magnetic mass, pushing the onset of the dilepton rate to slightly higher energies. As the dilepton energy increases, the rate approaches the behaviour observed in the absence of a magnetic field. In the right panel of Fig.8.7, the dilepton production rate remains relatively independent of temperature, T, because the magnetic field dominates. Beyond this energy threshold ($E = p_0 > 2m_{th}$), the rate increases with the increase in T, as Tbecomes the dominant scale in the weak field approximation.

In the left panel of Fig. 8.8, the pole-cut contribution is displayed for various magnetic fields with $T = 200$ MeV. The rate remains independent of the magnetic field because the magnetic field acts as a correction within the weak field approximation, where we have considered the rate up to $\mathcal{O}[(eB)]$.Conversely, in the left panel of Fig.8.8, it is plotted for various temperatures for a given magnetic field. Here, the rate is enhanced with an increase in temperature since the temperature dominates in the weak field approximation. The total dilepton rate is obtained by combining both the pole-pole and pole-cut contributions, as shown in Fig. 8.9.

8.4. Dilepton Rate from QGP in An Arbitrary Magnetic Field

In a recent study [74], the production of dileptons from a hot and dense QCD medium under the influence of an arbitrary external magnetic field was investigated. This analysis considered simultaneous nonzero values for both the parallel (aligned with the magnetic field) and perpendicular (in the transverse plane relative to the magnetic field) components
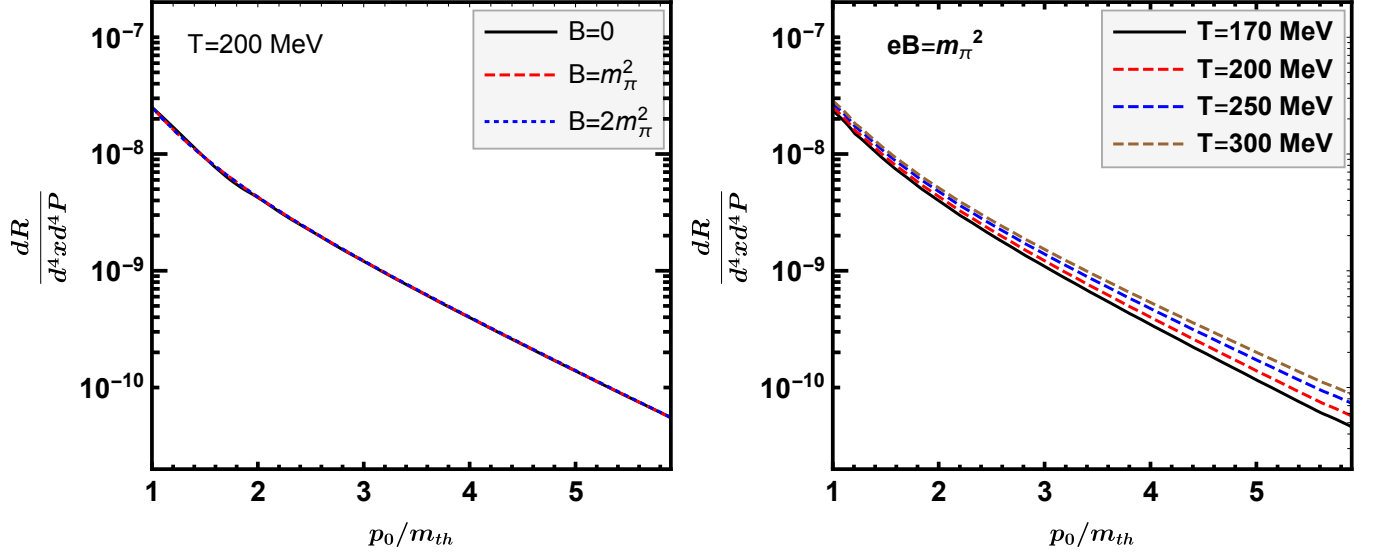
Figure 8.8: Same as Fig. 8.7 but for the pole-cut contribution.

of the dilepton momentum. This general treatment captures the full kinematics of dilepton production in a magnetized medium, accounting for the complex interplay between the external field and the thermal medium properties.

Due to kinematical reason there will be four delta functions in the expression of the dilepton production rate (DR), $\delta\left(p_0 - s_1 E_{f,\ell,k} - s_2 E_{f,n,q}\right)$, where p_0 is the energy of the virtual photon, $E_{f,\ell,k}$ and $E_{f,n,q}$ are, respectively, the energy of quark and and antiquark, and $s_1 = \pm 1$ and $s_2 = \pm 1$. These delta functions arise from energy and momentum conservation at each interaction vertex, ensuring that the production process satisfies the necessary physical laws. Specifically, they enforce the matching conditions between the energy and momentum of the virtual photon and the participating quarks or antiquarks in the hot and dense QCD medium. In this framework, the different combinations of s_1 and s_2 represent distinct processes:

1. $s_1 = s_2 = 1$ corresponds to the annihilation process $(q + \bar{q} \to \gamma^*)$.
2. $s_1 = -s_2 = 1$ describes the particle decay process $(q \to q + \gamma^*)$.
3. $s_1 = -s_2 = -1$ relates to the antiparticle decay process $(\bar{q} \to \bar{q} + \gamma^*)$.

The case $s_1 = s_2 = -1$ yields no contribution since its argument is always greater than zero, given that p_0, $E_{f,\ell,k}$ and $E_{f,n,q}$ are all strictly positive. Thus, this scenario is excluded from further consideration in the remainder of this analysis. Therefore, the total DR becomes

$$\left.\frac{dN}{d^4x d^4 P}\right|_{\text{Total}} = \left.\frac{dN}{d^4x d^4 P}\right|_{q+\bar{q}\to\gamma^*} + \left.\frac{dN}{d^4x d^4 P}\right|_{q\to q+\gamma^*} + \left.\frac{dN}{d^4x d^4 P}\right|_{\bar{q}\to\bar{q}+\gamma^*}. \tag{8.36}$$

We begin by presenting a key plot of the dilepton production rate (DR) in Fig.8.10 as a function of the invariant mass, M, for a fixed nonzero magnetic field, $eB = 5m_\pi^2$. The result is compared to the Born rate $(eB = 0)$ while keeping all other parameters identical for both cases. In this plot, the transverse momentum, $p_\perp$, is set to zero. Generalizations to nonzero values of $p_\perp$, which extend the analysis, will be addressed in detail later in this section. The specific parameter values used are as follows: longitudinal momentum along the magnetic field, $eB\,(p_z) = 0.2$ GeV, temperature $(T) = 0.15$ GeV and chemical potential $(\mu) = 0$.

From the left panel of Fig. 8.10, it is evident that the DR is enhanced in the presence of a magnetic field (eB) compared to the Born rate. This enhancement is most noticeable at lower invariant masses, M. At higher invariant masses, the

135
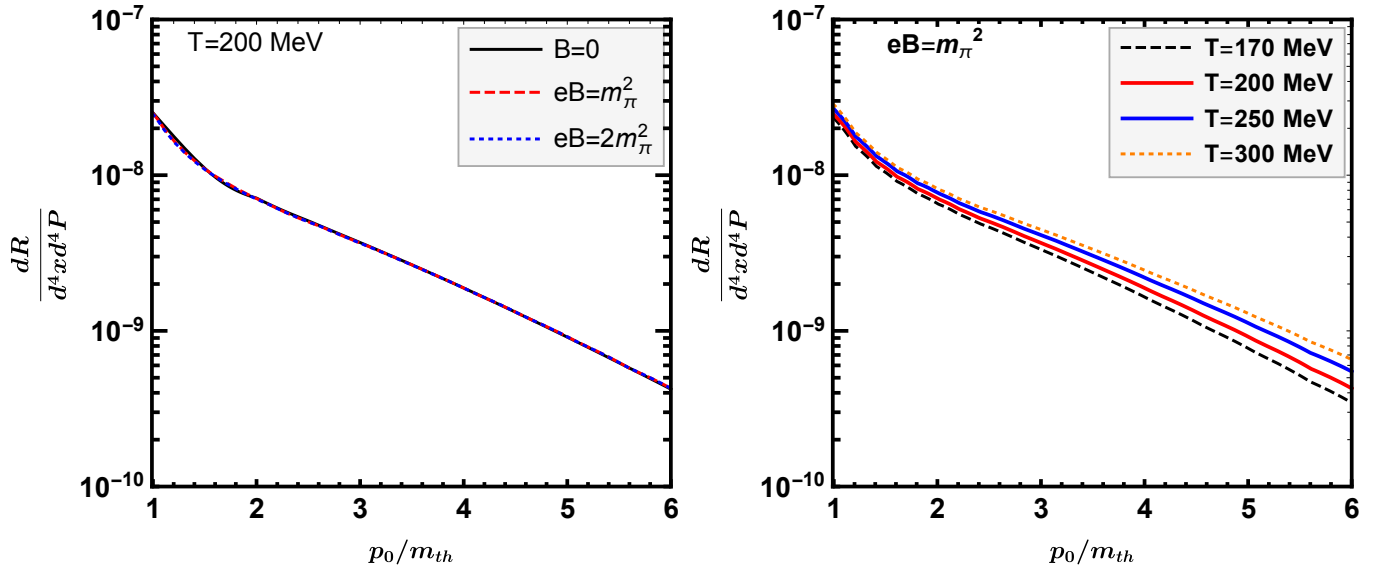
Figure 8.9: The total dilepton production rate, which combines the pole-pole and pole-cut contributions as a function of the dilepton energy for various magnetic fields left panel) and for various temperatures (right panel).
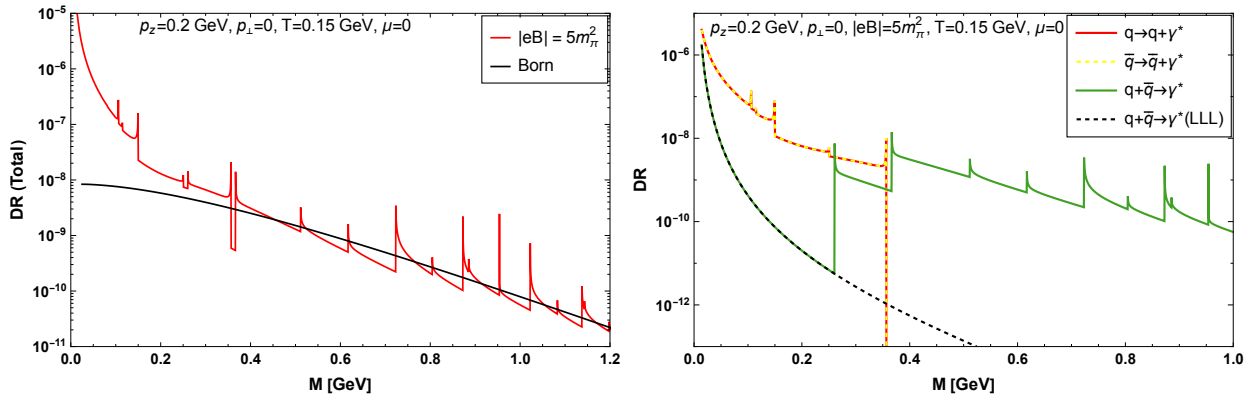
Figure 8.10: The left panel presents the DR as a function of the invariant mass for $eB = 5\,m_\pi^2$ with $p_\perp = 0$. In the right panel, the contributions from different processes are depicted individually, alongside the rate obtained under the LLL approximation, shown as a black dashed line.

influence of the external magnetic field diminishes, with the dilepton production rate for $eB \neq 0$ eventually matching the Born rate, except for the spikes associated with the crossing of LL thresholds. Crucially, this enhancement occurs within the range of invariant masses that are detectable by experimental setups in HIC.

In the right panel of Fig.8.10, the DR is separated into individual contributions from different processes, illustrating their respective roles in the total rate as expressed in Eq.(8.36). The contributions from quark and antiquark decay processes are symmetric due to the absence of chemical imbalance ($\mu = 0$)), which is consistent with expectations. These decay processes dominate at low M. As M increases, the decay contributions diminish rapidly, giving way to the quark-antiquark annihilation process, which becomes the primary contributor at higher invariant mass values. This shift reflects the kinematic and dynamic preferences of the underlying processes, with annihilation dominating in regions where decay processes are suppressed. It is important to clarify the interplay between the decay and annihilation processes contributing to the DR. For fixed values of the parameters' ($p_\parallel^2$, eB and m_f), only one of the three processes depicted in Fig. 8.10 is kinematically allowed for a specific combination of Landau levels $\{\ell, n\}$. However, when evaluating the DR at a particular invariant mass, overlapping contributions from decay and annihilation processes may arise. This overlap
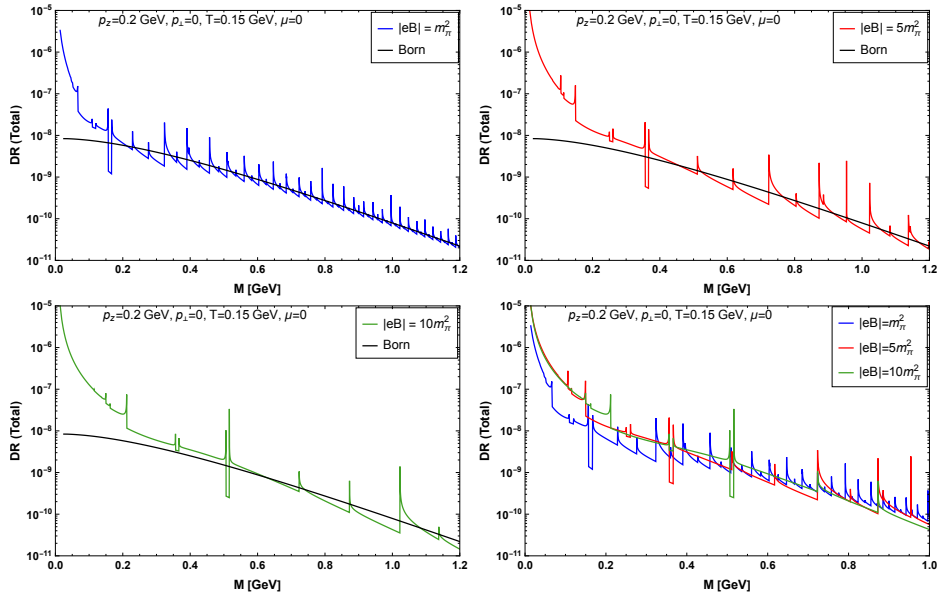
Figure 8.11: The plots display the dilepton production rate as a function of the invariant mass M for varying magnetic field strengths. The Born rate, representing the case of $eB = 0$, is included for comparison. All plots are generated for $p_\perp = 0$, with other relevant parameters provided in the legend and detailed discussion. In the final panel, the rates corresponding to different magnetic field values are compared directly, offering a clearer perspective on the influence of eB on the dilepton production rate.

occurs because the sets of Landau levels contributing to annihilation processes are distinct from those involved in decay processes. Nonetheless, there is no kinematic restriction preventing dileptons from being produced at the same invariant mass by both types of processes. Consequently, the total DR at a given M represents a combined effect, reflecting contributions from all allowed processes across different Landau level configurations.

The DR derived solely from the LLL in the strong magnetic field approximation is included, as also discussed in subsection 8.2.1. It is essential to emphasize that within the LLL approximation, the contribution arises exclusively from the annihilation process. This contribution diminishes rapidly due to the presence of only a single Landau level, as discussed in Ref.[71]. This behaviour explains why the rates for the LLL approximation and the annihilation process in arbitrary magnetic fields begin with the same initial values. However, the LLL rate decreases sharply with increasing invariant mass, whereas the rate for arbitrary magnetic fields remains significantly higher. This difference occurs because, in the latter case, contributions from multiple Landau levels, including the LLL, collectively sustain the rate. A comparable pattern, emphasizing the contrast between the results obtained under the LLL approximation and those for arbitrary magnetic fields, was also evident in the analysis of mesonic spectral functions, as discussed in Ref. [266].

The DR for three different values of eB, m_π^2, $5, m_\pi^2$, and $10, m_\pi^2$, is plotted in Fig.8.11, keeping all other parameters unchanged. These values span the range of magnetic field strengths relevant to conditions in both RHIC and LHC experiments. For each case, we compare the resulting rate with the Born rate obtained under analogous parameter settings. Figure 8.10 demonstrates that the enhancement in the dilepton production rate for $eB = 5\,m_\pi^2$ is a consistent feature across all magnetic field strengths analyzed. As eB increases, the range of invariant masses where the enhancement is observed broadens, but at sufficiently large M, the rate converges with the Born rate. This behaviour is further clarified in the bottom-right panel of Fig. 8.11, where the comparison across different eB values provides a more distinct view of the trends. It is also evident that for all considered magnetic field strengths, the low invariant mass region is dominated by decay processes, while the high invariant mass region is primarily driven by the annihilation process.
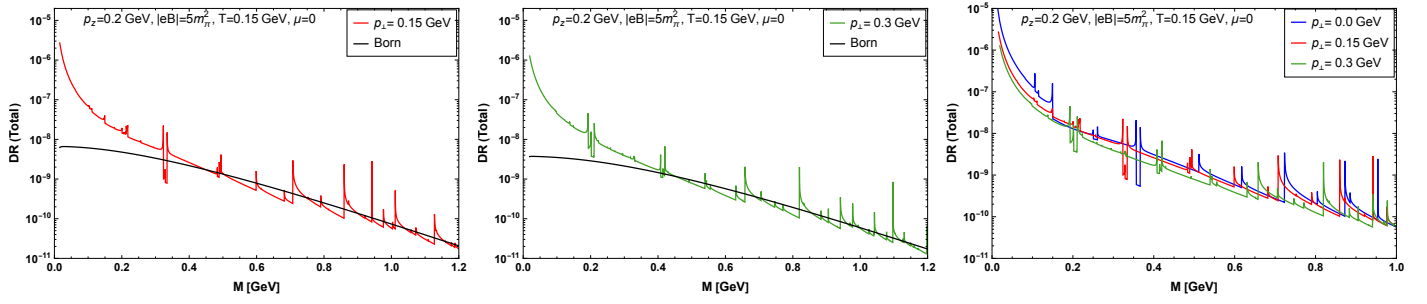
Figure 8.12: (The top-left and top-right panels display the DR as a function of invariant mass for two specific transverse momentum values, $p_\perp$, i.e. $\{0.15, 0.3\}$ GeV, along with eB and T. These rates are compared with the corresponding Born rates for each scenario. The bottom panel provides a closer examination of the impact of the transverse momentum $p_\perp$ on the total DR by comparing the results for three different $p_\perp$ values.
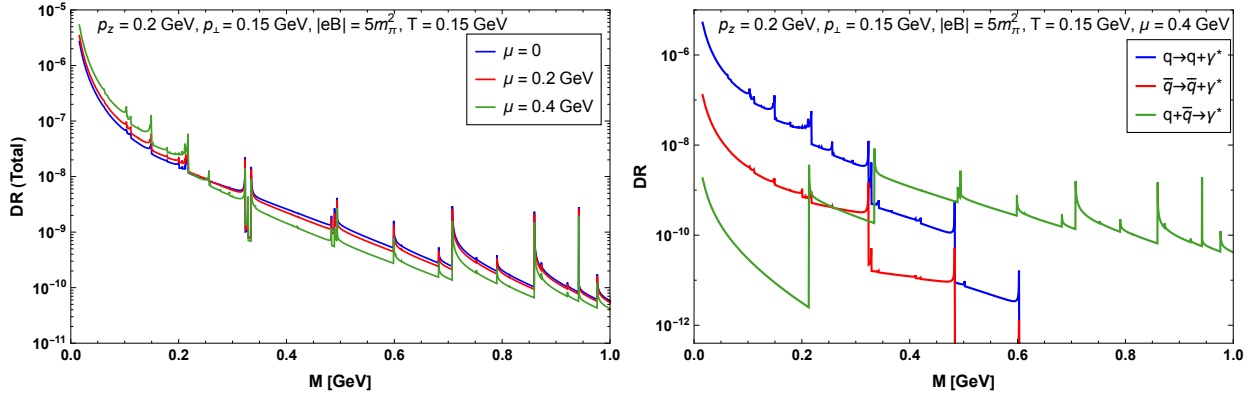

Figure 8.13: The left panel illustrates the impact of the chemical potential on the DR. It shows results for three different values of μ, i.e. $\{0, 0.2, 0.4\}$ GeV, with the transverse momentum $(p_\perp)$ fixed at 150 MeV. In the right panel, we decompose the same plot to separately display the contributions from the quark/antiquark decay and quark-antiquark annihilation processes. This separation highlights how μ influences the DR through its effects on the different processes.

In Fig. 8.12, we present a crucial feature of the DR enabled by the generalization of our calculation to arbitrary values of $p_\perp$. This plot shows how the rate varies as a function of the invariant mass for different values of the momentum components along the perpendicular direction to the magnetic field. To the best of our knowledge, this type of plot has not been reported before due to the absence of simultaneous calculations with non-zero values of both p_z and $p_\perp$. Previous studies either considered zero p_z (p_3 in their notation) as done in Ref. [70], or zero $p_\perp = 0$ as explored in Ref. [267].

For the nonzero $p_\perp$ cases, we consider two different values, $\{0.15, 0.3\}$ GeV, in the first two panels of Fig. 8.12 (top-left and top-right). The other parameters include $p_z = 0.2$ GeV, $T = 0.15$ GeV, $eB = 5\,m_\pi^2$ and $\mu = 0$. These are then compared with the corresponding Born rates. For both $p_\perp$ values, the DR is higher compared to the Born rate up to certain values of invariant masses. When comparing among different $p_\perp$ values themselves, we observe that the rate decreases with increasing $p_\perp$, with $p_\perp = 0$ remaining the highest among all. This trend is evident for both the decay and annihilation processes. The lower panel of the figure provides a closer view by focusing on the invariant mass range $0 < M < 1$ GeV, clearly highlighting these important features.

In the left panel of Fig. 8.13, we observe a similar trend in the DR to what is seen in panel three of Fig. 8.12 as μ increases. The DR decreases with higher μ due to the increased medium density, which reduces the likelihood of lepton pairs escaping. Conversely, for lower invariant masses where decay processes dominate, the DR actually increases

with increasing μ. From the right panel, which dissects the rate into different processes, another interesting observation emerges. The rate for quark decay is higher than for antiquark decay because of the nonzero μ. This is in sharp contrast to the plot in the right panel of Fig. 8.10 where $\mu = 0$. Apart from this difference, the other observations remain consistent across these plots. We intentionally do not show the LLL approximated DR plot for non-zero μ here, as it would again coincide with the annihilation process in the LLL. This discussion remains applicable even for vanishing $p_\perp$, as shown in Fig. 8.12, where the introduction of $p_\perp$ only leads to a suppression in the rate.

8.5. Dilepton Rate from Hadronic Matter in An Arbitrary Magnetic Field

Dilepton production occurs at every stage of a heavy-ion collision. To derive the spectrum observable in experiments, the dilepton production rate (DPR) contributions from both quark matter (QGP) and hadronic matter must be integrated over the entire space-time evolution of the system. The influence of a uniform background magnetic field on the DPR in the QGP has been widely studied through various methods [16, 17, 70–72, 74, 267–272]. As the system cools, the QGP transitions into hadronic matter through either a phase transition or crossover, which makes a significant contribution to dilepton emission, particularly in the low invariant mass region. The presence of an external magnetic field introduces complex modifications to the transport properties of hadronic matter, warranting an investigation of its impact on the DPR from this medium. However, such studies are currently sparse in the literature. A critical factor in determining the emission thresholds and intensity of dileptons is the imaginary part of the electromagnetic vector current correlator [273, 274], which is strongly affected by the thermo-magnetic modifications of charged meson propagators. These modifications, in turn, play a crucial role in altering the DPR from magnetized hadronic matter.

In a recent work [275], the DPR from magnetized hot hadronic matter has been investigated in details, focusing on the spectral function of the neutral rho meson. This spectral function is derived from the electromagnetic vector current correlation function, calculated within the framework of the real-time formalism of Thermal Field Theory. The analytic structure of the system is examined in the complex energy plane. Alongside the usual contribution from the Unitary cut beyond the two-pion threshold, a non-trivial Landau cut within the physical kinematic region has been identified. This Landau cut arises due to the finite magnetic field, as charged pions occupy distinct Landau levels before and after scattering with the neutral meson. As a result, the DPR yield in the low invariant mass region becomes non-zero, in contrast to the zero-field scenario where it vanishes. A particularly noteworthy observation is the continuous DPR spectrum, which emerges due to the shifting of the Unitary (Landau) cut thresholds towards lower (higher) invariant mass values for finite transverse momentum.

Figures 8.14(a) and (b) illustrate the DPR [275] as a function of invariant mass for the transverse momentum $q_\perp$=0, the longitudinal momentum q_z=150 MeV at temperatures $T = 130$ MeV and $T = 160$ MeV, respectively, under different magnetic field strengths. For reference, the corresponding results without a magnetic field (grey dotted lines) are also displayed, showing consistency with earlier studies [258, 276]. The plots reveal that, in the presence of a magnetic field, the DPR is influenced by contributions from both the Landau cut and the Unitary cut, highlighting the non-trivial effects introduced by the magnetic field. The emergence of nontrivial Landau cut contributions results in a significant enhancement of the DPR in the lower invariant mass region, which is otherwise absent without the background magnetic field. Additionally, at zero transverse momentum, for finite values of eB, the DPR is kinematically prohibited in the invariant mass range between the Landau and Unitary cut thresholds. This behaviour is clearly evident in both figures, highlighting the distinctive effects of the magnetic field on the DPR. The width of this kinematically forbidden gap
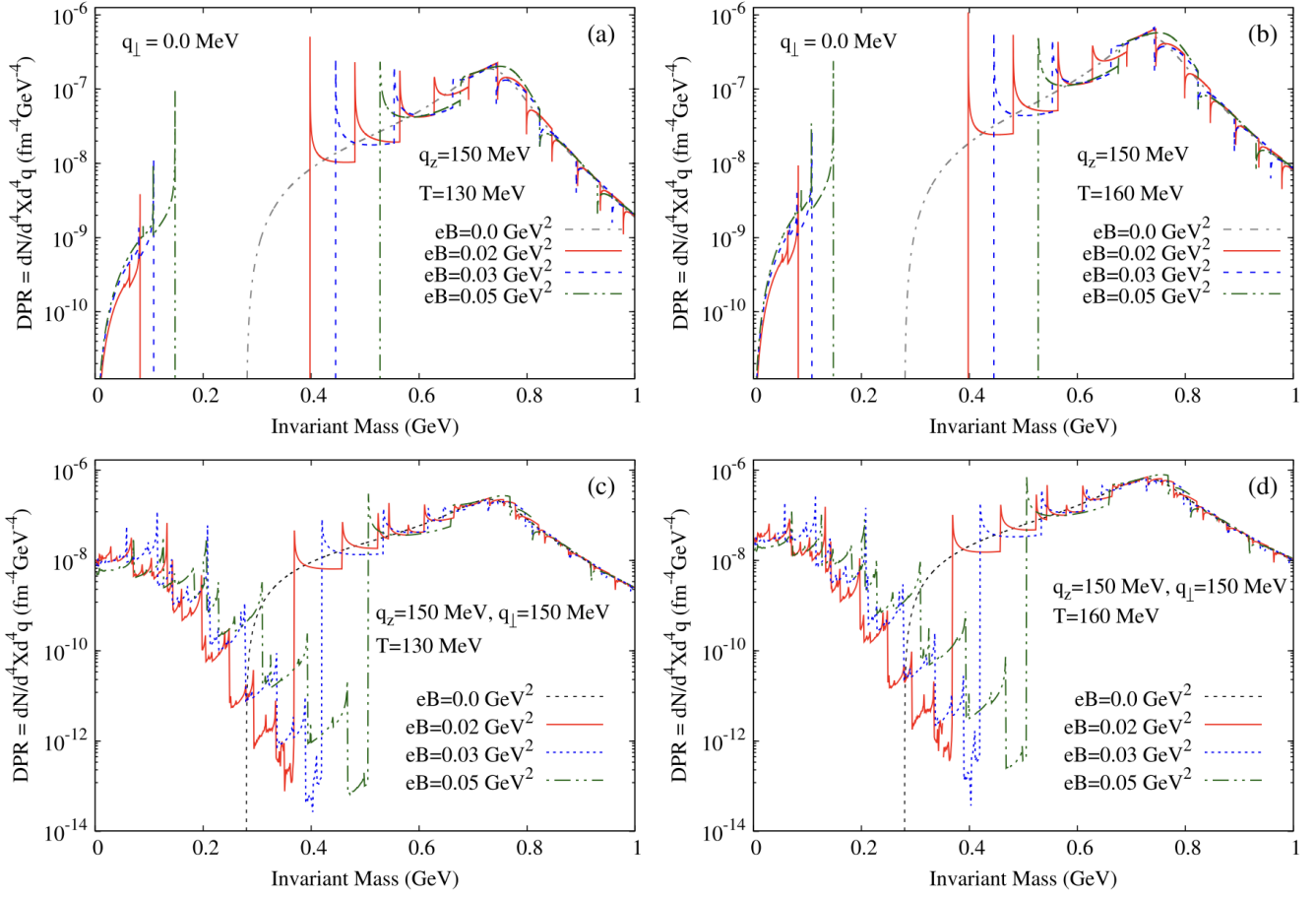
Figure 8.14: The DPR as a function of the invariant mass is presented for the longitudinal momentum $q_z = 150$ under varying background magnetic fields. The results are shown for two transverse momentum cases: the transverse momentum $q_\perp = 0$ at (a) $T = 130$ and (b) $T = 160$ MeV, and the transverse momentum $q_\perp = 150$ MeV at (c) $T = 130$ MeV and (d) $T = 160$ MeV. For comparison, the corresponding $eB = 0$ curves are also included, represented by grey dotted lines. This figure is adopted from Ref. [275].

between the Landau and Unitary cut thresholds is independent of temperature but grows with increasing magnetic field strength. The DPR with non-zero values of $q_\perp$ and q_z is shown in Figs.8.14(c) and (d). A key observation is that the DPR becomes continuous, and the forbidden gap, which exists between the Landau cut and Unitary cut when $q_\perp = 0$, disappears. Moreover, the DPR is significantly enhanced in the low invariant mass region, specifically in the Landau cut region. It is important to note that for $q_\perp = 0$, a pion in Landau level n could interact with pions in Landau levels $(n-1)$, n, $(n+1)$, producing a neutral rho meson. However, for non-zero $q_\perp$, there is no such restriction on Landau levels.

The DPR exhibits spike-like structures throughout the entire range of allowed invariant mass, which can be attributed to the phenomenon of "threshold singularities." These singularities, resulting from the Landau level quantization of pions in magnetized hadronic matter, arise from the specific functional dependence of the DPR. When $eB \neq 0$, for sufficiently high invariant masses, the DPR is similar to that for $eB = 0$, as seen for $\sqrt{q^2} > \sqrt{4(m_\pi^2 + eB) + q_\perp^2}$. However, in the low invariant mass region, where $\sqrt{q^2} < \sqrt{4(m_\pi^2 + eB) + q_\perp^2}$, the DPR is significantly enhanced compared to the case of zero magnetic field, as observed in Figs.8.14(c) and (d). Additionally, at higher temperatures, the increased thermal phase space leads to a general increase in the magnitude of the DPR, which can be confirmed by comparing the results in Figs.8.14(a) and (b) or Figs. 8.14(c) and (d).
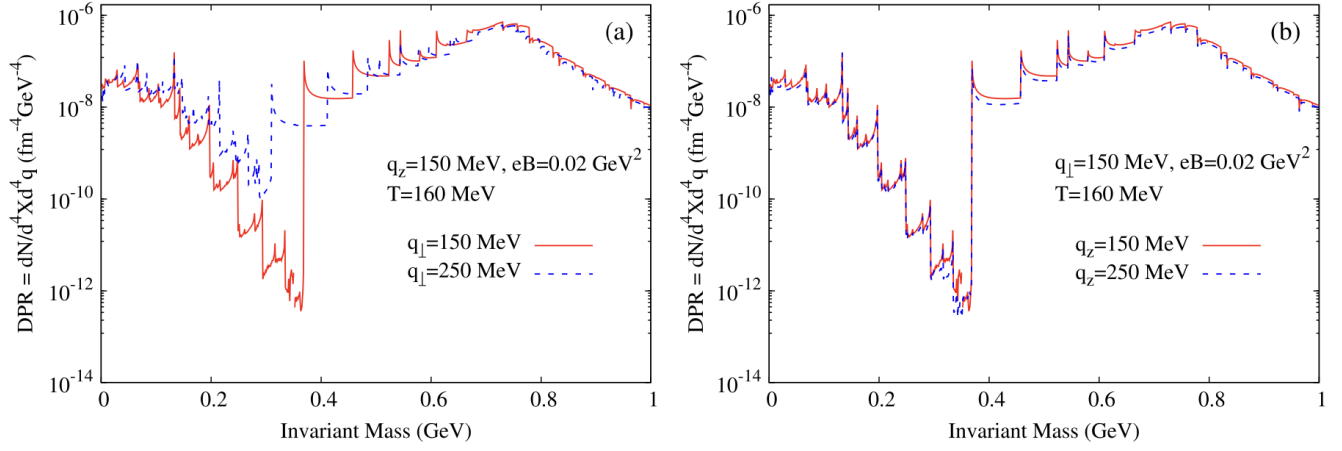
Figure 8.15: The DPR as a function of the invariant mass is analyzed at $T = 160$ MeV, $eB = 0.02$ GeV^2. In the left panel (a) the DPR is shown for various values of $q_\perp$ at $q_z = 150$ MeV, while in the right panel (b) it is presented for different values of q_z at $q_\perp = 150$ MeV. This figure is adopted from Ref. [275].

Figs.8.15(a) and (b) depict the DPR as function of invariant mass for varying transverse momentum $q_\perp$ at $q_z = 150$ MeV, and for different longitudinal momenta q_z at $q_\perp = 150$ MeV, respectively, with $eB = 0.02$ GeV^2 and $T = 160$ MeV. Both figures exhibit trends similar to those in Fig.8.14(d) for low and high invariant mass regions. In Fig.8.15(a), as $q_\perp$ increases, the threshold of the Unitary cut shifts to lower invariant masses, while the Landau cut threshold moves to higher invariant masses. When $q_\perp^2 \geq 4(m_\pi^2 + eB)$, contributions from both Landau and Unitary cuts influence the DPR across the entire invariant mass range. On the other hand, Fig. 8.15(b) shows that the DPR decreases as q_z increases. This reduction arises due to thermal suppression, which becomes more prominent at higher q_z.

9. Heavy Quarks in Presence of Thermo-Magnetic Medium

9.1. Heavy Quarks as QGP signatures

Heavy quarks (charm and bottom) are considered excellent probes for the quark-gluon plasma (QGP) for several reasons. Let us list them here.

- **Produced in the Initial Stages of Heavy-Ion Collisions -** Heavy quarks are created predominantly in the early stages of relativistic heavy-ion collisions via hard scatterings (high-energy gluon fusion and quark-antiquark annihilation). This means their production is largely unaffected by the later stages of the collision, making them a reliable probe of the QGP.

- **Do Not Undergo Significant Regeneration -** Unlike light quarks, which can be produced and annihilated throughout the evolution of the medium, charm and bottom quarks are mostly conserved due to their large mass. This allows their dynamics to be traced back to the QGP phase with minimal interference from later hadronic interactions.

- **Strong Interaction with the Medium -** Heavy quarks propagate through the hot and dense quark matter and experience energy loss via two key mechanisms:

1. Radiative energy loss (gluon bremsstrahlung): Heavy quarks emit gluons while moving through the QGP, though the suppression of small-angle radiation (the "dead cone effect") modifies this process compared to light quarks.

2. Collisional energy loss: Heavy quarks scatter elastically off medium constituents, transferring energy and momentum to the plasma.

Measuring the suppression of heavy-flavor mesons (e.g., D-mesons, B-mesons) via nuclear modification factors (R_{AA}) provides insights into the properties of the QGP.

- **Elliptic Flow and Thermalization -** The collective motion of heavy quarks in non-central heavy-ion collisions can be quantified by their elliptic flow coefficient (v_2), which measures their anisotropic distribution in momentum space. A significant v_2 for heavy quarks suggests strong interactions with the medium, potentially indicating partial thermalization.

- **Quarkonia Suppression as a QGP Signal -** Bound states of heavy quark-antiquark pairs (quarkonia), such as J/ψ (charmonium) and Υ (bottomonium), serve as key QGP probes. In a QGP, the color screening effect reduces the binding potential between the heavy quark and antiquark, leading to suppression of quarkonia yields. The sequential melting of different quarkonium states at different temperatures provides a "thermometer" for the QGP.

- **Comparison with Proton-Proton and Proton-Nucleus Collisions -** Heavy-flavor production in small systems like $p - p$ and $p - A$ collisions serves as a baseline to distinguish cold nuclear matter effects from QGP-induced modifications. Differences in observed spectra and nuclear modification factors (R_{AA}, v_2) between small and large collision systems help isolate QGP-specific phenomena.

To summarize this section, we can infer that HQs provide a unique window into QGP dynamics because they are produced early, they strongly interact with the medium, they exhibit energy loss and flow effects, and they offer quarkonium suppression as a diagnostic tool. Their study continues to refine our understanding of the properties of quark matter.

9.2. Heavy Quark diffusion

Heavy quarks, being external to the bulk medium, receive random kicks from the surrounding partons – light quarks and gluons – as they traverse through the deconfined plasma. Consequently, they undergo both energy loss and momentum diffusion due to repeated interactions with the medium. Since these interactions primarily involve multiple soft scatterings, the evolution of heavy quarks can be effectively described as Brownian motion, making the Langevin equation a natural framework for their dynamics. In this approach, the momentum diffusion coefficient κ quantifies the rate of momentum broadening induced by random interactions. In the following sections, we will explore this coefficient in different scenarios, including the presence of an external magnetic field.

9.2.1. Scales

Before going into the detailed formalism given in this section, we start by discussing the various scales in play. In the absence of an external magnetic field, there is only one external scale from heavy quarks, which is considered to be much higher than the corresponding temperature of the bulk medium i.e. $(M, p) \gg T$. In the presence of an external magnetic field, we have to consider the hierarchies between scales, $M, p, T, \sqrt{eB}$. One thing, we already can put, i.e.

$\{M, p\} \gg \{T, \sqrt{eB}\}$. It is the hierarchies between the scales T and $\sqrt{eB}$, which results in various approximations. Hard Thermal Loop approximation is an useful tool to extract gauge invariant analytic expressions out of a perturbative calculation and we will also use this tool which invokes an extra scale constraint, namely : $\alpha_s eB \ll T^2$.

We will discuss case-by-case, different scenarios consisting of various scale hierarchies.

9.2.2. $B = 0$, static limit of HQ

Since it takes many collisions to significantly alter the momentum of a HQ, its interaction with the medium can be approximated as a series of uncorrelated momentum kicks. In the simpler non-relativistic case, we can assume the HQ to be static, meaning its momentum p effectively vanishes. In this static limit, approximately M/T collisions are required to change the HQ's momentum by a factor of 1. Consequently, the equilibration timescale for the heavy quark is given by $\sim 1/\eta_D \approx (M/T) \times \tau$, where τ represents the time interval between hard collisions, estimated as $1/(g^4 T)$ [277]. The corresponding dynamics are then governed by the Langevin equation, as discussed below.

$$\frac{dp_i}{dt} = \xi_i(t) - \eta_D p_i, \ \langle \xi_i(t)\xi_j(t') \rangle = \kappa \delta_{ij}\delta(t - t'), \tag{9.1}$$

where $(i, j) = (x, y, z)$ and $\xi_i(t)$ represents the uncorrelated momentum kicks. η_D and κ are respectively known as the momentum drag and diffusion coefficient. Assuming $t > \eta_D^{-1}$, the solution of the above differential equation can be given as

$$p_i(t) = \int\limits_{-\infty}^{t} dt' e^{\eta_D(t'-t)}\xi_i(t'), \tag{9.2}$$

and the mean squared value of p is expresed as

$$\langle p^2 \rangle = \int dt_1 dt_2 e^{\eta_D(t_1+t_2)}\langle \xi_i(t_1)\xi_i(t_2) \rangle = \frac{3\kappa}{2\eta_D}, \tag{9.3}$$

where 3κ is the mean squared momentum transfer per unit time (factor 3 coming from the 3 isotropic spatial dimensions). One can then connect the diffusion and drag coefficients in the following way :

$$\frac{3\kappa}{2\eta_D} = \langle p^2 \rangle = 3MT$$

$$\therefore \eta_D = \frac{\kappa}{2MT}. \tag{9.4}$$

The spatial diffusion constant D is defined similarly as κ in position space, i.e.

$$\langle x_i(t)x_j(t) \rangle = 2D \ t \ \delta_{ij}, \tag{9.5}$$

which is further connected with η_D and κ in the following way :

$$D = \frac{T}{M\eta_D} = \frac{2T^2}{\kappa}. \tag{9.6}$$

9.2.3. $B = 0$, beyond the static limit of HQ

In high-energy collisions, the charm and bottom quark spectra indicate significantly large transverse momenta, making the relativistic case more relevant for study. In this scenario, we consider a heavy quark moving with velocity $\gamma v \approx 1$, where $v = p/p_0$. Due to the increased momentum, it takes approximately p/T collisions to alter the momentum of the HQ by a factor of 1. As a result, the equilibration timescale for the heavy quark is given by $\sim p/T \times \tau$. When accounting for the HQ's motion in a specific direction, the Langevin equation is modified accordingly, as we will discuss next.

$$\frac{dp_i}{dt} = \xi_i(t) - \eta_D(p)p_i, \tag{9.7a}$$

$$\langle \xi_i(t)\xi_j(t') \rangle = \kappa_{ij}(\vec{p})\delta(t - t'), \tag{9.7b}$$

where

$$\kappa_{ij}(\vec{p}) = \kappa_L(p)\,\hat{p}_i\hat{p}_j + \kappa_T(p)\,(\delta_{ij} - \hat{p}_i\hat{p}_j)\,, \tag{9.8}$$

where $\hat{p}_i$ denotes the unit vector of the heavy quark (HQ) momentum along a specific direction i with $(i,j) = (x,y,z)$. The quantities κ_L and κ_T represent the longitudinal and transverse momentum diffusion coefficients, respectively. In contrast to the non-relativistic case, the motion of the HQ in a preferred direction introduces an anisotropy, leading to the breakdown of the total momentum diffusion coefficient κ into its longitudinal and transverse components, satisfying the relation $3\kappa \equiv \kappa_L + 2\kappa_T$.

Now, considering a heavy quark with momentum $p\ (\gg T)$ we examine its momentum change over a time interval Δt, which is much longer than the microscopic collision time scale τ but shorter than the HQ equilibration time, i.e. $\tau \ll \Delta t \ll p/T \times \tau$. Given this condition, the number of collisions occurring in this interval is large, approximately $N \sim \Delta t/\tau$. The resulting change in HQ momentum is of the order $\sim T/p \times N \approx T/p \times \Delta t/\tau$, which remains small compared to p. Consequently, over the duration Δt, the HQ's momentum can be considered nearly constant. In other words, the probability distribution for the momentum transfer from a single collision remains approximately unchanged within this interval. Since the total momentum transfer is the sum of N individual contributions with an identical probability distribution, it follows a Gaussian distribution with negligible higher-order corrections of order $\sim 1/N$. As this process repeats itself independently over successive time intervals, it becomes convenient to express the momentum diffusion coefficient κ_{ij} in terms of the mean squared momentum fluctuations, as

$$\kappa_{ij}(\vec{p}) = \lim_{\Delta t \to 0} \frac{\langle \Delta p_i \Delta p_j \rangle}{\Delta t}, \tag{9.9}$$

with $\Delta p_i = p_i(t + \Delta t) - p_i(t)$. This in turn leads to the following macroscopic equations of motion

$$\frac{d}{dt}\langle p \rangle \equiv -\eta_D(p)p, \tag{9.10a}$$

$$\frac{1}{2}\frac{d}{dt}\langle (\Delta p_T)^2 \rangle \equiv \kappa_T(p), \tag{9.10b}$$

$$\frac{d}{dt}\langle (\Delta p_L)^2 \rangle \equiv \kappa_L(p), \tag{9.10c}$$

with p_L and p_T representing longitudinal and transverse momentum components.

9.2.4. $B \neq 0$, static limit of HQ

In the presence of an external magnetic field, although the HQ mass is considered to be the largest scale, the value of the external magnetic field eB will determine the further scale hierarchies, e.g. $M \gg \sqrt{eB} \gg T$ for the Lowest Landau Level dynamics. However, in this case, because of the spatial anisotropy introduced by the external magnetic field, we will again have a set of two equations for the longitudinal (∥) and transverse (⊥) momenta

$$\frac{dp_z}{dt} = -\eta_{\parallel}p_z + \xi_z, \quad \langle \xi_z(t)\xi_z(t') \rangle = \kappa_{\parallel}\delta(t - t'), \tag{9.11a}$$

$$\frac{d\vec{p}_\perp}{dt} = -\eta_\perp \vec{p}_\perp + \vec{\xi}_\perp, \quad \langle \xi_\perp^i(t)\xi_\perp^j(t') \rangle = \kappa_\perp \delta_{ij}\delta(t - t'), \tag{9.11b}$$

where $(i,j = x,y)$ and $\vec{A}_\perp = (A_x, A_y)$ are the transverse components of the momenta, random forces and drag coefficients. Consequently, the drag and diffusion coefficients are correlated

$$\eta_{\parallel} = \frac{\kappa_{\parallel}}{2MT}, \quad \eta_\perp = \frac{\kappa_\perp}{2MT}. \tag{9.12}$$

Moreover, similarly as the relativistic case at $B = 0$, for the magnetized medium also, within the static limit we can break down κ into longitudinal and transverse parts using the rotational symmetry

$$3\kappa = \kappa_{\parallel} + 2\kappa_\perp. \tag{9.13}$$

9.2.5. $B \neq 0$, beyond the static limit of HQ

When in presence of an external magnetic field we also have the finite velocity of HQ $\vec{v} = \vec{p}/E$, we have two anisotropic directions at our hand. The most ideal scenario is to define an angle between the two anisotropic directions, i.e. $\theta = \vec{v}\angle\vec{B}$, but usually people tackle this scenario by choosing two extreme scenarios, i.e. $\vec{v} \parallel \vec{B}$ and $\vec{v} \perp \vec{B}$.

$\vec{v} \parallel \vec{B}$ is simpler since the magnetic field and the heavy quark are considered to be moving in the same direction, e.g. z direction for our case. So the macroscopic equations of motion for this case can be given as :

$$\frac{d}{dt}\langle p \rangle \equiv -\eta_D(p)p, \tag{9.14a}$$

$$\frac{1}{2}\frac{d}{dt}\langle (\Delta p_T)^2 \rangle \equiv \kappa_T(p), \tag{9.14b}$$

$$\frac{d}{dt}\langle (\Delta p_z)^2 \rangle \equiv \kappa_L(p), \tag{9.14c}$$

where Δ signifies the respective variance of the momentum distributions with the transport coefficients.

For $\vec{v} \perp \vec{B}$ the HQ moves perpendicular to (i.e. x or y) the direction of the external anisotropic magnetic field (i.e. z). This gives three momentum diffusion coefficients (i.e. $\kappa_1, \kappa_2, \kappa_3$) in our hand,

$$\frac{d}{dt}\langle (\Delta p_x)^2 \rangle \equiv \kappa_1(p), \tag{9.15a}$$

$$\frac{d}{dt}\langle (\Delta p_y)^2 \rangle \equiv \kappa_2(p), \tag{9.15b}$$

$$\frac{d}{dt}\langle (\Delta p_z)^2 \rangle \equiv \kappa_3(p). \tag{9.15c}$$

9.2.6. Connection with the HQ scattering rate

At finite temperature, the uncorrelated momentum kicks experienced by the heavy quark (HQ) arise from its scattering with thermally populated light quarks and gluons, primarily through $2 \leftrightarrow 2$ scattering processes such as $qH \rightarrow qH$ and $gH \rightarrow gH$ ($q \rightarrow$ quark, $g \rightarrow$ gluon and $H \rightarrow$ HQ). At leading order in the strong coupling, these interactions are mediated by one-gluon exchange (see Fig. 9.1), with the scattering particles behaving as quasiparticles in a thermally equilibrated medium.

In the plasma rest frame, Compton scattering is suppressed by a factor of T/M, making the $qH \rightarrow qH$ and $gH \rightarrow gH$ processes predominantly occur via t-channel gluon exchange. As a result, the momentum transport coefficients are directly linked to the scattering (or interaction) rate Γ of the t-channel gluon exchange. These coefficients can be explicitly expressed in terms of Γ, as :

$$\kappa_i = \int d^3q \, \frac{d\Gamma}{d^3q} \, q_i^2. \tag{9.16}$$

where $\frac{d\Gamma}{d^3q}$ can be interpreted as the scattering rate of the HQ via one-gluon exchange with thermal particles per unit volume of momentum transfer q.

9.3. HQ scattering rate

As in the previous section we have established the connection between the HQ diffusion and the HQ scattering rate, this section is dedicated about the HQ scattering rate. We will be mainly focusing on the two dominant $2 \leftrightarrow 2$ scatterings through t-channel gluon exchange, shown in Fig. 9.1. The corresponding scattering rate or interaction rate can be expressed in a standard way as

$$\Gamma(P \equiv \{E, \vec{v}\}) = \frac{1}{2E} \int \frac{d^3p'}{(2\pi)^3 2p_0'} \int \frac{d^3k}{(2\pi)^3 2k_0} \int \frac{d^3k'}{(2\pi)^3 2k_0'} (2\pi)^4 \delta^4(P + K - P' - K') \times$$
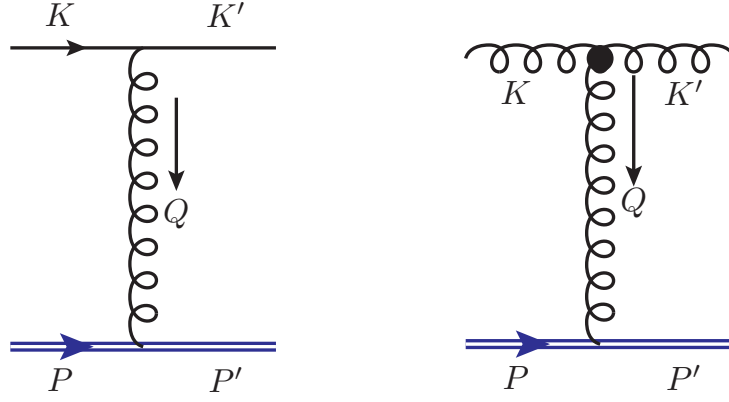
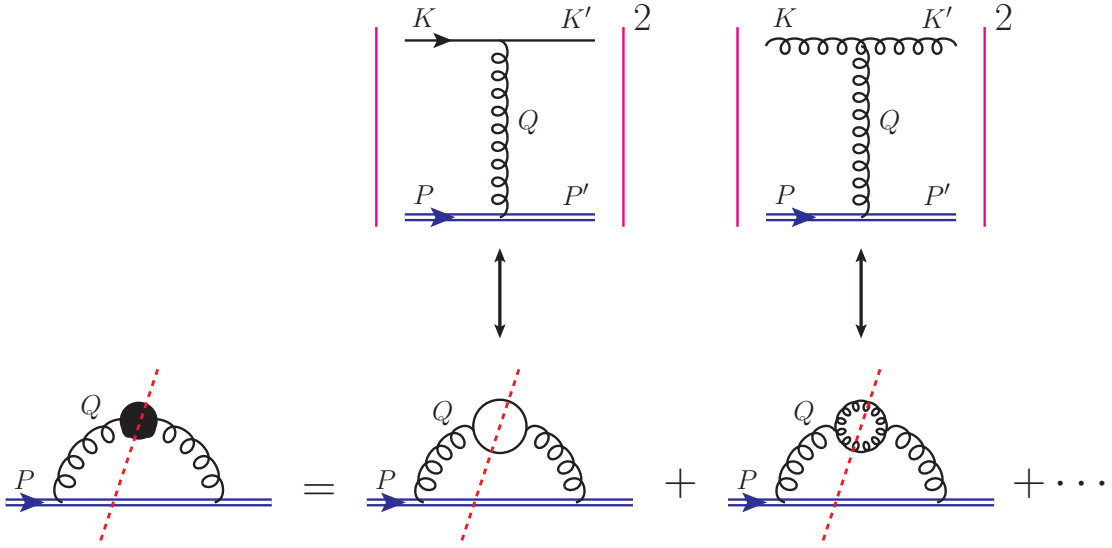Figure 9.1: The t-channel scatterings of the HQ, by light quarks (left) and gluons (right).

Figure 9.2: The equivalences of the t-channel scatterings of heavy quarks due to thermally generated light quarks and gluons, $qH \to qH$ (left) and $gH \to gH$ (right) are shown, as they can also be expressed as the cut (imaginary) part of the HQ self energy. An HTL resummed heavy quark self-energy with effective gluon propagator takes all the diagrams into account.

$$\left\{ N_f |\mathcal{M}|^2_{\text{quark}} n_f(k)[1 - n_f(k')] + |\mathcal{M}|^2_{\text{gluon}} n_b(k)[1 + n_b(k')] \right\}, \tag{9.17}$$

where P and K are the four-momenta of the incoming HQ and light quark/gluon respectively, while P' and K' are the four-momenta of the outgoing HQ and light quark/gluon respectively. $\mathcal{M}$ represents the scattering matrix elements for light quark/gluon.

There is another effective way of expressing the scattering rate, as proposed by Weldon [252] and demonstrated in Fig. 9.2. In this method, the scattering rate can be expressed in terms of the cut/imaginary part of the HQ self energy $\Sigma(P)$, as :

$$\Gamma(P \equiv \{E, \vec{v}\}) = -\frac{1}{2E} \frac{1}{1 + e^{-E/T}} \, \text{Tr}\left[(\slashed{P} + M) \, \text{Im}\Sigma(p_0 + i\epsilon, \vec{p}) \right]. \tag{9.18}$$

The advantage of Eq.(9.18) is that one can apply imaginary time formalism of thermal field theory to extract $\Sigma(P)$ including the necessary resummations as we will soon explain (also see Fig. 9.2).

While dealing with $2 \leftrightarrow 2$ scatterings through t-channel gluon exchange can be broadly separated into the regions of hard momentum transfer $q \sim T$ and soft momentum transfer $q \sim gT$, $Q = (q_0, q)$ being the exchange gluon momenta

(see Fig. 9.1) and g being the strong coupling. For heavy fermion energy loss in a hot QED plasma first by Braaten and Yuan [278] and then by Braaten and Thoma [193], it was established long ago, that this separation can be done by introducing an arbitrary momentum scale q^*. The hard region $q > q^*$ is usually calculated using the tree level scattering diagrams, i.e. using Eq. (9.17). On the other hand, to incorporate the soft region $q < q^*$, the Weldon technique is easier to employ, as one can then make use of the Hard Thermal Loop (HTL) approximations. Why? Because when the momentum Q flowing through the gluon line is soft, hard thermal loop corrections to the gluon propagator contribute at leading order in g. In this case, by the virtue of HTL approximation one can replace the two-loop diagrams for each separate process by an effective one-loop diagram involving a resummed gluon propagator, which is obtained by summing the geometric series of one-loop self-energy corrections proportional to $g^2 T^2$ (see Fig. 9.2). Using this approach, Braaten and Thoma showed that one can get rid of the arbitrary momentum scale q^*, when one properly adds the hard and soft contributions together [193].

With the preceding discussion we can now write down the expression for the HQ one-loop effective self energy (leftmost diagram in the bottom half of Fig. 9.2) as :

$$\Sigma(P) = ig^2 \int \frac{d^4 Q}{(2\pi)^4} \mathcal{D}^{\mu\nu}(Q) \gamma_\mu S_H(P - Q) \gamma_\nu, \tag{9.19}$$

where $\mathcal{D}^{\mu\nu}(Q)$ denotes the effective gluon propagator and $S_H(P - Q)$ is the HQ propagator. After this, the next steps are as follows :

- **Step 1 :** Evaluation of $\mathcal{D}^{\mu\nu}$ for hot/dense/magnetised medium which requires the calculation of the gluon self energy tensor $\Pi^{\mu\nu}$ and corresponding various associated form factors.

- **Step 2 :** Writing down the HQ propagator S_H in hot/dense/magnetised medium, either within an approximated limiting scenario or in the most general version without any approximations.

- **Step 3 :** Evaluation of HQ one-loop effective self energy by using Eq. (9.19).

- **Step 4 :** Evaluation of the scattering rate Γ by computing the discontinuity of Σ and then performing the trace, as given in Eq. (9.18).

- **Step 5 :** In the final step, estimation of HQ momentum diffusion coefficients for various scenarios involving different scale hierarchies by applying Γ in Eq. (9.16).

Finally we would like to mention that various studies have already been done for the computation of HQ momentum diffusion coefficients in a hot magnetized medium, both within and beyond the static limit of the HQ, employing strong and weak magnetic field approximations [279–283]. In the following sections we will discuss some recent results where the HQ momentum diffusion coefficients have been studied in the most general scenario for any arbitrary values of the external magnetic field and for both within and beyond the static limit of the HQ. The calculational details can be found in Ref [79].

9.4. Key Observations

9.4.1. Within the static limit

To discuss the results considering the static limit of the HQ, we will directly quote the expressions from Ref. [79] :

$$\kappa_T^{(s)} = \sum_{l=0}^{\infty} \frac{(-1)^l \pi g^2 T M}{\sqrt{M^2 + 2l|q_f B|}} \int \frac{d^3 q}{(2\pi)^3} q_\perp^2 e^{-q_\perp^2/|q_f B|} \left[\frac{\left(\frac{1}{q}(m_D^g)^2 + \delta(q_3) \sum_f \delta m_{D,f}^2\right) (L_l(\xi_q^\perp) - L_{l-1}(\xi_q^\perp))}{2(q^2 + (m_D')^2)^2} \right], \tag{9.20}$$

$$\kappa_L^{(s)} = \sum_{l=0}^{\infty} \frac{(-1)^l \, 2\pi g^2 T M}{\sqrt{M^2 + 2l|q_f B|}} \int \frac{d^3 q}{(2\pi)^3} q_3^2 e^{-q_\perp^2 / |q_f B|} \left[\frac{(m_D^g)^2 (L_l(\xi_q^\perp) - L_{l-1}(\xi_q^\perp))}{2q(q^2 + (m_D')^2)^2} \right]. \tag{9.21}$$

Here $L_l(\xi_q^\perp)$ denotes the Laguerre polynomials with Landau level l and argument $\xi_q^\perp = \frac{2q_\perp^2}{q_f B}$, q_3 and $q_\perp$ being the longitudinal and transverse components of the exchange gluon momentum q. m_D' is the full magnetized medium modified QCD Debye mass which consists of the pure glue part m_D^g and the magnetic field modified correction δm_D, given as

$$(m_D')^2 = (m_D^g)^2 + \sum_f \delta m_{D,f}^2, \tag{9.22}$$

$$(m_D^g)^2 = \frac{N_c g^2 T^2}{3}, \tag{9.23}$$

$$\delta m_{D,f}^2 = \frac{g^2 |q_f B|}{4\pi^2 T} \sum_{l=0}^{\infty} (2 - \delta_{l,0}) \int dk_3 \, n_F (1 - n_F). \tag{9.24}$$

From Eqs. (9.20) and (9.21), one can verify the results of the lowest Landau-level limit [279] by putting $l = 0$.

On the other hand, for the static limit result with vanishing magnetic field, there will be a single momentum diffusion coefficient $\kappa^{(s)}$ which can be straightaway expressed as

$$\kappa^{(s)} = 2\pi g^2 T \int \frac{d^3 q}{(2\pi)^3} \left[\frac{q \, m_D^2}{2(q^2 + m_D^2)^2} \right]. \tag{9.25}$$

An alternate procedure, where to get an estimate of the effects due to the external magnetic field, only the medium modified Debye screening mass is modified, can be directly extended from $eB = 0$ result $\kappa^{(s)}$ as

$$\kappa_T^{(s)'} = \pi g^2 T \int \frac{d^3 q}{(2\pi)^3} \left[\frac{q_\perp^2 (m_D')^2}{2q(q^2 + (m_D')^2)^2} \right], \tag{9.26}$$

$$\kappa_L^{(s)'} = 2\pi g^2 T \int \frac{d^3 q}{(2\pi)^3} \left[\frac{q_3^2 (m_D')^2}{2q(q^2 + (m_D')^2)^2} \right]. \tag{9.27}$$

One can now notice the key differences between the two approaches by carefully comparing between Eqs. (9.26)-(9.27) and Eqs. (9.20)-(9.21). The structural anisotropy induced by the magnetic field is not captured in Eqs.(9.26)-(9.27), leading to similar values for κ_L and κ_T, contrary to the exact results (Eqs.(9.20)-(9.21)). This discrepancy arises because, in the static limit, the quark loop contributions to κ_L vanish due to the $\delta(q_3)$ factor, leaving only gluon scatterings as the dominant contribution—an effect not accounted for when modifying the Debye mass alone. Moreover, the exact approach, incorporating HQ propagator modifications, naturally introduces a Gaussian suppression, eliminating the need for a UV cutoff. In contrast, the Debye mass approximation lacks this suppression, necessitating an ad-hoc cutoff q^*, discussed earlier in section 9.3, which can be estimated via a fitting procedure, as done in Ref. [284]. Lastly, the Debye mass-based expressions lack explicit HQ mass dependence, unlike the exact formulations that consider arbitrary Landau levels.

Figure 9.3 presents the observations from the HQ static limit results for the momentum diffusion coefficients. We consider a relatively high temperature $T = 0.4$ GeV to remain within the HTL approximation. In the left panel we show the variation of the ratio $\kappa_{L/T}^{(s)}/\kappa^{(s)}$ with the external magnetic field in a magnetized medium. The plot shows that at lower eB, both longitudinal (solid) and transverse (dashed) diffusion coefficients grow more rapidly compared to higher eB. This effect is more pronounced for charm quarks (red), leading to a crossover between charm and bottom (blue) curves. Throughout the range of eB, κ_L remains dominant over κ_T for both quark flavors.

The right panel compares the exact (κ) and Debye mass approximated (κ') results. To ensure UV finiteness in κ', we adopt a similar form of q^* as in Ref.[284], replacing $g(T)$ with the magnetized medium-modified $g(T, eB)$ [225, 232, 285], i.e., $q^* = 3.1 T g(T, eB)^{1/3}$. The same $g(T, eB)$ is used for the magnetic field correction to the Debye mass [282]. The right panel shows κ'/κ vs. eB, revealing a general trend: κ' underestimates κ at high eB and overestimates it at low eB, with more pronounced deviations for bottom quarks due to their larger mass ($M_b = 4.18$ GeV) vs. ($M_c = 1.27$ GeV). Additionally, κ_T'/κ_T remains consistently higher than κ_L'/κ_L, aligning with the left panel results, where κ_L dominates

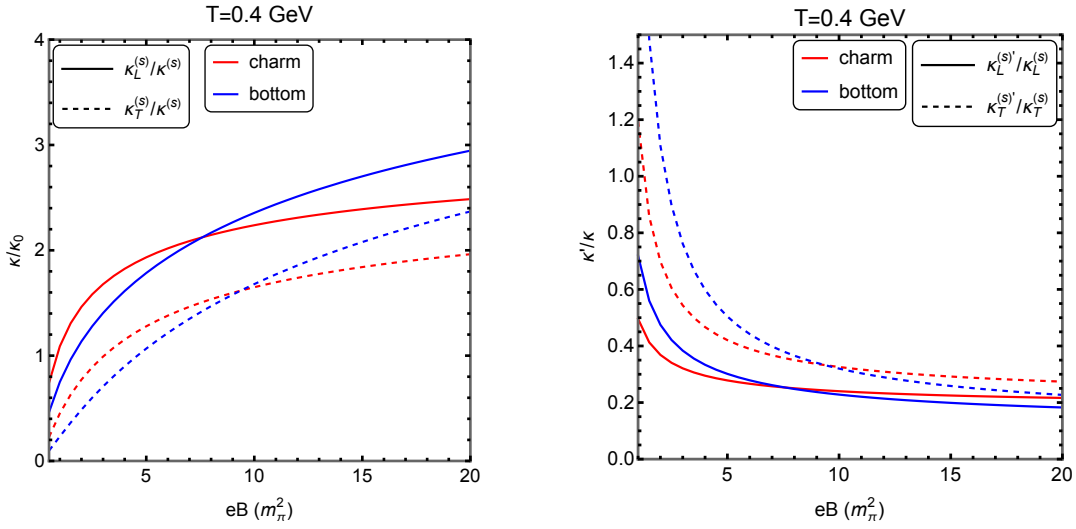Figure 9.3: Static limit results : (left panel) The magnetized medium modified exact results (κ) has been scaled with respect to the $eB = 0$ result (κ_0), variation of which with respect to eB has been shown for longitudinal (solid lines) and transverse (dashed lines) HQ momentum diffusion coefficients within the static limit of both charm (red curves) and bottom (blue curves) quarks. (right panel) Variation of the ratio between the Debye mass approximated results (κ') and the exact results (κ) with respect to eB has been shown for longitudinal (solid lines) and transverse (dashed lines) HQ momentum diffusion coefficients within the static limit of both charm (red curves) and bottom (blue curves) quarks.

κ_T. This dominance persists even without quark contributions, as the leading t-channel gluonic scatterings primarily influence κ_L.

9.4.2. Beyond the static limit

The beyond-static limit results are obtained within the small energy transfer regime, maintaining the hierarchy $M \geq p \gg T$ with $p = 1$ GeV and $T = 0.4$ GeV, ensuring consistency with the HTL approximation.

In the $\vec{v} \parallel \vec{B}$ case (left panel of Fig. 9.4), the variation of longitudinal and transverse momentum diffusion coefficients with eB follows a trend similar to the static limit. For high eB, $\kappa_{L/T}$ flattens, especially for charm quarks (red curves). Interestingly, for charm quarks, κ_T (dashed) dominates over κ_L (solid) across all eB, consistent with Ref.[286]. For bottom quarks (blue), κ_L initially exceeds κ_T but eventually undergoes a crossover at higher eB, reflecting the interplay of M, T and eB, with bottom quarks requiring a larger eB for similar behavior.

The $\vec{v} \perp \vec{B}$ case (right panel) has no $eB = 0$ counterpart, so we scale κ_j with T^3. Here, transverse components κ_1 (solid) and κ_2 (dashed) dominate over the longitudinal κ_3 (dotted) for charm quarks (for bottom quarks, see Ref. [79]) with $\kappa_1 > \kappa_2$ due to the specific choice of $p_\perp$ along the x direction. Unlike the previous case, no saturation occurs at high eB; instead, diffusion coefficients increase more steeply with eB.

Overall, at low eB, the magnetic field impact is stronger when the HQ moves parallel to B with high momentum, but it saturates at higher eB. Conversely, for perpendicular motion, the impact continues to grow with eB. The generality of our approach allows exploration across all eB, though we focus on fixed temperatures due to HTL constraints. The magnetic field's effects are more pronounced when varying eB rather than T.

There are several open directions in HQ dynamics in a magnetized medium. Current studies, including the one presented here, inherit limitations from the HTL approximation, such as assuming massless quarks in Landau levels, which
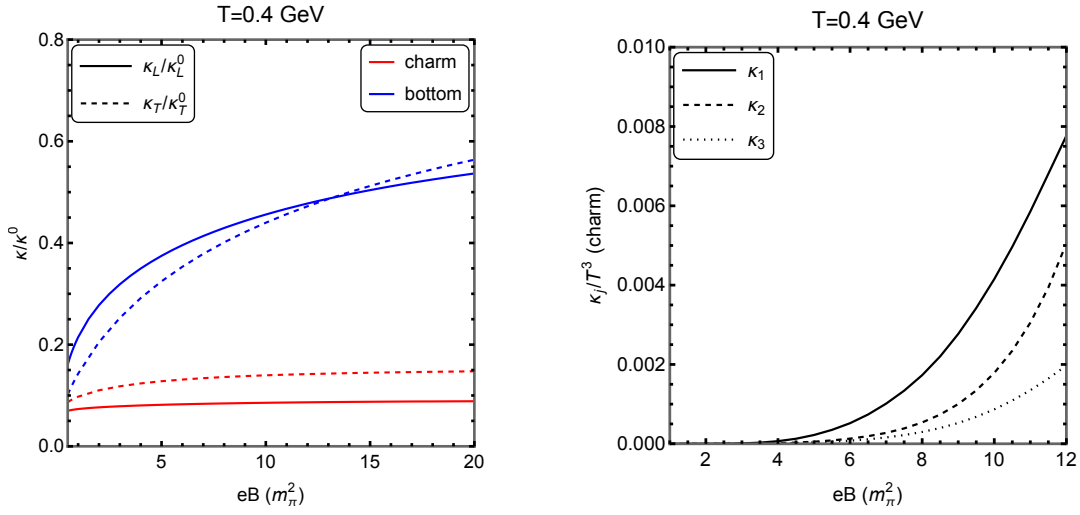
Figure 9.4: $\vec{v} \parallel \vec{B}$ case (left panel) : Variation of the longitudinal (solid curves) and transverse (dashed curves) momentum diffusion coefficients for charm (red curves) and bottom (blue curves) quarks with external magnetic field for $T = 0.4$ GeV.

$\vec{v} \perp \vec{B}$ case (right panel) : Variation of the transverse components κ_1 (solid curves), κ_2 (dashed curves) and longitudinal component κ_3 (dotted curves) of the momentum diffusion coefficient for charm (right panel) quarks with external magnetic field for $T = 0.4$ GeV.

The magnetized momentum diffusion coefficients are scaled with respect to their $eB = 0$ counterparts. HQ momentum p is taken to be 1 GeV.

leads to a vanishing quark contribution to κ_L. While HTL ensures gauge-independent, analytic expressions, it imposes strict scale constraints. A key challenge is computing hard scatterings in a magnetized medium to systematically remove the UV cutoff q^* [193, 194]. Additionally, the order-of-magnitude discrepancy between PQCD and LQCD predictions of the HQ spatial diffusion coefficient (D) highlights the need for non-perturbative studies in a magnetized medium, an avenue currently being explored. Our work also opens possibilities for studying HQ in-medium evolution via Langevin transport (e.g.,[287]) and its impact on experimental observables like directed and elliptic flow of open heavy-flavor mesons.

10. QCD Phase Diagram in the Presence of a Background Magnetic Field

One of the most important goals of the community studying QCD medium is to investigate and understand the QCD phase diagram. The QCD medium can exist in presence of different extreme conditions and accordingly there are possibilities of multi-faceted QCD phase diagrams. The phase diagram in the temperature (T) and baryon chemical potential (μ_B) plane is the most commonly known and finding out the existence of a potential critical point on this plane is one of the major driving force for the QCD community. In the same spirit, we can think of a phase diagram in the presence of a isospin chemical potential, magnetic field, angular momentum, current quark masses etc.

In this chapter, being a part of a review article on the magnetic field, we focus on the QCD phase diagram in the presence of a background magnetic field. First, we will discuss the phase diagram in the $T - eB$ plane at zero μ_B and then we will review the recent development for nonzero μ_B. In the process, we will touch on the significant developments of the field. The major focus will be on the theoretical advancement with the inclusion of important experimental results, if any. From the theoretical side, the field is mostly guided by lattice QCD, which is complemented by other theoretical methods such as effective QCD models, holographic QCD and functional methods. Here, we mention the major results from the lattice QCD and the impacts of those results on the development of different effective models and holographic

treatments of QCD.

10.1. A brief prelude

To understand a phase transition we can study the relevant order parameter. For example, the chiral condensate ($\sigma = \langle\bar{\psi}\psi\rangle^{1/3}$) is the order parameter for the chiral phase transition. A typical behaviour of σ as a function of T is depicted in the right panel of Fig. 10.1, which shows a crossover for nonzero current quark mass. At zero or small T, the condensate has a nonzero value signifying a phase with broken chiral symmetry. On the other hand, at higher T the condensate approaches to smaller values (it will be exactly zero in the chiral limit), representing a chiral symmetric phase. The crossover temperature (T_{CO}) is generally calculated from the inflection point of the condensate found by taking the temperature derivative. It is shown in the right panel, the peak represents the inflection point and the corresponding temperature is the T_{CO}. It can alternatively be calculated from the chiral susceptibility, estimated by taking the derivative of the condensate with respect to the current quark mass. The T_{CO} values mentioned in this article are calculated from the inflection point unless stated otherwise.
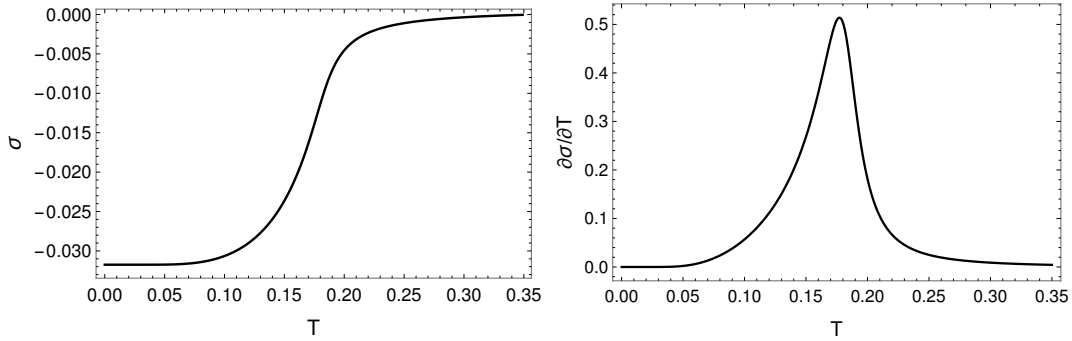
Figure 10.1: Left panel: typical temperature dependence of the chiral condensate at zero μ and zero eB. Right panel: the temperature derivative of the condensate.

Such a condensate can be easily calculated using simple QCD-inspired effective models, such as Nambu–Jona-Lasinio (NJL) model. A basic known form of the Lagrangian reads as

$$\mathcal{L}_{\mathrm{NJL}} = \bar{\psi}(i\partial\!\!\!/ - m)\psi + \frac{G_{\mathrm{S}}}{2}[(\bar{\psi}\psi)^2 + (\bar{\psi}i\gamma_5\vec{\tau}\psi)^2], \tag{10.1}$$

where, the first part is the Dirac kinetic term and the second term represents the interaction term. Spontaneous breaking of the chiral symmetry can be implemented via the second term. Such an implementation can be easily achieved by using the mean field approximation. After the chiral symmetry is spontaneously broken, the current quark mass (m) in the original Lagrangian is replaced by the effective mass (M) through the relation

$$M = m - G_{\mathrm{S}}\,\sigma, \tag{10.2}$$

which is also known as the gap equation. This brief discussion will be useful to understand the following discourse on the fate of chiral symmetry in the presence of eB and the associated phase diagram.

10.2. Features of QCD in the $T - eB$ plane

In this section, we review our existing knowledge on the features of QCD in the $T - eB$ plane, i.e., in absence of zero μ_B. This part is already well developed and we have acquired substantial amount of understanding.

10.2.1. Phase diagrams in the $T - eB$ plane: past and revised versions

Our present knowledge of the QCD phase diagram is shown in Fig. 10.2, in which the pseudocritical temperature or in other words the crossover temperature, T_{CO} is varied as a function of the magnetic field up to $1\,\text{GeV}^2$ of strength. This is found using a lattice QCD calculation [42]. The red band is obtained from the inflection point of the renormalised light quark chiral condensate, denoted as $\bar{u}u^r + \bar{d}d^r$. The renormalised condensate is introduced to eliminate additive and multiplicative divergences arising in lattice QCD calculations, which can be considered artifacts of the method. On the other hand, the blue band is procured from the strange quark number susceptibility, c_2^s, which however does not need any renormalisation. Both bands show a feature of decreasing T_{CO} as a function of eB. However, The major discussion in this review will focus on the red band, i.e., the fate of the T_{CO} for the light quark condensate.
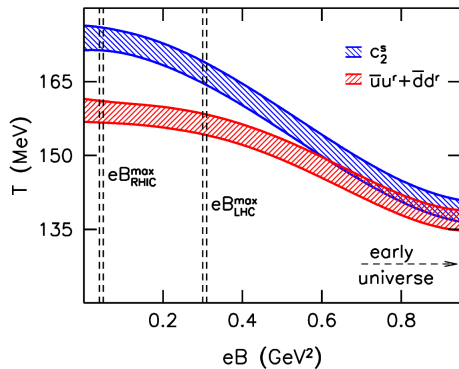
Figure 10.2: QCD phase diagram in the $T - eB$ plane with eB varied up to $1\ \text{GeV}^2$. The figure is adopted from Ref. [42].

Such a decreasing feature is a recent discovery due to the lattice QCD calculations [42, 288]. Previously, we knew of a phase diagram with an ever increasing T_{CO} with increasing eB as shown in figure 10.3. Such an understanding was first proponed by effective model calculations [289–291] and later on confirmed by lattice QCD calculation [292]. This points to an important lesson that we should always be careful when accepting lattice QCD results as the final word. Though it is a first principle calculation it comes with a lot of technical details and changing some of them could lead to qualitatively different results.

As we proceed, we discuss why lattice QCD initially confirmed the phase diagram depicted in Fig 10.3, which was later revised to Fig. 10.2. An obvious question is what happens if one increases the magnetic field further. Does the T_{CO} keep decreasing or does some nonmonotonicity arise? Does it always remain a crossover, or do we encounter a real phase transition as the strength of eB increases further? Such questions will be addressed later in the chapter.
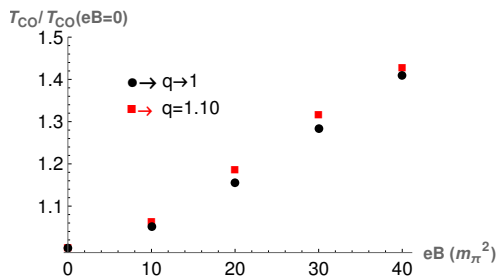
Figure 10.3: Our old understanding of the phase diagram before the recent discovery made by the lattice QCD [42].

10.2.2. Magnetic catalysis and inverse magnetic catalysis

In the presence of an external magnetic field another interesting feature arises along with the decreasing nature of the T_{CO}, which was previously not known. This particular feature concerns the behaviour of the chiral condensate in the presence of a magnetic field as shown in Fig. 10.4. This was a discovery again made by the lattice QCD calculation [288].
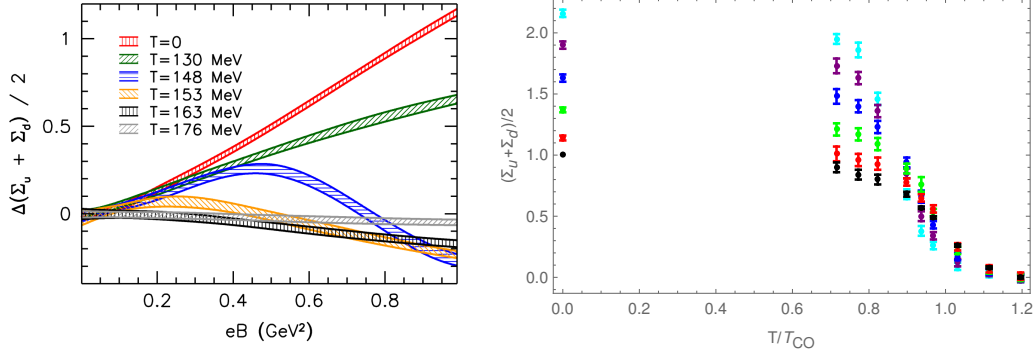
Figure 10.4: Left panel (adopted from Ref. [288]): change of the condensate as a function of eB for different values of the temperature. Right panel (drawn using the data from the Ref. [288]): condensate average as a function of scaled temperature for different values of eB.

In the Fig. 10.4, we observe an interesting behaviour of the condensate around the crossover temperature. In the left panel, which shows the change of the condensate, we notice the appearance of a hump like behaviour around the crossover temperature from a monotonous increase at zero and temperature below T_{CO}[23]. Such an observation is analogous to the left panel containing the temperature dependence of the condensate average. There we observe that around the T_{CO} the condensate average for the strongest value of eB attains the lowest strength. In other words, around T_{CO} increasing the strength of the external field decreases the strength of the condensate (in this case the average of the condensates). This feature is termed as inverse magnetic catalysis (IMC) effect[24], contrasting the behavior at low or zero temperature, where a stronger condensate is produced for a higher value of eB, a phenomenon known as magnetic catalysis (MC).

A typical plot of condensate featuring MC effect for all temperature range is shown in the Fig. 10.5. Before the discovery in 2012 [288], we only knew about MC which prevailed for all temperature range and confirmed by all possible theoretical studies including lattice QCD ones.
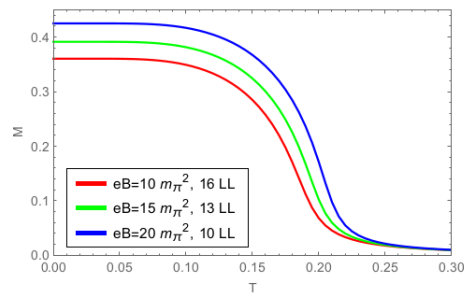
Figure 10.5: Effect of magnetic catalysis throughout the whole temperature range.

---

[23]It should be mentioned that, although it is not shown in the figure, there is again a monotonous increase in $\Delta\Sigma$ for $T \gtrsim 190\,\mathrm{MeV}$.

[24]The term "IMC" was first introduced in the context of a dense holographic QCD calculation [293]. There, it was termed the phenomenon of a decrease in the critical chemical potential for chiral symmetry restoration with increasing eB at zero or small temperature.

It is to be clearly stated here that the definition of (I)MC solely relies on the behaviour of the condensate in the presence of the magnetic field. The decreasing trend of T_{CO} accompanyin the decreasing in condensates (increasing T_{CO} with increase in the condensates) should not be used as a marker for IMC (MC) effects. Many existing literature, erroneously, use the characteristics of T_{CO} to decide on the (I)MC effects. However, one can devise scenarios "to disentangle" this to apparently interwoven phenomena, for example the chiral condensate increases with increasing magnetic field around the crossover region (a cursor for MC effect) but the T_{CO} still shows the decreasing trend [294–296]. We elaborate on this in the next section.

10.2.3. Impacts of pion mass on the features of QCD in the $T - eB$ plane

In the previous sections 10.2.1 and 10.2.2, we discussed some features of QCD and their revised versions. We discussed two different QCD phase diagrams in the $T - eB$ plane: older version (Fig. 10.3) and the revised version (Fig. 10.2). We also described the MC effect (Fig. 10.5) and the novel phenomenon of IMC (Fig. 10.4). All these novel features are discovered using lattice QCD, which also confirms the previous understanding initially estimated using effective QCD models.
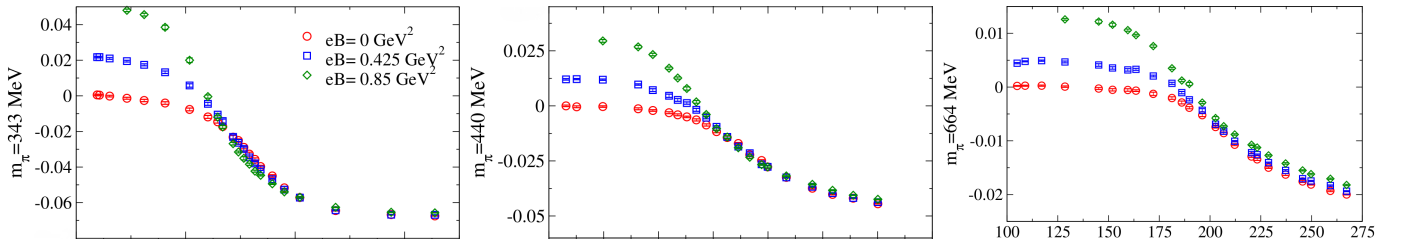
Figure 10.6: Effects of pion mass on the chiral condensate for three different values of them. The x-axis is for the temperature in MeV with the quoted values given in the right most panel. This figure is adopted from the Ref. [294].

Then, an important question is what really changed between the two lattice QCD calculations that led to a qualitatively different results. This question was first addressed in Ref. [294]. In Fig. 10.6, chiral condensate (y-axis) is ploted as a function of temperature (x-axis) for three different values of pion mass (m_π) for different strengths of the magnetic field. There, the inflection point of the condensate always moves to a lower temperature as we increase the magnetic field for all three pion masses. This feature is consistently captured using three different values of the magnetic field including the zero eB case. However, without explicitly calculating the inflection points, it is hard to be convinced just by looking at the curves that the crossover temperature is indeed decreasing. It should to be noted that a higher m_π signifies a higher current quark mass, m.
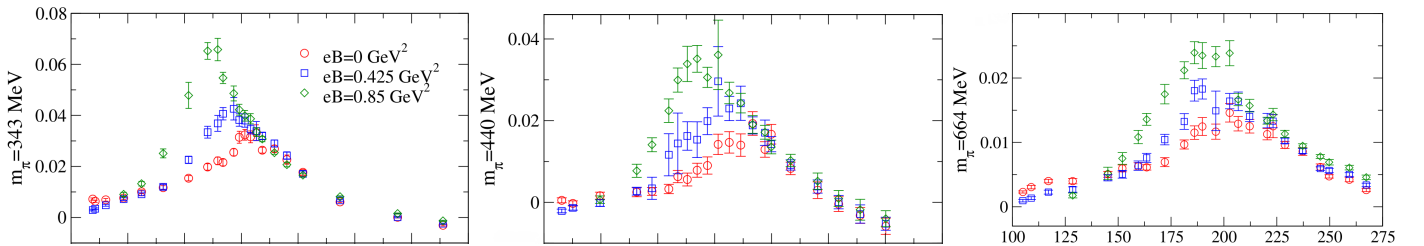
Figure 10.7: Chiral susceptibility for different values of the magnetic field at different pion masses. The x-axis represents the temperature with the values in MeV as given in the right most panel (adopted from Ref. [294]).

The same feature is captured by the plots of chiral susceptibility in Fig. 10.7, which is another quantity occasionally

utilised to signal the chiral transition. In this case, the decreasing trend of the crossover temperature is apparent. The exact estimation of the trend is shown in Fig. 10.8. There, three different types of symbols represent three different pion masses, with higher crossover temperatures corresponding to higher pion masses for a given value of eB.
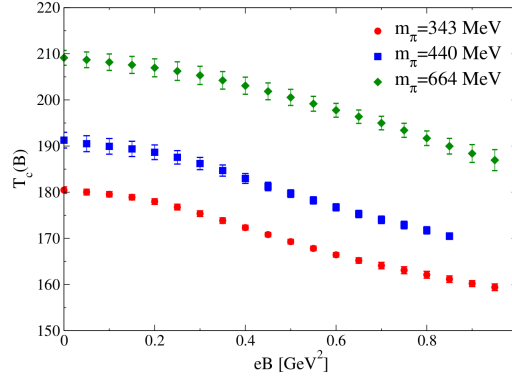

Figure 10.8: Phase diagram for different values of pion masses (adopted from Ref. [294]).

Then, it leads to the original question we asked: "Why could lattice QCD [292] not previously find such a phase diagram?" One major difference between Refs. [292] and [42] lies in their mass spectrum—the former incorporates unphysical pion mass values, whereas the latter uses physical ones. However, the discrepancy occured due to the discretisation effects and not due to the difference in the mass spectrum. This becomes evident from the exercise in the Ref. [297], where it is shown that the T_{CO} continues to be an increasing function of eB even for lighter than physical pion masses (quark masses).

Moving to the second important question of non-observation of IMC effect in earlier lattice QCD studies, the important observation from Fig. 10.6 is that the IMC effect present for the lowest value of m_π in (left panel) appears to diminish with increasing pion mass and certainly goes away at the highest value (right panel) of it. However, it cannot be stated with certainty on the status of the IMC effect for some values of m_π, for example, $m_\pi = 440\,\mathrm{MeV}$.
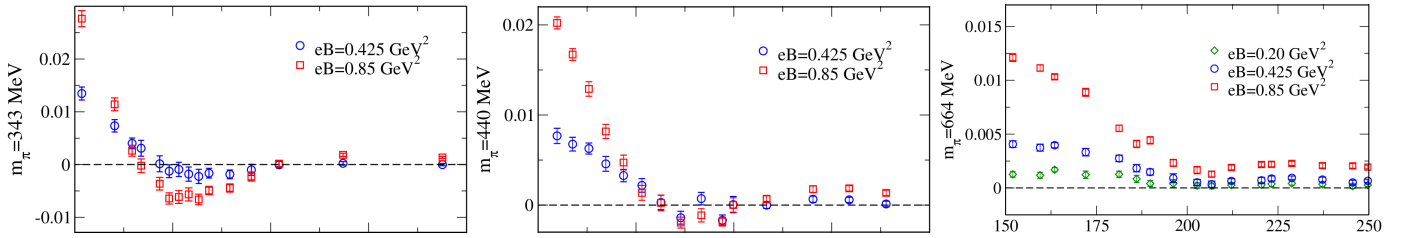
Figure 10.9: Impacts of the pion mass on the condensate difference at $B \neq 0$ and $B = 0$. The temperature is represented in the x-axis in MeV as given in the right most panel (adopted from Ref. [294]).

To be decisive about the elimination of IMC effect, difference between the condensate at $eB \neq 0$ and $eB = 0$ is plotted as a function of temperature in Fig. 10.9. There, the negative value of the condensate difference signifies the presence of the IMC effect. It is obvious that for $m_\pi = 343$ and $440\,\mathrm{MeV}$, the IMC effect appears around T_{CO}, whereas it is completely eliminated for $m_\pi = 664\,\mathrm{MeV}$. One can further estimate the m_π-value or for that matter the value of m beyond which the IMC effect disappears. This is calculated in Ref. [295] for a single value of the magnetic field, $eB = 0.6\,\mathrm{GeV}^2$. The pion mass value is found to be $497(4)\,\mathrm{MeV}$ which corresponds to the current quark mass equals to $14.07(55)\,\mathrm{MeV}$.

From the above discussion, it is obvious that the decreasing behaviour of T_{CO} and the IMC effect are not necessarily strictly connected. There exist scenarios, for example higher unphysical pion mass, for which the latter disappears

but the former persists. Thus, it is not proper to term the decreasing behaviour of T_{CO} as the IMC effect, which is occasionally used in the literature. Apart from the lexical issue, the discussion also raises the question whether the IMC effect is the driving force behind the decrease in T_{CO}. We can safely say that it is not strictly necessary, however it is difficult to say anything conclusive because of our poor knowledge on the connection between the chiral dynamics and the deconfiment dynamics. If some other phenomena, such as those related to the influence of the magnetic field on the confining properties, turn out to be the driving force behind the decreasing behaviour of T_{CO} the IMC effect would be a secondary phenomenon.

10.2.4. What happens when the magnetic field is increased further?

If one has a closer look at the right panel of Fig. 10.4 or at the Fig. 10.6 it is apparent that with the increase of the magnetic field the chiral crossover becomes sharper. Thus, it is intriguing to ask what happens if we increase the magnetic field further. From the two above-mentioned figures it seems that at some certain high enough value of the magnetic field the crossover turns into a real phase transition. In fact, such a question was previously indulged in Refs. [292] with some preliminary evidence for a first order phase transition. With a crossover ending on a first order phase transition, there arise a possibility of finding a critical point. This possibility was argued in Ref. [298] and later explored in details in Ref. [299], however for the deconfinement transition.
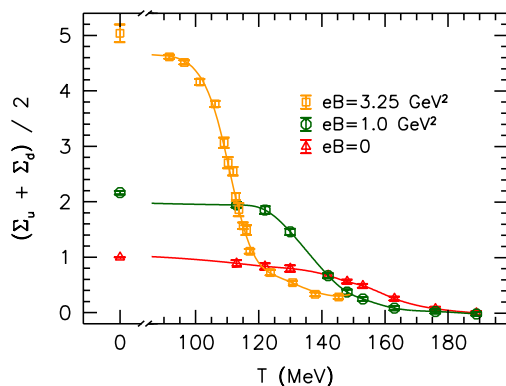
Figure 10.10: Condensate average as a function of temperature for three different values of the magnetic field. (taken from Ref. [299]).

Ref. [299], also looked into the chiral transition for higher magnetic field values than previously tested. The highest value that it explored is $3.25\,\mathrm{GeV}^2$, which is more than three times than previously examined [288]. The condensate average for such eB-values is displayed in Fig. 10.10. For the highest eB-value the crossover becomes much sharper, however it continues to be a crossover. This has been further analysed in the article [299] by looking at the peak width of the chiral susceptibility, which keeps on shrinking with increasing magnetic field.

In Ref. [300], the strongest magnetic field explored is almost three times the highest value in Ref. [299]. The authors tested two eB-values, 4 and 9 GeV^2 and calculated the sum of the light quark condensates divided by their values at $T = 0$, which is shown in Fig. 10.11. By comparing the two panels one notices a significant strengthening of the transition. At the larger value the transition seems to become first order with a large gap in the condensate. This is further examined in the same article [300] by looking at the strange quark number susceptibility. It has a jump for $eB = 9\,\mathrm{GeV}^2$ at the same temperature for which the condensate possesses a large gap suggesting a strong first order phase transition.
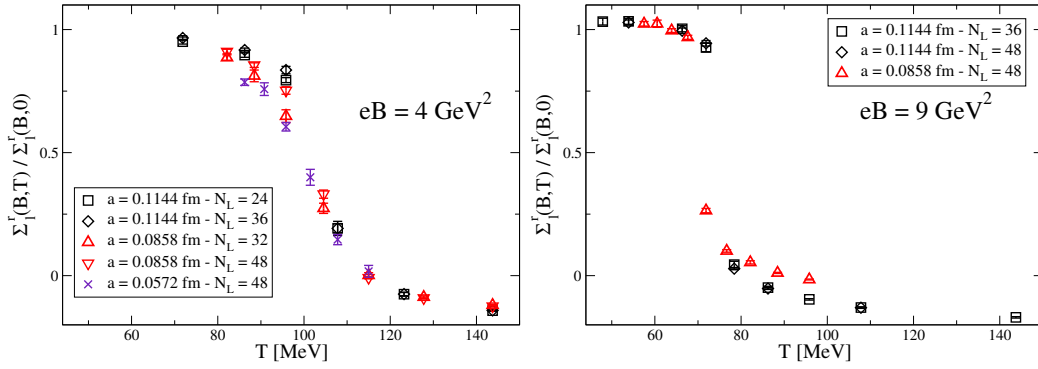
Figure 10.11: The sum of the light quark condensates is plotted for two eB-values at three different lattice spacings with different lattice sizes. (taken from Ref. [300]).

10.3. What we learnt from effective models?

In this section, we will look into the QCD matter in the $T - eB$ plane mostly from an effective model perspective. Our goal is to cover the major developments in the field. In the process, we will learn how effective model treatments of QCD matter under an external magnetic field enhance our understanding of the models' working principles. There are different effective model treatments of the subject matter: NJl model [291, 301–304], quark-meson model [305, 306], MIT bag model [307, 308], Polyakov loop extended models [309, 310] etc. Here, we will focus mainly on the NJL model. We will discuss results for both its local and nonlocals avatars.

We already described in the previous section that all our revised understanding of the magnetised QCD matter is primarily due to the lattice QCD. The novel features are not automatically captured within the regime of most of the effective model descriptions. However, some of them, when utilised appropriately, can capture the new features at least qualitatively.

10.3.1. Local NJL model

We have written down the basic Lagrangian for the NJL model in Eq. (10.1). It cosists of the quarks as the sole degrees of freedom and the gluons are integrated out. Depending on the construction of the current the model can be divided into two versions: local or nonlocal. First, we briefly discuss the working principle of local NJL model. However, we do not explicitly present any results, as this section is mainly intended to aid in understanding and appreciating the discussion on the nonlocal NJL model. A typical local four-point interaction arising from the interaction term in Eq. (10.1) is drawn in Fig. 10.12. As shown, in a local four point interaction, the four fermionic fields interact at the same spacetime point. Mathematically these models are characterised by the construction of the currents. A typical example of a local current

Figure 10.12: Local four point interaction.

is

$$j_a(x) = \bar{\psi}(x)\Gamma_a\psi(x), \tag{10.3}$$

where, Γ_a can assume different matrix form depending on the Dirac bilinears under consideration. The calculation in a local NJL model is simple yet qualitatively robust in numerous occasions. A major issue with such models is that they are non-renormalisable and require a regularisation scheme to have any meaningful results. There are multiple regularisation schemes, and the results can depend on the choice of regularisation, although they mostly remain qualitatively similar. However, this is not the case in the presence of an external magnetic field, and the results can even vary qualitatively from one scheme to another [311]. Among all the schemes, the three momentum cut-off is the most popular because of its simple working principle.

Before the novel findings by the lattice QCD [42, 288]: the decreasing T_{CO} with eB and the IMC effect, the NJL model including other models always found an increasing crossover temperature and MC effect. The new findings posed new challenges to an otherwise successful model. It turns out that the NJL model (at least the local version) cannot capture such novel features and needs to be tweaked.

These local models contain a coupling constant that remain constant for all ranges of the external parameters such as T, μ_B, eB etc. On the other hand, in QCD, the running of the coupling constant is an important feature for which the gluons play a crucial roles. As discussed at the end of the previos section, the gluons, through the sea quarks, play an important role for these newly found features. Thus, the model employed a trick and introduced a T and eB dependent coupling constant which enabled them to successfully reproduce the newly obtained features. There are two major examples—a) only an eB-dependent coupling constant [303] and b) the coupling constant depends both on T and eB [304]. The forms are as

$$G_S(\xi) = G_S^0 \frac{1 + a\xi^2 + b\xi^3}{1 + c\xi^2 + d\xi^4} \text{ and} \tag{10.4}$$

$$G_S(eB, T) = c(eB)\Big(1 - \frac{1}{1 + e^{\beta(eB)(T_a(eB)-T)}}\Big) + \gamma(eB), \tag{10.5}$$

respectively.

10.3.2. Nonlocal NJL model
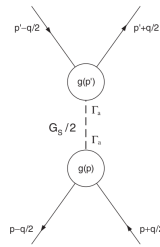
Figure 10.13: Nonlocal four point interaction.

On the other hand, when the interaction does not take place at the same spacetime point and is mediated through a form factor, it is termed as a nonlocal interaction as shown in Fig. 10.13. Using such a form factor Ref. [312] have been successfully reproduced the QCD phase diagram as given in Fig. 10.14. The grey band is the result from lattice QCD [42].

11. Summary and Outlook

In this review, we have introduced the key aspects of thermal field theory in the presence of a background magnetic field, focusing on its theoretical foundations and selected applications to the thermo-magnetic QCD plasma produced in
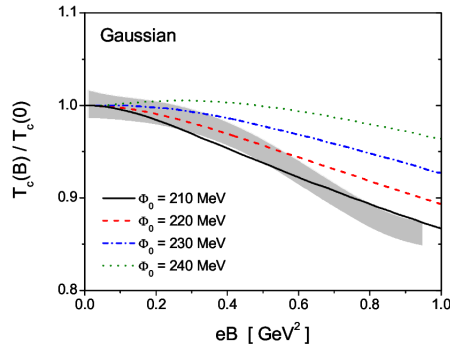
Figure 10.14: Phase diagram in nonlocal NJL model. The figure is taken from Ref. [312].

heavy-ion collisions. For brevity, our discussion has been confined to systems in thermal equilibrium. Specifically, we examined both bulk thermodynamic properties and real-time observables, exploring the dynamics of the thermo-magnetic QCD medium as it pertains to heavy-ion physics. We began by discussing the generation of magnetic fields in various contexts, including a single charge moving at constant velocity, heavy-ion collisions without medium formation, and those involving static and expanding media.

In Section 2, we examined how the Dirac equation and the energy levels of fermions are altered in the presence of a magnetic field. In Section 3, we analyzed the modifications to the free propagators of a charged scalar and a fermion in a background magnetic field. Additionally, we derived the free fermion propagator in both the strong and weak field approximations.

In section 4, we provided a concise overview of field theory in a thermal background, covering both the imaginary-time and real-time formalisms. We demonstrated how frequency summations in the imaginary-time formalism can be performed using contour integration and the Saclay method. Additionally, we discussed the connection between functional integration and the partition function. The modifications to the general structure of two-point functions in a thermal background were briefly outlined. We also addressed the subtleties that arise at finite temperature, including scale separations, and highlighted the limitations of bare perturbation theory at finite temperature with illustrative examples.

In Section 5, we developed the formalism of thermal field theory in the presence of a background magnetic field. We derived the most general structures of two-point functions, specifically the self-energy and propagator, for both fermions and gauge bosons in a thermo-magnetic medium. The need for strong and weak field approximations in calculating various physical quantities was then discussed, along with the scale hierarchies relevant in the weak field approximation. We further analyzed the dispersion relations and collective behaviour of quarks and gluons by examining their two-point functions in a thermo-magnetic QCD medium.

The collective excitations of quarks in this nontrivial background were analyzed for timelike momenta within the weak-field and HTL approximations, specifically in the domain $m_{th}^2(\sim g^2 T^2) < |q_f B| < T^2$. It was observed that the left- and right-handed modes, which are degenerate and symmetric in the absence of a magnetic field, become separated and asymmetric in its presence. We also studied how the effective propagator in a hot magnetized medium transforms under certain discrete symmetries and examined the implications of these transformations on the collective fermion modes in Landau levels. Additionally, we derived the Dirac spinors corresponding to various collective modes by solving the Dirac equation with the effective two-point function. The solutions of the propagator in the strong field approximation reveal four distinct modes. However, in the LLL approximation, only two modes are permitted: one corresponding to a positively charged fermion with spin up, and the other to a negatively charged fermion with spin down. In the LLL

approximation, the transverse momentum of the fermion vanishes, effectively reducing the dynamics of the system to two dimensions. We also note that the reflection symmetry is broken in the presence of a magnetic field.

Gluons are influenced by the presence of a magnetic field indirectly through the quark loop contribution to the gluon two-point functions. Using the effective two-point functions, we analyzed the collective behaviour of gluons in a hot magnetized medium. In the strong field approximation, three distinct modes emerge, which, in the limiting case of a propagation angle $\pi/2$, converge to the thermal modes or HTL modes. Similarly, in the weak field approximation, three distinct modes are observed: one magnetized plasmon and two transverse modes. In the zero magnetic field limit three disperson modes reduce two HTL mode in thermal medium containing plasmon and degenerate transverse mode. The corresponding results for photons can be directly derived from this calculation.

The Debye screening mass was obtained for an arbitrary magnetic field, and its reduction to the strong and weak field limits was demonstrated. We also discussed in detail the modifications to the QCD Debye mass, which depends on three scales: the thermal quark mass, the magnetic field scale, and the strong coupling constant. These modifications reflect the interplay between thermal effects and the external magnetic field, significantly altering the screening properties of the medium in different regimes. Additionally, we briefly discussed the role of strong coupling and various renormalization scales. Finally, we computed the quark-gluon three-point function and the two quark-two gluon four-point function.

In section 6 we developed a systematic framework based on the general structure of two-point functions for fermions and gauge bosons to compute the QCD free energy and pressure in complex environments, specifically considering both a heat bath and an external magnetic field simultaneously. This framework was applied to the scenario of a weakly and a strongly magnetized heat bath within the HTL approximation. The total pressure of the magnetized, hot, and dense deconfined QCD matter is composed of three contributions: (a) the quark contribution, (b) the gluonic contribution, and (c) the tree-level free energy from the constant magnetic field. The external magnetic field impacts the effective two-point functions (self-energy and propagator) of both fermions and gluons. While gluons are electrically neutral, they are significantly influenced by the magnetic field indirectly through quark loops, as the quark propagators are modified by the background magnetic field. Additionally, we incorporated a strong coupling constant that evolves with both the renormalization scale and the magnetic field strength. We analyzed the sensitivity of the pressure and other thermodynamic quantities to various scales, including the renormalization scale and magnetic field strength. The results exhibit a notable dependence on the renormalization scale, producing a band when its value is varied by a factor of two. The divergences encountered in free energy were addressed by redefining the magnetic field in the tree-level free energy term, introducing an HTL counterterm and $\overline{MS}$ renormalization scheme.

The weak field pressure is significantly influenced at low temperatures ($T < 0.8$ GeV), beyond which the HTL result becomes dominant. Through a high-temperature expansion, we obtained finite results that are entirely analytic and gauge-independent but exhibit dependence on the renormalization scale and magnetic field strength. These results were further validated by comparison with numerically evaluated full results, confirming the reliability and applicability of the high-temperature expansion approach. The sensitivity to the magnetic field is pronounced at low temperatures but becomes negligible at high temperatures.

In the strong field approximation, it is assumed that quarks are confined to the Lowest Landau Level. Within this framework, the hard and soft contributions to the quark-gluon free energy were calculated using the one-loop HTL approximation. The presence of a strong magnetic field imparts a paramagnetic nature to the hot QCD matter, resulting in anisotropy in the system. This anisotropy gives rise to different pressures in the directions parallel and perpendicular to

the magnetic field. By evaluating the system's magnetization, both the longitudinal pressure (aligned with the magnetic field) and the transverse pressure (orthogonal to the magnetic field) were derived in a fully analytic manner.

The derived free energy was utilized to compute key thermodynamic properties, including quark number susceptibility and chiral susceptibility. Additionally, the calculated pressure can contribute to magnetohydrodynamic models and provide insights into the elliptic flow behavior of hot and dense deconfined QCD matter generated in heavy-ion collisions. Additionally, we highlighted a general limitation of one-loop HTL perturbation theory, which introduces overcounting of certain contributions. To address this issue, extending the calculation to higher loop orders is necessary.

In section 7 we computed the soft contribution to the damping rate of a hard photon in a weakly magnetized QED medium, considering the momentum of one fermion in the loop as soft. In the presence of a weak magnetic field, the two degenerate transverse photon modes in a thermal medium are damped in a similar manner. The difference between the two transverse modes is minimal due to the weak field approximation. The soft contribution to the damping rate in the thermo-magnetic medium is found to be smaller than that in the purely thermal medium. When the magnetic field is turned off, the damping modes in the thermo-magnetic medium revert to their thermal counterparts. The influence of the magnetic field is most significant at low temperatures and low photon momenta. The damping rate for a hard photon in a QED medium with a soft contribution is found to be around 10^{-6} GeV. In a medium with a temperature of approximately 0.5 GeV and a background magnetic field of 0.005 GeV^2, this corresponds to a photon mean free path of just a few angstroms. However, when the analysis is applied to relativistic heavy-ion collisions, the photon's mean free path extends to several hundred femtometers. This significant difference confirms that photons, with their long mean free path compared to the fireball size, can act as reliable and direct probes of the medium created in such collisions. The damping rate is found to exhibit dependence on the separation scale Λ. To eliminate this dependence, the hard contribution must be combined with the soft contribution. The hard contribution to the photon damping rate arises at the two-loop level, involving hard particles in the loop with momenta comparable to or greater than the temperature. Calculating this contribution is a highly complex task and an open problem.

We also discussed a general expression for the fermion self-energy in a hot and strongly magnetized plasma using the Landau-level representation. At leading order, the one-loop self-energy is characterized by three velocity functions and two mass functions. The velocity functions consist of a spin-split pair of parallel components and a single perpendicular component. The two mass functions correspond to the spin-split states within each Landau level. As shown, all five functions exhibit a nontrivial dependence on the Landau-level index n and the longitudinal momentum p_z. The Landau-level-dependent fermion damping rates are calculated, using the imaginary parts of the self-energy functions. To achieve this, one employed two distinct methods. One approach utilized the general framework, which we adapted to accommodate the quantized nature of the Landau-level states in a hot plasma subjected to a magnetic field. This required modifying the method to correctly incorporate the quantum numbers associated with the Landau levels. As anticipated, the resulting damping rates are expressed in terms of the imaginary parts of the spin-averaged velocity and mass functions. The second approach to determine the damping rates involved identifying the poles of the full propagator. This method demonstrated that radiative corrections break the two-spin degeneracy of the Landau-level states. By calculating the imaginary parts of the particle energies, we derived the damping rates for the spin-split states, $\gamma_n^{(\pm)}(p_z)$. Interestingly, the spin-averaged damping rate, $\gamma_n^{(\mathrm{ave})} = (\gamma_n^{(+)} + \gamma_n^{(-)})/2$, was found to be identical to the result obtained using first method. Given the relatively small effect of spin splitting on the damping rates, the first method provides a reliable and efficient alternative for most practical purposes.

In section 8 we analyzed the electromagnetic spectral function by calculating the one-loop photon polarization tensor with quarks in the loop, focusing on the strong-field regime where the magnetic field dominates over the thermal scale. In this regime, the LLL behaves as an effectively $(1+1)$-dimensional system, creating a kinematic threshold determined by the quark mass. Once this threshold is exceeded, the photon begins to interact with the LLL. The spectral function starts with a high value due to the dimensional reduction but decreases with increasing photon energy, reflecting the dynamics of the LLL under a strong magnetic field. Additionally, we derived the dilepton production rates in this environment. For dileptons generated at the edge of the hot magnetized medium, where the magnetic field has no direct effect on the lepton pair, the rates are computed accordingly. In contrast, for dileptons produced inside the medium, where the magnetic field influences their dynamics, the production rate scales as $\mathcal{O}(|eB|^2)$. This scenario also introduces a kinematic threshold tied to the lepton mass, further modifying the production rate.

We have also computed the hard dilepton production rate from a weakly magnetized deconfined QCD medium using one-loop photon self-energy within HTL approximation, considering one hard quark and one thermomagnetic resummed quark propagator in the loop. With the presence of the magnetic field, the resummed propagator results in four quasi-particle modes. The production of a hard dilepton involves rates where each of the four quasiquarks, coming from the poles of the propagator, annihilates individually with a hard quark from a bare propagator in the loop. Alongside these, there are contributions from a mixture of pole and Landau cut parts. In the weak field approximation, the magnetic field acts as a perturbative correction to the thermal contribution. Due to the complexity of the calculation, we focused on obtaining the rate up to first order in the magnetic field, $\mathcal{O}(|eB|)$. This results in a minor enhancement compared to the rate in the absence of a magnetic field.

We have further examined the crucial quantity of lepton pair production from a hot and dense QCD medium in the presence of an arbitrary external magnetic field, considering both the parallel (along the direction of the external field) and perpendicular (transverse to the external field) components of the dilepton momentum. Unlike the scenario with no magnetic field (the so-called Born rate) or the rate approximated by the Lowest Landau Level, where only the annihilation process contributes, here we observe additional contributions from quark and antiquark decay processes. The results show a significant enhancement in lepton pair production due to the presence of an arbitrary magnetic field. We decompose the total rate into different physical processes and analyze their behaviours for both zero and nonzero baryon density conditions.

Section 9 focuses on the transport properties of heavy quarks (HQs) in a magnetized medium, specifically examining their momentum diffusion coefficients. These coefficients play a crucial role in the theoretical framework describing HQ dynamics, and their formulation must be appropriately modified in the presence of an external magnetic field. In this section, we discuss these modifications, which arise from the HQ scattering rate, primarily considering the dominant t-channel gluon exchange in $2 \leftrightarrow 2$ scatterings, where light quarks and gluons randomly impart momentum to HQs within the medium.

We have systematically outlined the necessary steps to compute the HQ scattering rate and, consequently, the momentum diffusion coefficients in the most general case, where the HQ possesses finite momentum and the external magnetic field can take any arbitrary value. A key aspect of our approach is the use of a resummed gluon propagator to evaluate the one-loop effective HQ self-energy, particularly in handling the soft contribution to the HQ scattering rate, i.e., when the exchanged gluon carries soft momentum ($\sim gT$). Notably, the hard scattering of HQs in a hot, magnetized medium remains unexplored in the existing literature but presents a promising direction for future investigations, as highlighted

Additionally, we have presented and analyzed the results of HQ momentum diffusion coefficients in an arbitrarily magnetized medium, considering both the static limit and the case of finite HQ momentum. In both scenarios, we observe a similar dependence on eB: the diffusion coefficients increase sharply at lower values of eB but tend to saturate at higher eB (more significantly for charm quarks). However, a contrasting trend emerges when the HQ moves perpendicular to the external magnetic field, where increasing eB leads to more pronounced changes in the momentum diffusion coefficients. In the static limit, the longitudinal diffusion coefficient – driven by soft gluon scattering, which dominates the t-channel at leading order in strong coupling – exceeds the transverse diffusion coefficient. This behavior reverses when moving beyond the static limit. Our results effectively capture the interplay between various physical scales, including the heavy quark mass (M), momentum (p), magnetic field strength (eB), and temperature (T).

In section 10, we reviewed some of the novel features of QCD that have been recently observed in the presence of an external magnetic field particularly in the $T - eB$ plane. All such new phenomena have been discovered primarily by lattice QCD, a first principle numerical technique. We focus on two important phenomena—the decreasing nature of the chiral crossover temperature ($T_{\rm CO}$) as a function of eB and the decrease of the chiral condensate with the increase of eB around the crossover region, termed as the inverse magnetic catalysis (IMC) effect. We reviewed the topics by drawing a comparison with our previous understanding of the subject matter. We knew of a $T_{\rm CO}$ that increases and a chiral condensate that strengthens with the increase of eB. The latter is known as the magnetic catalysis (MC).

The increasing $T_{\rm CO}$ and the MC effect were first discussed in effective QCD model calculations. Later, the same properties were also found in lattice QCD calculation. However, in 2011 – 2012, with further improvements in lattice QCD calculations (such as improved discretisation and calculations at the physical pion mass, made feasible by better numerical techniques and cost-effective, powerful machines), novel features were discovered. We retraced back the development and discussed the reason of such discrepancies in lattice QCD calculations. The unimproved lattice discretisation caused $T_{\rm CO}$ to increase with eB, but with improved lattice discretisation, it later exhibited the decreasing trend.

On the other hand, the value of the pion mass or the current quark mass is found to be responsible for (non)observation of the IMC effect. The IMC effect is observed for physical pion mass (quark mass) and with the increase of the pion mass it starts diminishing and at a certain value it is eliminated. Lattice QCD estimated this value to be $497(4)\,{\rm MeV}$ which corresponds to the current quark mass equals to $14.07(55)\,{\rm MeV}$. However, with increasing pion mass the decreasing behaviour of $T_{\rm CO}$ sustains, providing a strong hint that the decreasing $T_{\rm CO}$ and the IMC effect need not be strictly connected. It answers the question of whether the IMC effect is the driving force behind the decrease in $T_{\rm CO}$. We can safely say that it is not strictly necessary, however it is difficult to say anything conclusive because of our poor knowledge on the connection between the chiral dynamics and the deconfiment dynamics. We concluded this part by discussing the nature of the chiral phase transition for extremely high magnetic field. Lattice QCD has provided strong evidence that the crossover turns into a first order phase transition. This happens between the eB-values of 4 and 9 GeV^2. Thus, there is strong possibility of finding a critical point in the $T - eB$ plane.

Acknowledgements

A. Appendix

Solution of the Modified Dirac equation at Lowest Landau Level (LLL)

At LLL, $l \to 0 \Rightarrow p_\perp = 0$ and the effective Dirac equation becomes

$$\left(\mathcal{P}_+ \not{L} + \mathcal{P}_- \not{R}\right) U = 0$$

$$\begin{pmatrix} 0 & R_0 - \sigma^3 R_z \\ L_0 + \sigma^3 L_z & 0 \end{pmatrix} U = 0, \tag{A.1}$$

where $U = \begin{pmatrix} \psi_L \\ \psi_R \end{pmatrix}$ with $\psi_{L(R)}$ are 2×1 blocks. Now, the condition for the non-trivial solution to exist is given as

$$\det \begin{pmatrix} 0 & R_0 - \sigma^3 R_z \\ L_0 + \sigma^3 L_z & 0 \end{pmatrix} = 0$$

$$\left[(R_0)^2 - (R_z)^2\right]\left[(L_0)^2 - (L_z)^2\right] = 0$$

$$\text{or, } R_0 = \pm R_z, \ L_0 = \pm L_z, \tag{A.2}$$

- Case-I: For $R_0 = R_z$ one can write (A.1) as

$$\begin{pmatrix} 0 & 0 & 0 & 0 \\ 0 & 0 & 0 & 2R_z \\ L_0 + L_z & 0 & 0 & 0 \\ 0 & L_0 - L_z & 0 & 0 \end{pmatrix} \cdot \begin{pmatrix} \psi_L^{(1)} \\ \psi_L^{(2)} \\ \psi_R^{(1)} \\ \psi_R^{(2)} \end{pmatrix} = 0, \tag{A.3}$$

which leads to the following conditions:

$$2R_z \, \psi_R^{(2)} = 0,$$

$$(L_0 + L_z) \, \psi_L^{(1)} = 0,$$

$$(L_0 - L_z) \, \psi_L^{(2)} = 0,$$

$$\psi_R^{(1)} = \text{Arbitrary.} \tag{A.4}$$

For normalisation, we choose only non-zero component, $psi_R^{(1)} = 1$ which leads to

$$U_R^{(+)} = \begin{pmatrix} 0 \\ 0 \\ 1 \\ 0 \end{pmatrix}. \tag{A.5}$$

Now, for $R_0 = -R_z$, similarly one can obtain as

$$U_R^{(-)} = \begin{pmatrix} 0 \\ 0 \\ 0 \\ 1 \end{pmatrix} . \tag{A.6}$$

- Case-II: For $L_0 = L_z$, one gets

$$U_L^{(+)} = \begin{pmatrix} 0 \\ 1 \\ 0 \\ 0 \end{pmatrix} , \tag{A.7}$$

whereas for $L_0 = -L_z$, one finds

$$U_L^{(-)} = \begin{pmatrix} 1 \\ 0 \\ 0 \\ 0 \end{pmatrix} . \tag{A.8}$$

B. Appendix

Analytical Solution of the Dispersion Relations and the Effective Mass in LLL

The dispersion relations at LLL can be written from the equations (5.21a) and (5.21b) as

$$L_{LLL}^2 = (\mathcal{A}p_0 + \mathcal{B}_+)^2 - (\mathcal{A}p_z + c')^2 = L_0^2 - L_z^2 = 0 \,, \tag{B.1a}$$

$$R_{LLL}^2 = (\mathcal{A}p_0 + \mathcal{B}_-)^2 - (\mathcal{A}p_z - c')^2 = R_0^2 - R_z^2 = 0 \,, \tag{B.1b}$$

each of which leads to two modes, respectively, as

$$L_0 = \pm L_z$$
$$\mathcal{A}p_0 + \mathcal{B}_+ = \pm (\mathcal{A}p_z + c') \,, \tag{B.2a}$$

and

$$R_0 = \pm R_z$$
$$\mathcal{A}p_0 + \mathcal{B}_- = \pm (\mathcal{A}p_z - c') \,. \tag{B.3a}$$

Below we try to get approximate analytical solution of these equations at small and high p_z limits.

B.1. Low p_z limit

In the low p_z region, one needs to expand $a(p_0, |p_z|)$, $b(p_0, |p_z|)$, $b'(p_0, 0, p_z)$ and $c'(p_0, |p_z|)$ defined in (5.61a), (5.61b), (5.70a) and (5.70b), respectively, which depend on Legendre function of second kind $Q_0(x)$ and $Q_1(x)$ as given in equations (5.62a) and (5.62b), respectively. The Legendre function Q_0 and structure coefficients are expanded in powers of $\dfrac{|p_z|}{p_0}$ as

$$Q_0 \left(\frac{p_0}{|p_z|} \right) = \frac{|p_z|}{p_0} + \frac{1}{3} \frac{|p_z|^3}{p_0^3} + \frac{1}{5} \frac{|p_z|^5}{p_0^5} + \cdots \tag{B.4a}$$

$$a(p_0, |p_z|) = -\frac{m_{th}^2}{p_0^2} \left(\frac{1}{3} + \frac{1}{5} \frac{|p_z|^2}{p_0^2} + \cdots \right) , \tag{B.4b}$$

$$b(p_0, |p_z|) = -2 \frac{m_{th}^2}{p_0} \left(\frac{1}{3} + \frac{1}{15} \frac{|p_z|^2}{p_0^2} + \cdots \right) , \tag{B.4c}$$

165

$$b'(p_0, 0, p_z) = 4\,g^2\,C_F\,M^2(T, m, qB)\,p_z\left(\frac{1}{3\,p_0^2} + \frac{|p_z|^2}{5\,p_0^4} + \cdots\right), \tag{B.4d}$$

$$c'(p_0, |p_z|) = 4\,g^2\,C_F\,M^2(T, m, qB)\left(\frac{1}{p_0} + \frac{|p_z|^2}{p_0^3} + \cdots\right). \tag{B.4e}$$

Now retaining the terms that are *upto the order of p_z* in (B.4b), (B.4c), (B.4d), (B.4e), we obtain the following expressions for the dispersion relation of various modes:

1. $L_0 = L_z$ leads to a mode $L^{(+)}$ as

$$\omega_{L^{(+)}}(p_z) = m_{LLL}^{*+} + \frac{1}{3}\,p_z. \tag{B.5}$$

2. $L_0 = -L_z$ leads to a mode $L^{(-)}$ as

$$\omega_{L^{(-)}}(p_z) = m_{LLL}^{*-} - \frac{1}{3}\,p_z. \tag{B.6}$$

3. $R_0 = R_z$ leads to a mode $R^{(+)}$ as

$$\omega_{R^{(+)}}(p_z) = m_{LLL}^{*-} + \frac{1}{3}\,p_z. \tag{B.7}$$

4. $R_0 = -R_z$ leads to a mode $R^{(-)}$ as

$$\omega_{R^{(-)}}(p_z) = m_{LLL}^{*+} - \frac{1}{3}\,p_z. \tag{B.8}$$

where the effective masses of various modes are given as

$$m_{LLL}^{*\pm} = \begin{cases} \sqrt{m_{th}^2 + 4g^2 C_F M^2(T, M, q_f B)}, & \text{for} \quad L^{(+)}\ \&\ R^{(-)}, \\ \\ \sqrt{m_{th}^2 - 4g^2 C_F M^2(T, M, q_f B)}, & \text{for} \quad R^{(+)}\ \&\ L^{(-)}. \end{cases} \tag{B.9}$$

B.2. High p_z limit

We note that p_z can be written as

$$p_z = \begin{cases} |p_z|, & \text{for } p_z > 0 \\ -|p_z|. & \text{for } p_z < 0 \end{cases}$$

In high p_z limit, we obtain

(i)

$$[1 + a(p_0, |p_z|)]\,(p_0 - p_z) + b(p_0, |p_z|) = \begin{cases} p_0 - |p_z| - \frac{m_{th}^2}{|p_z|}, & \text{for } p_z > 0 \\ 2\,|p_z| + \frac{m_{th}^2}{|p_z|} - \frac{m_{th}^2}{|p_z|}\,\ln\left(\frac{2\,|p_z|}{p_0 - |p_z|}\right), & \text{for } p_z < 0 \end{cases} \tag{B.10}$$

(ii)

$$[1 + a(p_0, |p_z|)]\,(p_0 + p_z) + b(p_0, |p_z|) = \begin{cases} 2\,|p_z| + \frac{m_{th}^2}{|p_z|} - \frac{m_{th}^2}{|p_z|}\,\ln\left(\frac{2\,|p_z|}{p_0 - |p_z|}\right), & \text{for } p_z > 0 \\ p_0 - |p_z| - \frac{m_{th}^2}{|p_z|}, & \text{for } p_z < 0 \end{cases} \tag{B.11}$$

(iii)

$$b'(p_0, 0, p_z) + c'(p_0, |p_z|) = \begin{cases} \frac{4g^2 C_F M^2}{|p_z|}\,\ln\left(\frac{2|p_z|}{p_0 - |p_z|}\right) - \frac{4g^2 C_F M^2}{|p_z|}, & \text{for } p_z > 0 \\ \frac{4g^2 C_F M^2}{|p_z|} & \text{for } p_z < 0 \end{cases} \tag{B.12}$$

(iv)

$$b'(p_0, 0, p_z) - c'(p_0, |p_z|) = \begin{cases} -\frac{4g^2 C_F M^2}{|p_z|} & \text{for } p_z > 0 \\ -\frac{4g^2 C_F M^2}{|p_z|}\,\ln\left(\frac{2|p_z|}{p_0 - |p_z|}\right) + \frac{4g^2 C_F M^2}{|p_z|}. & \text{for } p_z < 0 \end{cases} \tag{B.13}$$

1. $L_0 = L_z$ leads to a mode $L^{(+)}$:

   For $p_z > 0$,

   $$\omega_{L^{(+)}}(p_z) = |p_z| + \frac{(m^{*+}_{LLL})^2}{|p_z|}. \tag{B.14}$$

   For $p_z < 0$,

   $$\omega_{L^{(+)}}(p_z) = |p_z| + \frac{2\,|p_z|}{e}\,\exp\left(-\frac{2\,p_z^2}{(m^{*+}_{LLL})^2}\right). \tag{B.15}$$

2. $L_0 = -L_z$ leads to a mode $L^{(-)}$:

   For $p_z > 0$,

   $$\omega_{L^{(-)}}(p_z) = |p_z| + \frac{2\,|p_z|}{e}\,\exp\left(-\frac{2\,p_z^2}{(m^{*-}_{LLL})^2}\right). \tag{B.16}$$

   For $p_z < 0$,

   $$\omega_{L^{(-)}}(p_z) = |p_z| + \frac{(m^{*-}_{LLL})^2}{|p_z|}. \tag{B.17}$$

3. $R_0 = R_z$ leads to a mode $R^{(+)}$:

   For $p_z > 0$,

   $$\omega_{R^{(+)}}(p_z) = |p_z| + \frac{(m^{*-}_{LLL})^2}{|p_z|}. \tag{B.18}$$

   For $p_z < 0$,

   $$\omega_{R^{(+)}}(p_z) = |p_z| + \frac{2\,|p_z|}{e}\,\exp\left(-\frac{2\,p_z^2}{(m^{*-}_{LLL})^2}\right). \tag{B.19}$$

4. $R_0 = -R_z$ leads to a mode $R^{(-)}$:

   For $p_z > 0$,

   $$\omega_{R^{(-)}}(p_z) = |p_z| + \frac{2\,|p_z|}{e}\,\exp\left(-\frac{2\,p_z^2}{(m^{*+}_{LLL})^2}\right). \tag{B.20}$$

   For $p_z < 0$,

   $$\omega_{R^{(-)}}(p_z) = |p_z| + \frac{(m^{*+}_{LLL})^2}{|p_z|}. \tag{B.21}$$

Note that In the high momentum limit the above dispersion relations are given in terms of absolute values of p_z, i.e. $|p_z|$.

We further note that the above dispersion relations in the absence of the magnetic field reduce to HTL results, where left and right handed are degenerate.

References

[1] V. P. Gusynin, V. A. Miransky, I. A. Shovkovy, Dimensional reduction and catalysis of dynamical symmetry breaking by a magnetic field, Nucl. Phys. B 462 (1996) 249–290. arXiv:hep-ph/9509320, doi:10.1016/0550-3213(96)00021-1.

[2] I. A. Shovkovy, Magnetic Catalysis: A Review, Lect. Notes Phys. 871 (2013) 13–49. arXiv:1207.5081, doi:10.1007/978-3-642-37305-3_2.

[3] M. D'Elia, Lattice QCD Simulations in External Background Fields, Lect. Notes Phys. 871 (2013) 181–208. arXiv:1209.0374, doi:10.1007/978-3-642-37305-3_7.

[4] K. Fukushima, Views of the Chiral Magnetic Effect, Lect. Notes Phys. 871 (2013) 241–259. arXiv:1209.5064, doi:10.1007/978-3-642-37305-3_9.

[5] G. Basar, G. V. Dunne, The Chiral Magnetic Effect and Axial Anomalies, Lect. Notes Phys. 871 (2013) 261–294. arXiv:1207.4199, doi:10.1007/978-3-642-37305-3_10.

[6] M. N. Chernodub, Electromagnetic superconductivity of vacuum induced by strong magnetic field, Lect. Notes Phys. 871 (2013) 143–180. `arXiv:1208.5025`, `doi:10.1007/978-3-642-37305-3_6`.

[7] E. S. Fraga, Thermal chiral and deconfining transitions in the presence of a magnetic background, Lect. Notes Phys. 871 (2013) 121–141. `arXiv:1208.0917`, `doi:10.1007/978-3-642-37305-3_5`.

[8] F. Preis, A. Rebhan, A. Schmitt, Inverse magnetic catalysis in field theory and gauge-gravity duality, Lect. Notes Phys. 871 (2013) 51–86. `arXiv:1208.0536`, `doi:10.1007/978-3-642-37305-3_3`.

[9] R. L. S. Farias, K. P. Gomes, G. I. Krein, M. B. Pinto, Importance of asymptotic freedom for the pseudocritical temperature in magnetized quark matter, Phys. Rev. C 90 (2) (2014) 025203. `arXiv:1404.3931`, `doi:10.1103/PhysRevC.90.025203`.

[10] N. Mueller, J. A. Bonnet, C. S. Fischer, Dynamical quark mass generation in a strong external magnetic field, Phys. Rev. D 89 (9) (2014) 094023. `arXiv:1401.1647`, `doi:10.1103/PhysRevD.89.094023`.

[11] J. O. Andersen, W. R. Naylor, A. Tranberg, Phase diagram of QCD in a magnetic field: A review, Rev. Mod. Phys. 88 (2016) 025001. `arXiv:1411.7176`, `doi:10.1103/RevModPhys.88.025001`.

[12] V. A. Miransky, I. A. Shovkovy, Quantum field theory in a magnetic field: From quantum chromodynamics to graphene and Dirac semimetals, Phys. Rept. 576 (2015) 1–209. `arXiv:1503.00732`, `doi:10.1016/j.physrep.2015.02.003`.

[13] G. Endrodi, QCD with background electromagnetic fields on the lattice: A review, Prog. Part. Nucl. Phys. 141 (2025) 104153. `arXiv:2406.19780`, `doi:10.1016/j.ppnp.2024.104153`.

[14] P. Adhikari, et al., Strongly interacting matter in extreme magnetic fields (12 2024). `arXiv:2412.18632`.

[15] K. Tuchin, Particle production in strong electromagnetic fields in relativistic heavy-ion collisions, Adv. High Energy Phys. 2013 (2013) 490495. `arXiv:1301.0099`, `doi:10.1155/2013/490495`.

[16] K. Tuchin, Electromagnetic radiation by quark-gluon plasma in a magnetic field, Phys. Rev. C 87 (2) (2013) 024912. `arXiv:1206.0485`, `doi:10.1103/PhysRevC.87.024912`.

[17] K. Tuchin, Magnetic contribution to dilepton production in heavy-ion collisions, Phys. Rev. C 88 (2013) 024910. `arXiv:1305.0545`, `doi:10.1103/PhysRevC.88.024910`.

[18] M. I. D. e. a. B. A. Boyko, A. I. Bykov, With record magnetic fields to the 21st century, in Proceedings of the 12th IEEE International Pulsed Power Conference, 1999, pp. 746–749.

[19] C. Kouveliotou, R. C. Duncan, C. Thompson, Magnetars, Sci. Am. 288N2 (2003) 24–31.

[20] V. de la Incera, Nonperturbative Physics in a Magnetic Field, AIP Conf. Proc. 1361 (2011) 74–82. `arXiv:1004.4931`, `doi:10.1063/1.3622687`.

[21] D. Bandyopadhyay, S. Chakrabarty, S. Pal, The Quantizing magnetic field and quark - hadron phase transition in a neutron star, Phys. Rev. Lett. 79 (1997) 2176–2179. `arXiv:astro-ph/9703066`, `doi:10.1103/PhysRevLett.79.2176`.

[22] S. Chakrabarty, D. Bandyopadhyay, S. Pal, Dense nuclear matter in a strong magnetic field, Phys. Rev. Lett. 78 (1997) 2898–2901. `arXiv:astro-ph/9703034`, `doi:10.1103/PhysRevLett.78.2898`.

[23] A. Bandyopadhyay, Non-perturbative study of spectral function and its application in Quark Gluon Plasma, Ph.D. thesis, Saha Inst. (2017). `arXiv:1710.06226`.

[24] D. E. Kharzeev, L. D. McLerran, H. J. Warringa, The Effects of topological charge change in heavy ion collisions:

'Event by event P and CP violation', Nucl. Phys. A 803 (2008) 227–253. `arXiv:0711.0950`, `doi:10.1016/j.nuclphysa.2008.02.298`.

[25] K. Fukushima, D. E. Kharzeev, H. J. Warringa, The Chiral Magnetic Effect, Phys. Rev. D 78 (2008) 074033. `arXiv:0808.3382`, `doi:10.1103/PhysRevD.78.074033`.

[26] J. D. Jackson, Classical Electrodynamics (3rd Edison), Wiley, Singapore Press Ltd., 2007.

[27] J. Ambjorn, P. Olesen, W condensate formation in high-energy collisions, Phys. Lett. B 257 (1991) 201–206. `doi:10.1016/0370-2693(91)90882-Q`.

[28] A. Bzdak, V. Skokov, Event-by-event fluctuations of magnetic and electric fields in heavy ion collisions, Phys. Lett. B 710 (2012) 171–174. `arXiv:1111.1949`, `doi:10.1016/j.physletb.2012.02.065`.

[29] V. Skokov, A. Y. Illarionov, V. Toneev, Estimate of the magnetic field strength in heavy-ion collisions, Int. J. Mod. Phys. A 24 (2009) 5925–5932. `arXiv:0907.1396`, `doi:10.1142/S0217751X09047570`.

[30] V. Voronyuk, V. D. Toneev, W. Cassing, E. L. Bratkovskaya, V. P. Konchakovski, S. A. Voloshin, (Electro-)Magnetic field evolution in relativistic heavy-ion collisions, Phys. Rev. C 83 (2011) 054911. `arXiv:1103.4239`, `doi:10.1103/PhysRevC.83.054911`.

[31] W.-T. Deng, X.-G. Huang, Event-by-event generation of electromagnetic fields in heavy-ion collisions, Phys. Rev. C 85 (2012) 044907. `arXiv:1201.5108`, `doi:10.1103/PhysRevC.85.044907`.

[32] H.-T. Ding, A. Francis, O. Kaczmarek, F. Karsch, E. Laermann, et al., Thermal dilepton rate and electrical conductivity: An analysis of vector current correlation functions in quenched lattice QCD, Phys. Rev. D83 (2011) 034504. `arXiv:1012.4963`, `doi:10.1103/PhysRevD.83.034504`.

[33] G. Aarts, C. Allton, J. Foley, S. Hands, S. Kim, Spectral functions at small energies and the electrical conductivity in hot, quenched lattice QCD, Phys. Rev. Lett. 99 (2007) 022002. `arXiv:hep-lat/0703008`, `doi:10.1103/PhysRevLett.99.022002`.

[34] S. Gupta, Analyticity and the phase diagram of QCD, Phys. Lett. B 588 (2004) 136–144. `arXiv:hep-lat/0307007`, `doi:10.1016/j.physletb.2004.03.018`.

[35] J. D. Bjorken, Highly Relativistic Nucleus-Nucleus Collisions: The Central Rapidity Region, Phys. Rev. D 27 (1983) 140–151. `doi:10.1103/PhysRevD.27.140`.

[36] D. E. Kharzeev, Topologically induced local P and CP violation in QCD x QED, Annals Phys. 325 (2010) 205–218. `arXiv:0911.3715`, `doi:10.1016/j.aop.2009.11.002`.

[37] J. Alexandre, K. Farakos, G. Koutsoumbas, Magnetic catalysis in QED(3) at finite temperature: Beyond the constant mass approximation, Phys. Rev. D 63 (2001) 065015. `arXiv:hep-th/0010211`, `doi:10.1103/PhysRevD.63.065015`.

[38] V. P. Gusynin, I. A. Shovkovy, Chiral symmetry breaking in QED in a magnetic field at finite temperature, Phys. Rev. D 56 (1997) 5251–5253. `arXiv:hep-ph/9704394`, `doi:10.1103/PhysRevD.56.5251`.

[39] V. P. Gusynin, D. K. Hong, I. A. Shovkovy, Chiral symmetry breaking by a nonAbelian external field in (2+1)-dimensions, Phys. Rev. D 57 (1998) 5230–5235. `arXiv:hep-th/9711016`, `doi:10.1103/PhysRevD.57.5230`.

[40] D. S. Lee, C. N. Leung, Y. J. Ng, Chiral symmetry breaking in a uniform external magnetic field, Phys. Rev. D 55 (1997) 6504–6513. `arXiv:hep-th/9701172`, `doi:10.1103/PhysRevD.55.6504`.

[41] R. Ghosh, M. Y. Jamal, M. Kurian, Impact of the chiral asymmetry and a magnetic field on the passage of

an energetic test parton in a QCD medium, Phys. Rev. D 108 (5) (2023) 054035. `arXiv:2306.10247`, `doi:10.1103/PhysRevD.108.054035`.

[42] G. S. Bali, F. Bruckmann, G. Endrodi, Z. Fodor, S. D. Katz, S. Krieg, A. Schafer, K. K. Szabo, The QCD phase diagram for external magnetic fields, JHEP 02 (2012) 044. `arXiv:1111.4956`, `doi:10.1007/JHEP02(2012)044`.

[43] V. G. Bornyakov, P. V. Buividovich, N. Cundy, O. A. Kochetkov, A. Schäfer, Deconfinement transition in two-flavor lattice QCD with dynamical overlap fermions in an external magnetic field, Phys. Rev. D 90 (3) (2014) 034501. `arXiv:1312.5628`, `doi:10.1103/PhysRevD.90.034501`.

[44] N. Mueller, J. M. Pawlowski, Magnetic catalysis and inverse magnetic catalysis in QCD, Phys. Rev. D 91 (11) (2015) 116010. `arXiv:1502.08011`, `doi:10.1103/PhysRevD.91.116010`.

[45] A. Ayala, M. Loewe, A. J. Mizher, R. Zamora, Inverse magnetic catalysis for the chiral transition induced by thermo-magnetic effects on the coupling constant, Phys. Rev. D 90 (3) (2014) 036001. `arXiv:1406.3885`, `doi:10.1103/PhysRevD.90.036001`.

[46] A. Ayala, M. Loewe, R. Zamora, Inverse magnetic catalysis in the linear sigma model with quarks, Phys. Rev. D 91 (1) (2015) 016002. `arXiv:1406.7408`, `doi:10.1103/PhysRevD.91.016002`.

[47] A. Ayala, M. Loewe, R. Zamora, Inverse magnetic catalysis in the linear sigma model, J. Phys. Conf. Ser. 720 (1) (2016) 012026. `doi:10.1088/1742-6596/720/1/012026`.

[48] A. Ayala, C. A. Dominguez, L. A. Hernandez, M. Loewe, R. Zamora, Inverse magnetic catalysis from the properties of the QCD coupling in a magnetic field, Phys. Lett. B 759 (2016) 99–103. `arXiv:1510.09134`, `doi:10.1016/j.physletb.2016.05.058`.

[49] A. Bandyopadhyay, R. L. S. Farias, Inverse magnetic catalysis: how much do we know about?, Eur. Phys. J. ST 230 (3) (2021) 719–728. `arXiv:2003.11054`, `doi:10.1140/epjs/s11734-021-00023-1`.

[50] S. Fayazbakhsh, N. Sadooghi, Phase diagram of hot magnetized two-flavor color superconducting quark matter, Phys. Rev. D 83 (2011) 025026. `arXiv:1009.6125`, `doi:10.1103/PhysRevD.83.025026`.

[51] S. Fayazbakhsh, N. Sadooghi, Color neutral 2SC phase of cold and dense quark matter in the presence of constant magnetic fields, Phys. Rev. D 82 (2010) 045010. `arXiv:1005.5022`, `doi:10.1103/PhysRevD.82.045010`.

[52] J. O. Andersen, W. R. Naylor, A. Tranberg, Chiral and deconfinement transitions in a magnetic background using the functional renormalization group with the Polyakov loop, JHEP 04 (2014) 187. `arXiv:1311.2093`, `doi:10.1007/JHEP04(2014)187`.

[53] M. Strickland, V. Dexheimer, D. P. Menezes, Bulk Properties of a Fermi Gas in a Magnetic Field, Phys. Rev. D 86 (2012) 125032. `arXiv:1209.3276`, `doi:10.1103/PhysRevD.86.125032`.

[54] A. Bandyopadhyay, B. Karmakar, N. Haque, M. G. Mustafa, Pressure of a weakly magnetized hot and dense deconfined QCD matter in one-loop hard-thermal-loop perturbation theory, Phys. Rev. D 100 (3) (2019) 034031. `arXiv:1702.02875`, `doi:10.1103/PhysRevD.100.034031`.

[55] B. Karmakar, R. Ghosh, A. Bandyopadhyay, N. Haque, M. G. Mustafa, Anisotropic pressure of deconfined QCD matter in presence of strong magnetic field within one-loop approximation, Phys. Rev. D 99 (9) (2019) 094002. `arXiv:1902.02607`, `doi:10.1103/PhysRevD.99.094002`.

[56] B. Karmakar, N. Haque, M. G. Mustafa, Second-order quark number susceptibility of deconfined QCD matter in the presence of a magnetic field, Phys. Rev. D 102 (5) (2020) 054004. `arXiv:2003.11247`, `doi:10.1103/PhysRevD.102.054004`.

[57] R. Ghosh, B. Karmakar, M. Golam Mustafa, Chiral susceptibility in a dense thermomagnetic QCD medium within the hard thermal loop approximation, Phys. Rev. D 103 (7) (2021) 074019. `arXiv:2103.08407`, `doi:10.1103/PhysRevD.103.074019`.

[58] A. Jaiswal, et al., Dynamics of QCD matter — current status, Int. J. Mod. Phys. E 30 (02) (2021) 2130001. `arXiv:2007.14959`, `doi:10.1142/S0218301321300010`.

[59] S. Fayazbakhsh, S. Sadeghian, N. Sadooghi, Properties of neutral mesons in a hot and magnetized quark matter, Phys. Rev. D 86 (2012) 085042. `arXiv:1206.6051`, `doi:10.1103/PhysRevD.86.085042`.

[60] S. Fayazbakhsh, N. Sadooghi, Weak decay constant of neutral pions in a hot and magnetized quark matter, Phys. Rev. D 88 (6) (2013) 065030. `arXiv:1306.2098`, `doi:10.1103/PhysRevD.88.065030`.

[61] G. Basar, D. Kharzeev, D. Kharzeev, V. Skokov, Conformal anomaly as a source of soft photons in heavy ion collisions, Phys. Rev. Lett. 109 (2012) 202303. `arXiv:1206.1334`, `doi:10.1103/PhysRevLett.109.202303`.

[62] G. Basar, D. E. Kharzeev, E. V. Shuryak, Magneto-sonoluminescence and its signatures in photon and dilepton production in relativistic heavy ion collisions, Phys. Rev. C 90 (1) (2014) 014905. `arXiv:1402.2286`, `doi:10.1103/PhysRevC.90.014905`.

[63] A. Ayala, J. D. Castano-Yepes, C. A. Dominguez, L. A. Hernandez, Thermal photons from gluon fusion with magnetic fields, EPJ Web Conf. 141 (2017) 02007. `arXiv:1604.02713`, `doi:10.1051/epjconf/201714102007`.

[64] N. Sadooghi, F. Taghinavaz, Magnetized plasminos in cold and hot QED plasmas, Phys. Rev. D 92 (2) (2015) 025006. `arXiv:1504.04268`, `doi:10.1103/PhysRevD.92.025006`.

[65] A. Das, A. Bandyopadhyay, P. K. Roy, M. G. Mustafa, General structure of fermion two-point function and its spectral representation in a hot magnetized medium, Phys. Rev. D 97 (3) (2018) 034024. `arXiv:1709.08365`, `doi:10.1103/PhysRevD.97.034024`.

[66] B. Karmakar, A. Bandyopadhyay, N. Haque, M. G. Mustafa, General structure of gauge boson propagator and its spectra in a hot magnetized medium, Eur. Phys. J. C 79 (8) (2019) 658. `arXiv:1804.11336`, `doi:10.1140/epjc/s10052-019-7154-0`.

[67] B. Karmakar, R. Ghosh, A. Mukherjee, Collective modes of gluons in an anisotropic thermomagnetic medium, Phys. Rev. D 106 (11) (2022) 116006. `arXiv:2204.09646`, `doi:10.1103/PhysRevD.106.116006`.

[68] R. Ghosh, B. Karmakar, M. G. Mustafa, Soft contribution to the damping rate of a hard photon in a weakly magnetized hot medium, Phys. Rev. D 101 (5) (2020) 056007. `arXiv:1911.00744`, `doi:10.1103/PhysRevD.101.056007`.

[69] R. Ghosh, I. A. Shovkovy, Fermion self-energy and damping rate in a hot magnetized plasma, Phys. Rev. D 109 (9) (2024) 096018. `arXiv:2402.04307`, `doi:10.1103/PhysRevD.109.096018`.

[70] N. Sadooghi, F. Taghinavaz, Dilepton production rate in a hot and magnetized quark-gluon plasma, Annals Phys. 376 (2017) 218–253. `arXiv:1601.04887`, `doi:10.1016/j.aop.2016.11.008`.

[71] A. Bandyopadhyay, C. A. Islam, M. G. Mustafa, Electromagnetic spectral properties and Debye screening of a strongly magnetized hot medium, Phys. Rev. D 94 (11) (2016) 114034. `arXiv:1602.06769`, `doi:10.1103/PhysRevD.94.114034`.

[72] A. Bandyopadhyay, S. Mallik, Effect of magnetic field on dilepton production in a hot plasma, Phys. Rev. D 95 (7) (2017) 074019. `arXiv:1704.01364`, `doi:10.1103/PhysRevD.95.074019`.

[73] A. Das, N. Haque, M. G. Mustafa, P. K. Roy, Hard dilepton production from a weakly magnetized hot QCD medium, Phys. Rev. D 99 (9) (2019) 094022. `arXiv:1903.03528`, `doi:10.1103/PhysRevD.99.094022`.

[74] A. Das, A. Bandyopadhyay, C. A. Islam, Lepton pair production from a hot and dense QCD medium in the presence of an arbitrary magnetic field, Phys. Rev. D 106 (5) (2022) 056021. `arXiv:2109.00019`, `doi:10.1103/PhysRevD.106.056021`.

[75] A. Das, Quark propagator and di-lepton production rate in a hot, dense and very strongly magnetized rotating Quark-Gluon Plasma (10 2023). `arXiv:2310.11869`.

[76] K. A. Mamo, Enhanced thermal photon and dilepton production in strongly coupled $N = 4$ SYM plasma in strong magnetic field, JHEP 08 (2013) 083. `arXiv:1210.7428`, `doi:10.1007/JHEP08(2013)083`.

[77] R. Ghosh, I. A. Shovkovy, Electrical conductivity of hot relativistic plasma in a strong magnetic field (4 2024). `arXiv:2404.01388`.

[78] R. Ghosh, N. Haque, Shear viscosity of hadronic matter at finite temperature and magnetic field, Phys. Rev. D 105 (11) (2022) 114029. `arXiv:2204.01639`, `doi:10.1103/PhysRevD.105.114029`.

[79] A. Bandyopadhyay, Heavy quark diffusion coefficients in magnetized quark-gluon plasma, Phys. Rev. D 109 (3) (2024) 034013. `arXiv:2307.09655`, `doi:10.1103/PhysRevD.109.034013`.

[80] A. Bandyopadhyay, S. Ghosh, R. L. S. Farias, S. Ghosh, Quantum version of transport coefficients in Nambu–Jona-Lasinio model at finite temperature and strong magnetic field, Eur. Phys. J. C 83 (6) (2023) 489. `arXiv:2305.15844`, `doi:10.1140/epjc/s10052-023-11655-z`.

[81] R. Ghosh, M. Kurian, Magnetic-field-dependent electric-charge transport in hadronic medium at finite temperature, Phys. Rev. C 107 (3) (2023) 034903. `arXiv:2211.06729`, `doi:10.1103/PhysRevC.107.034903`.

[82] M. Y. Jamal, J. Prakash, I. Nilima, A. Bandyopadhyay, Energy loss of heavy quarks in the presence of magnetic field, J. Phys. G 51 (4) (2024) 045104. `arXiv:2304.09851`, `doi:10.1088/1361-6471/ad290d`.

[83] J. Sebastian, L. Thakur, H. Mishra, N. Haque, Heavy quarkonia in QGP medium in an arbitrary magnetic field, Phys. Rev. D 108 (9) (2023) 094001. `arXiv:2308.04410`, `doi:10.1103/PhysRevD.108.094001`.

[84] R. Ghosh, A. Bandyopadhyay, I. Nilima, S. Ghosh, Anisotropic tomography of heavy quark dissociation by using the general propagator structure in a finite magnetic field, Phys. Rev. D 106 (5) (2022) 054010. `arXiv:2204.02312`, `doi:10.1103/PhysRevD.106.054010`.

[85] I. Nilima, A. Bandyopadhyay, R. Ghosh, S. Ghosh, Heavy quark potential and LQCD based quark condensate at finite magnetic field, Eur. Phys. J. C 83 (1) (2023) 30. `arXiv:2204.02388`, `doi:10.1140/epjc/s10052-023-11194-7`.

[86] K. Bhattacharya, P. B. Pal, Inverse beta decay of arbitrarily polarized neutrons in a magnetic field, Pramana 62 (2004) 1041–1058. `arXiv:hep-ph/0209053`, `doi:10.1007/BF02705251`.

[87] K. Bhattacharya, P. B. Pal, Neutrinos and magnetic fields: A Short review, Proc. Indian Natl. Sci. Acad. A70 (1) (2004) 145–161. `arXiv:hep-ph/0212118`.

[88] A. K. Ganguly, S. Konar, P. B. Pal, Faraday effect: A Field theoretical point of view, Phys. Rev. D60 (1999) 105014. `arXiv:hep-ph/9905206`, `doi:10.1103/PhysRevD.60.105014`.

[89] J. C. D'Olivo, J. F. Nieves, S. Sahu, Field theory of the photon selfenergy in a medium with a magnetic field and the Faraday effect, Phys. Rev. D67 (2003) 025018. `arXiv:hep-ph/0208146`, `doi:10.1103/PhysRevD.67.025018`.

[90] S. P. Adhya, M. Mandal, S. Biswas, P. K. Roy, Pionic dispersion relations in the presence of a weak magnetic field, Phys. Rev. D93 (7) (2016) 074033. arXiv:1601.04578, doi:10.1103/PhysRevD.93.074033.

[91] A. Mukherjee, S. Ghosh, M. Mandal, P. Roy, S. Sarkar, Mass modification of hot pions in a magnetized dense medium, Phys. Rev. D96 (1) (2017) 016024. arXiv:1708.02385, doi:10.1103/PhysRevD.96.016024.

[92] S. Ghosh, A. Mukherjee, M. Mandal, S. Sarkar, P. Roy, Spectral properties of ρ meson in a magnetic field, Phys. Rev. D94 (9) (2016) 094043. arXiv:1612.02966, doi:10.1103/PhysRevD.94.094043.

[93] A. Bandyopadhyay, S. Mallik, Rho meson decay in the presence of a magnetic field, Eur. Phys. J. C 77 (11) (2017) 771. arXiv:1610.07887, doi:10.1140/epjc/s10052-017-5357-9.

[94] S. Ghosh, A. Mukherjee, M. Mandal, S. Sarkar, P. Roy, Thermal effects on ρ meson properties in an external magnetic field, Phys. Rev. D 96 (11) (2017) 116020. arXiv:1704.05319, doi:10.1103/PhysRevD.96.116020.

[95] A. Das, K. Tuchin, Rotational stability of magnetic field in rotating quark-gluon plasma (2 2025). arXiv:2502.18354.

[96] A. Adare, et al., Observation of direct-photon collective flow in $\sqrt{s_{NN}} = 200$ GeV Au+Au collisions, Phys. Rev. Lett. 109 (2012) 122302. arXiv:1105.4126, doi:10.1103/PhysRevLett.109.122302.

[97] J. S. Schwinger, On gauge invariance and vacuum polarization, Phys. Rev. 82 (1951) 664–679. doi:10.1103/PhysRev.82.664.

[98] V. I. Ritus, METHOD OF EIGENFUNCTIONS AND MASS OPERATOR IN QUANTUM ELECTRODYNAMICS OF A CONSTANT FIELD, Sov. Phys. JETP 48 (1978) 788.

[99] V. I. Ritus, Radiative corrections in quantum electrodynamics with intense field and their analytical properties, Annals Phys. 69 (1972) 555–582. doi:10.1016/0003-4916(72)90191-1.

[100] E. J. Ferrer, V. de la Incera, Dynamically Generated Anomalous Magnetic Moment in Massless QED, Nucl. Phys. B 824 (2010) 217–238. arXiv:0905.1733, doi:10.1016/j.nuclphysb.2009.08.024.

[101] E. J. Ferrer, V. de la Incera, D. Manreza Paret, A. Pérez Martínez, A. Sanchez, Insignificance of the anomalous magnetic moment of charged fermions for the equation of state of a magnetized and dense medium, Phys. Rev. D 91 (8) (2015) 085041. arXiv:1501.06616, doi:10.1103/PhysRevD.91.085041.

[102] N. Sadooghi, F. Taghinavaz, Local electric current correlation function in an exponentially decaying magnetic field, Phys. Rev. D 85 (2012) 125035. arXiv:1203.5634, doi:10.1103/PhysRevD.85.125035.

[103] T. Matsubara, A New approach to quantum statistical mechanics, Prog. Theor. Phys. 14 (1955) 351–378. doi:10.1143/PTP.14.351.

[104] J. S. Schwinger, Brownian motion of a quantum oscillator, J. Math. Phys. 2 (1961) 407–432. doi:10.1063/1.1703727.

[105] C. Møller, P. T. Matthews, J. S. Schwinger, N. Fukuda, J. J. Sakurai (Eds.), Proceedings, 3rd Brandeis University Summer Institute in Theoretical Physics: Waltham, MA, USA, 1960, Brandeis U., Waltham, MA, 1960.

[106] L. V. Keldysh, Diagram technique for nonequilibrium processes, Zh. Eksp. Teor. Fiz. 47 (1964) 1515–1527.

[107] J. I. Kapusta, C. Gale, Finite-temperature field theory: Principles and applications, Cambridge Monographs on Mathematical Physics, Cambridge University Press, 2011. doi:10.1017/CBO9780511535130.

[108] M. L. Bellac, Thermal Field Theory, Cambridge Monographs on Mathematical Physics, Cambridge University Press, 2011. doi:10.1017/CBO9780511721700.

[109] A. K. Das, Finite Temperature Field Theory, World Scientific, New York, 1997.

[110] M. Laine, A. Vuorinen, Basics of Thermal Field Theory, Vol. 925, Springer, 2016. `arXiv:1701.01554`, `doi:10.1007/978-3-319-31933-9`.

[111] S. Mallik, S. Sarkar, Hadrons at Finite Temperature, Cambridge University Press, Cambridge, 2016. `doi:10.1017/9781316535585`.

[112] M. G. Mustafa, An introduction to thermal field theory and some of its application, Eur. Phys. J. ST 232 (9) (2023) 1369–1457. `arXiv:2207.00534`, `doi:10.1140/epjs/s11734-023-00868-8`.

[113] N. Haque, M. G. Mustafa, Hard Thermal Loop—Theory and applications, Prog. Part. Nucl. Phys. 140 (2025) 104136. `arXiv:2404.08734`, `doi:10.1016/j.ppnp.2024.104136`.

[114] R. D. Pisarski, Computing Finite Temperature Loops with Ease, Nucl. Phys. B 309 (1988) 476–492. `doi:10.1016/0550-3213(88)90454-3`.

[115] H. A. Weldon, Effective Fermion Masses of Order gT in High Temperature Gauge Theories with Exact Chiral Invariance, Phys. Rev. D 26 (1982) 2789. `doi:10.1103/PhysRevD.26.2789`.

[116] H. A. Weldon, Covariant Calculations at Finite Temperature: The Relativistic Plasma, Phys. Rev. D26 (1982) 1394. `doi:10.1103/PhysRevD.26.1394`.

[117] A. D. Linde, Phase Transitions in Gauge Theories and Cosmology, Rept. Prog. Phys. 42 (1979) 389. `doi:10.1088/0034-4885/42/3/001`.

[118] A. D. Linde, Infrared Problem in Thermodynamics of the Yang-Mills Gas, Phys. Lett. B96 (1980) 289. `doi:10.1016/0370-2693(80)90769-8`.

[119] E. Braaten, R. D. Pisarski, Soft Amplitudes in Hot Gauge Theories: A General Analysis, Nucl. Phys. B337 (1990) 569. `doi:10.1016/0550-3213(90)90508-B`.

[120] E. Braaten, R. D. Pisarski, Simple effective Lagrangian for hard thermal loops, Phys. Rev. D45 (1992) 1827–1830. `doi:10.1103/PhysRevD.45.R1827`.

[121] E. Braaten, R. D. Pisarski, Deducing Hard Thermal Loops From Ward Identities, Nucl. Phys. B339 (1990) 310–324. `doi:10.1016/0550-3213(90)90351-D`.

[122] J. Taylor, S. Wong, The Effective Action of Hard Thermal Loops in QCD, Nucl. Phys. B346 (1990) 115–128. `doi:10.1016/0550-3213(90)90240-E`.

[123] J. Frenkel, J. C. Taylor, Hard thermal QCD, forward scattering and effective actions, Nucl. Phys. B 374 (1992) 156–168. `doi:10.1016/0550-3213(92)90480-Y`.

[124] G. Barton, On the Finite Temperature Quantum Electrodynamics of Free Electrons and Photons, Annals Phys. 200 (1990) 271. `doi:10.1016/0003-4916(90)90276-T`.

[125] J. O. Andersen, E. Braaten, M. Strickland, Hard thermal loop resummation of the free energy of a hot gluon plasma, Phys. Rev. Lett. 83 (1999) 2139–2142. `arXiv:hep-ph/9902327`, `doi:10.1103/PhysRevLett.83.2139`.

[126] J. O. Andersen, E. Braaten, M. Strickland, Hard thermal loop resummation of the thermodynamics of a hot gluon plasma, Phys. Rev. D61 (2000) 014017. `arXiv:hep-ph/9905337`, `doi:10.1103/PhysRevD.61.014017`.

[127] J. O. Andersen, E. Braaten, M. Strickland, Hard thermal loop resummation of the free energy of a hot quark - gluon plasma, Phys. Rev. D61 (2000) 074016. `arXiv:hep-ph/9908323`, `doi:10.1103/PhysRevD.61.074016`.

[128] J. O. Andersen, E. Braaten, E. Petitgirard, M. Strickland, HTL perturbation theory to two loops, Phys. Rev. D66 (2002) 085016. `arXiv:hep-ph/0205085`, `doi:10.1103/PhysRevD.66.085016`.

[129] J. O. Andersen, E. Petitgirard, M. Strickland, Two loop HTL thermodynamics with quarks, Phys. Rev. D70 (2004) 045001. `arXiv:hep-ph/0302069`, `doi:10.1103/PhysRevD.70.045001`.

[130] J. O. Andersen, M. Strickland, N. Su, Three-loop HTL Free Energy for QED, Phys. Rev. D80 (2009) 085015. `arXiv:0906.2936`, `doi:10.1103/PhysRevD.80.085015`.

[131] J. O. Andersen, M. Strickland, N. Su, Gluon Thermodynamics at Intermediate Coupling, Phys. Rev. Lett. 104 (2010) 122003. `arXiv:0911.0676`, `doi:10.1103/PhysRevLett.104.122003`.

[132] J. O. Andersen, M. Strickland, N. Su, Three-loop HTL gluon thermodynamics at intermediate coupling, JHEP 1008 (2010) 113. `arXiv:1005.1603`, `doi:10.1007/JHEP08(2010)113`.

[133] J. O. Andersen, L. E. Leganger, M. Strickland, N. Su, NNLO hard-thermal-loop thermodynamics for QCD, Phys. Lett. B696 (2011) 468–472. `arXiv:1009.4644`, `doi:10.1016/j.physletb.2010.12.070`.

[134] J. O. Andersen, L. E. Leganger, M. Strickland, N. Su, Three-loop HTL QCD thermodynamics, JHEP 1108 (2011) 053. `arXiv:1103.2528`, `doi:10.1007/JHEP08(2011)053`.

[135] J. O. Andersen, L. E. Leganger, M. Strickland, N. Su, The QCD trace anomaly, Phys. Rev. D84 (2011) 087703. `arXiv:1106.0514`, `doi:10.1103/PhysRevD.84.087703`.

[136] N. Haque, M. G. Mustafa, M. Strickland, Two-loop HTL pressure at finite temperature and chemical potential, Phys. Rev. D87 (2013) 105007. `arXiv:1212.1797`, `doi:10.1103/PhysRevD.87.105007`.

[137] S. Mogliacci, J. O. Andersen, M. Strickland, N. Su, A. Vuorinen, Equation of State of hot and dense QCD: Resummed perturbation theory confronts lattice data, JHEP 1312 (2013) 055. `arXiv:1307.8098`, `doi:10.1007/JHEP12(2013)055`.

[138] N. Haque, M. G. Mustafa, M. Strickland, Quark Number Susceptibilities from Two-Loop Hard Thermal Loop Perturbation Theory, JHEP 1307 (2013) 184. `arXiv:1302.3228`, `doi:10.1007/JHEP07(2013)184`.

[139] N. Haque, J. O. Andersen, M. G. Mustafa, M. Strickland, N. Su, Three-loop HTLpt Pressure and Susceptibilities at Finite Temperature and Density, Phys. Rev. D89 (2014) 061701. `arXiv:1309.3968`, `doi:10.1103/PhysRevD.89.061701`.

[140] N. Haque, A. Bandyopadhyay, J. O. Andersen, M. G. Mustafa, M. Strickland, et al., Three-loop HTLpt thermodynamics at finite temperature and chemical potential, JHEP 1405 (2014) 027. `arXiv:1402.6907`, `doi:10.1007/JHEP05(2014)027`.

[141] J. O. Andersen, N. Haque, M. G. Mustafa, M. Strickland, Three-loop hard-thermal-loop perturbation theory thermodynamics at finite temperature and finite baryonic and isospin chemical potential, Phys. Rev. D 93 (5) (2016) 054045. `arXiv:1511.04660`, `doi:10.1103/PhysRevD.93.054045`.

[142] F. Karsch, A. Patkos, P. Petreczky, Screened perturbation theory, Phys. Lett. B401 (1997) 69–73. `arXiv:hep-ph/9702376`, `doi:10.1016/S0370-2693(97)00392-4`.

[143] S. Chiku, T. Hatsuda, Optimized perturbation theory at finite temperature, Phys. Rev. D 58 (1998) 076001. `arXiv:hep-ph/9803226`, `doi:10.1103/PhysRevD.58.076001`.

[144] J. O. Andersen, E. Braaten, M. Strickland, Screened perturbation theory to three loops, Phys. Rev. D63 (2001) 105008. `arXiv:hep-ph/0007159`, `doi:10.1103/PhysRevD.63.105008`.

[145] J. Andersen, M. Strickland, Mass expansions of screened perturbation theory, Phys.Rev. D64 (2001) 105012. `arXiv:hep-ph/0105214`, `doi:10.1103/PhysRevD.64.105012`.

[146] J. O. Andersen, L. Kyllingstad, Four-loop Screened Perturbation Theory, Phys. Rev. D78 (2008) 076008. `arXiv:0805.4478`, `doi:10.1103/PhysRevD.78.076008`.

[147] J. Ghiglieri, A. Kurkela, M. Strickland, A. Vuorinen, Perturbative Thermal QCD: Formalism and Applications, Phys. Rept. 880 (2020) 1–73. `arXiv:2002.10188`, `doi:10.1016/j.physrep.2020.07.004`.

[148] N. Haque, M. G. Mustafa, A Modified Hard Thermal Loop Perturbation Theory (2010). `arXiv:1007.2076`.

[149] N. Haque, M. G. Mustafa, M. H. Thoma, Conserved Density Fluctuation and Temporal Correlation Function in HTL Perturbation Theory, Phys. Rev. D84 (2011) 054009. `arXiv:1103.3394`, `doi:10.1103/PhysRevD.84.054009`.

[150] P. Chakraborty, M. G. Mustafa, M. H. Thoma, Quark number susceptibility in hard thermal loop approximation, Eur. Phys. J. C23 (2002) 591–596. `arXiv:hep-ph/0111022`, `doi:10.1007/s100520200899`.

[151] P. Chakraborty, M. G. Mustafa, M. H. Thoma, Chiral susceptibility in hard thermal loop approximation, Phys. Rev. D67 (2003) 114004. `arXiv:hep-ph/0210159`, `doi:10.1103/PhysRevD.67.114004`.

[152] P. Chakraborty, M. G. Mustafa, M. H. Thoma, Quark number susceptibility, thermodynamic sum rule, and hard thermal loop approximation, Phys. Rev. D68 (2003) 085012. `arXiv:hep-ph/0303009`, `doi:10.1103/PhysRevD.68.085012`.

[153] L. D. McLerran, T. Toimela, Photon and Dilepton Emission from the Quark - Gluon Plasma: Some General Considerations, Phys. Rev. D 31 (1985) 545. `doi:10.1103/PhysRevD.31.545`.

[154] R. Baier, B. Pire, D. Schiff, Dilepton production at finite temperature: Perturbative treatment at order α_s, Phys. Rev. D 38 (1988) 2814. `doi:10.1103/PhysRevD.38.2814`.

[155] E. Braaten, R. D. Pisarski, T.-C. Yuan, Production of Soft Dileptons in the Quark - Gluon Plasma, Phys. Rev. Lett. 64 (1990) 2242. `doi:10.1103/PhysRevLett.64.2242`.

[156] C. Greiner, N. Haque, M. G. Mustafa, M. H. Thoma, Low Mass Dilepton Rate from the Deconfined Phase, Phys. Rev. C83 (2011) 014908. `arXiv:1010.2169`, `doi:10.1103/PhysRevC.83.014908`.

[157] I. Ghisoiu, M. Laine, Interpolation of hard and soft dilepton rates, JHEP 10 (2014) 083. `arXiv:1407.7955`, `doi:10.1007/JHEP10(2014)083`.

[158] J. Ghiglieri, G. D. Moore, Low Mass Thermal Dilepton Production at NLO in a Weakly Coupled Quark-Gluon Plasma, JHEP 12 (2014) 029. `arXiv:1410.4203`, `doi:10.1007/JHEP12(2014)029`.

[159] J. Ghiglieri, The thermal dilepton rate at NLO at small and large invariant mass, Nucl. Part. Phys. Proc. 276-278 (2016) 305–308. `arXiv:1510.00525`, `doi:10.1016/j.nuclphysbps.2016.05.070`.

[160] P. Aurenche, F. Gelis, R. Kobes, H. Zaraket, Bremsstrahlung and photon production in thermal QCD, Phys. Rev. D58 (1998) 085003. `arXiv:hep-ph/9804224`, `doi:10.1103/PhysRevD.58.085003`.

[161] P. Aurenche, F. Gelis, R. Kobes, H. Zaraket, Two loop Compton and annihilation processes in thermal QCD, Phys. Rev. D60 (1999) 076002. `arXiv:hep-ph/9903307`, `doi:10.1103/PhysRevD.60.076002`.

[162] F. Karsch, M. Mustafa, M. Thoma, Finite temperature meson correlation functions in HTL approximation, Phys. Lett. B497 (2001) 249–258. `arXiv:hep-ph/0007093`, `doi:10.1016/S0370-2693(00)01322-8`.

[163] M. H. Thoma, C. T. Traxler, Production of energetic dileptons with small invariant masses from the quark - gluon plasma, Phys. Rev. D56 (1997) 198–202. `arXiv:hep-ph/9701354`, `doi:10.1103/PhysRevD.56.198`.

[164] P. Aurenche, F. Gelis, H. Zaraket, Enhanced thermal production of hard dileptons by $3 \to 2$ processes, JHEP 0207 (2002) 063. `arXiv:hep-ph/0204145`, `doi:10.1088/1126-6708/2002/07/063`.

[165] P. Aurenche, F. Gelis, G. Moore, H. Zaraket, Landau-Pomeranchuk-Migdal resummation for dilepton production, JHEP 0212 (2002) 006. `arXiv:hep-ph/0211036`, `doi:10.1088/1126-6708/2002/12/006`.

[166] M. Carrington, A. Gynther, P. Aurenche, Energetic di-leptons from the Quark Gluon Plasma, Phys. Rev. D77 (2008) 045035. `arXiv:0711.3943`, `doi:10.1103/PhysRevD.77.045035`.

[167] J. I. Kapusta, P. Lichard, D. Seibert, High-energy photons from quark - gluon plasma versus hot hadronic gas, Phys. Rev. D44 (1991) 2774–2788. `doi:10.1103/PhysRevD.47.4171,10.1103/PhysRevD.44.2774`.

[168] R. Baier, H. Nakkagawa, A. Niegawa, K. Redlich, Production rate of hard thermal photons and screening of quark mass singularity, Z. Phys. C 53 (1992) 433–438. `doi:10.1007/BF01625902`.

[169] P. B. Arnold, G. D. Moore, L. G. Yaffe, Photon emission from ultrarelativistic plasmas, JHEP 11 (2001) 057. `arXiv:hep-ph/0109064`, `doi:10.1088/1126-6708/2001/11/057`.

[170] P. B. Arnold, G. D. Moore, L. G. Yaffe, Photon emission from quark gluon plasma: Complete leading order results, JHEP 0112 (2001) 009. `arXiv:hep-ph/0111107`, `doi:10.1088/1126-6708/2001/12/009`.

[171] T. Peitzmann, M. H. Thoma, Direct photons from relativistic heavy ion collisions, Phys. Rept. 364 (2002) 175–246. `arXiv:hep-ph/0111114`, `doi:10.1016/S0370-1573(02)00012-1`.

[172] J. Ghiglieri, J. Hong, A. Kurkela, E. Lu, G. D. Moore, D. Teaney, Next-to-leading order thermal photon production in a weakly coupled quark-gluon plasma, JHEP 05 (2013) 010. `arXiv:1302.5970`, `doi:10.1007/JHEP05(2013)010`.

[173] M. G. Mustafa, M. H. Thoma, P. Chakraborty, Screening of a moving parton in the quark gluon plasma, Phys. Rev. C71 (2005) 017901. `arXiv:hep-ph/0403279`, `doi:10.1103/PhysRevC.71.017901`.

[174] M. G. Mustafa, P. Chakraborty, M. H. Thoma, Dynamical screening in a quark gluon plasma, J. Phys. Conf. Ser. 50 (2006) 438–441. `arXiv:hep-ph/0504174`, `doi:10.1088/1742-6596/50/1/066`.

[175] P. Chakraborty, M. G. Mustafa, M. H. Thoma, Wakes in the quark-gluon plasma, Phys. Rev. D74 (2006) 094002. `arXiv:hep-ph/0606316`, `doi:10.1103/PhysRevD.74.094002`.

[176] P. Chakraborty, M. G. Mustafa, R. Ray, M. H. Thoma, Wakes in a Collisional Quark-Gluon Plasma, J. Phys. G34 (2007) 2141–2152. `arXiv:0705.1447`, `doi:10.1088/0954-3899/34/10/004`.

[177] M. Laine, O. Philipsen, P. Romatschke, M. Tassler, Real-time static potential in hot QCD, JHEP 0703 (2007) 054. `arXiv:hep-ph/0611300`, `doi:10.1088/1126-6708/2007/03/054`.

[178] A. Dumitru, Y. Guo, M. Strickland, The Heavy-quark potential in an anisotropic (viscous) plasma, Phys. Lett. B662 (2008) 37–42. `arXiv:0711.4722`, `doi:10.1016/j.physletb.2008.02.048`.

[179] A. Dumitru, Y. Guo, A. Mocsy, M. Strickland, Quarkonium states in an anisotropic QCD plasma, Phys. Rev. D79 (2009) 054019. `arXiv:0901.1998`, `doi:10.1103/PhysRevD.79.054019`.

[180] L. Thakur, U. Kakade, B. K. Patra, Dissociation of Quarkonium in a Complex Potential, Phys. Rev. D 89 (9) (2014) 094020. `arXiv:1401.0172`, `doi:10.1103/PhysRevD.89.094020`.

[181] R. Pisarski, Damping rates for moving particles in hot QCD, Phys. Rev. D47 (1993) 5589–5600. `doi:10.1103/PhysRevD.47.5589`.

[182] E. Braaten, R. D. Pisarski, Calculation of the quark damping rate in hot QCD, Phys. Rev. D 46 (1992) 1829–1834. `doi:10.1103/PhysRevD.46.1829`.

[183] S. Peigne, E. Pilon, D. Schiff, The Heavy fermion damping rate puzzle, Z. Phys. C60 (1993) 455–460. `arXiv:hep-ph/9306219`, `doi:10.1007/BF01560043`.

[184] M. H. Thoma, Applications of high temperature field theory to heavy ion collisions, Quark Gluon Plasma 2, ed. R.C. Hwa (World Scientific, Singapore, 1995) 51.

[185] M. H. Thoma, New developments and applications of thermal field theory (10 2000). arXiv:hep-ph/0010164.

[186] M. H. Thoma, M. Gyulassy, Quark Damping and Energy Loss in the High Temperature QCD, Nucl. Phys. B351 (1991) 491–506. doi:10.1016/S0550-3213(05)80031-8.

[187] M. H. Thoma, Parton interaction rates in the quark - gluon plasma, Phys. Rev. D 49 (1994) 451–459. arXiv:hep-ph/9308257, doi:10.1103/PhysRevD.49.451.

[188] M. H. Thoma, Damping rate of a hard photon in a relativistic plasma, Phys. Rev. D 51 (1995) 862–865. arXiv:hep-ph/9405309, doi:10.1103/PhysRevD.51.862.

[189] A. Abada, N. Daira-Aifa, Photon Damping in One-Loop HTL Perturbation Theory, JHEP 1204 (2012) 071. arXiv:1112.6065, doi:10.1007/JHEP04(2012)071.

[190] E. Braaten, R. D. Pisarski, Resummation and Gauge Invariance of the Gluon Damping Rate in Hot QCD, Phys. Rev. Lett. 64 (1990) 1338. doi:10.1103/PhysRevLett.64.1338.

[191] E. Braaten, R. D. Pisarski, Calculation of the gluon damping rate in hot QCD, Phys. Rev. D42 (1990) 2156–2160. doi:10.1103/PhysRevD.42.2156.

[192] R. D. Pisarski, Resummation and the gluon damping rate in hot QCD, Nucl. Phys. A525 (1991) 175–188. doi:10.1016/0375-9474(91)90325-Z.

[193] E. Braaten, M. H. Thoma, Energy loss of a heavy fermion in a hot plasma, Phys. Rev. D44 (1991) 1298–1310. doi:10.1103/PhysRevD.44.1298.

[194] E. Braaten, M. H. Thoma, Energy loss of a heavy quark in the quark - gluon plasma, Phys. Rev. D44 (1991) R 2625–2630. doi:10.1103/PhysRevD.44.R2625.

[195] M. H. Thoma, Collisional energy loss of high-energy jets in the quark gluon plasma, Phys. Lett. B 273 (1991) 128–132. doi:10.1016/0370-2693(91)90565-8.

[196] P. B. Arnold, G. D. Moore, L. G. Yaffe, Photon and gluon emission in relativistic plasmas, JHEP 06 (2002) 030. arXiv:hep-ph/0204343, doi:10.1088/1126-6708/2002/06/030.

[197] S. Jeon, G. D. Moore, Energy loss of leading partons in a thermal QCD medium, Phys. Rev. C 71 (2005) 034901. arXiv:hep-ph/0309332, doi:10.1103/PhysRevC.71.034901.

[198] M. G. Mustafa, Energy loss of charm quarks in the quark-gluon plasma: Collisional versus radiative, Phys. Rev. C72 (2005) 014905. arXiv:hep-ph/0412402, doi:10.1103/PhysRevC.72.014905.

[199] M. G. Mustafa, M. H. Thoma, Quenching of hadron spectra due to the collisional energy loss of partons in the quark gluon plasma, Acta Phys. Hung. A22 (2005) 93–102. arXiv:hep-ph/0311168, doi:10.1556/APH.22.2005.1-2.10.

[200] P. Chakraborty, M. G. Mustafa, M. H. Thoma, Energy gain of heavy quarks by fluctuations in the QGP, Phys. Rev. C75 (2007) 064908. arXiv:hep-ph/0611355, doi:10.1103/PhysRevC.75.064908.

[201] G.-Y. Qin, J. Ruppert, C. Gale, S. Jeon, G. D. Moore, M. G. Mustafa, Radiative and collisional jet energy loss in the quark-gluon plasma at RHIC, Phys. Rev. Lett. 100 (2008) 072301. arXiv:0710.0605, doi:10.1103/PhysRevLett.100.072301.

[202] J. Ghiglieri, G. D. Moore, D. Teaney, Jet-Medium Interactions at NLO in a Weakly-Coupled Quark-Gluon Plasma, JHEP 03 (2016) 095. arXiv:1509.07773, doi:10.1007/JHEP03(2016)095.

[203] Y. Guo, L. Qiu, R. Zhao, M. Strickland, Energy loss of a heavy fermion in a collisional QED plasma (3 2024). arXiv:2403.06739.

[204] S. Mrowczynski, M. H. Thoma, Hard loop approach to anisotropic systems, Phys. Rev. D62 (2000) 036011. arXiv:hep-ph/0001164, doi:10.1103/PhysRevD.62.036011.

[205] P. Romatschke, M. Strickland, Collective modes of an anisotropic quark gluon plasma, Phys. Rev. D68 (2003) 036004. arXiv:hep-ph/0304092, doi:10.1103/PhysRevD.68.036004.

[206] P. Romatschke, M. Strickland, Collective modes of an anisotropic quark-gluon plasma II, Phys. Rev. D70 (2004) 116006. arXiv:hep-ph/0406188, doi:10.1103/PhysRevD.70.116006.

[207] A. Rebhan, P. Romatschke, M. Strickland, Hard-loop dynamics of non-Abelian plasma instabilities, Phys. Rev. Lett. 94 (2005) 102303. arXiv:hep-ph/0412016, doi:10.1103/PhysRevLett.94.102303.

[208] B. Schenke, M. Strickland, Fermionic Collective Modes of an Anisotropic Quark-Gluon Plasma, Phys. Rev. D74 (2006) 065004. arXiv:hep-ph/0606160, doi:10.1103/PhysRevD.74.065004.

[209] A. Rebhan, M. Strickland, M. Attems, Instabilities of an anisotropically expanding non-Abelian plasma: 1D+3V discretized hard-loop simulations, Phys. Rev. D78 (2008) 045023. arXiv:0802.1714, doi:10.1103/PhysRevD.78.045023.

[210] M. Attems, A. Rebhan, M. Strickland, Instabilities of an anisotropically expanding non-Abelian plasma: 3D+3V discretized hard-loop simulations, Phys. Rev. D87 (2013) 025010. arXiv:1207.5795, doi:10.1103/PhysRevD.87.025010.

[211] D. F. Litim, C. Manuel, Transport theory for a two flavor color superconductor, Phys. Rev. Lett. 87 (2001) 052002. arXiv:hep-ph/0103092, doi:10.1103/PhysRevLett.87.052002.

[212] P. Graf, F. D. Steffen, Thermal axion production in the primordial quark-gluon plasma, Phys. Rev. D 83 (2011) 075011. arXiv:1008.4528, doi:10.1103/PhysRevD.83.075011.

[213] C. Kiessig, M. Plumacher, Hard-Thermal-Loop Corrections in Leptogenesis II: Solving the Boltzmann Equations, JCAP 1209 (2012) 012. arXiv:1111.1235, doi:10.1088/1475-7516/2012/09/012.

[214] C. Kiessig, M. Plumacher, Hard-Thermal-Loop Corrections in Leptogenesis I: CP-Asymmetries, JCAP 1207 (2012) 014. arXiv:1111.1231, doi:10.1088/1475-7516/2012/07/014.

[215] Q. Du, M. Strickland, U. Tantary, B.-W. Zhang, Two-loop HTL-resummed thermodynamics for $\mathcal{N} = 4$ supersymmetric Yang-Mills theory, JHEP 09 (2020) 038. arXiv:2006.02617, doi:10.1007/JHEP09(2020)038.

[216] Q. Du, M. Strickland, U. Tantary, $\mathcal{N} = 4$ supersymmetric Yang-Mills thermodynamics to order λ^2, JHEP 08 (2021) 064, [Erratum: JHEP 02, 053 (2022)]. arXiv:2105.02101, doi:10.1007/JHEP08(2021)064.

[217] J. O. Andersen, Q. Du, M. Strickland, U. Tantary, N=4 supersymmetric Yang-Mills thermodynamics from effective field theory, Phys. Rev. D 105 (1) (2022) 015006. arXiv:2111.12160, doi:10.1103/PhysRevD.105.015006.

[218] D. J. Gross, R. D. Pisarski, L. G. Yaffe, QCD and Instantons at Finite Temperature, Rev. Mod. Phys. 53 (1981) 43. doi:10.1103/RevModPhys.53.43.

[219] T. Appelquist, R. D. Pisarski, High-Temperature Yang-Mills Theories and Three-Dimensional Quantum Chromodynamics, Phys. Rev. D 23 (1981) 2305. doi:10.1103/PhysRevD.23.2305.

[220] S. Nadkarni, Dimensional Reduction in Hot QCD, Phys. Rev. D 27 (1983) 917. doi:10.1103/PhysRevD.27.917.

[221] S. Nadkarni, Dimensional Reduction in Finite Temperature Quantum Chromodynamics. 2., Phys. Rev. D 38 (1988) 3287. doi:10.1103/PhysRevD.38.3287.

[222] S. Nadkarni, Large Scale Structure of the Deconfined Phase, Phys. Rev. Lett. 60 (1988) 491–494. doi:10.1103/PhysRevLett.60.491.

[223] M. Nopoush, Y. Guo, M. Strickland, The static hard-loop gluon propagator to all orders in anisotropy, JHEP 09 (2017) 063. arXiv:1706.08091, doi:10.1007/JHEP09(2017)063.

[224] K. Hattori, D. Satow, Gluon spectrum in a quark-gluon plasma under strong magnetic fields, Phys. Rev. D 97 (1) (2018) 014023. arXiv:1704.03191, doi:10.1103/PhysRevD.97.014023.

[225] A. Ayala, C. A. Dominguez, S. Hernandez-Ortiz, L. A. Hernandez, M. Loewe, D. Manreza Paret, R. Zamora, Thermomagnetic evolution of the QCD strong coupling, Phys. Rev. D 98 (3) (2018) 031501. arXiv:1805.08198, doi:10.1103/PhysRevD.98.031501.

[226] S. Ghosh, A. Mukherjee, P. Roy, S. Sarkar, General structure of the neutral ρ meson self-energy and its spectral properties in a hot and dense magnetized medium, Phys. Rev. D 99 (9) (2019) 096004. arXiv:1901.02290, doi:10.1103/PhysRevD.99.096004.

[227] A. Bzdak, V. Skokov, Anisotropy of photon production: initial eccentricity or magnetic field, Phys. Rev. Lett. 110 (19) (2013) 192301. arXiv:1208.5502, doi:10.1103/PhysRevLett.110.192301.

[228] L. McLerran, V. Skokov, Comments About the Electromagnetic Field in Heavy-Ion Collisions, Nucl. Phys. A 929 (2014) 184–190. arXiv:1305.0774, doi:10.1016/j.nuclphysa.2014.05.008.

[229] R. C. Duncan, C. Thompson, Formation of very strongly magnetized neutron stars - implications for gamma-ray bursts, Astrophys. J. Lett. 392 (1992) L9. doi:10.1086/186413.

[230] T.-K. Chyi, C.-W. Hwang, W. F. Kao, G.-L. Lin, K.-W. Ng, J.-J. Tseng, The weak field expansion for processes in a homogeneous background magnetic field, Phys. Rev. D 62 (2000) 105014. arXiv:hep-th/9912134, doi:10.1103/PhysRevD.62.105014.

[231] A. Ayala, A. Sanchez, G. Piccinelli, S. Sahu, Effective potential at finite temperature in a constant magnetic field. I. Ring diagrams in a scalar theory, Phys. Rev. D 71 (2005) 023004. arXiv:hep-ph/0412135, doi:10.1103/PhysRevD.71.023004.

[232] A. Ayala, J. J. Cobos-Martínez, M. Loewe, M. E. Tejeda-Yeomans, R. Zamora, Finite temperature quark-gluon vertex with a magnetic field in the Hard Thermal Loop approximation, Phys. Rev. D 91 (1) (2015) 016007. arXiv:1410.6388, doi:10.1103/PhysRevD.91.016007.

[233] N. Haque, Finite temperature QCD four-point function in the presence of a weak magnetic field within the hard thermal loop approximation, Phys. Rev. D 96 (1) (2017) 014019. arXiv:1704.05833, doi:10.1103/PhysRevD.96.014019.

[234] H. A. Weldon, Structure of the quark propagator at high temperature, Phys. Rev. D 61 (2000) 036003. arXiv:hep-ph/9908204, doi:10.1103/PhysRevD.61.036003.

[235] J. Alexandre, Vacuum polarization in thermal QED with an external magnetic field, Phys. Rev. D 63 (2001) 073010. arXiv:hep-th/0009204, doi:10.1103/PhysRevD.63.073010.

[236] B. Singh, L. Thakur, H. Mishra, Heavy quark complex potential in a strongly magnetized hot QGP medium, Phys. Rev. D 97 (9) (2018) 096011. arXiv:1711.03071, doi:10.1103/PhysRevD.97.096011.

[237] M. Hasan, B. Chatterjee, B. K. Patra, Heavy Quark Potential in a static and strong homogeneous magnetic field, Eur. Phys. J. C 77 (11) (2017) 767. arXiv:1703.10508, doi:10.1140/epjc/s10052-017-5346-z.

[238] J. Beringer, et al., Review of Particle Physics (RPP), Phys. Rev. D 86 (2012) 010001. `doi:10.1103/PhysRevD.86.010001`.

[239] J. Frenkel, J. Taylor, High Temperature Limit of Thermal QCD, Nucl. Phys. B334 (1990) 199. `doi:10.1016/0550-3213(90)90661-V`.

[240] A. Bazavov, et al., The QCD Equation of State to $\mathcal{O}(\mu_B^6)$ from Lattice QCD, Phys. Rev. D 95 (5) (2017) 054504. `arXiv:1701.04325`, `doi:10.1103/PhysRevD.95.054504`.

[241] A. Bazavov, P. Petreczky, J. H. Weber, Equation of State in 2+1 Flavor QCD at High Temperatures, Phys. Rev. D 97 (1) (2018) 014510. `arXiv:1710.05024`, `doi:10.1103/PhysRevD.97.014510`.

[242] G. Inghirami, L. Del Zanna, A. Beraudo, M. H. Moghaddam, F. Becattini, M. Bleicher, Numerical magneto-hydrodynamics for relativistic nuclear collisions, Eur. Phys. J. C 76 (12) (2016) 659. `arXiv:1609.03042`, `doi:10.1140/epjc/s10052-016-4516-8`.

[243] V. Roy, S. Pu, L. Rezzolla, D. H. Rischke, Effect of intense magnetic fields on reduced-MHD evolution in $\sqrt{s_{NN}} = 200$ GeV Au+Au collisions, Phys. Rev. C 96 (5) (2017) 054909. `arXiv:1706.05326`, `doi:10.1103/PhysRevC.96.054909`.

[244] G. S. Bali, F. Bruckmann, G. Endrödi, S. D. Katz, A. Schäfer, The QCD equation of state in background magnetic fields, JHEP 08 (2014) 177. `arXiv:1406.0269`, `doi:10.1007/JHEP08(2014)177`.

[245] L. Dolan, R. Jackiw, Symmetry Behavior at Finite Temperature, Phys. Rev. D 9 (1974) 3320–3341. `doi:10.1103/PhysRevD.9.3320`.

[246] J. O. Andersen, S. Mogliacci, N. Su, A. Vuorinen, Quark number susceptibilities from resummed perturbation theory, Phys. Rev. D87 (2013) 074003. `arXiv:1210.0912`, `doi:10.1103/PhysRevD.87.074003`.

[247] N. Haque, M. G. Mustafa, Quark Number Susceptibility and Thermodynamics in HTL approximation, Nucl. Phys. A 862-863 (2011) 271–274. `arXiv:1109.0799`, `doi:10.1016/j.nuclphysa.2011.05.070`.

[248] N. Haque, Quark mass dependent collective excitations and quark number susceptibilities within the hard thermal loop approximation, Phys. Rev. D 98 (1) (2018) 014013. `arXiv:1804.04996`, `doi:10.1103/PhysRevD.98.014013`.

[249] A. Das, N. Haque, Neutral pion mass in the linear sigma model coupled to quarks at arbitrary magnetic field, Phys. Rev. D 101 (7) (2020) 074033. `arXiv:1908.10323`, `doi:10.1103/PhysRevD.101.074033`.

[250] A. Perez Martinez, H. Perez Rojas, H. Mosquera Cuesta, Anisotropic Pressures in Very Dense Magnetized Matter, Int. J. Mod. Phys. D 17 (2008) 2107–2123. `arXiv:0711.0975`, `doi:10.1142/S0218271808013741`.

[251] G. S. Bali, F. Bruckmann, G. Endrodi, A. Schafer, Paramagnetic squeezing of QCD matter, Phys. Rev. Lett. 112 (2014) 042301. `arXiv:1311.2559`, `doi:10.1103/PhysRevLett.112.042301`.

[252] H. A. Weldon, Simple Rules for Discontinuities in Finite Temperature Field Theory, Phys. Rev. D 28 (1983) 2007. `doi:10.1103/PhysRevD.28.2007`.

[253] G. Jackson, M. Laine, Testing thermal photon and dilepton rates, JHEP 11 (2019) 144. `arXiv:1910.09567`, `doi:10.1007/JHEP11(2019)144`.

[254] J. Ghiglieri, O. Kaczmarek, M. Laine, F. Meyer, Lattice constraints on the thermal photon rate, Phys. Rev. D 94 (1) (2016) 016005. `arXiv:1604.07544`, `doi:10.1103/PhysRevD.94.016005`.

[255] E. L. Feinberg, Direct Production of Photons and Dileptons in Thermodynamical Models of Multiple Hadron Production, Nuovo Cim. A 34 (1976) 391.

[256] P. Ruuskanen, Particle production in highly excited matter, (ed.: Hans h. gutbrod and johann rafelski, (Plenum

Press, New York, 1993).

URL https://api.semanticscholar.org/CorpusID:118262819

[257] H. A. Weldon, Reformulation of finite temperature dilepton production, Phys. Rev. D 42 (1990) 2384–2387. doi:10.1103/PhysRevD.42.2384.

[258] C. Gale, J. I. Kapusta, Vector dominance model at finite temperature, Nucl. Phys. B357 (1991) 65–89. doi:10.1016/0550-3213(91)90459-B.

[259] R. L. Kobes, G. W. Semenoff, Discontinuities of Green Functions in Field Theory at Finite Temperature and Density, Nucl. Phys. B 260 (1985) 714–746. doi:10.1016/0550-3213(85)90056-2.

[260] R. L. Kobes, G. W. Semenoff, Discontinuities of Green Functions in Field Theory at Finite Temperature and Density. 2, Nucl. Phys. B 272 (1986) 329–364. doi:10.1016/0550-3213(86)90006-4.

[261] G. Calucci, R. Ragazzon, Nonlogarithmic terms in the strong field dependence of the photon propagator, J. Phys. A 27 (1994) 2161–2166.

[262] C. A. Islam, S. Majumder, N. Haque, M. G. Mustafa, Vector meson spectral function and dilepton production rate in a hot and dense medium within an effective QCD approach, JHEP 02 (2015) 011. arXiv:1411.6407, doi:10.1007/JHEP02(2015)011.

[263] A. Das, R. R. Francisco, J. Frenkel, Causal amplitudes in the Schwinger model at finite temperature, Phys. Rev. D 86 (2012) 047702. arXiv:1206.5677, doi:10.1103/PhysRevD.86.047702.

[264] E. J. Ferrer, V. de la Incera, Ward-Takahashi identity with external field in ladder QED, Phys. Rev. D 58 (1998) 065008. arXiv:hep-th/9803226, doi:10.1103/PhysRevD.58.065008.

[265] L. D. Landau, Lifshitz, Quantum Mechanics: Non-relativistic Theory (Pergamon Press), 1977.

[266] P. Chakraborty, Meson spectral function and screening masses in magnetized quark gluon plasma, Eur. Phys. J. Plus 134 (10) (2019) 478. arXiv:1711.04404, doi:10.1140/epjp/i2019-12847-y.

[267] S. Ghosh, V. Chandra, Electromagnetic spectral function and dilepton rate in a hot magnetized QCD medium, Phys. Rev. D 98 (7) (2018) 076006. arXiv:1808.05176, doi:10.1103/PhysRevD.98.076006.

[268] C. A. Islam, A. Bandyopadhyay, P. K. Roy, S. Sarkar, Spectral function and dilepton rate from a strongly magnetized hot and dense medium in light of mean field models, Phys. Rev. D 99 (9) (2019) 094028. arXiv:1812.10380, doi:10.1103/PhysRevD.99.094028.

[269] S. Ghosh, N. Chaudhuri, S. Sarkar, P. Roy, Effects of the anomalous magnetic moment of quarks on the dilepton production from hot and dense magnetized quark matter using the NJL model, Phys. Rev. D 101 (9) (2020) 096002. arXiv:2004.09203, doi:10.1103/PhysRevD.101.096002.

[270] K. Hattori, H. Taya, S. Yoshida, Di-lepton production from a single photon in strong magnetic fields: vacuum dichroism, JHEP 01 (2021) 093. arXiv:2010.13492, doi:10.1007/JHEP01(2021)093.

[271] N. Chaudhuri, S. Ghosh, S. Sarkar, P. Roy, Dilepton production from magnetized quark matter with an anomalous magnetic moment of the quarks using a three-flavor PNJL model, Phys. Rev. D 103 (9) (2021) 096021. arXiv:2104.11425, doi:10.1103/PhysRevD.103.096021.

[272] X. Wang, I. A. Shovkovy, Rate and ellipticity of dilepton production in a magnetized quark-gluon plasma, Phys. Rev. D 106 (3) (2022) 036014. arXiv:2205.00276, doi:10.1103/PhysRevD.106.036014.

[273] J. Alam, B. Sinha, S. Raha, Electromagnetic probes of quark gluon plasma, Phys. Rept. 273 (1996) 243–362. doi:10.1016/0370-1573(95)00084-4.

[274] J. Alam, S. Sarkar, P. Roy, T. Hatsuda, B. Sinha, Thermal photons and lepton pairs from quark gluon plasma and hot hadronic matter, Annals Phys. 286 (2001) 159–248. `arXiv:hep-ph/9909267`, `doi:10.1006/aphy.2000.6091`.

[275] R. Mondal, N. Chaudhuri, S. Ghosh, S. Sarkar, P. Roy, Dilepton production from hot and magnetized hadronic matter, Phys. Rev. D 107 (3) (2023) 036017. `arXiv:2301.09475`, `doi:10.1103/PhysRevD.107.036017`.

[276] C. Gale, J. I. Kapusta, Dileptons as a Probe of Pion, Kaon, Nucleon and Anti-nucleon Dynamics in Nuclear Matter, Phys. Rev. C 38 (1988) 2659–2663. `doi:10.1103/PhysRevC.38.2659`.

[277] G. D. Moore, D. Teaney, How much do heavy quarks thermalize in a heavy ion collision?, Phys. Rev. C 71 (2005) 064904. `arXiv:hep-ph/0412346`, `doi:10.1103/PhysRevC.71.064904`.

[278] E. Braaten, T. C. Yuan, Calculation of screening in a hot plasma, Phys. Rev. Lett. 66 (1991) 2183–2186. `doi:10.1103/PhysRevLett.66.2183`.

[279] K. Fukushima, K. Hattori, H.-U. Yee, Y. Yin, Heavy Quark Diffusion in Strong Magnetic Fields at Weak Coupling and Implications for Elliptic Flow, Phys. Rev. D 93 (7) (2016) 074028. `arXiv:1512.03689`, `doi:10.1103/PhysRevD.93.074028`.

[280] M. Kurian, S. K. Das, V. Chandra, Heavy quark dynamics in a hot magnetized QCD medium, Phys. Rev. D 100 (7) (2019) 074003. `arXiv:1907.09556`, `doi:10.1103/PhysRevD.100.074003`.

[281] B. Singh, S. Mazumder, H. Mishra, HQ Collisional energy loss in a magnetized medium, JHEP 05 (2020) 068. `arXiv:2002.04922`, `doi:10.1007/JHEP05(2020)068`.

[282] A. Bandyopadhyay, J. Liao, H. Xing, Heavy quark dynamics in a strongly magnetized quark-gluon plasma, Phys. Rev. D 105 (11) (2022) 114049. `arXiv:2105.02167`, `doi:10.1103/PhysRevD.105.114049`.

[283] D. Dey, B. k. Patra, Dynamics of heavy flavor in a weakly magnetized hot QCD medium, Phys. Rev. D 109 (11) (2024) 116008. `arXiv:2307.00420`, `doi:10.1103/PhysRevD.109.116008`.

[284] A. Beraudo, A. De Pace, W. M. Alberico, A. Molinari, Transport properties and Langevin dynamics of heavy quarks and quarkonia in the Quark Gluon Plasma, Nucl. Phys. A 831 (2009) 59–90. `arXiv:0902.0741`, `doi:10.1016/j.nuclphysa.2009.09.002`.

[285] A. Ayala, C. A. Dominguez, L. A. Hernandez, M. Loewe, A. Raya, J. C. Rojas, C. Villavicencio, Thermomagnetic properties of the strong coupling in the local Nambu–Jona-Lasinio model, Phys. Rev. D 94 (5) (2016) 054019. `arXiv:1603.00833`, `doi:10.1103/PhysRevD.94.054019`.

[286] S. I. Finazzo, R. Critelli, R. Rougemont, J. Noronha, Momentum transport in strongly coupled anisotropic plasmas in the presence of strong magnetic fields, Phys. Rev. D 94 (5) (2016) 054020, [Erratum: Phys.Rev.D 96, 019903 (2017)]. `arXiv:1605.06061`, `doi:10.1103/PhysRevD.94.054020`.

[287] S. Li, J. Liao, Data-driven extraction of heavy quark diffusion in quark-gluon plasma, Eur. Phys. J. C 80 (7) (2020) 671. `arXiv:1912.08965`, `doi:10.1140/epjc/s10052-020-8243-9`.

[288] G. S. Bali, F. Bruckmann, G. Endrodi, Z. Fodor, S. D. Katz, A. Schafer, QCD quark condensate in external magnetic fields, Phys. Rev. D 86 (2012) 071502. `arXiv:1206.4205`, `doi:10.1103/PhysRevD.86.071502`.

[289] K. G. Klimenko, Three-dimensional Gross-Neveu model at nonzero temperature and in an external magnetic field, Z. Phys. C 54 (1992) 323–330. `doi:10.1007/BF01566663`.

[290] I. A. Shushpanov, A. V. Smilga, Quark condensate in a magnetic field, Phys. Lett. B 402 (1997) 351–358. `arXiv:hep-ph/9703201`, `doi:10.1016/S0370-2693(97)00441-3`.

[291] J. K. Boomsma, D. Boer, The Influence of strong magnetic fields and instantons on the phase structure of the two-flavor NJL model, Phys. Rev. D 81 (2010) 074005. `arXiv:0911.2164`, `doi:10.1103/PhysRevD.81.074005`.

[292] M. D'Elia, S. Mukherjee, F. Sanfilippo, QCD Phase Transition in a Strong Magnetic Background, Phys. Rev. D 82 (2010) 051501. `arXiv:1005.5365`, `doi:10.1103/PhysRevD.82.051501`.

[293] F. Preis, A. Rebhan, A. Schmitt, Inverse magnetic catalysis in dense holographic matter, JHEP 03 (2011) 033. `arXiv:1012.4785`, `doi:10.1007/JHEP03(2011)033`.

[294] M. D'Elia, F. Manigrasso, F. Negro, F. Sanfilippo, QCD phase diagram in a magnetic background for different values of the pion mass, Phys. Rev. D 98 (5) (2018) 054509. `arXiv:1808.07008`, `doi:10.1103/PhysRevD.98.054509`.

[295] G. Endrodi, M. Giordano, S. D. Katz, T. Kovács, F. Pittler, Magnetic catalysis and inverse catalysis for heavy pions, JHEP 07 (2019) 007. `arXiv:1904.10296`, `doi:10.1007/JHEP07(2019)007`.

[296] M. S. Ali, C. A. Islam, R. Sharma, QCD phase diagram in the T–eB plane for varying pion mass, Phys. Rev. D 110 (9) (2024) 096011. `arXiv:2407.14449`, `doi:10.1103/PhysRevD.110.096011`.

[297] A. Tomiya, H.-T. Ding, S. Mukherjee, C. Schmidt, X.-D. Wang, Chiral phase transition of three flavor QCD with nonzero magnetic field using standard staggered fermions, EPJ Web Conf. 175 (2018) 07041. `arXiv:1711.02884`, `doi:10.1051/epjconf/201817507041`.

[298] T. D. Cohen, N. Yamamoto, New critical point for QCD in a magnetic field, Phys. Rev. D 89 (5) (2014) 054029. `arXiv:1310.2234`, `doi:10.1103/PhysRevD.89.054029`.

[299] G. Endrodi, Critical point in the QCD phase diagram for extremely strong background magnetic fields, JHEP 07 (2015) 173. `arXiv:1504.08280`, `doi:10.1007/JHEP07(2015)173`.

[300] M. D'Elia, L. Maio, F. Sanfilippo, A. Stanzione, Phase diagram of QCD in a magnetic background, Phys. Rev. D 105 (3) (2022) 034511. `arXiv:2111.11237`, `doi:10.1103/PhysRevD.105.034511`.

[301] D. Ebert, K. G. Klimenko, M. A. Vdovichenko, A. S. Vshivtsev, Magnetic oscillations in dense cold quark matter with four fermion interactions, Phys. Rev. D 61 (2000) 025005. `arXiv:hep-ph/9905253`, `doi:10.1103/PhysRevD.61.025005`.

[302] D. P. Menezes, M. Benghi Pinto, S. S. Avancini, A. Perez Martinez, C. Providencia, Quark matter under strong magnetic fields in the Nambu-Jona-Lasinio Model, Phys. Rev. C 79 (2009) 035807. `arXiv:0811.3361`, `doi:10.1103/PhysRevC.79.035807`.

[303] M. Ferreira, P. Costa, O. Lourenço, T. Frederico, C. Providência, Inverse magnetic catalysis in the (2+1)-flavor Nambu-Jona-Lasinio and Polyakov-Nambu-Jona-Lasinio models, Phys. Rev. D 89 (11) (2014) 116011. `arXiv:1404.5577`, `doi:10.1103/PhysRevD.89.116011`.

[304] R. L. S. Farias, V. S. Timoteo, S. S. Avancini, M. B. Pinto, G. Krein, Thermo-magnetic effects in quark matter: Nambu–Jona-Lasinio model constrained by lattice QCD, Eur. Phys. J. A 53 (5) (2017) 101. `arXiv:1603.03847`, `doi:10.1140/epja/i2017-12320-8`.

[305] E. S. Fraga, A. J. Mizher, Chiral transition in a strong magnetic background, Phys. Rev. D 78 (2008) 025016. `arXiv:0804.1452`, `doi:10.1103/PhysRevD.78.025016`.

[306] M. Ruggieri, M. Tachibana, V. Greco, Renormalized vs Nonrenormalized Chiral Transition in a Magnetic Background, JHEP 07 (2013) 165. `arXiv:1305.0137`, `doi:10.1007/JHEP07(2013)165`.

[307] S. Chakrabarty, Quark matter in strong magnetic field, Phys. Rev. D 54 (1996) 1306–1316. `arXiv:hep-ph/9603406`, `doi:10.1103/PhysRevD.54.1306`.

[308] E. S. Fraga, L. F. Palhares, Deconfinement in the presence of a strong magnetic background: an exercise within the MIT bag model, Phys. Rev. D 86 (2012) 016008. `arXiv:1201.5881`, `doi:10.1103/PhysRevD.86.016008`.

[309] R. Gatto, M. Ruggieri, Dressed Polyakov loop and phase diagram of hot quark matter under magnetic field, Phys. Rev. D 82 (2010) 054027. `arXiv:1007.0790`, `doi:10.1103/PhysRevD.82.054027`.

[310] A. J. Mizher, M. N. Chernodub, E. S. Fraga, Phase diagram of hot QCD in an external magnetic field: possible splitting of deconfinement and chiral transitions, Phys. Rev. D 82 (2010) 105016. `arXiv:1004.2712`, `doi:10.1103/PhysRevD.82.105016`.

[311] S. S. Avancini, R. L. S. Farias, N. N. Scoccola, W. R. Tavares, NJL-type models in the presence of intense magnetic fields: the role of the regularization prescription, Phys. Rev. D 99 (11) (2019) 116002. `arXiv:1904.02730`, `doi:10.1103/PhysRevD.99.116002`.

[312] V. P. Pagura, D. Gomez Dumm, S. Noguera, N. N. Scoccola, Magnetic catalysis and inverse magnetic catalysis in nonlocal chiral quark models, Phys. Rev. D 95 (3) (2017) 034013. `arXiv:1609.02025`, `doi:10.1103/PhysRevD.95.034013`.